

University of Northern Colorado

## Scholarship & Creative Works @ Digital UNC

---

Master's Theses

Student Work

---

5-2021

### Synthesis of Functionalized Ionic Liquids for Coal Dissolution and Pretreatment

Michael Franklin

*University of Northern Colorado*

Follow this and additional works at: <https://digscholarship.unco.edu/theses>

---

#### Recommended Citation

Franklin, Michael, "Synthesis of Functionalized Ionic Liquids for Coal Dissolution and Pretreatment" (2021). *Master's Theses*. 198.

<https://digscholarship.unco.edu/theses/198>

This Thesis is brought to you for free and open access by the Student Work at Scholarship & Creative Works @ Digital UNC. It has been accepted for inclusion in Master's Theses by an authorized administrator of Scholarship & Creative Works @ Digital UNC. For more information, please contact [Nicole.Webber@unco.edu](mailto:Nicole.Webber@unco.edu).

© 2021

MICHAEL SEAN FRANKLIN

ALL RIGHTS RESERVED

UNIVERSITY OF NORTHERN COLORADO

Greeley, Colorado

The Graduate School

SYNTHESIS OF FUNCTIONALIZED IONIC LIQUIDS FOR  
COAL DISSOLUTION AND PRETREATMENT

A Thesis Submitted in Partial Fulfillment  
of the Requirements for the Degree of  
Master of Science

Michael Franklin

College of Natural and Health Sciences  
Department of Chemistry and Biochemistry

May 2021

This Thesis by: Michael Franklin

Entitled: *Synthesis of Functionalized Ionic Liquids for Coal Dissolution and Pretreatment*

has been approved as meeting the requirements for the Degree of Master of Science in the Department of Chemistry and Biochemistry in the College of Natural and Health Sciences.

Accepted by the Thesis Committee:

---

Hua Zhao, Ph.D., Chair

---

Michael D. Mosher, Ph.D., Committee Member

---

Richard W. Schwenz, Ph.D., Committee Member

Accepted by the Graduate School

---

Jeri-Anne Lyons, Ph.D.  
Dean of the Graduate School  
Associate Vice President for Research



## ABSTRACT

Franklin, Michael. *Synthesis of Functionalized Ionic Liquids for Coal Dissolution and Pretreatment*. Unpublished Master of Science thesis, University of Northern Colorado, 2021.

Brown coal (lignite) is a bulk organic mixture of conjugated hydrocarbons that are complexed together via hydrogen bonds. Coal [partial] dissolution is essential to the better utilization of low-rank coal for power sources because the direct combustion of brown coal is not energy efficient. To break hydrogen bonds of low-rank coal and make it partially soluble, this project evaluates a series of ionic liquids (ILs) with specific properties as non-volatile alternatives to conventional organic solvents. A series of nitrogen- and phosphorus-based cations have been synthesized via a nucleophilic substitution reaction, the resultant bromide-based IL being converted to an acetate-based IL through an ion-exchange procedure in methanol. Water concentration and viscosity measurements, along with thermogravimetric and nuclear magnetic resonance ( $^1\text{H}$  and  $^{13}\text{C}$  NMR) analyses, were conducted to confirm the IL structure and thermal stability. Hydrogen-bond acidity, basicity, and polarity of these ILs were measured using various dyes. We further determined the capability of these ILs for dissolving cellulose and pretreating brown coal at 100 °C. The IL-treated coal samples were analyzed by Fourier Transform Infrared (FTIR) spectroscopy, thermogravimetric analysis (TGA), scanning electron microscopy (SEM), and X-ray diffraction (XRD). Through a combined analysis of our experimental results, we concluded that hydrophilic acetate-ILs dissolve both cellulose and lignite, the latter evidenced through thorough evaluation of FTIR, XRD, and SEM analysis.

## TABLE OF CONTENTS

I.	INTRODUCTION.....	01
II.	REVIEW OF LITERATURE.....	05
	Ionic Liquids and How They Came to Mean So Much	
	Physiochemical Properties of Ionic Liquids	
	Coal and What it is Made Of	
	Use of Ionic Liquids to Pretreat (Dissolve or Swell) Coal	
III.	METHODOLOGY.....	20
	Research Objectives	
	Synthesis of Ionic Liquids	
	Characterization of Ionic Liquids	
	Dissolution of a Model Coal Compound: Cellulose	
	Dissolution and Fragmentation of Lignite	
IV.	RESULTS.....	34
	Synthesis of Ionic Liquids	
	Appel Reaction	
	Synthesis of Brominated Ionic Liquids	
	Ion Exchange	
	Structure Verification via Nuclear Magnetic Resonance	
	IL Characterization of Physicochemical Properties	
	Water Titration	
	Viscometry	
	Thermogravimetric Analysis	
	Kamlet-Taft Parameters of Polarity/Polarizability	
	Dissolution of a Model Coal Compound: Cellulose	
	Dissolution of Coal in Select Ionic Liquids	
	Thermogravimetric Analysis of Coal/Ionic Liquid Samples	
	Fourier Transform Infrared (FTIR) Spectroscopy Analysis of Cellulose and Coal Dissolution	
	Liquid Chromatography-Mass Spectrometry (LC-MS)	
	Scanning Electron Microscope (SEM) with Energy Dispersive X-ray Spectroscopy (EDS)	
	X-ray Diffraction (XRD) Analysis	
	Discussion	
V.	CONCLUSION.....	87

REFERENCES.....	90
-----------------	----

APPENDIX

A. Reagent Specifications and Sources.....	97
B. Ionic Liquid Structures and Naming Schematic.....	99
C. Comprehensive Physiochemical Properties of Ionic Liquids.....	112
D. Instrumental Analysis Spectra and Photos.....	136
FTIR Spectra for IL Structure Confirmation	
FTIR Spectra for Cellulose Dissolution	
TGA Scans for Coal Dissolution	
<sup>1</sup> H NMR Spectra for IL Structure Confirmation	
LC-MS Spectra for Coal Dissolution Analysis	
SEM Images for Coal After Dissolution	
EDS Analysis for Coal Samples After Dissolution	
XRD Spectra and Calculations	

## LIST OF TABLES

<b>2.1</b>	Dynamic viscosities ( $\eta$ ) of selected ILs (in mPa·s).....	11
<b>3.1</b>	The Chosen Ones. The five (5) ILs identified for cellulose and coal dissolution due to low viscosity, high temperature of degradation, and ideal hydrogen-bond basicity ( $\beta$ ) values.....	29
<b>4.1</b>	Products of the Appel reaction synthesis. Sample AR01 is reacted with pyridine to produce sample R29, as outlined in section 4.1.2.....	38
<b>4.2</b>	Viscosity measurements for chosen ILs. IL A28 is much higher than preferred; however, it is a tried and tested IL that is found throughout the literature. Cellulose and coal are expected to dissolve very well in A28.....	44
<b>4.3</b>	Comparison of TGA profiles for three ILs with the same cation. Anions $\text{Tf}_2\text{N}^-$ and $\text{PF}_6^-$ cause the IL to display hydrophobic characteristics. These ILs were synthesized and analyzed by Zhao et al. (2018).....	45
<b>4.4</b>	Results of TGA for the five chosen ILs to be used for cellulose and coal dissolution. Char (wt %) is “the amount of carbon char residue determined from the relative mass remaining at 600 °C; a residue amount on the order of $\pm 1$ -2% should be considered within the error of the measurement baseline” (Zhao et al., 2018). RG28 is the reagent grade [BMIM][OAc] for comparison to A28.....	50
<b>4.5</b>	Literature values for Kamlet-Taft measurements of water, organic solvents, and select BMIM <sup>+</sup> ILs. $E_T^N$ , $\alpha$ , $\beta$ , and $\pi^*$ values were provided by Lee et al. (2008); $E_T(30)$ , $\lambda_{RD}(nm)$ , $\lambda_{NA}(nm)$ , $\nu_{NA}$ , $\lambda_{DENA}(nm)$ , and $\nu_{DENA}$ values were backwards calculated using Equations 2.2.1 through 2.2.5.....	51
<b>4.6</b>	Experimental values for the dissolution of cellulose. Samples A01, A12, A16, A28, and A30 were synthesized in lab and the corresponding $\beta$ values were derived from UV-Vis analysis discussed in section 4.2.4. <sup>(a)</sup> Literature value for $\beta$ for RG28 is found in Ladesov et al. (2015).....	54
<b>4.7</b>	Masses of IL and coal used in the dissolution process and the mass of coal recovered after dissolution and washing.....	56
<b>4.8</b>	FTIR peaks identified by the OMNIC FTIR software. Lignite (top) shows evidence of alkane, alkene, and alkyne stretching, as well as C-H bending and some C-O	64

stretching. IL-dissolved samples show an increase in C-C, C=C, and C≡C stretching, increased C-H bending, and more peaks in the fingerprint region.....

**4.9** Characteristics of lignite following IL pretreatment..... 65

**4.10** LC-MS results for liquid portion of IL/coal dissolution. All peaks are reported in mass-to-charge (m/z) ratios. IL molecular weight are listed below each sample batch for reference..... 66

**4.11** EDS results for lignite and IL-pretreated lignite. Sample nomenclature uses CXX-AXX naming scheme, with CXX referring to vial number and AXX referring to the IL used to pretreat lignite. All samples were solid and dried prior to SEM/EDS analysis. The first sample listed is the EDS spectrum for a particle, second sample represents area analysis at 750× zoom..... 73

**4.12** XRD analysis derived after the fit of two Gaussian distribution curves for the 20° (100, γ-band) and 26° (002, π-band) peaks..... 75

**4.13** Analysis of UV-Vis measurements for Reichardt’s dye using known organic solvents; literature values provided by Lee et al. (2008)..... 80

## LIST OF FIGURES

<b>1.1</b>	Nucleophilic substitution reaction ( $S_N2$ ) between 1-methylimidazole and bromoethane.....	02
<b>2.1</b>	Nucleophilic substitution between 1-methylimidazole and bromoethane in acetonitrile to form 1-ethyl-3-methylimidazolium bromide, abbreviated as [EMIM][Br], ~96% yield with 10% molar excess of bromoethane.....	07
<b>2.2</b>	Representative structures of cations and anions that are of interest to this study.....	09
<b>2.3</b>	Model representations of chemical structures of various classes of coal. This model serves to represent the differences in aromatic carbons between the high ranked anthracite and that of the low ranked lignite (brown coal).....	16
<b>2.4</b>	Lignin, a complex polymer found in the degradation process of plant material, is the second most abundant natural polymer.....	17
<b>3.1</b>	Synthesis of IL [BMIM][Br].....	22
<b>3.2</b>	Visual representation of ion exchange procedure.....	25
<b>4.1</b>	Appel reaction, converting diethylene glycol monomethyl ether into 2-bromoethyl 2-methoxyethyl ether. The Appel reaction is used to convert primary or secondary alcohols into brominated compounds to be used in IL synthesis.....	35
<b>4.2</b>	Results of the three Appel reactions.....	36
<b>4.3</b>	Results of the IL synthesis (left) and ion exchange (right). Color, physical state, and viscosity vary greatly depending on the cation used to synthesize each IL.....	40
<b>4.4</b>	$^1\text{H}$ NMR spectrum comparison for the synthesis of R28. Top-left: $^1\text{H}$ NMR for 1-ethylimidazole. Top-right: $^1\text{H}$ NMR for 1-bromobutane. Right: $^1\text{H}$ NMR for product [BMIM][Br].....	44
<b>4.5</b>	Comparison of $^1\text{H}$ NMR for sample R28 (left) to sample A28 (right). The acetate functional group is shifted to the left (down field?) and interacts with the acidic proton of imidazole.....	45

<b>4.6</b>	Thermogravimetric analysis (TGA) of sample A30. “ $T_{der}$ is determined from the maximum in the first-derivative profile of the TGA scan. $T_{dcp}$ is the decomposition temperature measured as the onset of decomposition, using the common criterion of 10% total mass loss”.....	47
<b>4.7</b>	Kamlet-Taft dyes. Top: Reichardt’s dye. Bottom left: 4-nitroaniline. Bottom right: N,N-diethyl-4-nitroaniline.....	50
<b>4.8</b>	Cellulose monomer, otherwise known as cellobiose (Hamad, 2017).....	52
<b>4.9</b>	Experimental set-up of dissolution of cellulose.....	53
<b>4.10</b>	TGA scan of untreated lignite (left) and lignite treated with A30 (right).....	57
<b>4.11</b>	TGA scans of the chosen ILs and RG28.....	58
<b>4.12</b>	FTIR scans for ILs.....	61
<b>4.13</b>	FTIR scans for Cellulose and IL after dissolution.....	61
<b>4.14</b>	FTIR scans of lignite before (top) and after dissolution with the specific ILs.....	63
<b>4.15</b>	SEM images taken of lignite 30x (left) and 1000x (right) zoom. All samples were coated with ~15 nm of elemental gold (Au) to reduce charging, which is still evidenced in the brighter particles in each image.....	67
<b>4.16</b>	SEM images of lignite before and after dissolution with ILs. Samples use a CXX-AXX nomenclature, with CXX referring to the vial number and AXX referring to the IL used for dissolution. Photos on the left are at 100× zoom and the photos on the right were taken at 1,000× zoom.....	70
<b>4.17</b>	EDS analysis of $KMnO_4$ resulted in detection of oxidation of the sample. The experimental formula was determined to be $KMnO_{5.22}$ . Electron accelerating voltage was 15 kV, SS60, and the image was taken at 750x zoom.....	72
<b>4.18</b>	Graphical representation of the number of X-ray counts vs. angle measure detected via XRD. The gray data points represent raw data; the red and green curves were calculated via Gaussian distributions; the black curve is a linear combination of the two Gaussian distributions.....	74
<b>4.19</b>	NMR spectra for sample A28 before (left) and after (right) modification of the ion exchange procedure.....	77
<b>4.20</b>	Thermogravimetric analysis of IL A01 before (left) and after (right) modification to the ion exchange procedure.....	79

**4.21** SEM images of coal dissolution of lignite (left) versus lignite after dissolution with A30 (right). Parameters of the SEM was an accelerating voltage of 15 kV, spot size of 60, and 1000x zoom. Fiduciary in the lower right corner of each image is scaled to 10  $\mu\text{m}$ ..... 83

**4.22** EDS analysis of Lignite, taken with accelerating voltage of 15 kV, spot size of 60, and 750x zoom. Spectrum 1 was performed on single mass of lignite, Spectrum 2 was an area analysis outlined in the above image..... 85

**4.23** EDS analysis of Lignite after dissolution with IL A30, taken with accelerating voltage of 15 kV, spot size of 60, and 750x zoom. .... 86



## CHAPTER I

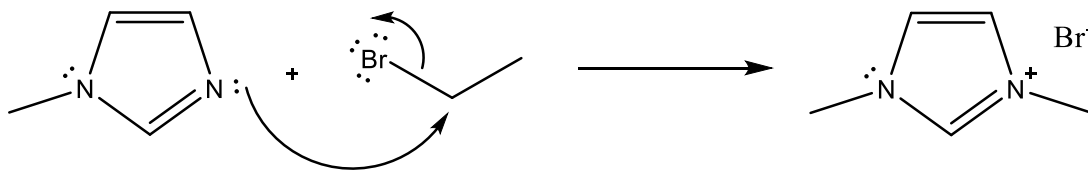
### INTRODUCTION

An ionic compound is defined as “a substance in which component species are cations and anions” (Masterton et al., 1985), examples of which include sodium chloride (NaCl), calcium hydroxide (Ca(OH)<sub>2</sub>), and ammonium nitrate (NH<sub>4</sub>NO<sub>3</sub>). Introductory students learn to distinguish between ionic and covalent-bonded organic compounds by comparing the included species: a cation (positively charged atom or molecule) and an anion (negatively charged atom or molecule) form an ionic compound, while carbon, hydrogen, nitrogen, and oxygen atoms combine to form organic species via covalent bonds. The definition of an ionic compound doesn't mention metals, nonmetals, or even carbon, hydrogen, and oxygen-containing compounds; rather the definition only refers to the formal charge of the ions present in the compound.

Consider an organic nucleophilic substitution reaction between a nitrogen-containing heterocyclic nucleophile, such as 1-methylimidazole, and a halogen-containing electrophile, such as bromoethane (Figure 1.1). A lone-pair of electrons from one of the imidazole nitrogen atoms reacts with the electrophilic carbon of the bromoethane, with the bromide ion acting as the leaving group. The resultant product is 1-ethyl-3-methylimidazolium ion, a cation that is stabilized via resonance. The leaving group, Br<sup>-</sup>, is then electrostatically attracted to the cation, and an ionic compound is formed. These ionic compounds have lower melting points (<100 °C) than traditional ionic compounds (i.e. NaCl) and are known as ILs.

Ionic liquids (ILs) have been at the forefront of chemical research since the 1990s, with the number of potential compounds numbering in the millions (Caminiti & Gontrani, 2014). IL refers to any ionic compound that exists as a liquid at or below 100 °C. Molten salts, for example, are ionic compounds that are liquids at very high temperatures, whereas RTIL refers to room-temperature ILs, examples of which include the 1-ethyl-3-methylimidazolium acetate compound. Of particular interest are some applications of ILs in various industries, specifically the coal and energy industry.

**Figure 1.1:** Nucleophilic substitution reaction ( $S_N2$ ) between 1-methylimidazole and bromoethane.



ILs have revolutionized research labs and industrial processes, due not only to their versatility, but also their potential for green chemistry. Green chemistry refers to the belief that advancements in science and technology should be done without harming or negatively impacting the environment (Rogers et al., 2002). Too many chemical processes require egregious amounts of organic solvents or produce entirely too much waste that is not disposed of simply. Toxic industrial chemicals and materials pose a significant threat to plants, animals, and water sources; significant advances in chemistry have been made to reduce these wastes. "... [I]t should be noted that one property of low vapor pressure does not make ILs green. If ILs are toxic and non-biodegradable, they are not green" (Plechkova & Seddon, 2008).

The first principle of green chemistry, as written by Anastas and Warner (1998) and endorsed by the ACS, is that "it is better to prevent waste than to treat or clean up waste after it is formed." There exist twelve (12) principles of green chemistry that establish basic guidelines for

chemists and engineers to follow that will improve upon the efficiency of chemistry and protect the environment from needless waste and abuse. Seeing how IL research is a fundamentally new division of chemical research, researchers must consider all of these principles and adapt their research to best support this particular initiative.

ILs have the potential to be used in novel applications that would better develop chemical processes and uphold the principles of green chemistry. ILs as solvents could effectively reduce the number of solvents required for chemical reactions, thus keeping to the fifth principle: benign solvents and auxiliaries. With regards to laboratory safety, utilizing chemicals and procedures that are inherently benign reduces the risk to human health, as well as the use of chemicals that pose little threat to health and environmental risks, following the principles for green chemistry. Conforming to the twelve principles of green chemistry “is doing chemistry the way nature does chemistry – using renewable, biodegradable materials which do not persist in the environment” (Anastas & Warner, 1998).

Coal and other petroleum-based compounds are precious resources that researchers cannot seem to find a viable application that limits the amount of waste produced during consumption. It stands to reason that any advancement in the complete and effective usage of coal would be an ideal research topic to investigate and could very well contribute significant findings to the industrial applications of coal. By identifying the specific characteristics of some novel ILs, it is possible to identify suitable ILs to aid in the liquefaction, dissolution, or separation of coal and its substituents to better separate and consume the entirety of coal samples.

## Research Objectives

- O1 Synthesize ILs by combining different cations and anions. Cost, ease of synthesis, and variations in physicochemical properties were considered during synthesis. Hydrophilic ILs were the primary focus of this project.
- O2 Characterize ILs to identify physical and chemical properties that assisted in the coal dissolution process. The focus was placed on water concentration, viscosity, degradation temperature, structure verification, and hydrogen bond donor/acceptor properties.
- O3 Dissolution and characterization of coal model compounds to determine the viability of specific ILs for coal dissolution.
- O4 Dissolution and characterization of brown coal (lignite) using select ILs. Identification of extent of dissolution, swelling, and fragmentation was verified via instrumental analysis of samples. Recovery of IL from coal was possible; however, it is not a primary task for this analysis.

## CHAPTER II

### REVIEW OF LITERATURE

#### **Ionic Liquids and How They Came to Mean So Much**

In 1914, a Russian/Latvian/German chemist named Paul Walden documented the formation of an ionic liquid via a neutralization reaction of ethylamine ( $\text{CH}_3\text{CH}_2\text{NH}_2$  or  $\text{EtNH}_2$ ) and concentrated nitric acid ( $\text{HNO}_3$ ). The resultant compound, ethyl ammonium nitrate,  $[\text{EtNH}_3][\text{NO}_3]$ , has a melting point of 13-14 °C and opened a realm of possibilities for chemistry and chemical engineering research and development (Plechko & Seddon, 2008). Over the next half-century, researchers dabbled with molten salts, which are ionic compounds with melting points well above 250 °C, and decided that compounds with significantly lower melting points were necessary if they were to find suitable applications in industry and manufacturing processes (Welton, 2018).

The difference between conventional molten salts and ILs is the temperature at which the compound becomes a liquid. High-melting salts, or conventional molten salts, are considered ionic compounds with a melting point above 250 °C (e.g., sodium hydroxide,  $\text{NaOH}$ , 318 °C), low-melting ionic salts have a melting point between 100 °C and 250 °C (lithium aluminum chloride,  $\text{LiAlCl}_4$ , 148 °C), while ILs have melting points below 100 °C (e.g., 1-ethyl-3-methylimidazolium bromide,  $[\text{EMIM}][\text{Br}]$ , 79 °C) (Marcus, 2016).

Chloroaluminate molten salts, discovered by the Osteryoung group in 1975, fluctuate with regards to melting points depending on the molar ratio of their anion and cation. For

example, 100 mol% of  $\text{AlCl}_3$  has a melting point of  $192\text{ }^\circ\text{C}$ ,  $\text{NaCl-AlCl}_3$  (considered as  $\text{Na}^+$  and  $\text{AlCl}_4^-$ ) has a melting point of  $151\text{ }^\circ\text{C}$ , and  $\text{LiCl-AlCl}_3$  ( $\text{Li}^+$  and  $\text{AlCl}_4^-$ ) has a melting point of  $144\text{ }^\circ\text{C}$  (Plechko & Seddon, 2008). It was determined that the stability/moisture-sensitivity of these compounds made them difficult to work with, as impurities from reactions with water required the use of a dry box (Welton, 2018).

The development of air and water-stable ILs began a new era of research. As an example, Wilkes, Evans, Magnuson, Pacholec, Poole, Seddon, and Osteryoung began investigating molten salts with lowered melting points and their respective physical properties, considering their applications in chromatography and synthesis (Welton, 2018). In 1992, the Wilkes' group investigated the preparation and characterization of low melting salts previously only predicted to exist (Wilkes & Zaworotko, 1992). Research by Welton (2018) discovered that there “appear[s] to have initiated a period of growth in the number and range of ILs.” This period also saw a growth in the interest in ILs as solvents for chemical reactions, without necessarily “being a component of the reaction itself” (Welton, 2018).

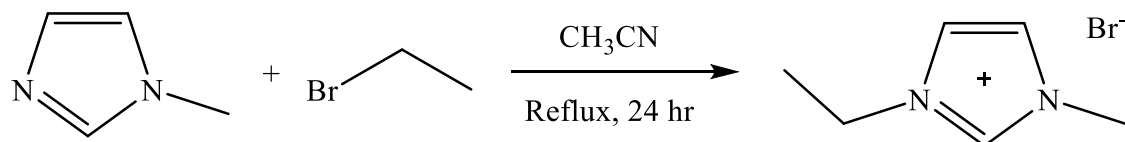
To further understand these novel solvents, we must define certain terms regarding ILs. We begin by defining what an IL is and why it is important in this research. There is not a strict definition of an ionic liquid. A common understanding of an ionic liquid is that it is a pure compound consisting entirely of ions with a melting point below  $100\text{ }^\circ\text{C}$ ; therefore, the first variable in defining an ionic liquid is to recognize that it has a low melting point. Sodium chloride has a melting point of  $801\text{ }^\circ\text{C}$  as compared [BMIM][Cl] which has a melting point of  $73\text{ }^\circ\text{C}$ ; the former is the molten salt while the latter is an IL.

According to researchers at the Beijing Key Laboratory of Lignocellulosic Chemistry, an ionic liquid “is defined as a class of environmentally friendly organic salts with high thermal

stability, negligible vapor pressure, wide liquid range, and tunable solvation properties” (Pang et al., 2016). ILs are comprised of a cation and anion bound to one another through “the electrostatic attraction between the ions” (Daintith, 2008). Changing either ion will inevitably alter the physicochemical properties of the compound, a point of emphasis for this research project.

Generally referred to as RTILs, or room-temperature ILs, these are “salts with a melting point below room temperature at atmospheric pressure. They consist of an organic cation and an inorganic or organic anion” (Romich et al., 2012). Using the vernacular associated with organic chemistry, a second-order nucleophilic substitution reaction ( $S_N2$ ) between a nucleophile and electrophile has the potential of producing this type of ionic structure. Figure 2.1 illustrates the synthesis scheme of 1-ethyl-3-methylimidazolium bromide, [EMIM][Br], one of the many IL precursors that are of interest to this study. The reaction between 1-methylimidazole as nucleophile and ethyl bromide as the electrophile is the classical nucleophilic attack of the electrophilic carbon of ethyl bromide by a lone-pair-containing nucleophile. The resultant ionic compound consists of a cation [EMIM]<sup>+</sup> and an anion [Br]<sup>-</sup>, which attract each other via the electrostatic interaction forming an ionic network.

**Figure 2.1:** Nucleophilic substitution between 1-methylimidazole and bromoethane in acetonitrile to form 1-ethyl-3-methylimidazolium bromide, abbreviated as [EMIM][Br], ~96% yield with 10% molar excess of bromoethane.



While some common ILs comprise an organic heterocyclic cation and either inorganic or organic anions, these are not the only ILs that can be produced (Seddon, 1997). Many ILs have non-heterocyclic cations, such as quaternary alkylammonium, phosphonium, and sulfonium, etc.

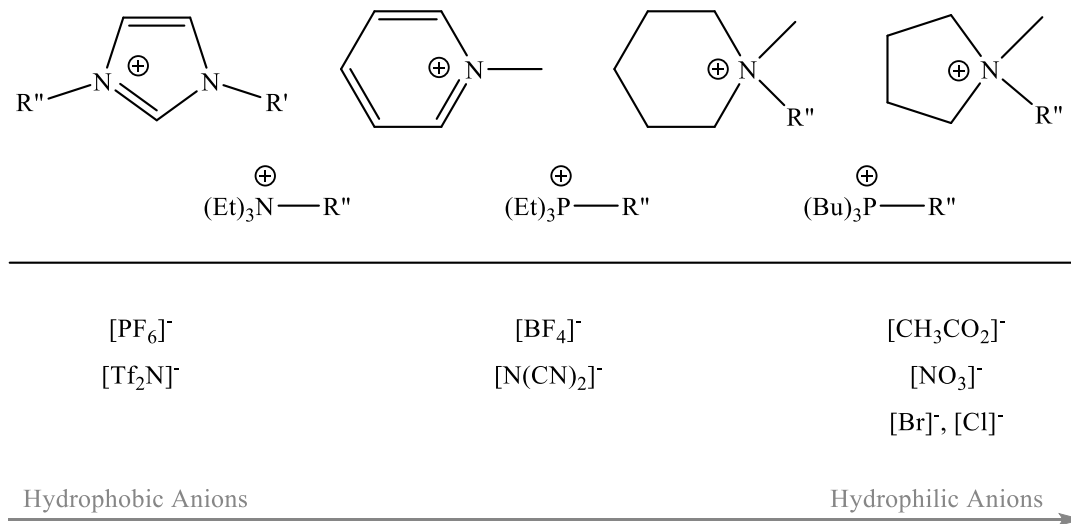
ILs have been nicknamed ‘designer’ solvents for their variations of cation and anion, with the creativity of the researcher being the only restriction of possible structures. There exist so many combinations of cation and anion that in 2000 an Advanced Research Workshop sponsored by NATO met to establish guidelines for research and development of ILs and the systematic accounting of structures and their properties (Plechkova & Seddon, 2008). This committee established ten criteria that must be met by the scientific community, one of which required “a public (free), verified, web-based database of physical, thermodynamic, and related data (*i.e.*, not process specific)” (Rogers et al., 2002).

The database required by the NATO-sponsored workshop was established in 2003 by the National Institute of Standards and Technology (NIST) in Boulder, CO, developed by A. Kazakov, J.W. Magee, R.D. Chirico, E. Paulechka, V. Kiky, C.D. Muzny, K. Kroenlein, and M. Frenkel. ILThermo, formally named NIST Standard Reference Database #147 (Kazakov et al., 2019), was established as a means of providing a current, worldwide database on ILs that provides information on types and structures of ILs, thermodynamic and thermochemical properties, as well as references to scientific journals pertinent to the characterizations of said ILs. As of July 14, 2020, the database included information on 706,888 pure, binary, and ternary mixtures of ILs (Dong et al., 2004; Kazakov et al., 2019).

Figure 2.2 is a representation of some common cation and anion constituents that will be the focus of this proposal. While not all cations consist of heterocyclic structures, they all contain either nitrogen or phosphorus with varying lengths of ether-functionalized or alkyl chains attached to the non-carbon heteroatom. Regarding anions, acetate will be the primary focus; however, dicyanamide, bromide, and chloride anions will be considered.



**Figure 2.2:** Representative structures of cations and anions that are of interest to this study (Plechko & Seddon, 2008).



### Physiochemical Properties of Ionic Liquids

Physiochemical properties are important to the understanding of IL structures and their applications. These properties include the basics (i.e., formula weight, boiling point, melting point, and density, etc.) as well as other properties (i.e., viscosity, vapor pressure, crystallographic structure, thermal stability, and decomposition temperature/pattern, etc.). Many of these properties are simple to identify using established laboratory techniques in a controlled environment. Others are more difficult to ascertain due to the complexity of instrumentation and available resources; however, their results can speak volumes on the applicability and versatility of newly synthesized compounds.

ILs are designer compounds, meaning they can be “tailored to have a specific property or...be used in a specific application” (Corchero et al., 2019). Before discussing the surfeit of applications for which ILs have been applied, we should consider why and how ILs can be tailored to exhibit various properties. “Their physical and chemical properties (such as hydrophobicity, polarity, and miscibility) can be finely customized for a range of applications

through varying the structures of cations or anions and their combinations” (Zhao, 2006). We will first consider a few highly important characteristics of ILs, followed by an evaluation of that elusive categorization as ‘green’ chemical agents.

Manipulation of the cation and anion results in different physicochemical properties of ILs. Instead of a traditional metal cation in an ionic compound, the use of “unsymmetrical organic cations depress the melting point to temperatures at or below room temperature” (Seddon, 1997). The use of symmetrical or long-chain alkyl groups on the cation will do the opposite, increasing the melting point and viscosity of the ionic liquid (Zhao et al., 2018). Manipulation of the structure of the anion will affect properties such as hydrophobicity, viscosity, and thermal stability of ILs.

In the case of all chemical analysis, the purity of our compounds can make a significant difference in our observations and conclusions. “Probably the most amateurish error present in unreliable ionic liquid papers is [the] failure to report the purity of the employed ionic liquid(s)” (Deetlefs & Seddon, 2006). There is no ignominy in accounting for impurities in reagents and products; however, it is improper not to disclose this information. Part of the scientific method is to allow for results to be reproducible and confirmable, and the lack of purity analysis undermines the value of these results (Deetlefs & Seddon, 2006).

The three most immediately recognizable physical properties of ILs include their physical state at room temperature, viscosity, and color. The color of the ionic liquid can be attributed to three phenomena: overheating of ILs, chromophores generated in isothermal reactions at room temperature, or chromophoric impurities resulting during synthesis. “Although the colored impurities might be aesthetically displeasing, there is no evidence that the chromophoric impurities affect either the chemistry or the physical properties of ILs,” however spectroscopic

analysis of ILs can be impacted when the measurement relies on light absorption or emission, i.e., UV-Vis, FT-IR, and Raman spectroscopy (Earle et al., 2007).

Temperature-dependent properties, such as physical form and viscosity, must be considered during the analysis of ILs. As mentioned previously, RTILs are special ILs that are liquid at room temperature and atmospheric pressure. Viscosity is an important property of liquids, and thus an analysis of RTIL will take precedence over ILs that are liquids closer to 100 °C. Table 2.1 is a representation of many different ILs and their respective viscosity measurements, many taken from literature sources, while some ILs have been evaluated for this research project.

**Table 2.1:** Dynamic viscosities ( $\eta$ ) of selected ILs (in mPa·s)  
Note: Reference (1) is Fendt et al., 2011, and reference (2) is Zhao et al., 2019.

Ionic Liquid	Solvent Water Content (% by mass)	Dynamic Viscosity at 30°C (mPa·s)
(1) [BMIM][PF <sub>6</sub> ]	0.01	205.8
(1) [BMIM][Tf <sub>2</sub> N]	0.01	41.4
(1) [BMIM][BF <sub>4</sub> ]	0.03	85
(1) [BMIM][dca]	0.05	26
(2) [BMIM][dca]	0.012	31
(2) [BMIM][OAc]	0.0085	485
(2) [EMIM][OAc]	0.012	17 (80°C)
(2) [CH <sub>3</sub> OCH <sub>2</sub> CH <sub>2</sub> -Et-Im][Tf <sub>2</sub> N]	0.01	33.1
(2) [CH <sub>3</sub> OCH <sub>2</sub> CH <sub>2</sub> -Et <sub>3</sub> P][Tf <sub>2</sub> N]	0.01	36

The dynamic viscosity measurements listed in Table 2.1 are representative of a small set of ILs that are considered during this project. “The viscosity of an ionic liquid influence[s] the solubility of cellulose-containing natural products. Undesirable high viscosity impedes [the] dissolution of biomass composites” (Fendt et al., 2011). As is the case with [CH<sub>3</sub>OCH<sub>2</sub>CH<sub>2</sub>-Et<sub>3</sub>N][OAc], a viscosity around or above 100 mPa·s would not be an ideal compound to dissolve biomass, whereas [CH<sub>3</sub>OCH<sub>2</sub>CH<sub>2</sub>-Et<sub>3</sub>P][Ac] has a significantly lower and thus preferred

viscosity for the dissolution of biomass. Also, compounds with an acetate ion tend to have lower viscosities than those carrying halides, thereby “they hold promise as solvents for pretreatment of lignocellulosic biomass [before] enzymatic hydrolysis” (Fendt et al., 2011).

Another property that differentiates ILs from other organic solvents or compounds is their relatively low vapor pressure. At or near room temperature, vapor pressures of most ILs are immeasurably small; for this reason, they are often considered to be ‘vapor-less’ compounds. ILs can be heated well past the boiling point of traditional organic solvents, thus making them better reaction media for high-temperature reactions. Instead of boiling at atmospheric pressure, thermal decomposition might occur at elevated temperatures, a phenomenon that can be analyzed via thermogravimetric analysis (TGA) (Deetlefs & Seddon, 2006).

Viscosity measurements produce two values, one being absolute or dynamic viscosity and the other kinematic viscosity. Dynamic viscosity, measured in  $\text{mPa}\cdot\text{s}$ , is “the tangential force per unit area required to slide one layer (*A*) against another layer (*B*)” (Viswanath et al., 2007). Dynamic viscosity is considered the fluids’ amount of resistance to flow. Kinematic viscosity takes into consideration the density of the liquid at a temperature and pressure. Equal to the dynamic viscosity divided by the density, kinematic viscosity is measured in  $\text{mm}^2/\text{s}$ . All values of viscosity will be reported for both dynamic and kinematic viscosity, however the dynamic viscosity and density were considered in results analysis.

Another important characteristic of ILs is a complex description of the ILs compatibility with water. A majority of ILs are hygroscopic, meaning they absorb water from the atmosphere. The ILs anions tends to form a complex with water molecules, creating an anion-water-anion interaction. Increasing concentrations of water lead to more complex micelles and aggregates, increasing the difficulty of extracting water from ILs to produce neat, otherwise known as dry,

ILs. “The micellization and aggregation of ILs are dependent on the alkyl chain length, the type of cations, and the nature of the anions. ILs with longer alkyl chains or hydrophobic anions form aggregates more easily” (Chen et al., 2012). Removing water from ILs depends on many factors, the least of which is whether ILs are hydrophobic or hydrophilic.

Hydrophobic ILs are less likely to form complexes than hydrophilic ILs. “Hydrophobic ILs can be removed easily by organic solvent extraction owing to their poor solubility in aqueous solution. However, that is not suitable for hydrophilic ILs. Therefore, the removal or recovery of hydrophilic ILs is much more difficult in comparison to hydrophobic ILs” (Wu et al., 2016). Studies have shown that hydrophobic ILs will continue to have trace amounts of water complexed to the compound, however more research has been done regarding the separation of hydrophilic ILs from water, particularly in aqueous biphasic systems (ABS) (Palumbo, et al., 2019) or salting-out reactions using potassium phosphate (Wu et al., 2008).

Thus far, consideration has been given to the physical and chemical characteristics of ILs themselves. More important is the ability of ILs to solvate and interact with various other molecules, specifically lignocellulosic biomass and other biomass particles. Consideration of polarity and polarizability can be expressed by a complex formula using the solvatochromic parameters  $\alpha$ ,  $\beta$ , and  $\pi^*$  (Kamlet & Taft, 1976). The values for electron-accepting,  $\alpha$ , and electron-donating,  $\beta$ , abilities of a solvent and polarity/polarizability,  $\pi^*$ , are used to “describe the effect a solvent has on the properties and reactivity of dissolved compounds using the principle of the linear solvation energy relationships (LSER) in the Kamlet-Taft formalism.” These three parameters were calculated using the following formulas:

$$E_T(30) = \frac{28591}{\lambda_{RD}(nm)} \quad \text{Equation 2.1}$$

$$E_T^N = \frac{E_T(30) - 30.7}{32.4} \quad \text{Equation 2.2}$$

$$\pi^* = \frac{\tilde{\nu}_{DENA} - 27.52}{-3.183} \quad \text{Equation 2.3}$$

$$\beta = \frac{(1.035) \cdot \tilde{\nu}_{DENA} - \tilde{\nu}_{NA} + 2.64}{2.8} \quad \text{Equation 2.4}$$

$$\alpha = \frac{E_T(30) - 14.6 \cdot (\pi^* - 0.23) - 30.321}{16.5} \quad \text{Equation 2.5}$$

In these formulae,  $\tilde{\nu}_{NA}$  and  $\tilde{\nu}_{DENA}$  are the maximum absorption wavenumbers ( $\text{cm}^{-1}$ ) for 4-nitroaniline and diethyl-4-nitroaniline, respectively. The value  $\lambda_{RD}$  is the absorption maximum wavelength for Reichardt betaine, a zwitterion compound with a quantized electron transition (Ladesov et al., 2015).

### Coal and What it is Made Of

One particularly interesting application of ILs is the liquefaction and dissolution of coal. According to the U.S. Energy Information Administration, coal-based energy consumption for 2019 in the United States is valued at 11.3 quadrillion British thermal units (BTU) ( $1.13 \times 10^{16}$  BTU), making coal the third most consumed energy source after petroleum and dry natural gas (U.S. Energy Information Administration, 2020). “It is estimated that the world coal reserves are currently  $1.53 \times 10^{20}$  BTU or 71.4% of the total world fossil fuel resource” (Sekhohola et al., 2013). What is coal, what is it made of, and how can it be used more efficiently?

ASTM International, formerly known as American Society for Testing and Materials (ASTM), established a classification system to be used for coal that categorizes the material into ranks. Based on the calorific value, expressed as BTU per pound, coal can be classified as anthracite, bituminous, sub-bituminous, and lignite/brown coal (Sekhohola et al., 2013), the latter two classifications are considered the lowest ranks and thus the focus of this research project. Low-rank coal produces the least energy when degraded, 5500 to 8300 BTU/lb, compared to the higher-ranked anthracite that produces 13,500 to 15,600 BTU/lb, which results in more waste produced during consumption and an increase in organic pollutants (Sekhohola et

al., 2013). Non-combustible waste is created when hydrogen, oxygen, and nitrogen impurities strengthen the structure of coal, resulting in chemical bonds that are not broken during use.

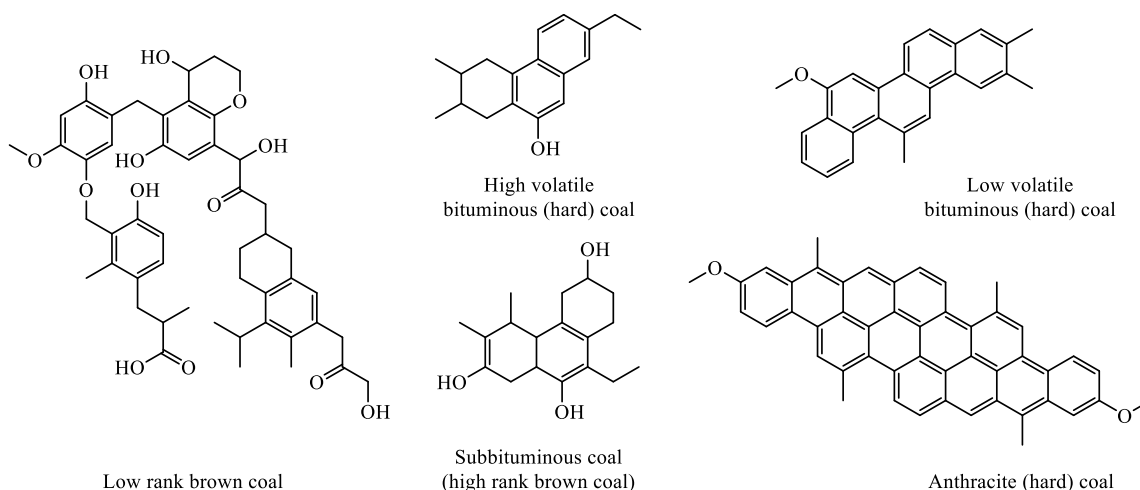
Figure 2.3 illustrates the structures of four ranks of coal, designed to convey the complexity of each structure and to display their differences in connectivity between aromatic rings. Anthracite, being the highest rank and largest energy producer, contains 86 to 98% on a fixed carbon content scale, whereas lignite and sub-bituminous coal range from 46 to 60% fixed carbon content (Sekhohola et al., 2013). This fixed carbon content, FC, was derived as a means to relate the amount of aromatic carbon with non-volatile carbon, aromatic hydrogen, and nitrogen concentrations (Ahamed et al., 2019). As indicated in the figure, brown coal contains fewer aromatic rings and is connected via ether and hydroxy-based linkages. These linkages result in less energy consumption, and is, therefore, a focus for researchers in regards to increasing the efficiency of consumption of lignite and sub-bituminous coals.

The coalification process is a natural phenomenon studied rigorously by petroleum geologists. Two factors dictate the extent of the process and the rank of coal being formed: temperature and pressure. Lignite, low-rank brown coal, “one of the initial products of the coalification process formed under moderate temperature and pressure,” is estimated to constitute roughly 45% of total global deposits (Ghani et al., 2015). When conditions become unfavorable for plant biodegradation, complex polymers are added to the coalification process. One such polymer from lignocelluloses, known as lignin (Figure 2.4), resembles some structural features of lignite, along with various silicon, oxygen, nitrogen, and sulfur-containing minerals (Ahamed et al., 2019).

Poor energy production and pollution during degradation implies that an alternative solution must be found to increase the efficiency of low-rank coal. Three techniques are used

today, each with its advantages and disadvantages. First, pretreatment of coal using organic solvents, nitric acid, or oxidizing agents like hydrogen peroxide or potassium permanganate can be used to cleave some of the bonds in lignin-like structure (Strzelecki et al., 2015). Reducing the number of oxygen atoms reduces the number of ether and hydrogen bonding linkages that interfere with chemical combustion. Second, biosolubilization via bacteria or fungi has shown promising advances in the liquification and biodegradation of low-rank coals (Sekhohola et al., 2013). Last, and most importantly for this project, ILs can be used to liquify and isolate low-rank coals for further use in energy or industrial applications (Lei et al., 2019).

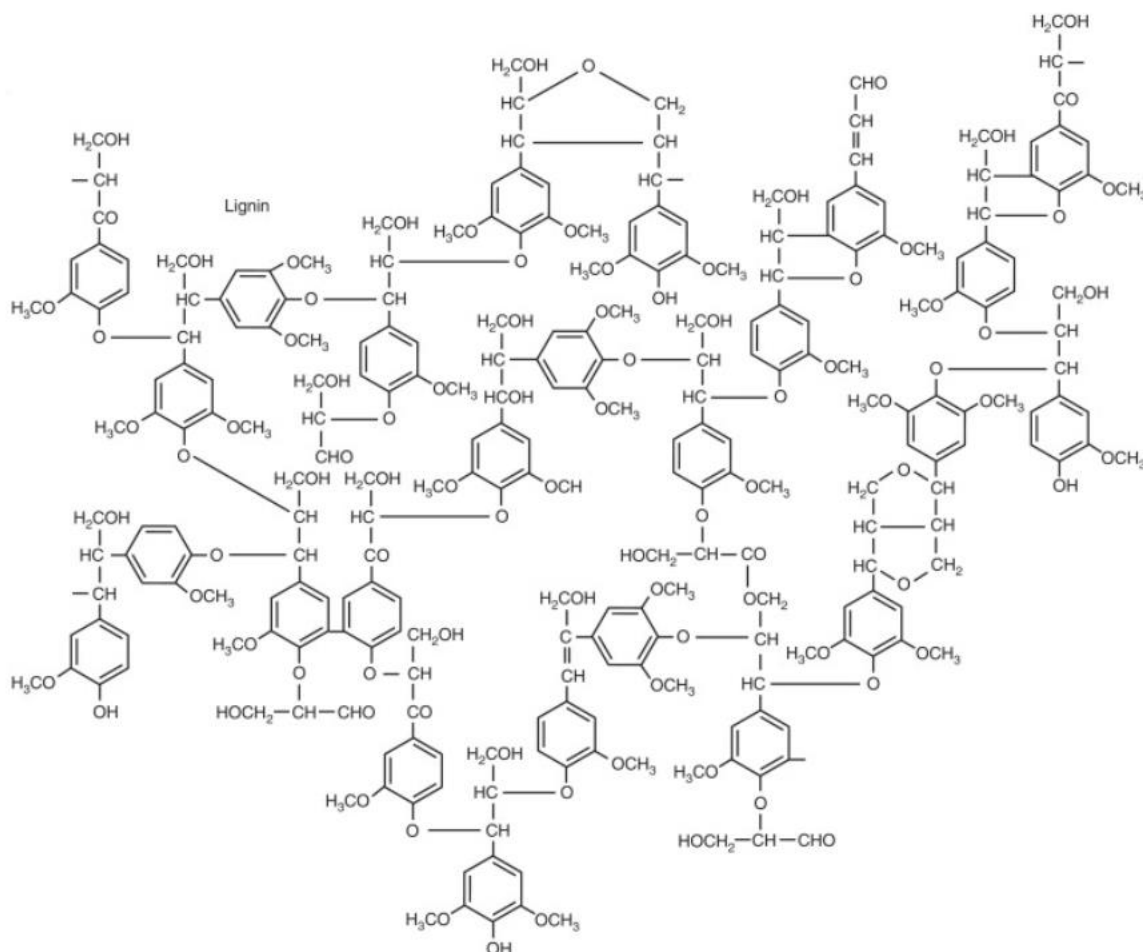
**Figure 2.3:** Model representations of chemical structures of various classes of coal. This model serves to represent the differences in aromatic carbons between the high ranked anthracite and that of the low ranked lignite (brown coal) (Ghani et al., 2015).



Researchers state that “if the cross-link density of the network is high and the chains are relatively stiff, a significant portion of the soluble fraction can be trapped and inaccessible” (Painter et al., 2010). The primary dilemma associated with coal dissolution via organic solvents. Pyridine, a common organic solvent that solubilizes coal to an extent, lacks the ability to complex with cations that result from the cleavage of networked compounds, and thus falls short of maximizing the efficiency of coal dissolution.



**Figure 2.4:** Lignin, a complex polymer found in the degradation process of plant material, is the second most abundant natural polymer (Watkins et al., 2015).



Pretreatment of coal poses the same waste and pollution problems found when using organic solvents but play a role in the biosolubility of coal via bacterial or fungal liquification. Pretreatment of coal “enhances the brown coal biosolubilization process through oxidation and loosening of coal structure”. Pretreatment of brown coal with hydrogen peroxide and nitric acid, followed by treatment with *F. oxysporum 1101*, resulted in 100% liquefaction (Strzelecki et al., 2015).

### Use of Ionic Liquids to Pretreat (Dissolve or Swell) Coal

Pretreatment of coal is used as a means of disrupting the intramolecular forces that bind various substituents of coal together. These forces, namely hydrogen bonds,  $\pi$ - $\pi$  interactions, and charge transfer complexes, have been found to dissociate with the pretreatment by [BMIM][Cl] (Painter et al., 2010). Further testing has identified that this IL, among others, works to “fragment, swell, partially solubilize, and disperse some coals” (Lei et al., 2019). Continued investigation into the extent of swelling, fragmenting, and solubilizing is necessary to understand the limitations that ILs have, as well as to identify cost-effective and efficient dissociation techniques.

In 2019, researchers began investigating the dissociation behaviors of coal using ILs in model compounds. The complexity of coal makes it difficult to understand the limitations of the dissociation, while the use of model compounds, or complex organic species that model the chemical behavior of coal, gives insight into the ideal characteristics of ILs. According to Lei et al., [EMIM][OAc] (OAc being the shorthand notation for the acetate anion), [BMIM][Cl], and [B(SO<sub>3</sub>H)MIM][OTf] (OTf is shorthand for the triflate group) had the highest conversion percentages for the dissociation of their model compounds (Lei et al., 2019).

Computer modeling has also been employed to predict the dissolution of lignite using ILs, utilizing the principle of hydrogen bond disruption to predict which ILs would have the greatest dissociation effect on lignite. Bhoi et al. (2014) determined two principles: first, the solubility of coal in ILs will increase with an increase in temperature, and second, nitrogen-containing rings that are not aromatic have higher solubilities than phosphorus or aromatic ring containing cations. Their results show that using [BMIM][Cl] will extract “mainly aromatic

structures” from lignite, “but it mainly contains more aliphatic alkyl structures in the [BMIM][PF<sub>6</sub>] extraction case.’

“Two key objectives of the pretreatment of coal are [1] softening, swelling and dissolution of coal particles and [2] removal of the extra elements” (To et al., 2017). Identifying the complexity of the coal matrix will open an avenue to understand what type of intramolecular forces need be disrupted to propagate the dissolution and extraction of impurities, which will then allow researchers to identify ideal IL properties that will maximize the dissolution process. Understanding which IL properties contribute to the dissolution of coal will allow for cross-testing of ideal IL(s) with coal samples from different physical locations with various physical characteristics.

## CHAPTER III

### METHODOLOGY

#### **Research Objectives**

There exist millions of combinations of ILs, with only a handful of which have been tested against coal or coal model systems. Researchers have built a foundation of understanding of ILs and their applications to coal dissolution that must be built upon. The research objectives outlined in this section were used to design experimental parameters to synthesize and characterize various ILs, characterize available coal samples, and test the dissolution properties of select ILs on coal.

- O1 Synthesize ILs by combining different cations and anions. Cost, ease of synthesis, and variations in physicochemical properties were considered during synthesis. Hydrophilic ILs were the primary focus of this project.
- O2 Characterize ILs to identify physical and chemical properties that assisted in the coal dissolution process. The focus was placed on water concentration, viscosity, degradation temperature, structure verification, and hydrogen bond donor/acceptor properties.
- O3 Dissolution and characterization of coal model compounds to determine the viability of specific ILs for coal dissolution.
- O4 Dissolution and characterization of brown coal (lignite) using select ILs. Identification of extent of dissolution, swelling, and fragmentation was verified via instrumental analysis of samples. Recovery of IL from coal was possible; however, it is not a primary task for this analysis.

#### **Synthesis of Ionic Liquids**

General synthesis procedures for producing most ILs started with a “quaternization step followed by a metathesis step-anion exchange” (Earle et al., 2007). Special considerations must

be made to produce “spectroscopic grade” ILs, which can be achieved “in four ways, notably (i) purification of starting materials, (ii) control of conditions for quaternization reactions, (iii) anion exchange, and (iv) cleaning of the ionic liquid” (Gordon et al., 2003).

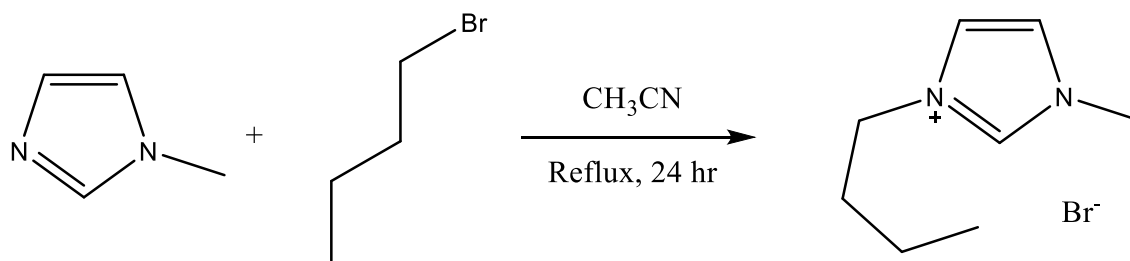
Synthesis of the bromide type of ILs occurred in acetonitrile ( $\text{CH}_3\text{CN}$ ), an anhydrous polar organic solvent, which was easily evaporated from the IL via rotary evaporation at 50 °C and 50-100 mbar of vacuum. Ion exchange from the bromide ion to acetate ion was performed in an ion-exchange column filled with Amberlyst™ A26 OH resin and required approximately 450 mL of methanol to fill, rinse, and perform the ion exchange. Regeneration of the resin required an additional 400 mL of methanol and one liter of one molar sodium hydroxide (NaOH) in water. Increasing the temperature of the water bath used with the rotary evaporator from 50 °C to 75 °C allowed for complete removal of methanol from the acetate-based ionic liquid; treatment of this ionic liquid in a vacuum oven at 80 °C at 25 mbar of vacuum for 2 or more days reduced the water concentration below 1%.

Commercially available compounds were used as the starting reactants for the nucleophilic substitution by direct displacement ( $\text{S}_{\text{N}}2$ ) reaction. The first two compounds reacted were 1-ethyl imidazole and 2-bromoethyl methyl ether, resulting in the ionic liquid 1-ethyl-3-(2-methoxyethyl) imidazolium bromide (R01,  $[\text{MeOCH}_2\text{CH}_2\text{-Et-Im}][\text{Br}]$ ). Further reactions with 2-bromoethyl methyl ether occurred with 1-methyl imidazole, triethylamine, triethyl phosphorus, tributyl phosphorus, pyridine, N-methyl pyrrole, and N-methyl piperidine. Other brominated compounds reacted with this full set of nitrogen or phosphorus-based compounds included 2-bromoethyl ethyl ether, bromoethane, and 1-bromobutane.

Shorthand notation is used when describing ILs and IL synthesis. In general, [BMIM] represents 1-butyl-3-methyl imidazolium ion, [Br] is short-hand for bromide anion, [PF<sub>6</sub>] is

short-hand for hexafluorophosphate anion, and [OAc] represents the acetate anion. Figure 3.1 represents the synthetic process for [BMIM][Br] which also applies for the synthesis of [BMIM][PF<sub>6</sub>]. The method for synthesizing [BMIM][Br] was to combine 17.649 g (215.0 mmol) of 1-methyl imidazole with 32.440 g (236.8 mmol, 10% molar excess) of 1-bromobutane in 150 mL acetonitrile. The solution was refluxed at 55 °C for 24 hours, washed twice with 150 mL of diethyl ether and the remaining solvent was evaporated via a rotary evaporator (rotovap). This reaction produced 46.084 g of [BMIM][Br] (210.31 mmol), a 97.82% yield; the resultant compound was a light brown, relatively viscous liquid, stored at room temperature in a closed glass vial sealed with parafilm.

**Figure 3.1:** Synthesis of IL [BMIM][Br].



Zhao et al. studied the characteristics of glycol-functionalized ILs (Zhao et al., 2018) using hydrophobic anions instead of hydrophilic anions. In order to investigate similar ILs with hydrophilic anions, we must first synthesize more complex brominated glycols to then react with our other nucleophilic compounds. The Appel reaction is a basic reaction between an alcohol and carbon tetrabromide in the presence of triphenylphosphine to produce a brominated compound. Various glycols were reacted with 10% molar excess of CBr<sub>4</sub> and PPh<sub>3</sub> at room temperature for 24 hours to produce the brominated glycol that could further react to produce an ionic liquid. Copious washings of the product with hexane was used to remove unreacted CBr<sub>4</sub>, PPh<sub>3</sub>, and byproducts O=PPh<sub>3</sub> and CHBr<sub>3</sub>. NMR analysis was used to verify product formation

and purity before further experimentation was conducted. Synthetically, 18.203 g (122.83 mmol) methyldiethylene glycol was added to a 250-mL Erlenmeyer flask with 150 mL acetonitrile, along with 37.883 g (114.24 mmol) carbon tetrabromide. The mixture was dissolved on a stir plate, to which 30.005 g (114.40 mmol) triphenylphosphine was added very slowly, ensuring the solution did not heat to the point of boiling. After 24 hours of stirring at room temperature, the solution was filtered, washed twice with *n*-hexane, and placed in a freezer for a minimum of 72 hours. The solution was filtered again, rotovapped at 55°C and 50 mbar of pressure, and the resultant oil was placed in a glass vial. This reaction yielded 15.965 g (87.22 mmol) of 1-(2-bromoethoxy)-2-methoxy ethane and translated into an 83.96% yield.

In order to perform the ion exchange to replace the bromide ion with a more complex anion, the relative solubility of the compound in organic solvents and water had to be understood. Addition of NaPF<sub>6</sub> to [BMIM][Br] in acetone, both of which are soluble, results in the exchange of Br<sup>-</sup> by PF<sub>6</sub><sup>-</sup>. The resultant NaBr, being insoluble in acetone, precipitated out of solution. Upon completion of the ion exchange, all NaBr will be precipitated, and the washed ionic liquid can be tested with AgNO<sub>3</sub> to verify Br<sup>-</sup> is no longer present in the ionic liquid.

Ion exchange was performed in a glass column filled with a slurry comprised of 50 grams of Amberlyst™ A26 OH resin in methanol. A dissolved solution of 150 grams of ammonium acetate in 250 mL methanol was flushed through the column, followed by 200 mL methanol. Approximately 10 grams of brominated ionic liquid was dissolved in 100 mL methanol and slowly passed through the column. The collected solution was tested periodically with silver nitrate to verify the full exchange of bromide ion in the column (silver bromide precipitated in water if bromide ion was present). Figure 3.2 is a visual representation of the ion exchange process. The collected solution was concentrated via rotovap at 75 °C and 50 mbar for 2 hours,

transferred to a glass vial, and heated in a vacuum oven at 80 °C and 25 mbar of vacuum for a minimum of 48 hours.

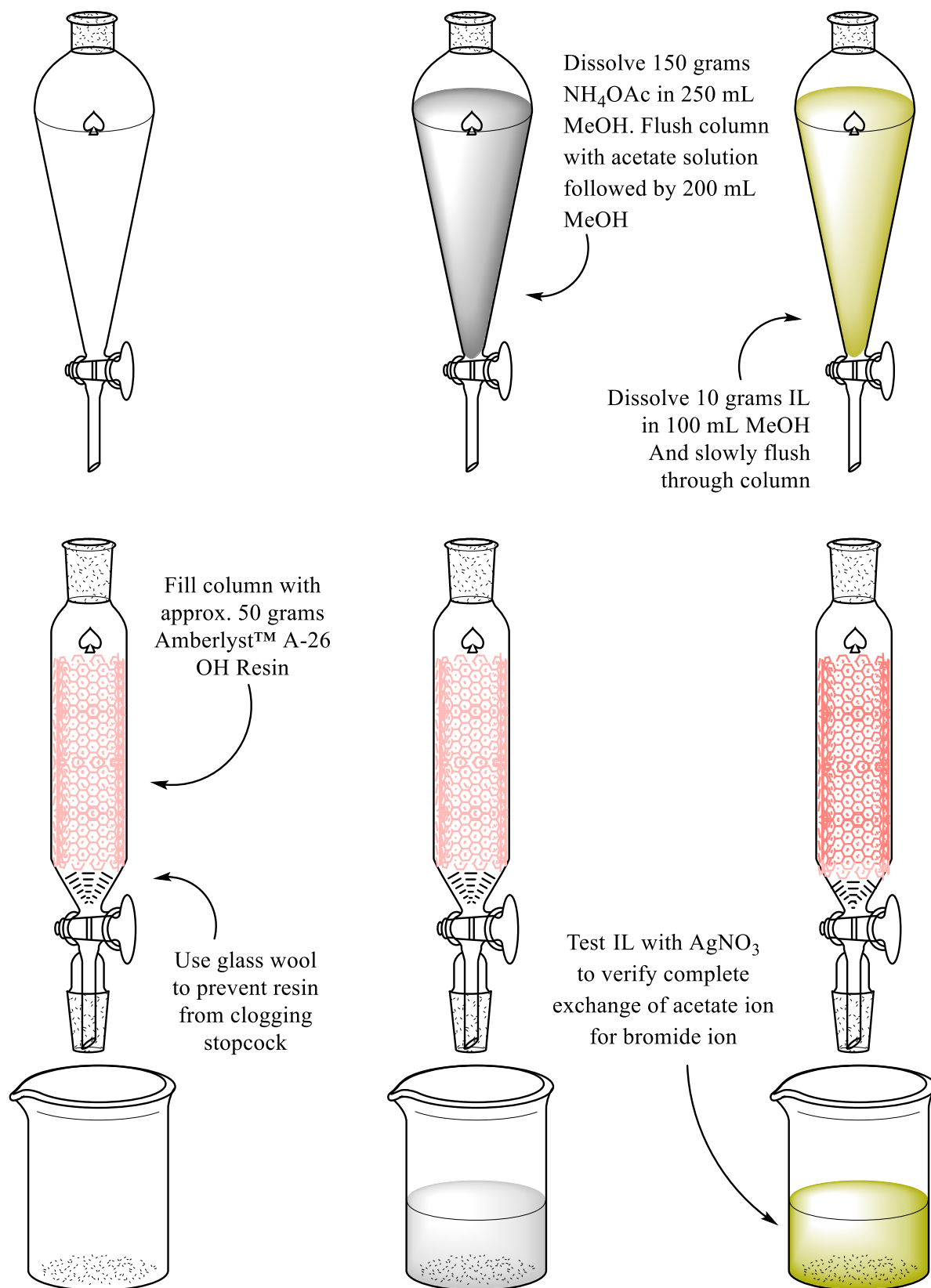
Verification of the water concentration in an IL was necessary before further characterization could occur. For example, IR analysis of a sample with too much water will give misleading absorption peaks, and the TGA will indicate the evaporation of water rather than the decomposition of the ionic liquid. A Karl Fischer titration method of chemical analysis using coulometric titration was used to determine the water concentration of ILs. Hydrophilic ILs absorb water from the atmosphere, so it was necessary that ILs be stored in either an inert or vacuum atmosphere and retested periodically to ensure neat (a.k.a. dry) samples were analyzed. Water concentration within the samples was analyzed using Karl Fischer (KF) titration via a Mettler Toledo C20X compact coulometric titrator with a detection limit of 1 ppm water. The titrator used Hydranal® Coulomat AG analyte. Adequately dry samples were stored in a vacuum desiccator at 50 mbar pressure and room temperature. Phosphorous pentoxide ( $P_2O_5$ ) was placed in the vicinity of the sample during drying and storage to absorb atmospheric moisture before the hygroscopic ionic liquid became saturated with water.

### **Characterization of Ionic Liquids**

In order of analysis, the techniques utilized in this research project included viscometry, thermogravimetric analysis (TGA), hydrogen bond acidity, hydrogen bond basicity, dipolarity/polarizability effects, structure and purity confirmation via NMR and IR analysis, LC-MS, SEM/EDS, and XRD. Each analysis method will be discussed in further detail, specifically relating to the predicted results of this project.



**Figure 3.2:** Visual representation of ion exchange procedure.



The viscosity and density of a liquid were determined using an Anton Paar SVM 3000 viscometer set at 30 °C. The viscometer takes a 3 mL sample and determines the dynamic and kinematic viscosity as well as density at a specified temperature. The more viscous an ionic liquid, the more difficult it will be to treat solid biomass or coal samples. Detailed information regarding viscosity is typically required to better characterize ILs. The dynamic viscosity is reported in units of mPa·s and the density is reported in units of g·cm<sup>-3</sup>; kinematic viscosity, a function of both dynamic viscosity and density, was not be reported at this time.

Thermogravimetric analysis (TGA) is a destructive analysis that measures the  $T_{\text{der}}$  and  $T_{\text{dep}}$ , where the “ $T_{\text{der}}$  is determined from the maximum in the first-derivative profile of the TGA scan and the  $T_{\text{dep}}$  is the decomposition temperature measured as the onset of decomposition, using the common criteria of 10% total mass loss” (Zhao et al., 2018). TGA analysis was completed by Dr. Gary Baker, collaborator and fellow IL specialist at the University of Missouri-Columbia.

Thermogravimetric analysis (TGA) scans were measured on a TA Instruments TGA Q50 under a nitrogen atmosphere (60 mL min<sup>-1</sup>) using Pt pans with a heating rate of 10 °C min<sup>-1</sup>.  $T_{\text{der}}$  is determined using the global maximum of the first-derivative profile of the TGA scan.  $T_{\text{dep}}$  is the decomposition temperature measured as the onset of decomposition, using the criterion of a 10% total mass loss. Uncertainties in the temperatures are estimated to be ±2–3 °C. The TGA mass loss behavior is qualitatively characterized on the basis of whether it occurs essentially in a single, discrete step (S) or exhibits multiple step (M) thermal decomposition. The designation S is thus applied if >90% of the weight loss occurs in a single, discrete step. The latter designation of M is typically associated with a significant mass loss step which occurs at a temperature 50–100 °C above or below the primary event at  $T_{\text{der}}$ . It should be noted that, for this reason, profiles

that display multi-step thermal decomposition behavior frequently exhibit lower effective  $T_{\text{dcp}}$  values. The amount of carbon char residue is determined from the relative mass remaining at 600 °C. A residual mass of  $\pm 0.5\text{--}2\%$  at the upper temperature is within the error of the measurement's baseline and represents essentially quantitative mass loss over the thermal interval.

Nuclear magnetic resonance was used to confirm the structure and purity of the ILs. The NMR analysis was completed using a Bruker 400 MHz NMR paired with TopSpin processing software. The  $^1\text{H}$ ,  $^{13}\text{C}/\text{DEPT}$ , COSY, HMBC, and HMQC spectra were used to verify each structure dissolved in  $\text{CDCl}_3$  solvent. The  $\text{CDCl}_3$  solvent was received from the manufacturer containing tetramethylsilane, or TMS, which acts as a reference peak to verify accurate NMR spectroscopic analysis.

Hydrogen bond acidity ( $\alpha$ ), hydrogen bond basicity ( $\beta$ ), and dipolarity/ polarizability effects ( $\pi^*$ ), known together as Kamlet-Taft parameters, were combined in a multi-parameter polarity scale that was used to evaluate the polarity of our ILs. The ionic liquid was mixed with a particular dye set and the resultant mixtures were analyzed using a UV-Vis spectrometer. This dye set includes Reichardt's Dye (2,6-diphenyl-4-(2,4,6-triphenylpyridin-1-ium-1-yl) phenolate), *N,N*-diethyl-4-nitroaniline, and 4-nitroaniline, all three of which are considered solvatochromic compounds, meaning they change colors depending on the other species they interact with.

The solvent dipolarity/polarizability,  $\pi^*$ , was calculated from the maximum wavelength of the lowest-energy band of *N,N*-diethyl-4-nitroaniline, the scale has dimethylsulfoxide ( $\pi^*=1.00$ ) and cyclohexane ( $\pi^*=0.00$ ) as fixed references. A one nanometer shift in maximum absorption of *N,N*-diethyl-4-nitroaniline gives an error in  $\pi^*$  of 0.02. The hydrogen-bond-accepting (HBA) basicity,  $\beta$ , was determined from the absorptions of 4-nitroaniline and *N,N*-

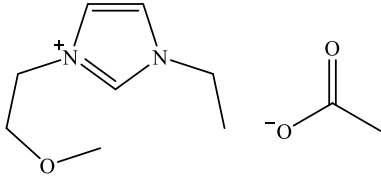
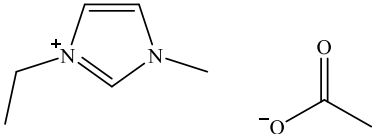
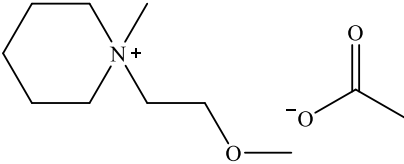
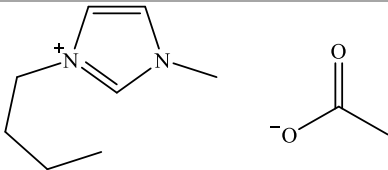
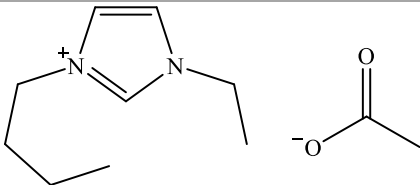
diethyl-4-nitroaniline and the scale has hexamethylphosphoramide as  $\beta=1$  (now accepted to be 1.05) as a fixed reference. Compounding the error of a single nanometer error in each dye gives an error in  $\beta$  of 0.03. The hydrogen-bond-donating (HBD) acidity,  $\alpha$ , was calculated using the maximum absorption wavelength of Burgess' dye and *N,N*-diethyl-4-nitroaniline (Dolan et al., 2016).

Three dyes were added to each sample and the wavelength of maximum absorption was measured using UV-Vis spectroscopy, namely Reichardt's dye (RD), 4-nitroaniline (NA), and *N,N*-diethyl-4-nitroaniline (DNA). Each solution was prepared by dissolving 25.0 mg of the respective dye in 25.0 mL of chloroform. The resultant concentrations were 1.81 mM RD, 7.24 mM NA, and 5.15 mM DNA. A micropipette was used to transfer 20  $\mu$ L of each dye into a 2-mL conical vial, whereupon ambient air was blown over each vial to evaporate the chloroform. The vial was then filled with 2.0 mL of an IL and agitated for 30 minutes until all evidence of dye was dissolved. A 2 mm quartz cuvette was the sample holder for the UV-Vis spectrometer, the blank being the un-dyed IL. Wavelength of maximum absorption was determined by analyzing the full spectrum, from 300 to 4000 nm.

### **Dissolution of a Model Coal Compound: Cellulose**

Five ILs were selected to evaluate the degree of pretreatment and dissolution of both cellulose and coal. Table 3.1 shows which ILs were chosen and provides the chemical structure, name, and basic information regarding molecular formula and weight. The Chosen Ones, as they were referred to, displayed the water concentration, viscosity, and Kamlet-Taft characteristics we considered most important in the dissolution process.

**Table 3.1:** The Chosen Ones. The five (5) ILs identified for cellulose and coal dissolution due to low viscosity, high temperature of degradation, and ideal hydrogen-bond basicity ( $\beta$ ) values.

A01	IUPAC Nomenclature	1-ethyl-3-(2-methoxyethyl) imidazolium acetate		
	Chemical Formula	$[\text{CH}_3\text{OCH}_2\text{CH}_2\text{-EIM}][\text{OAc}]$	Molecular Weight	214.25 g/mol
				
A12	IUPAC Nomenclature	1-ethyl-3-methyl imidazolium acetate		
	Chemical Formula	$[\text{EMIM}][\text{OAc}]$	Molecular Weight	170.20 g/mol
				
A16	IUPAC Nomenclature	N-(2-methoxyethyl)-N-methyl piperidinium acetate		
	Chemical Formula	$[\text{CH}_3\text{CH}_2\text{OCH}_2\text{CH}_2\text{-MPip}][\text{OAc}]$	Molecular Weight	231.32 g/mol
				
A28	IUPAC Nomenclature	1-butyl-3-methyl imidazolium acetate		
	Chemical Formula	$[\text{BMIM}][\text{OAc}]$	Molecular Weight	182.26 g/mol
				
A30	IUPAC Nomenclature	1-butyl-3-ethyl imidazolium acetate		
	Chemical Formula	$[\text{BEIM}][\text{OAc}]$	Molecular Weight	212.29 g/mol
				

Emphasis was placed on measuring the quantity of cellulose dissolved in each IL as well as any fraction patterns measurable via FT-IR and LC-MS. A Teflon<sup>®</sup> stir-bar was added to a 10-mL Pyrex<sup>®</sup> glass vial, weighed, placed in a low temperature oil bath and heated to  $105 \pm 3$  °C. A 1.0 g sample of IL was carefully added to the bottom of the vial so as to avoid any residue from sticking to the top or sides of the vial. Avicell<sup>®</sup> PH-101 was added in 0.20 g aliquots to the IL and stirred until fully dissolved. Proper dissolution of cellulose in an IL happens gradually. When cellulose was initially added, the powder clumps, indicative of the hydrogen bonding of the cellulose resisting interaction with the organic IL. However, given time and agitation, the cellulose dissolved and dispersed throughout the IL. Dissolution was considered complete when the viscosity of the IL/cellulose mixture ceased movement of the stir bar.

The IL/cellulose mixture was transferred to a clean, dry, pre-weighed glass vial with a screw-top lid. The weight of the mixture was compared to the total IL and cellulose added, confirming that a maximized amount of the mixture was extracted from the vial. Percent dissolution was calculated for each trial. Further analysis of the IL/cellulose mixture was completed in-house via the FT-IR and submitted to Colorado State University-Fort Collins for LC-MS analysis.

### **Dissolution and Fragmentation of Lignite**

Dissolution and fragmentation of lignite coal was completed using the five Chosen Ones. Lignite coal was obtained from Bowman, ND, USA, lot number 367025. The coal rocks were broken into smaller chunks and pulverized using a mortar and pestle. The pulverized coal was sifted through a 150  $\mu$ m sieve to ensure all particles are smaller in diameter than 150  $\mu$ m. Following the procedure of Cummings et al. (2017), a 1:5 mass ratio of coal to IL was added to a

clean, dry, pre-weighed glass vial with stir bar and placed in the same heating bath. The mixture was left to stir for 24 hours before reclaiming undissolved coal.

The reclamation process occurred in three steps. First, 8 mL of methanol was added to the mixture to aid in transferring the coal/IL mixture into a 15-mL conical vial. This mixture was centrifuged at 3000 rpm for 30 minutes. The liquid layer was decanted into a plastic syringe and filtered through an attached 0.4  $\mu\text{m}$  filter, ensuring all free coal particles were removed from the liquid layer. The solid material was washed with water, centrifuged, and the eluent was collected in a separate flask. After three iterations of this washing, acetone was used to wash the coal to remove any remaining water from the solid material. Acetone was then used to transfer the coal material onto a 5-in diameter watch glass and the acetone was evaporated in the chemical hood. Each watch glass was left to dry at 60  $^{\circ}\text{C}$  for 48 hours before being weighed and saved in glass vials.

Instrumental analysis of the dissolution of coal includes analysis by FT-IR, LC-MS, optical microscopy, SEM/EDS, and XRD. The five ILs and one reagent-grade version of A28 (referred to as RG28) were used to produce both the reclaimed coal (RCC) and IL/coal (ILC) mixture used for analysis.

Fourier Transform Infrared Spectroscopy (FTIR) has proven to be an effective method of evaluating surface functional groups of coal samples (Zhang et al., 2019). A ThermoFisher Scientific Nicolet™ iS™5 FTIR spectrometer with an iD5 ATR (Attenuated Total Reflection) accessory allowed for analysis of both solid and liquid materials. Each spectra required 32 scans at a resolution of 4  $\text{cm}^{-1}$  collected over one minute thirteen seconds, along with ATR correction and 5-point smoothing (2.411  $\text{cm}^{-1}$ ) operation. FTIR spectra were collected for the six ILs, lignite, six RCC and six ILC samples.

Initially, the GC-MS (Gas Chromatography-Mass Spectrometer) was used to evaluate the ILC mixtures for possible dissolution fragmentations. This effort was abandoned and replaced with LC-MS (Liquid Chromatography-Mass Spectrometer) due to the incompatibility of the GC with non-volatile samples and the possible sloughing of the column due to the presence of IL. LC-MS analysis was completed in the instrumental facility at CSU-FC for a nominal fee.

Both optical microscopy and SEM (Scanning Electron Microscopy) were used to analyze the surface of solid samples. “Scanning electron microscopy provides morphologic and topographic information about the surfaces of solids that is usually necessary in understanding the behavior of surfaces” (Skoog et al., 1998). The surfaces of both untreated and treated coal samples were compared, and the effect of each IL on the surface chemistry of coal was evaluated. As coal has been shown to be susceptible to dissociation by IL, the extent and patterns of dissociation by each IL were of most import.

Scanning electron microscopy (SEM) analyzes the surface topography of a solid substance using “a raster pattern with a finely focused beam of electrons” (Skoog et al., 1998, p. 550). The two types of signals of import include (1) the “backscattered and secondary electrons” detected after the focused beam of electrons from the electron gun strike the surface of the sample, and (2) the X-ray emissions released by the sample resulting from the relaxation of an excited electron. The latter signal, detected using X-ray spectroscopy, allows the researcher to evaluate the atoms energy signature present in the sample.

The instrument used for analysis at the University of Northern Colorado was a JEOL JSM-6610LV Series Scanning Electron Microscope with backscattered electron detector, low vacuum secondary electron detector, and an energy dispersive X-ray analyzer (EDS). With a 300,000× magnification capability, 0.3 to 30 kV accelerating voltage, and 3.0 nm resolution, the



SEM is capable of producing clear topographic images of particles smaller than 150  $\mu\text{m}$ . Due to backscattering of the semi-conductive material, a 15 nm coating of gold was placed on each sample using an EMS 550 Sputter Coater.

Sample analysis began by coating of each sample to mitigate charging during analysis. SEM images were taken of each sample at 30 $\times$ , 100 $\times$ , 500 $\times$ , and 1000 $\times$  zoom. Image location was chosen to include the largest range of particle size to best represent the topographic structure of the coal sample. EDS analysis was performed twice for each sample at 15 kV accelerating voltage, 60 spot size (SS60), and 750 $\times$  zoom. The first analysis was performed on a large particle of coal, the second analysis an area analysis on the same image. Average weight percent for C, O, Ca, and Br were used to determine an empirical formula for each sample. Proximate and ultimate analysis was not available, thus carbon, oxygen, calcium, and bromide were the suspected atoms with identifiable signatures provided by EDS software.

X-ray diffraction (XRD) was completed by Dr. Graham Baird, Professor of Geology and the XRD guru at the University of Northern Colorado. The XRD was a GBC MMA (Mini-Materials Analyzer) with a copper anode tuned to produce a wavelength of 1.54056  $\text{\AA}$ . Starting angle ( $2\theta$ ) was 10.00 $^\circ$  with a 0.02 $^\circ$  per minute step size up to 90.00 $^\circ$ . Raw data was saved in a CPI file and converted to an Excel spreadsheet for further manipulation. The technician experienced minor power issues during analysis, visible in the spectrum for sample C05-A6. Angles 33.58 $^\circ$  through 37.14 $^\circ$  reported zero counts of X-ray when there was expected to be between 40 and 50 counts per degree. Each spectrum was fit with three Gaussian curves, the linear combination of these curves providing a best-fit to the original data.

## CHAPTER IV

### RESULTS

Research results were separated into five individual sections: synthesis of ILs, characterization of ILs, dissolution of a model coal compound with select ILs, dissolution and pretreatment of lignite using select ILs, and the characterization and instrumental analysis of the dissolution of cellulose and coal. The experimental procedure for each step was outlined, in great detail, in Chapter III. The following sections describe the results for each section, while evaluation of the effectiveness and lessons learned from each step will be discussed in Chapter V.

#### **Synthesis of Ionic Liquids**

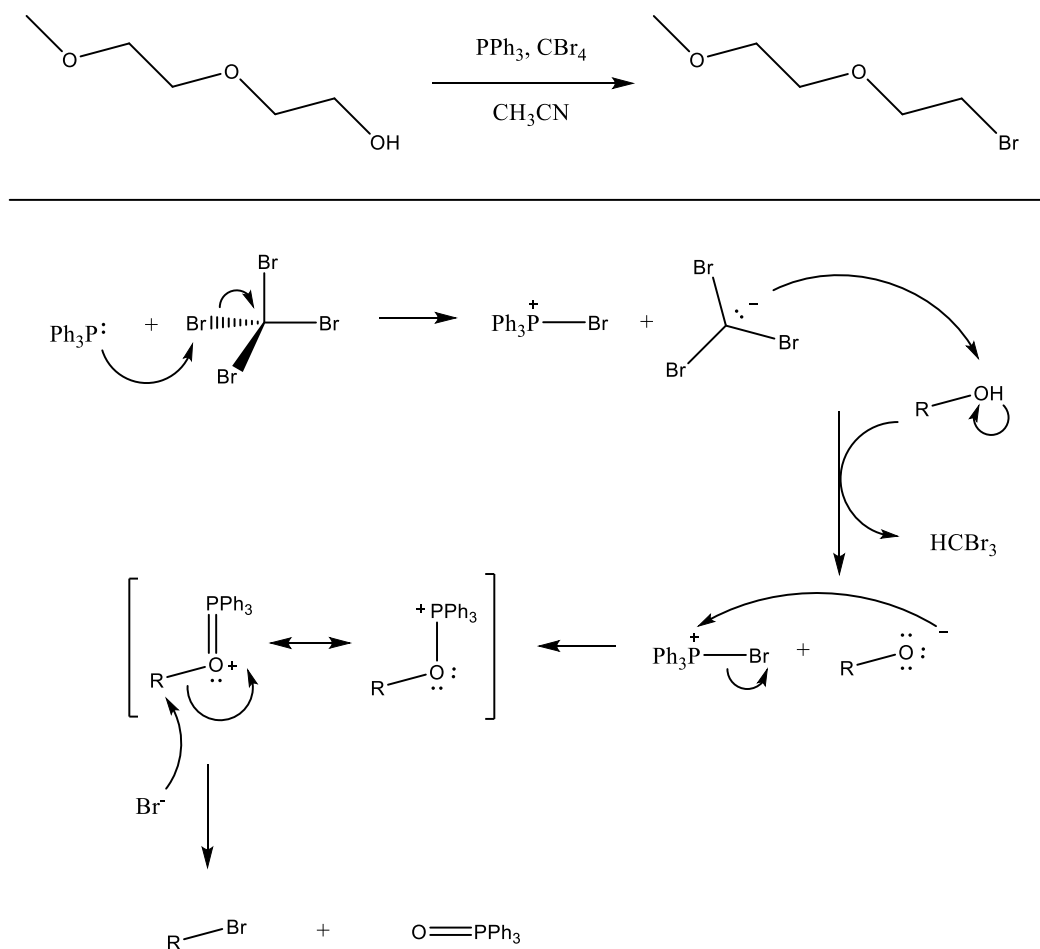
The first step of this research endeavor was the synthesis of ILs. Nitrogen- and phosphorus-based ILs with varying functional groups were explored in order to best represent symmetrical and non-symmetrical hydrophilic ILs. The Appel reaction, discussed first, was used to synthesize complex brominated glycols that were not readily available from chemical manufacturers. The synthesis of brominated ILs used one of these products as well as several commercially available brominated compounds. The last step in the synthesis of ILs was the ion exchange necessary to replace the bromide ion with the hydrophilic acetate ion of interest in this research project.

#### **Appel Reaction**

The Appel reaction (Figure 4.1) is the synthetic process of exchanging the alcohol functional group of a glycol with a halogen, in this case bromine. Using carbon tetrabromide and triphenylphosphine in acetonitrile, the glycol was left to stir at room temperature for 24 hours. It

was imperative that  $\text{CBr}_4$  and glycol were dissolved in acetonitrile before  $\text{PPh}_3$  was added. Due to the exothermic process of dissolving  $\text{PPh}_3$  in acetonitrile, the addition was performed in small aliquots, allowing enough time for all compounds to dissolve before adding more. An ice bath was held in reserve to prevent the mixture from overheating (defined as being too hot to hold the reaction vessel with your hand). Evidence of adequate mixing after 24 hours was the formation of  $\text{PPh}_3=\text{O}$  precipitate and the occasional color change from colorless to light yellow.

**Figure 4.1:** Appel reaction, converting diethylene glycol monomethyl ether into 2-bromoethyl 2-methoxyethyl ether. The Appel reaction is used to convert primary or secondary alcohols into brominated compounds to be used in IL synthesis.

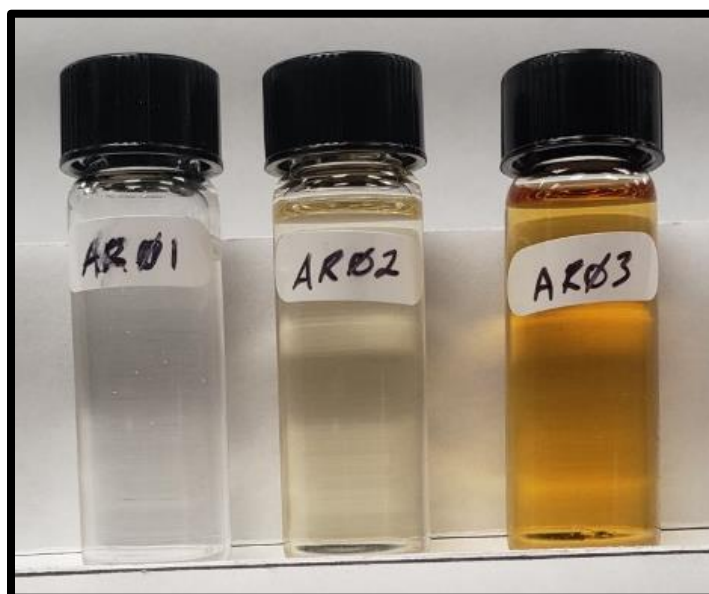


The reaction mixture was then filtered using a vacuum filtration apparatus with an 8  $\mu\text{m}$ , medium flow, Whatman Grade 40 ashless filter paper. Approximately 100 mL of *n*-hexane was

added to the filtrate and placed in the freezer for 48 hours. The precipitate was collected via vacuum filtration, the filtrate rotovapped at 50 °C and 50 mbar of pressure until the solvent was removed. The remaining liquid was washed with approximately 100 mL of *n*-hexane and placed in the freezer for 48 hours. This procedure was repeated until no precipitate formed after 48 hours of freezer time, upon which the solvent was rotovapped and the resultant liquid was collected in a vial for further testing.

Figure 4.2 is an image of the products of the Appel reaction. Table 4.1 summarizes the brominated-glycols synthesized. Referred to by the AR## nomenclature, only AR01 was used in the synthesis of ILs discussed in section 4.1.2. As shown in Figure 4.1, byproducts of this reaction included  $\text{PPh}_3=\text{O}$  and  $\text{CHBr}_3$ . Bromoform, like its chlorinated counterpart chloroform, is a liquid at room temperature with a boiling point of 147-151 °C and is soluble in water, ethanol, ether, and benzene (among other organic solvents not listed in the CRC) (Lide, 1995). Washing the mixture with *n*-hexane and rotovapping removes this impurity, as is evident in the NMR spectra discussed in section 4.1.4.

**Figure 4.2:** Results of the three Appel reactions



## Synthesis of Brominated Ionic Liquids

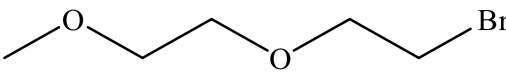
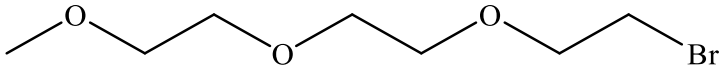
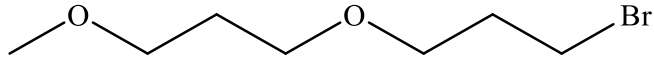
The synthesis of a quaternary ammonium or phosphonium compound was the preferred synthetic route for the synthesis of ILs. The lone pair of electrons of nitrogen or phosphorus reacts in a nucleophilic substitution reaction with the brominated compound. Heated to 50 °C under reflux conditions for 24 hours, 100 mmol of the nitrogen- or phosphorus-based nucleophile is reacted with 1.1 molar excess (110 mmol) of the brominated electrophile in acetonitrile. The resultant solution was rotovapped at 60 °C and 50 mbar of pressure until all solvent has been removed, at which time the remaining solution was washed twice with diethyl ether. Most ILs precipitated at this step. After a final rotovap to remove the ether, the sample was placed in a 50 mL beaker, topped with aluminum foil, and placed in the vacuum oven at 80 °C and 25 mbar of vacuum for a minimum of 48 hours.

Appendix B lists all synthesized ILs with their *R* or *A* designation. Bromide-based ILs are referred to by the *R* designation, whereas the acetate-based ILs all start with *A*. The nucleophilic substances used include 1-ethylimidazole, 1-methylimidazole, pyridine, triethyl amine, tributyl phosphine, *N*-methylpiperidine, triethyl phosphonium, and *N*-methylpyrrolidine. Brominated electrophiles included AR01 (see section 4.1.2), 1-bromo-2-methoxyethane, 1-bromo-2-ethoxyethane, bromoethane, bromobutane, and 1-chloro-2-methoxyethane. Sample R09 was a futile effort of reacting 1-methylpyridine with 1-bromo-2-methoxyethane to break the resonance of pyridine to favor the IL. Predictably, that experiment failed and the designations R09 and A09 were aborted.

A total of 28 bromide-based ILs and one (1) chloride-based IL were synthesized at 90-96% yield. Samples R10 and R27 produced similar ILs, differing only in the halogen coordinated

with the  $(\text{CH}_3\text{OCH}_2\text{CH}_2)(\text{Bu})_3\text{P}$  cation. Sample R10 was treated with the ion exchange procedure outlined in section 3.2 to produce the acetate-based IL A10. Sample R27 was not treated similarly, as redundant samples of the same composition were not the focus of this project. Figure 4.3 includes all bromide-based ILs, pictured on the left, and the acetate-based ILs derived from the ion exchange, pictured on the right.

**Table 4.1:** Products of the Appel reaction synthesis. Sample AR01 is reacted with pyridine to produce sample R29, as outlined in section 4.1.2.

AR01	IUPAC Nomenclature	1-(2-bromoethoxy)-2-methoxy ethane		
	Chemical Formula	$\text{C}_5\text{H}_{11}\text{O}_2\text{Br}$	Formula Weight	183.04 g/mol
				
AR02	IUPAC Nomenclature	1-(2-bromoethoxy)-2-(2-methoxyethoxy)-ethane		
	Chemical Formula	$\text{C}_7\text{H}_{15}\text{O}_3\text{Br}$	Formula Weight	227.10 g/mol
				
AR03	IUPAC Nomenclature	1-bromo-3-(3-methoxypropoxy)-propane		
	Chemical Formula	$\text{C}_7\text{H}_{15}\text{O}_2\text{Br}$	Formula Weight	211.10 g/mol
				

### Ion Exchange

Amberlyst™ A26 OH Polymeric Catalyst is an industrial-grade resin that is a “microporous, polymeric catalyst based on crosslinked styrene-divinylbenzene copolymer containing quaternary ammonium groups.” While the Product Data Sheet describes its use

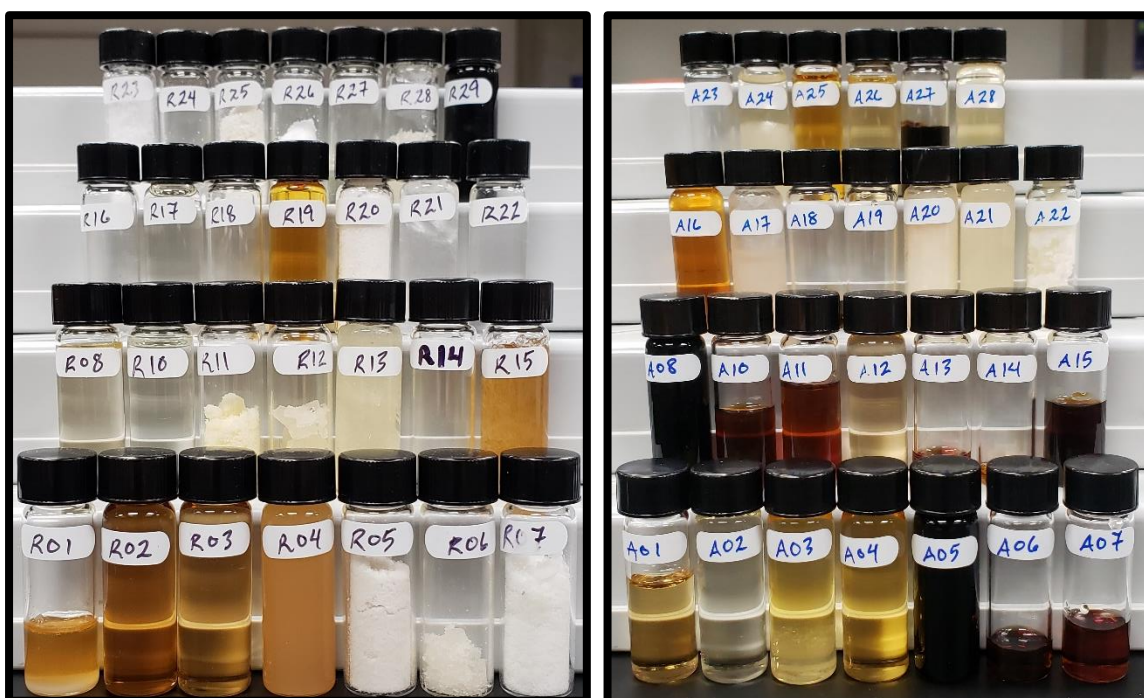
primarily as a catalyst in aldol condensation and carbonylation reactions, its unique porous structure and properties make it an ideal medium for both aqueous and non-aqueous ion exchange reactions. This resin has a Total Exchange Capacity (on a water-wet basis) greater than or equal to 0.80 eq/L and is compatible with water, methanol, ethanol, and acetone solvents. If used in acetone, the resin has a shrinkage of 34%, which in turn affects the available surface area for ion exchange to occur. After an initial ion exchange, the Amberlyst™ A26 OH resin can be regenerated using 1 M NaOH solution, thus allowing multiple ion exchanges to occur for each quantity of resin used (DuPont de Nemours, Inc., 2019).

Using the Amberlyst™ A26 OH resin for ion exchange can be done in water, ethanol, methanol, or acetone. Since the resin shrinks in acetone, it is advised not to use acetone as the medium for ion exchange. Performing the ion exchange of hydrophilic ILs is most efficient in water; however, the removal of water after ion exchange presents a tremendous problem, as the water complexes with the ionic liquid and requires extreme amounts of energy and effort to remove (Shi et al., 2012). As ethanol forms an azeotropic with water (Faghihi et al., 2020), it too presents the same problem of water extraction after ion exchange. Methanol does not form an azeotropic mixture with water, which makes the extraction of methanol from the ionic liquid feasible in a rotovap, as well as the transition to a neat IL via drying of the IL in a vacuum oven.

Considerable amounts of time and effort were spent identifying and improving the ion exchange procedure. When performed with hydrophobic ILs, as was done by Zhao et al. (2018), water is a suitable solvent for the ion exchange to occur between the halogen-based IL and the new anion. Acetate, on the other hand, displays different solubility patterns with acetone and other organic solvents, and thus the ion exchange had to occur in a polar organic solvent. Water was initially used as the solvent for the ion exchange, as it dissolves all substances and is

compatible with the Amberlyst™ A-26 resin. However, as is explained in section 5.1, water forms a complex with hydrophilic ILs that is virtually impossible to break. Initial efforts using water as the solvent led to no lower than 3.5% water concentration in the final acetate-based IL. Thus, a new solvent had to be identified to rectify this problem.

**Figure 4.3:** Results of the IL synthesis (left) and ion exchange (right). Color, physical state, and viscosity vary greatly depending on the cation used to synthesize each IL.



Acetone and dichloromethane were not compatible with the resin, as well as being toxic to the environment (halogenated solvent). Ethanol was compatible with the resin, dissolved both ammonium acetate and the brominated IL, and was simple to rotovap. However, ethanol forms an azeotropic mixture with water. As the acetate-based IL is hygroscopic, water from the atmosphere was being absorbed into the product, and the ethanol prevented water from fully separating from the IL during the procedure. Methanol, on the other hand, does not form an azeotropic mixture with water. It displays the same compatibility with the resin and reactant species and was thus chosen for ion exchange.



As will be discussed in further detail in section 5.1, water must still be used on the ion exchange column in order to fully remove excess acetate ion from the resin beads. Loading of the column occurred by dissolving ammonium acetate in methanol and flushing the resin beads with the solution. Without water, the excess acetate clung to the resin and complexed with the IL as it passed through the column. Evaluation of the NMR (discussed in section 4.1.4) displayed a higher concentration of acetate in the sample than was expected. However, flushing the column with water after flushing the column with the ammonium acetate in methanol solution, followed by a copious amount of methanol, the resultant IL had a relatively low water concentration (around 0.5%) and zero acetate contamination.

This correction in the procedure was not enacted until after initial TGA and NMR results were obtained. Evaluation of the NMR led us to change the ion exchange procedure, whereas the five *Chosen Ones* were reanalyzed via TGA and NMR. The difference is considered in detail in section 5.1 of this manuscript. The silver nitrate test was performed during all ion exchange procedures to ensure the bromide ion was removed by the resin. Each sample was purified using the rotovap, set at 75 °C and 25 mbar of pressure, then dried in the vacuum oven for a minimum of 48 hours at 80 °C and 25 mbar of vacuum. The structure was verified via NMR and the water concentration was tested using a Karl Fisher titrator.

### **Structure Verification via Nuclear Magnetic Resonance**

A 400 MHz nuclear magnetic resonance (NMR) spectrometer was used to evaluate structure and product purity by evaluating the  $^1\text{H}$ ,  $^{13}\text{C}$ , and COSY spectra. Proton NMR spectroscopy uses the magnetic property of the proton nucleus to evaluate the absorption of energy as a function of frequency, which is the foundation of the NMR spectrum. The nature of the functional group to which the proton is attached will dictate the frequency of energy

absorption, and thus a shift of this signal corresponds to the specific functional group of interest. Likewise, spin coupling, or the coupling of proton spins through intervening bonding electrons, provides information on the chemical structure for which the observed protons are associated. Carbon-13 ( $^{13}\text{C}$ ) behaves similarly when exposed to a magnetic field, however the “natural abundance of  $^{13}\text{C}$  is only 1.1% of  $^{12}\text{C}$  and its sensitivity is only about 1.6% that of  $^1\text{H}$ , [meaning] the overall sensitivity of  $^{13}\text{C}$  compared with  $^1\text{H}$  is about 1/5700” (Silverstein et al., 2005).

**Figure 4.4:**  $^1\text{H}$  NMR spectrum comparison for the synthesis of R28. Top-left:  $^1\text{H}$  NMR for 1-ethylimidazole. Top-right:  $^1\text{H}$  NMR for 1-bromobutane. Right:  $^1\text{H}$  NMR for product [BMIM][Br].

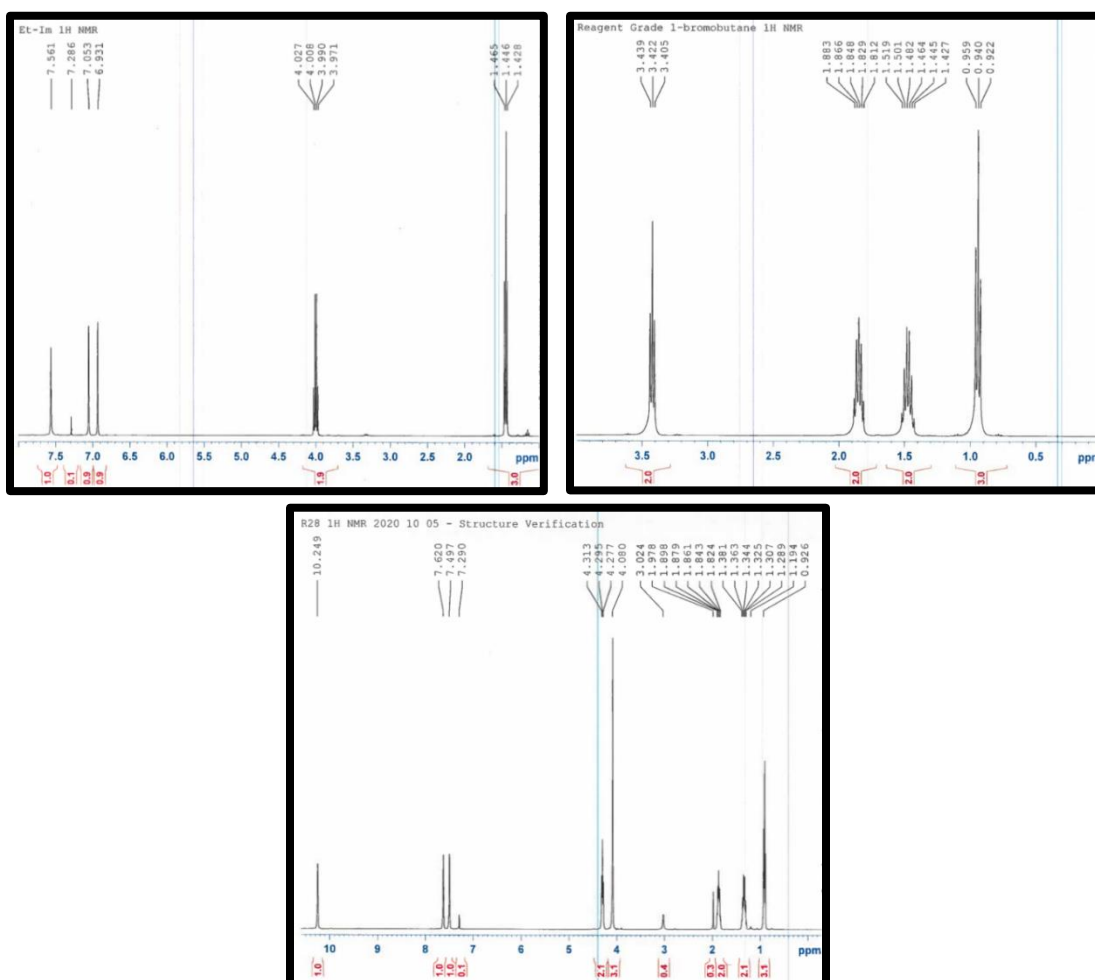
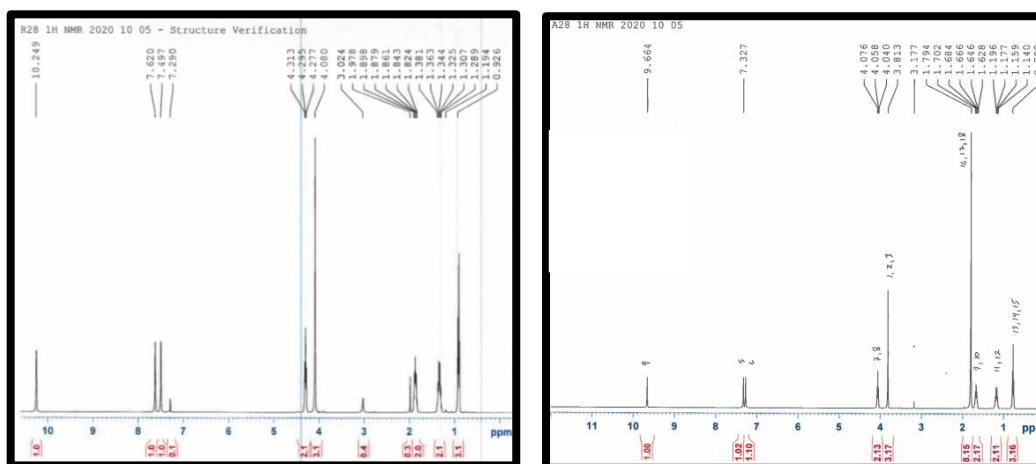


**Figure 4.5:** Comparison of  $^1\text{H}$  NMR for sample R28 (left) to sample A28 (right). The acetate functional group is shifted to the left (down field?) and interacts with the acidic proton of imidazole.



We began the NMR analysis by observing the spectrum of our pure compounds as received from the manufacturer. Figure 4.4 shows three NMR spectra associated with the synthesis of sample R28. The first image is that of the  $^1\text{H}$  spectrum for 1-ethyl-imidazole, the nitrogen-containing nucleophile used to react with 1-bromobutane ( $^1\text{H}$  NMR in the middle). The image on the bottom is the  $^1\text{H}$  NMR for the product, [1-butyl-3-methylimidazolium][bromide] or [BMIM][Br]. Appendix D.i. lists all NMR spectrum, categorized by the R- and A- identification number, and is reported in proper NMR format.

The acetate-based IL NMR spectra are used in conjunction with the silver nitrate test performed after ion exchange to verify the presence of the acetate ion. Acetate, or  $\text{CH}_3\text{CO}_2^-$ , has two peaks on a  $^1\text{H}$  NMR spectra. The first peak,  $\sim 3.8$  ppm, corresponds to the three protons of the methyl group of acetate that has a singlet splitting pattern and integrates for 3. The other peak,  $\sim 10$  ppm, corresponds with the protonated carboxylic acid of acetate that occurs when the acidic proton of imidazole interacts with the anion of the acetate ion. An integration value greater than one indicates an impure IL had indicates an excess quantity of acetate ion complexed in the

IL. Figure 4.5 exemplifies the presence of these two peaks and is the baseline for evaluation for all imidazole based ILs.

### **Characterization of Ionic Liquid Physicochemical Properties**

Upon the completion of structure verification via  $^1\text{H}$ ,  $^{13}\text{C}$ , and COSY NMR, the physicochemical properties of acetate-based ILs were determined. Four analyses were used in the characterization process, starting with the determination of water concentration and viscosity measurements. Thermogravimetric analysis (TGA) was used to evaluate the decomposition profile of each IL, and finally the Kamlet-Taft parameters were analyzed via UV-Vis spectroscopy.

#### **Water Titration**

Water concentration of each acetate-based IL was determined using Karl Fischer titration. To ensure the lowest water concentration was recorded, ILs were placed in a vacuum oven at 80 °C and 25 mbar of vacuum for at least 48 hours prior to testing. The Mettler Toledo C20 Coulometric KF Titrator generates iodine through electrochemical oxidation in the cell. Water concentration must be in the range of 1 ppm to 50,000 ppm (5% water by mass). The KF titration was performed using Hydranal™ solvent, specially formulated for analysis of water concentration.

Atmospheric water is sufficient to interfere with the KF titration, thus requiring speed and accuracy when adding the sample to the analyte. Water already present in the analyte must first be reduced such that a baseline voltametric reading is established. Minimum sample aliquots are inversely proportional to water concentration; that is, 1 ppm water concentration will require a minimum of 10 grams of substance to be titrated whereas 10,000 ppm (or 1% by mass) of water requires no less than 0.1 grams of analyte being tested. IL sample size ranged from 0.149 grams

to 0.514 grams with the average amount of IL was 0.383 grams of IL. Ideal water concentrations for ILs was 0.00%, but realistic/achievable concentrations for hydrophilic ILs were less than 0.250% water by mass. Sample A06 had the highest water concentration at 0.255% and sample A07 had the lowest water concentration at 0.014%. Appendix C(i) lists all ILs synthesized for this project, the mass tested via KF titration, and the measured water concentration.

### **Viscometry**

Kinematic and dynamic viscosity and density were determined using a Stabinger Viscometer SVM 3000 at 30 °C, requiring 3.0 mL of sample that could be recovered and reanalyzed. Kinematic viscosity is a combination of dynamic viscosity and density and is not emphasized in this research. Instead, dynamic viscosity and density were determined and compared for all acetate-based ILs. The dynamic viscosity is reported in mPa·s while density is reported in g/cm<sup>3</sup>.

Dynamic viscosity measures the shearing resistance as two layers of compound pass over one another in opposite directions. Larger mPa·s values indicate more resistance and thus indicate greater viscosity. While viscosity decreases as a measure of temperature, and our analyses using ILs will occur at relatively higher temperatures than viscometrical analysis was performed, ILs with lower viscosity measurements are considered as viable candidates for cellulose and coal dissolution. Appendix C lists dynamic and kinematic viscosities, as well as density, of all acetate-based ILs synthesized in this work. Low viscosity ILs took precedence moving forward with coal dissolution. Samples A20, A22, A24, and A26 were solid at room temperature, therefore neither water concentration nor viscosity were measured. Sample A03 reported the dynamic viscosity at 150.110 mPa·s while sample A14 had the lowest viscosity at

19.162 mPa·s. Samples A01, A12, A16, A28, and A30 had viscosities of 36.620, 22.928, 49.889, 203.100, and 71.703 mPa·s, respectively.

**Table 4.2:** Viscosity measurements for chosen ILs. IL A28 is much higher than preferred; however, it is a tried and tested IL that is found throughout the literature. Cellulose and coal are expected to dissolve very well in A28.

IL	Dynamic Viscosity (mPa·s)	Kinematic Viscosity (mm <sup>2</sup> /s)	Density (g/cm <sup>3</sup> )
A01	36.620	33.498	1.0932
A12	22.928	20.907	1.0967
A16	49.889	47.197	1.0570
A28	203.100	194.110	1.0463
A30	71.703	69.299	1.0547

### Thermogravimetric Analysis

Thermogravimetric analysis (TGA) was conducted by Dr. Gary Baker, Associate Professor of Chemistry at the University of Missouri, using a TA Instruments TGA Q50 under a nitrogen atmosphere (60 mL/min flow rate). Chemical decomposition and phase transitions are monitored using TGA by measuring the mass of the sample as the temperature of the reaction chamber increases. A graph of percent mass remaining against time, as shown in Figure 4.6, is the decomposition profile of IL A30. The initial decrease in mass is attributed to the loss of water complexed within the IL, which occurs ~100°C.  $T_{dcp}$  is the temperature of which 10% of the mass has decomposed, while  $T_{der}$  is the maximum in the first-derivative profile of the TGA scan.

The TGA profile of each of the acetate-based ILs provides information regarding the maximum temperature the IL can be exposed without fear of decomposition. As ILs decompose rather than evaporate, the maximum operating temperature for coal dissolution is set by the TGA analysis. Hydrophilic ILs have consistently lower decomposition temperatures than their hydrophobic counterparts. For example, consider the  $T_{der}$  and  $T_{dcp}$  for three ILs that all have the

same cation, as shown in Table 4.3. The anions  $\text{Tf}_2\text{N}^-$  and  $\text{PF}_6^-$  result in hydrophobic properties of the IL while acetate ( $\text{OAc}^-$  or  $\text{CH}_3\text{CO}_2^-$ ) anion results in a hydrophilic IL. The hydrophilic nature means more water complexes with the IL from the atmosphere, thus resulting in the large discrepancy between  $T_{dcp}$  and  $T_{der}$ , as well as the lower decomposition temperature. Appendix C lists the results of all TGA's performed for the acetate based ILs.

**Figure 4.6:** Thermogravimetric analysis (TGA) of sample A30. “ $T_{der}$  is determined from the maximum in the first-derivative profile of the TGA scan.  $T_{dcp}$  is the decomposition temperature measured as the onset of decomposition, using the common criterion of 10% total mass loss” (Zhao et al., 2018, p.36029).

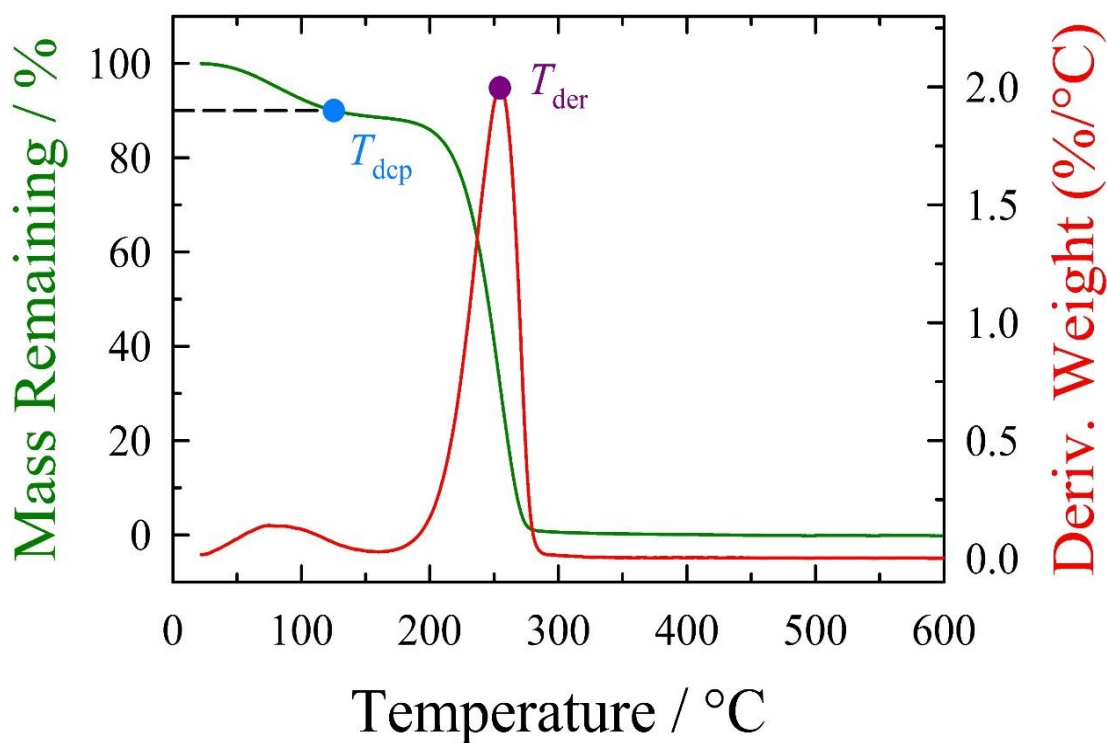


**Table 4.3:** Comparison of TGA profiles for three ILs with the same cation. Anions  $\text{Tf}_2\text{N}^-$  and  $\text{PF}_6^-$  cause the IL to display hydrophobic characteristics. These ILs were synthesized and analyzed by Zhao et al. (2018).

Ionic Liquid	$T_{der}$ (°C)	$T_{dcp}$ (°C)	Transition Shape
* [BMIM][ $\text{Tf}_2\text{N}$ ]	464	406	Singlet
* [BMIM][ $\text{PF}_6$ ]	472	424	Singlet
[BMIM][ $\text{OAc}$ ]	237	191	Singlet

Table 4.4 summarizes the TGA results for the five ILs chosen for dissolution of cellulose and coal. The ideal IL had higher  $T_{der}$  values and decomposed in a single phase. Residual char for sample A01 is outside of the error of the measurement baseline, inferring that not all the IL decomposes at 600 °C. Decomposition temperatures for acetate-ILs are notoriously lower than other ILs, particularly ILs with hydrophobic anions. ILs A01 and A30 are both imidazole based ILs with acetate anion, both have an ethyl substituent at the #3 position and a four-member chain on the #1 position. However, A01's four-member chain is  $-\text{CH}_2\text{CH}_2\text{OCH}_3$  while A30 is a straight butyl chain. ILs A12 and A28 can be similarly compared, with both having an imidazole base, a methyl substituent at the #3 position, and A28 having a longer straight carbon chain. Very slight variations in decomposition temperature come from the symmetry and "stackability" of the cations, with less polar functional groups leading to more stability. IL A16 does not compare to the other four because it has a base group of piperidine, a non-conjugated six-membered ring containing nitrogen, and has a functional group that is more polar ( $-\text{CH}_2\text{CH}_2\text{OCH}_2\text{CH}_3$ ). This compound has a lower decomposition temperature than the imidazole-based ILs.

### **Kamlet-Taft Parameters of Polarity/Polarizability**

Polarity and polarizability of traditional organic solvents is determined by the unequal sharing of electrons, or polarity, of the molecular compound. The existence of a polar moment that isn't offset by another polar bond of equal magnitude and opposite direction means a compound is polar. Dichloromethane,  $\text{CH}_2\text{Cl}_2$ , is a prime example: with a tetrahedral molecular geometry, the more electronegative chlorine atoms pull the electrons to one side of the molecule, which results in a polar molecule. However, ILs are comprised of two formally charged species, and thus the traditional comparison of electronegativity is insufficient in evaluating polar



properties. Thus, Mortimer J. Kamlet and Robert W. Taft developed a set of parameters that, when used together, describe the polarity and polarizability of ILs (Crowhurst et al., 2003).

**Table 4.4:** Results of TGA for the five chosen ILs to be used for cellulose and coal dissolution. Char (wt %) is “the amount of carbon char residue determined from the relative mass remaining at 600 °C; a residue amount on the order of  $\pm 1$ -2% should be considered within the error of the measurement baseline” (Zhao et al., 2018). RG28 is the reagent grade [BMIM][OAc] for comparison to A28.

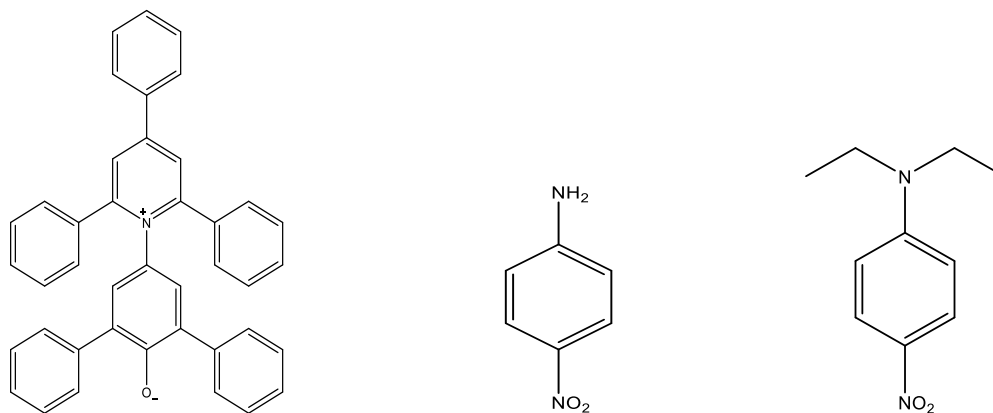
Ionic Liquid	$T_{\text{der}}$ (°C)	$T_{\text{dcp}}$ (°C)	Transition Shape	Char (wt %)
A01	237.5	183.1	S	3.0%
A12	241.9	170.8	S	0.0%
A16	199.5	120.0	S	0.0%
A28	237.4	190.8	S	0.0%
RG28	239.2	193.7	S	0.4%
A30	254.6	125.4	S	0.0%

The Kamlet-Taft equation uses three distinct variables to measure a compound’s overall polarity. These values,  $\alpha$ ,  $\beta$ , and  $\pi^*$ , are determined by a solvatochromic analysis of the interaction of the compound and an organic dye. “Parameter  $\alpha$  provides a measure of a solvent’s hydrogen-bond-donating acidity (HBD), parameter  $\pi^*$  provides a measure of a solvent’s dipolarity/polarizability ratio,” and the parameter  $\beta$ , which measures the hydrogen-bond-accepting acidity (HBA), “was obtained by measuring the relative difference of solvatochromism between” the two dyes (Lee et al., 2008, P. 1474).

An Agilent UV-Visible ChemStation with an Agilent 8453 Spectrophotometer was programmed to analyze the full ultraviolet/visible spectrum using both a deuterium and a tungsten lamp. An Optical Glass cuvette has a transmission range of 340 to 2500 nm, so it is imperative to use a UV Quartz cuvette, which transmit between 190 and 2500 nm, in order to detect light transmission through the samples for all applicable wavelengths. Once obtained, the spectrum was analyzed for the wavelength of maximum absorbance, whose value was recorded

as either  $\lambda_{RD}(nm)$ ,  $\lambda_{NA}(nm)$ , or  $\lambda_{DENA}(nm)$ . Wavelengths, measured in nanometers, for NA and DENA should be converted to wavenumbers ( $\nu$ ) with the unit of kiloKeyser ( $1 \text{ kK} = 10^3 \text{ cm}^{-1}$ ).

**Figure 4.7:** Kamlet-Taft dyes. Left: Reichardt's dye. Middle: 4-nitroaniline. Right: N,N-diethyl-4-nitroaniline



Emphasis was originally placed on reproducing literature values for water, select organic solvents, and ILs. Table 4.5 lists the literature values for water, four organic solvents, and four ILs with the BMIM<sup>+</sup> cation. Percent error was calculated before any mathematical permutations were applied to avoid compounding error. For example, the  $\lambda_{DENA}(nm)$  was measured at 396 nm, a 0.253% error from literature wavelength values; conversion to  $\pi^*$  resulted in a 1.43% error.

Table 4.6 lists the standard samples used to evaluate methodology of the UV-Vis spectroscopic analysis of the Kamlet-Taft parameters. All ILs tested were reagent grade, sealed and stored at room temperature in the laboratory stock shelves. The largest percent error in measurement occurred with [BMIM][TfO] at 1.06% error. Wavelength of maximum absorption for Reichardt's dye is not included as all measurements were in excess of 200% error. Evaluation of Kamlet-Taft parameters were thus reduced to  $\pi^*$  and  $\beta$  values for analysis of synthesized ILs.

**Table 4.5:** Literature values for Kamlet-Taft measurements of water, organic solvents, and select BMIM<sup>+</sup> ILs.  $E_T^N$ ,  $\alpha$ ,  $\beta$ , and  $\pi^*$  values were provided by Lee et al. (2008);  $E_T(30)$ ,  $\lambda_{RD}(nm)$ ,  $\lambda_{NA}(nm)$ ,  $\nu_{NA}$ ,  $\lambda_{DENA}(nm)$ , and  $\nu_{DENA}$  values were backwards calculated using Equations 2.2.1 through 2.2.5.

Compound	$\lambda_{RD}$	$\lambda_{NA}$	$\nu_{NA}$	$\lambda_{DENA}$	$\nu_{DENA}$	$E_T(30)$	$E_T^N$	$\alpha$	$\beta$	$\pi^*$
Water	453	380	26.35	429	23.29	63.1	1.00	1.12	0.14	1.33
Acetone	680	366	27.29	396	25.28	42.0	0.350	0.202	0.539	0.704
Acetonitrile	627	364	27.45	400	24.98	45.6	0.460	0.350	0.370	0.799
Dichloromethane	702	350	28.55	400	25.01	40.7	0.309	0.040	-0.010	0.790
Methanol	516	370	27.01	397	25.20	55.4	0.762	1.050	0.610	0.730
[BMIM][PF <sub>6</sub> ]	546	368	27.14	413	24.24	52.4	0.669	0.634	0.207	1.032
[BMIM][BF <sub>4</sub> ]	546	376	26.62	413	24.19	52.4	0.670	0.627	0.376	1.047
[BMIM][TfO]	550	377	26.51	411	24.32	52.0	0.656	0.625	0.464	1.006
[BMIM][OAc]	581	409	24.48	413	24.21	49.2	0.570	0.440	1.150	1.040

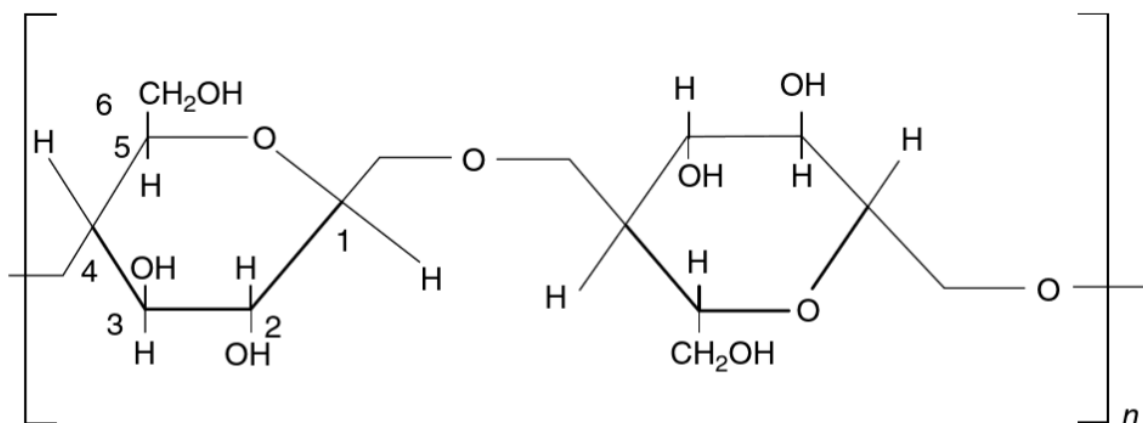
Validation of the UV-Vis spectroscopy procedure could only be attained for NA and DENA dyes. Appendix C lists all acetate-based ILs and their corresponding  $\lambda_{NA}(nm)$ ,  $\nu_{NA}$ ,  $\lambda_{DENA}(nm)$ ,  $\nu_{DENA}$ ,  $\pi^*$ , and  $\beta$  values. The five ILs chosen to proceed to dissolution of cellulose and coal include A01, A12, A16, A28, and A30. The values for these specific ILs can be found in Table 4.7. ILs with larger  $\pi^*$  values, or greater dipolarity/polarizability ratios, are predicted to dissociate cellulose and coal better than higher  $\beta$ , hydrogen-bond-donating acidity (HBA), would predict. Compounds that are high in both  $\pi^*$  and  $\beta$ , specifically sample A28 and A30, are predicted to dissociate the best of five samples.

### Dissolution of a Model Coal Compound: Cellulose

Characterization of the physiochemical properties of all synthesized bromide- and acetate-based ILs provided ample information to make a decision regarding the five ILs with the highest likelihood of dissolving coal. These ILs, affectionately referred to as the Chosen Ones, exhibit lower viscosities, high TGA profiles, and strong hydrogen-bond-basicity properties that should work to weaken the hydrogen bonding of coal. Before pretreating coal, we are interested

in the ability these Chosen Ones have in disrupting a known organic compound that resembles the complex coal structure. The five ILs that make up the Chosen Ones include: ILs A01, A12, A16, A28, and A30. Refer to Table 3.1 for names, formula, molecular weight, and structures of these compounds.

**Figure 4.8:** Cellulose monomer, otherwise known as cellobiose (Hamad, 2017).



Cellulose (Figure 4.8) is “a polydisperse, linear, crystalline (polysaccharide) macromolecule of high molecular weight” and “a high degree of polymerization” (Hamad, 2017). More affordable and more readily available than coal, cellulose behaves similarly to low rank coal and can thus be used as a preliminary evaluation test for predicting IL behavior with lignite. “Coal-related compounds must be used to study the dissociation of ILs on coal under mild conditions” (Lei et al., 2019). Avicel<sup>®</sup> PH-101, a commercially available microcrystalline cellulose powder, was used to evaluate the dissolution properties of the chosen ILs.

Dissolution of cellulose was observed to predict the likelihood of dissociation of coal by our five select ILs. Cellulose is one of the components that, when exposed to pressure and temperature, will eventually transform into coal. Cellulose is used as a model coal compound due to the H-bond complex network resembling that of coal. Avicel<sup>®</sup> PH-101 is a microcrystalline

cellulose powder with approximately 50  $\mu\text{m}$  particle size. The cost is relatively low, abundance high, and ease of use particularly simple. The intent of this phase of the study was to determine (1) whether each of the five IL would dissolve cellulose, and (2) how much cellulose would dissolve per gram of IL.

**Figure 4.9:** Experimental set-up of dissolution of cellulose



The experimental set-up is demonstrated in Figure 4.9. A low temperature oil bath, rated at temperatures less than 250  $^{\circ}\text{C}$ , was centered on a stir/hot plate. A clamp system was used to hold the thermometer and two 5-mL Pyrex<sup>®</sup> glass vials in suspension in the oil bath. The bath was heated to  $107 \pm 4$   $^{\circ}\text{C}$  and constantly monitored for fluctuations in temperature.

Approximately 1.0 g of IL was added to each vial, making sure that all IL was in the bottom of the vial and not stuck to the sides of the glass. The vials were placed back into the oil bath and allowed sufficient time for the IL to equilibrate temperature. Cellulose was added in 0.02 g aliquots and left to stir until all visible particulates had been dissolved. Dissolution is evidenced by initial clumping of the cellulose upon addition to the IL followed by slow dissolving and eventual disappearance of particulate matter. The IL/cellulose solution was considered saturated when the viscosity of the solution was too high for the stir bar to move.

The solubility of cellulose in each IL was calculated by dividing the mass of IL by the mass of cellulose added. The results of these calculations are presented in Table 4.7, with two trials per IL having been recorded. RG28 corresponds with reagent grade [BMIM][OAc] used to measure the relative consistency of analysis between the synthesized IL and that which was purchased as pure. The Kamlet-Taft parameter,  $\beta$ , is included in this table to aid in examining of larger  $\beta$  values would correlate with larger dissolution of cellulose.

**Table 4.6:** Experimental values for the dissolution of cellulose. Samples A01, A12, A16, A28, and A30 were synthesized in lab and the corresponding  $\beta$  values were derived from UV-Vis analysis discussed in section 4.2.4. <sup>(a)</sup>Literature value for  $\beta$  for RG28 is found in Ladesov et al. (2015).

IL	Vial	Mass IL	Mass Cellulose	% Dissociation	$\beta$
A01	1	0.996 g	0.095 g	9.5%	0.767
	2	1.005 g	0.095 g	9.5%	
A12	3	0.990 g	0.111 g	11.2%	1.000
	4	1.019 g	0.112 g	11.0%	
A16	7	0.873 g	0.121 g	13.9%	1.270
	8	0.998 g	0.135 g	13.5%	
A28	5	1.064 g	0.184 g	17.3%	1.257
	6	0.910 g	0.163 g	17.9%	
RG28	9	1.061 g	0.182 g	17.2%	1.257
	10	1.256 g	0.212 g	16.9%	
R30	11	1.328 g	0.205 g	15.4%	1.254
	12	1.255 g	0.194 g	15.5%	

### Dissolution of Coal in Select Ionic Liquids

Dissolution of coal was conducted in the same apparatus described in section 4.3.1. Coal samples required processing in order to reduce the particle size from the hard chunk of coal 5-10 cm in diameter. A mortar and pestle was used to pulverize the coal until the particulate matter was consistent with dust. A sieve with 150  $\mu\text{m}$  stainless steel mesh screen was used to sift the particulate coal to ensure the diameter of coal particles do not exceed 150  $\mu\text{m}$ . A ratio of 5:1 IL to

coal was added to each vial with two trials per IL. On average, 1 g of IL was mixed with 0.2 g of coal and left to stir at 105 °C for 24 hours.

Upon the completion of 24 hours of stirring, methanol was added to the vial to facilitate the transfer of the coal/IL mixture to a plastic conical centrifuge vial. Each sample was centrifuged for 30 minutes, the supernatant was extracted from the vial and heated on a stir plate until methanol was completely removed. The solid material left in the conical vial was washed with deionized water, subjected to centrifugation for 30 minutes, and then the liquid was decanted once again. After three washings with water, the solid was washed once with acetone, centrifuged for 30 minutes, the liquid decanted into the same receptacle as the water washings. Acetone was used to transfer the solid material onto a glass watch plate, the acetone was evaporated in the laboratory hood, and then placed in an oven set at 65 °C for at least 48 hours. The solid material was scraped off the watch glass, collected in a glass vial, and weighed.

Table 4.8 shows the masses of each IL and the vial number, mass of coal added to the IL, and mass of recovered coal after the drying process was complete. Characterization of the dissolution of coal occurred in five steps: TGA, FTIR, LC-MS, SEM/EDS, and XRD spectroscopy. TGA and LC-MS analysis were completed offsite; TGA was completed by Dr. Baker, and LC-MS was completed by Colorado State University-Fort Collins researchers. The results of each analysis will be reported in detail in the following sections.

### **Thermogravimetric Analysis of Coal/Ionic Liquid Samples**

Samples of dissolved coal were sent to the University of Missouri for Dr. Baker to analyze via TGA. The results of the scans were considerably different than those of IL as coal is an amalgam of monomers complexed together via ether linkages and hydrogen bonds. As such,

the decomposition profile is not sharp and clean, nor is it complete at 600 °C. Figure 4.10 is a comparison of TGA scans for untreated lignite and that of lignite after treatment with IL A30. Whereas each IL decomposed by 600 °C, leaving only residual char, coal did not combust more than 50% of its mass. Lignite appeared to have more water, referencing the decomposition around 100 °C, while coal treated with A30 had a larger decomposition spike between 300 and 500 °C. Both samples reached 90% mass remaining at approximately 300 °C.

**Table 4.7:** Masses of IL and coal used in the dissolution process and the mass of coal recovered after dissolution and washing.

IL	Vial	Mass IL (g)	Mass Coal (g)	Mass of Coal Recovered	Mass of Coal Dissolved	% Mass Dissolved
A01	C01	1.072	0.208	0.158	0.050	24.0
	C02	1.240	0.246	0.198	0.048	19.5
A12	C03	0.998	0.206	0.151	0.055	26.7
	C04	1.011	0.211	0.164	0.047	22.3
A16	C05	0.997	0.194	0.159	0.035	18.0
	C06	0.983	0.199	0.128	0.071	35.7
A28	C07	0.946	0.197	0.167	0.030	15.2
	C08	0.957	0.197	0.165	0.032	16.2
RG28	C09	1.163	0.235	0.220	0.015	6.38
	C10	1.308	0.263	0.228	0.035	13.3
A30	C11	1.144	0.232	0.200	0.032	13.8
	C12	1.115	0.225	0.182	0.043	19.1

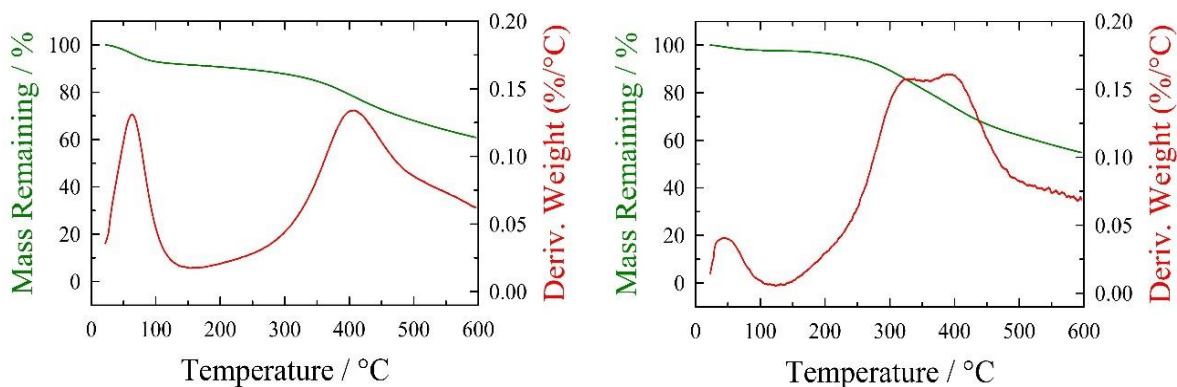
All scans exhibit similar decomposition patterns consistent with dissolution or rearrangement of lignite. No evidence of residual IL is present, as each IL used in the dissolution of coal decomposes before 300 °C. Incomplete decomposition of coal indicates that any fragmentation caused by ILs is insufficient to produce readily-combustible materials. Figure 4.11 shows the TGA scans for all five chosen ILs and reagent grade [BMIM][OAc]. The relative values for  $T_{dcp}$  and  $T_{der}$  are close together, implying accurate representation of the decomposition analysis. Sample A28 and RG28 differ in  $T_{der}$  by 1.8 °C and 2.9 °C in  $T_{dcp}$ , establishing that the



synthesized IL and reagent grade IL have similar physical characteristics. This leads to increased reliability regarding analytical accuracy.

**Figure 4.10:** TGA scan of untreated lignite (left) and lignite treated with A30 (right)

### Fourier Transform Infrared (FTIR) Spectroscopy Analysis of Cellulose and Coal Dissolution



The Thermo Scientific Nicolet iS5 FTIR with iD5 ATR attachment allows for analysis of both solid and liquid materials. FTIR analysis was performed on cellulose, cellulose dissolved in IL, untreated lignite, and the lignite solid retrieved after dissolution with ILs. Figure 4.13 shows FTIR scans of the cellulose/IL mixture presented as % Transmittance against Wavenumber ( $\text{cm}^{-1}$ ), whereas Figure 4.13 shows stacked spectra for lignite before and after dissolution with IL. Changes to the IR spectrum gives insight into the effect ILs have on cellulose and coal dissolution.

Figure 4.11 is a stacked comparison of the FTIR spectra for cellulose, before (top) and after dissolution in each of the ILs. Avicell<sup>®</sup> PH-101 is the undissolved cellulose for comparison with the other scans. Peak growth in the  $3100\text{-}2800\text{ cm}^{-1}$  range correspond with the ILs, as evidenced in the FTIR spectra of ILs in Figure 4.11. Similar peaks can be seen around  $1550\text{ cm}^{-1}$

that can be attributed to the ILs. Figure 4.12 simply shows the presence of both cellulose and ILs in the sample, a phenomenon that should not be evidenced in the coal dissolution spectra.

**Figure 4.11:** TGA scans of the chosen ILs and RG28.

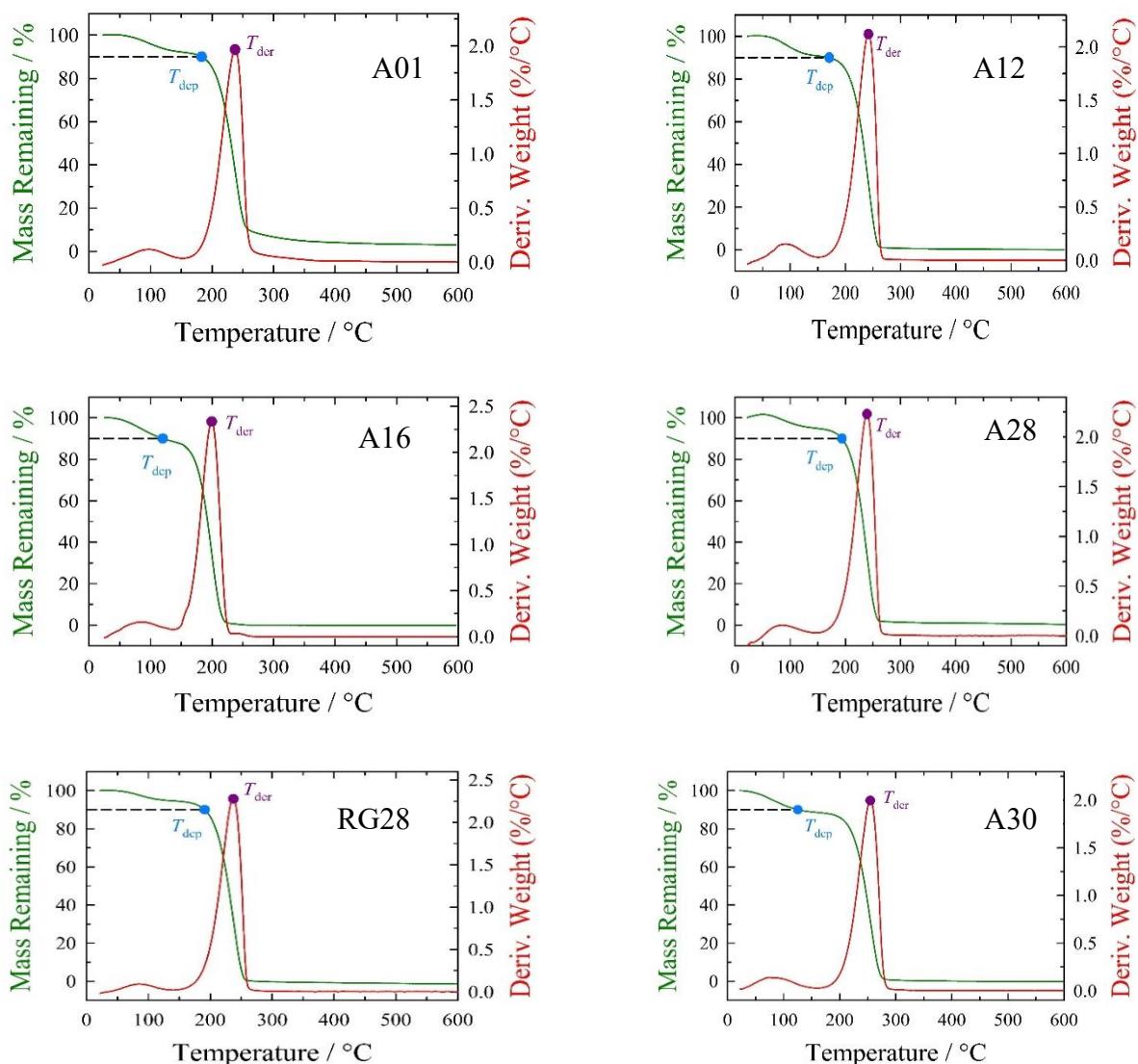


Figure 4.13 displays the accumulated spectra for lignite and the coal samples after dissolution with ILs. The naming scheme of these spectra use the CXX-AXX designation, with CXX referring to the vial number and AXX referring to the IL used in the dissolution process. Any changes to the IR spectra should be attributed to the changes in the coal conformation, as

each IL has been washed and removed prior to drying of the coal samples. Table 4.9 compares the noteworthy peaks identified during FTIR analysis, for lignite and all other IL dissolved coal samples. An increase in FTIR signals results from the disruption of C-O bonds in coal, resulting in more exposed C-C, C=C, and C≡C bonds and C-H wagging, bending, and stretching.

Dissolution of coal resulted in less complex structures and more free particles that can respond to FTIR analysis. This disruption in the complex is evidenced by the increase in FTIR signals and the change to the FTIR scan patterns.

To demonstrate the concept of coal dissolution in task-specific ILs, we conducted the lignite pretreatment by 6 ILs and compared their FT-IR spectra to one another (Figure 4.14). Several peaks of interest include 3420, 2920, and 1600  $\text{cm}^{-1}$  representing hydrogen bonds (-OH stretching), aliphatic C-H stretching, and aromatic ring stretching, respectively (Lei et al., 2019). We observed that all ILs could dissolve lignite (greater than 10 wt %). Table 4.10 compares some peak ratios to represent the lignite characteristics. It appears that IL A12 extracted more aliphatic components from lignite while the other ILs extracted more aromatic compounds. All ILs reduced hydrogen bonds in lignite to various degrees, with IL A28/RG28 being most effective in disrupting H-bonding.

### **Liquid Chromatography-Mass Spectroscopy (LC-MS)**

Two products were isolated after the dissolution of coal via IL: solid, reclaimed and washed coal particulates and a liquid with the dissolved coal and IL. Original characterization of the liquid substance involved Gas Chromatography-Mass Spectroscopy (GC-MS); it is apparent after TGA that vaporization of any coal material would not occur at temperatures less than 600 °C. Considering the GC column and oven would not endure temperatures above 325 °C, we settled on analyzing the liquid substance using Liquid Chromatography-Mass Spectrometry (LC-

MS). Samples were sent to Colorado State University-Fort Collins for analysis using an Agilent B-TOF LCMS 6230 instrument.

Evaluation of the LC-MS results occurs in two steps: first, identification of the known material, in this case our ILs, and second, identification of possible fragments arising from the dissolution of coal. Sample A01 has a molecular weight of 214.25 g/mol with 59.04 g/mol attributed to the acetate anion and 155.21 g/mol from the imidazolium cation. When analyzing the LC-MS spectra it is important to look in the mass-to-charge ( $m/z$ ) range of these molecular weights to identify the IL. The scan for sample C01-A01 has a significant peak at 141.10258 and a smaller peak at 142.10569, most likely caused by fragmented IL A01. Notable peaks of more than 20 counts occurred at 157.09753, 158.10050, 449.33938, 450.34205, and 451.34512  $m/z$  ratios, all most likely associated with the dissolved coal particulates. Table 4.11 presents the major peaks (peaks with counts greater than 20) from LC-MS analysis for all samples.

The molecular mass for each cation can be calculated by subtracting the mass of acetate anion, 59.04 g/mol. Coal fragments that register on the LC-MS detector have the general formula,  $C_xH_yO_mN_n$ , where subscripts  $x$ ,  $y$ ,  $m$ , and  $n$  range from 0 to 50. For example, the database used by the LC-MS program attributes the peak at 450.34235 as having a chemical formula of  $C_{24}H_{43}N_5O_3$ . It is conceivable for a polymeric structure like coal to fragment into particles of this magnitude. Smaller units (i.e., mass less than 100 g/mol) could and probably do exist in the IL/coal solution, however there is no evidence from LC-MS to validate or refute this speculation.

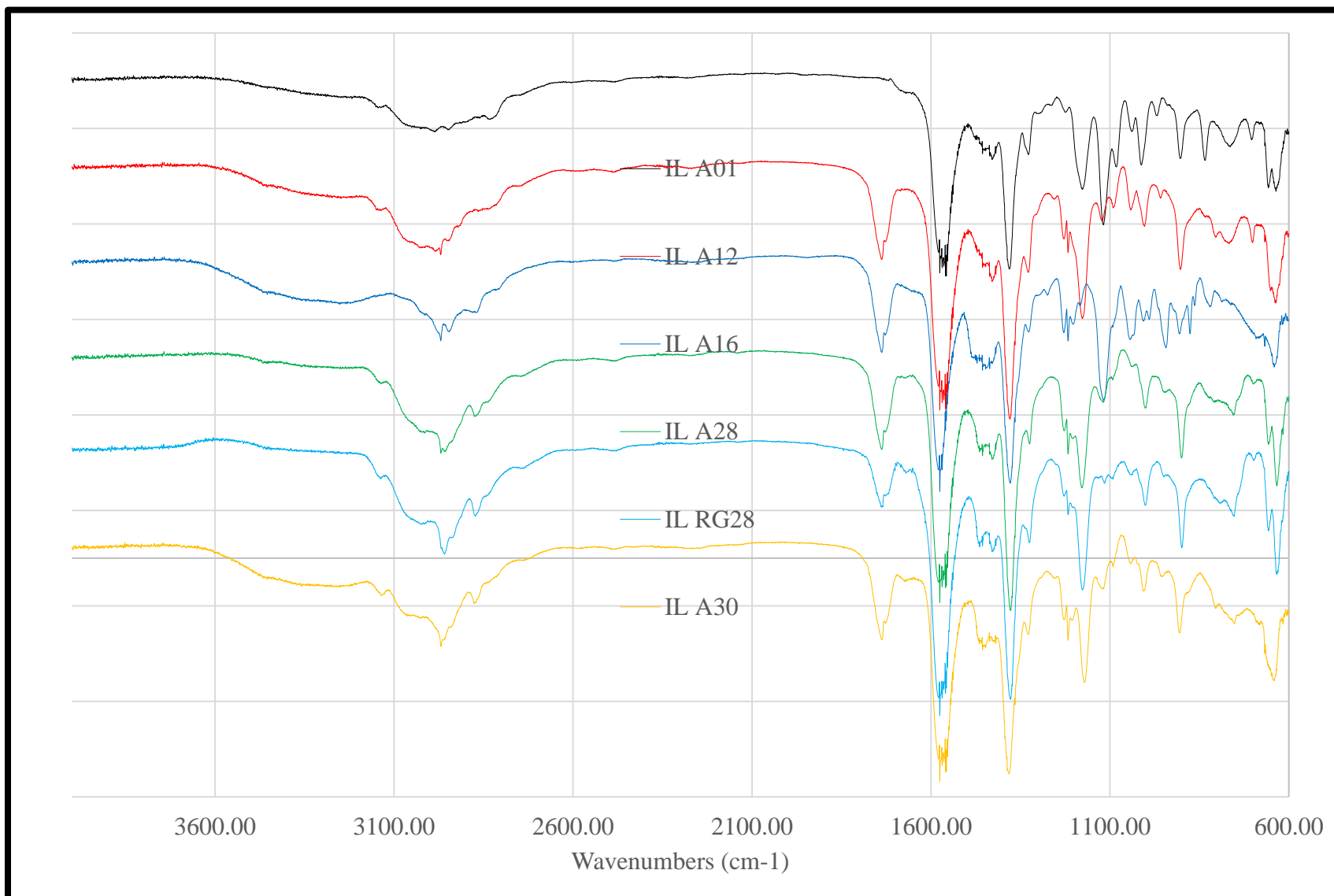
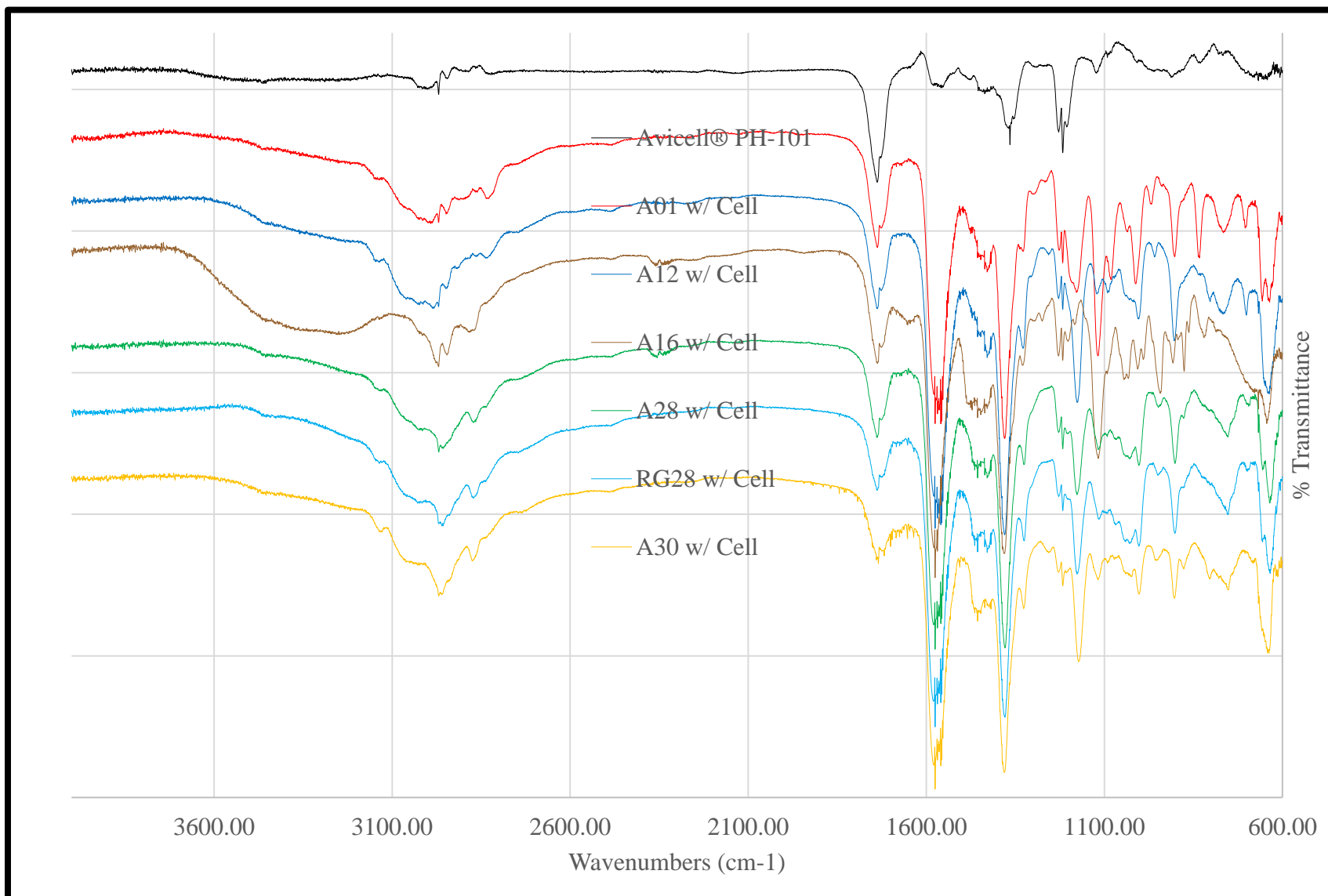
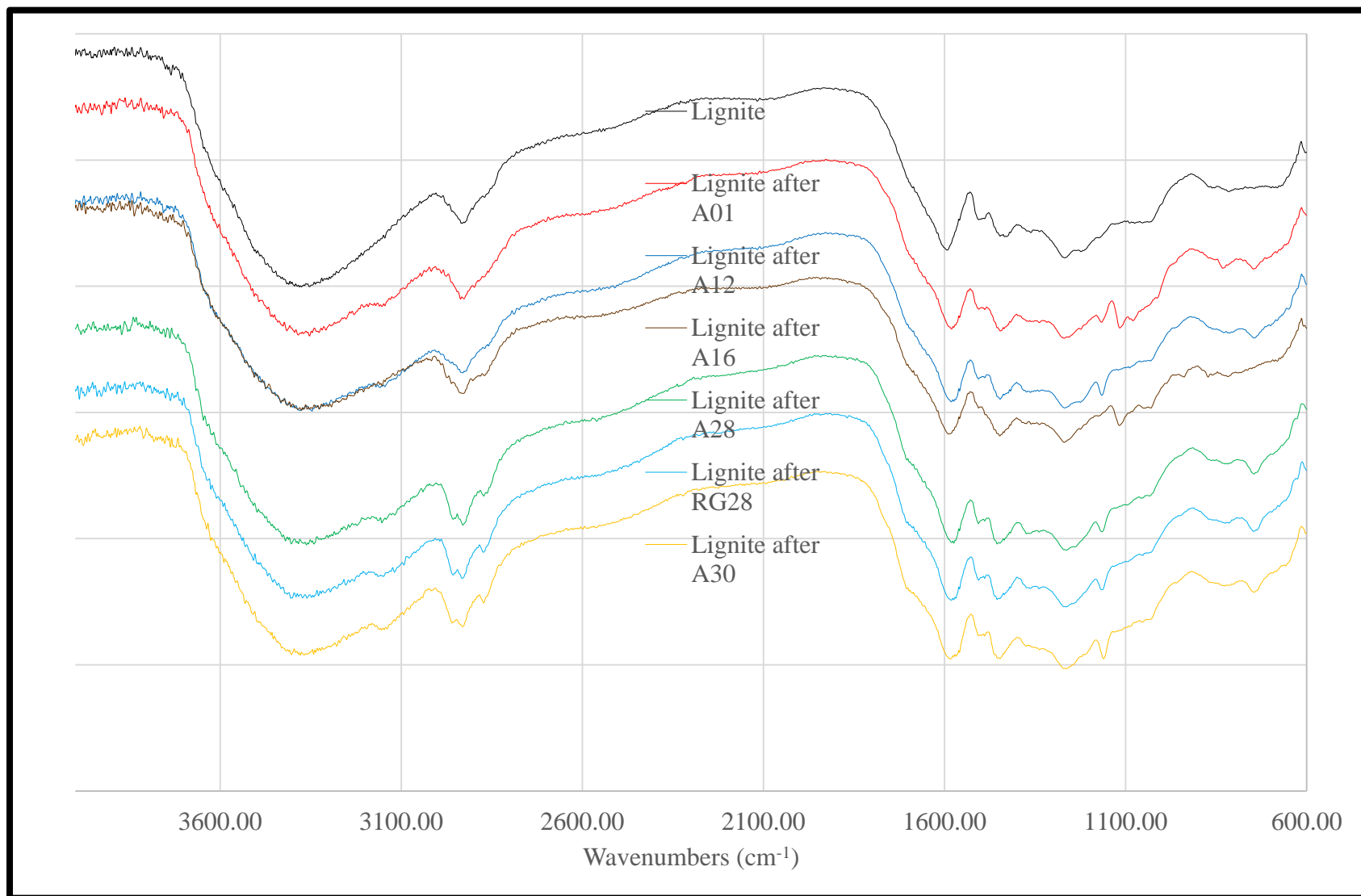
**Figure 4.12:** FTIR scans for ILs.

Figure 4.13: FTIR scans for Cellulose and IL after dissolution.



**Figure 4.14:** FTIR scans of lignite before (top) and after dissolution with the specific ILS.



**Table 4.8:** FTIR peaks identified by the OMNIC FTIR software. Lignite (top) shows evidence of alkane, alkene, and alkyne stretching, as well as C-H bending and some C-O stretching. IL-dissolved samples show an increase in C-C, C=C, and C≡C stretching, increased C-H bending, and more peaks in the fingerprint region.

Sample	Peaks >2000 cm <sup>-1</sup>	Peaks <2000 cm <sup>-1</sup>		Sample	Peaks >2000 cm <sup>-1</sup>	Peaks <2000 cm <sup>-1</sup>	
Lignite	3345 2923	1594	1030				
		1495	813				
		1428	676				
		1262	634				
		1216					
C01-A01	3568 3127 2924 2852	1582	1114	C07-A28	3564 3101 3027 2968 2925 2853	1581	1162
		1507	1080			1507	1091
		1435	1008			1435	1001
		1377	867			1374	873
		136	827			1338	818
		1272	268			1272	749
		1229	749			1228	730
		1163	727				648
			648				
C03-A12	3130 2925 2853 2786	1573	1090	C09-RG28	3102 3027 2968 2927 2853	1582	1163
		1507	1002			1506	1091
		1435	867			1434	1003
		1376	819			1374	873
		1337	766			1338	819
		1272	749			1272	749
		1224	730			1227	731
		1163	648				648
C05-A16	3228 3027 2968 2925 2853		1112	C11-A30	3102 3015 2968 2925 2852	1583	1160
		1583	1026			1557	1091
		1506	1002			1506	1002
		1435	937			1436	873
		1375	873			1375	818
		1338	813			1338	749
		1272	771			1272	730
		1226	756				645
		1162	690				
			644				



**Table 4.9:** Characteristics of lignite following IL pretreatment

IR Spectrum	Aliphatic/Aromatic Ratio <sup>1</sup>	H-Bonding <sup>2</sup>
No Pretreatment	0.824	1.24
IL A01	0.826	1.05
IL A12	0.838	1.04
IL A16	0.728	0.831
IL A28	0.909	1.01
IL RG28	0.884	0.985
IL A30	0.823	0.972

Note: <sup>1</sup>Peak height (2920 cm<sup>-1</sup>) / peak height (1600 cm<sup>-1</sup>); <sup>2</sup>Peak height (3350 cm<sup>-1</sup>) / peak height (1600 cm<sup>-1</sup>)

### Scanning Electron Microscope (SEM) with Energy Dispersive X-ray Spectroscopy (EDS)

Firing electrons at a solid material is a useful way to image microscopic materials. This method, known as SEM, accelerates electrons to a particular energy and an attached detector measures the reflection and deflection of these electrons to form topographical maps of the surface of the material. Considered a non-destructive qualitative technique, SEM allows researchers to view a material at 30× to 10,000× times magnification. Subsequently, striking a material with energized electrons results in the buildup and eventual release of energy from the material in the form of X-rays. EDS is an attachment to the SEM that detects and quantifies those X-rays and can be used to supplement the analysis of the atomic particles present in the observed material.

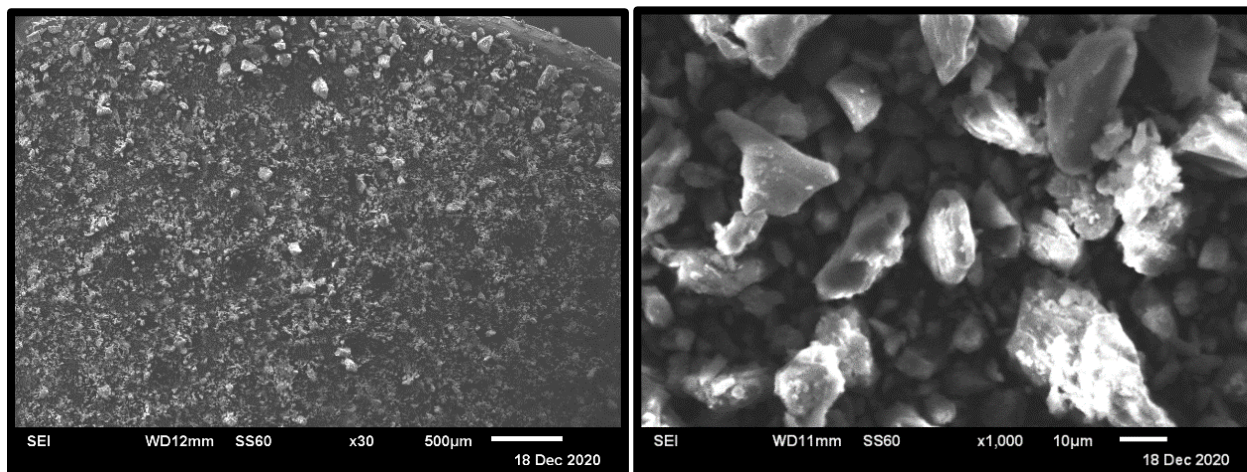
The University of Northern Colorado owns and operates a JEOL JSM-6610LV scanning electron microscope (SEM) with an Oxford Instruments X-Max 20 mm<sup>2</sup> energy dispersive X-ray spectroscope (EDS). Figure 4.15 includes images taken with the SEM, one at 30x zoom and the other at 1000× zoom. Charging “relates to the build-up of either positive or negative potential at

or near the surface of a sample while it is being irradiated by a particle beam” (Postek & Vladár, 2015) and occurs when a sample is not completely conductive. Evidence of charging was present in all images. To mitigate this effect, an EMS 550 Sputter Coater was used to coat each sample with an ~15 nm layer of gold (Au). As evidenced in Figure 4.15, charging, even after the Au coating, interferes with the contrast of the image.

**Table 4.10:** LC-MS results for the liquid portion of IL/coal dissolution. All peaks are reported in mass-to-charge ( $m/z$ ) ratios. IL molecular weight are listed below each sample batch for reference.

	141.10258		111.09235		172.17014
	142.10569		112.09532		173.17384
	157.09753		127.08684		232.19131
C01-A01	158.10050	C03-A12	128.09002	C05-A16	233.19387
	449.33938		449.33915		---
	450.34205		450.34235		---
	451.34512		451.34505		---
A01 – 214.25 g/mol		A12 – 170.20 g/mol		A16 – 231.32 g/mol	
	155.11862		213.17204		169.13415
	156.12158		214.17546		170.13700
	157.08716		309.22972		227.18736
	213.17180		310.23265		228.19047
C07-A28	214.17484	C09-RG28	---	C11-A30	449.33925
	279.16034		---		450.34235
	280.16340		---		---
	337.21327		---		---
	338.21639		---		---
A28 – 182.26 g/mol		RG28 – 182.26 g/mol		A30 – 212.29 g/mol	

**Figure 4.15:** SEM images taken of lignite 30x (left) and 1000x (right) zoom. All samples were coated with ~15 nm of elemental gold (Au) to reduce charging, which is still evidenced in the brighter particles in each image.



The results of the SEM analysis can be seen in Figure 4.16. Two images are included per sample: one taken at 100 $\times$  zoom and the other at 1,000 $\times$  zoom. The images taken at 30 $\times$  and 500 $\times$  zoom can be found in Appendix D(vi). Morphology changes are evidenced when comparing the 1,000 $\times$  zoom images of lignite (top) with the IL induced dissolution samples. Lignite appears to have larger fragments, whereas lignite fragments dissolved in ILs appear smaller in comparison. It appears as though the dissolved lignite fragments are more numerous in each image, another indicator that ILs disrupt the hydrogen-bond and ether linkages in coal.

Energy from the accelerated electrons is absorbed by the atoms and eventually released in the form of X-rays. Every atom has a unique energy signature as the energy released due to relaxation of an electron from an excited state to a ground state is unique to each atom's quantum state. As such, the EDS detector monitors the energy of X-rays releasing from the imaged material and analyzes the energy signature, comparing the patterns to the known energy states of all possible atoms. EDS analysis of all samples resulted in the detection of carbon, oxygen, calcium, and bromine in each of the coal and coal/IL dissociated samples.

Before analyzing the coal/IL samples via EDS, an inorganic reagent of known molecular formula was analyzed and evaluated for accuracy. Potassium permanganate,  $\text{KMnO}_4$ , is an aesthetically pleasing purple in color. A small mass of  $\text{KMnO}_4$  crystals were reduced to powder bromine exist in trace amounts, which is expected in mined coal. Positive identification of these two atoms is not possible without proximate or ultimate analyses, therefore we consider the likelihood of calcium and bromine presence in coal. Carbon and oxygen, on the other hand, are known to be present in lignite. EDS analysis of lignite, unaltered by ILs, results in an average of 64.70% carbon and 34.34% oxygen. As determined by the  $\text{KMnO}_4$  analysis, the oxygen concentration is expected to be higher for the EDS analysis than is actually present due to oxidation of the sample before and during SEM and EDS analysis. Via EDS calculations, the experimental formula for this sample was  $\text{KMnO}_{5.22}$ , indicating oxidation had occurred with the sample prior to analysis. Without knowing when or how the oxidation took place, it must be assumed that a certain degree of oxidation will be detected with the EDS.

A comprehensive collection of images taken for all samples using the SEM, as well as results of EDS analysis of the six samples, can be found in Appendix D.iv. Each sample includes images taken with 30 $\times$ , 100 $\times$ , 500 $\times$ , and 1000 $\times$  zoom. The instrument was set with a 15 kV accelerating voltage and spot size (SS) of 60. Resolution scales range from 500  $\mu\text{m}$  at 30 $\times$  zoom to 10  $\mu\text{m}$  at 1000 $\times$  zoom. EDS analysis for each sample provided weight percent comparisons for all identified atoms, specifically carbon, oxygen, calcium, and bromine.

Table 4.11 is a summarization of EDS analysis for lignite and the six IL dissolved coal samples. The X-ray signature for hydrogen is not detectable to a reliable degree, so the four atoms identified in the EDS are carbon, oxygen, calcium, and bromine. Calcium and bromine are

commonly found in coal samples due to geological impurities collected during the mining process.

Dissolution of coal with ILs should not result in the loss or gain of carbon or oxygen, rather it should affect the arrangement of atoms. EDS analysis showed consistent measures of carbon and oxygen in each lignite sample, inferring no considerable loss in mass during dissolution. SEM analysis showed minor variations in the morphology of lignite, and EDS analysis implies a change in conformation occurred, not a change in the material.

### **X-ray Diffraction (XRD) Analysis**

The last method of instrumental analysis used to evaluate the dissolution of coal via ILs was that of X-ray diffraction (XRD). Sample holders were prepared by lightly packing the solid material to be analyzed flush with the top of the sample holder, smoothed to a flat surface. The sample holders were placed in a GBC MMA X-ray Diffractometer at the University of Northern Colorado. As the sample holder was tilted, the scattering of the X-rays was detected and measured in the number of counts received by the detector at the specified angle. X-rays with a wavelength ( $\lambda$ ) of 1.54056 angstroms (Å), ranging from 10° to 90° with a 0.02° step size, were used to evaluate the crystallographic structure of the solid material.

Microsoft Excel® was used for deconvolution and interpretation of the diffractograms. As evidenced in Figure 4.18, 4000 data points makes for a messy and difficult-to-read graph. To simplify the graph, two Gaussian distributions were fit to the original data points and the linear combination of those two curves was adapted to best-fit the original data points. The Gaussian distributions were centered around 20° and 26°, referred to as the  $\gamma$ -band and  $\pi$ -band, respectively. Integration of these two peaks provided the number of aromatic carbons ( $C_{ar}$ ) and

the number of aliphatic carbons ( $C_{al}$ ). Application of Equations 4.1 through 4.7 provided information regarding aromaticity ( $f_a$ ), coal rank, lateral size ( $L_a$ ), stacking height ( $L_c$ ), number of parallel layers ( $N$ ), and the average number of carbon atoms per aromatic lamellae ( $n$ ) (Manoj & Kunjomana, 2012).

**Figure 4.16a:** SEM images of lignite before and after dissolution with ILs. Samples use a CXX-AXX nomenclature, with CXX referring to the vial number and AXX referring to the IL used for dissolution. Photos on the left are at 100 $\times$  zoom and the photos on the right were taken at 1,000 $\times$  zoom.

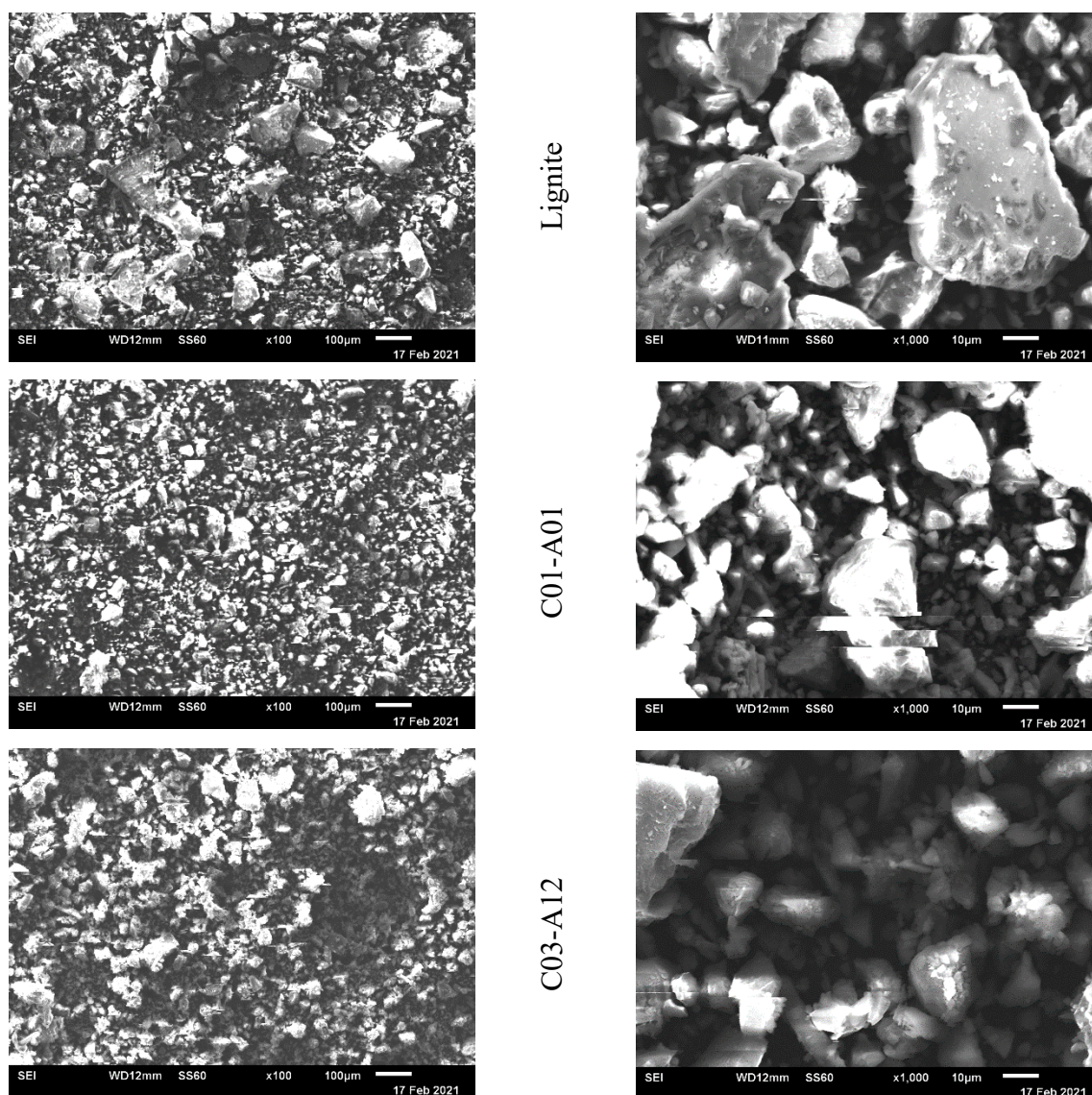




**Figure 4.16b:** SEM images of lignite before and after dissolution with ILs. Samples use a CXX-AXX nomenclature, with CXX referring to the vial number and AXX referring to the IL used for dissolution. Photos on the left are at 100 $\times$  zoom and the photos on the right were taken at 1,000 $\times$  zoom.

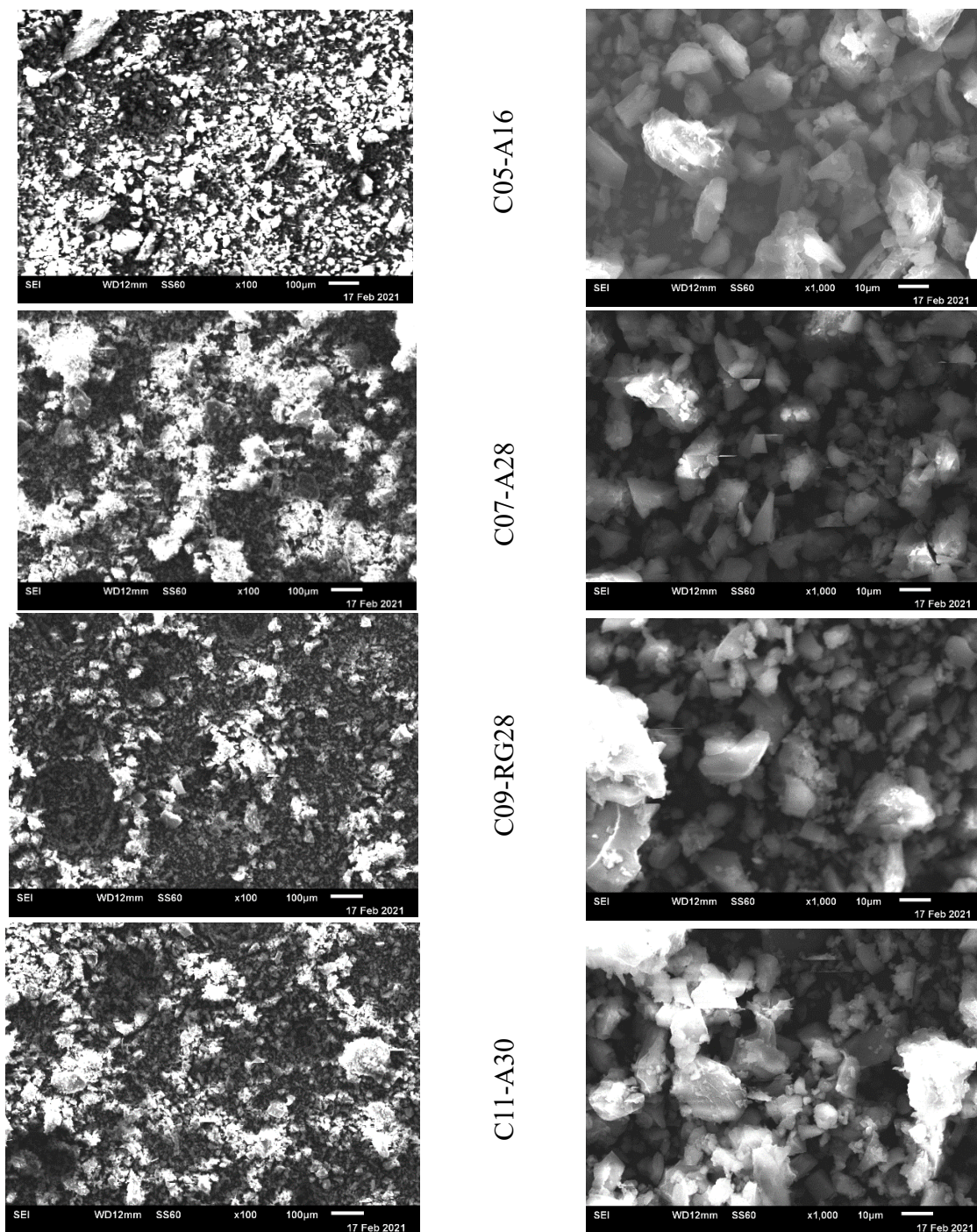
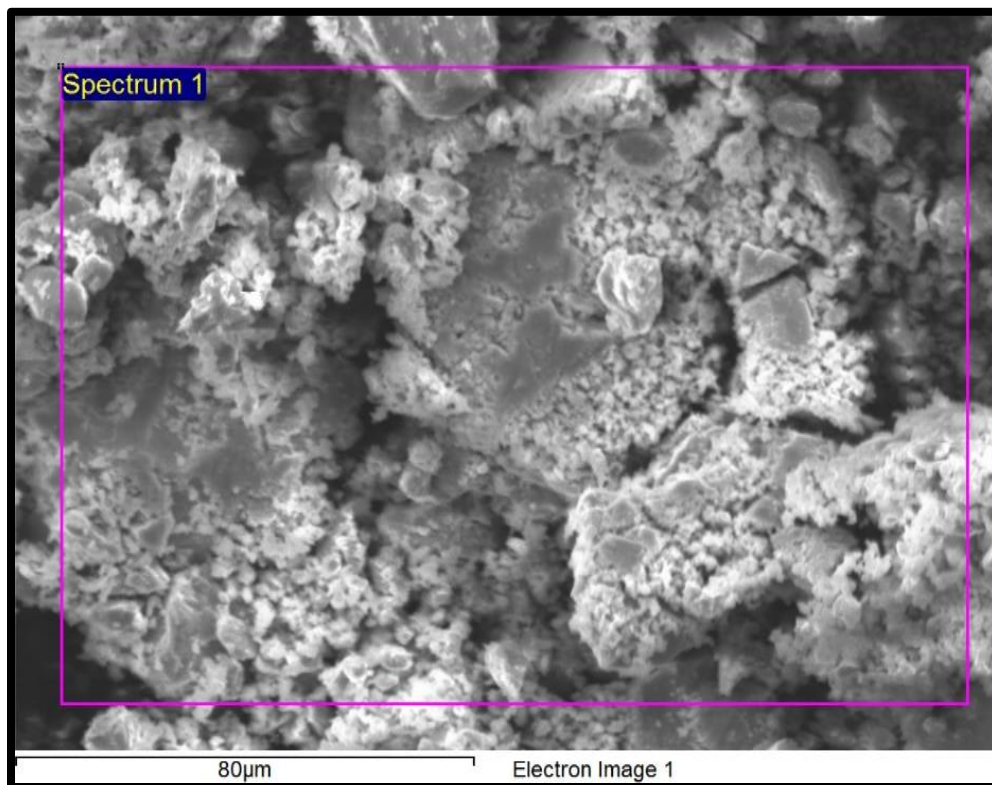


**Figure 4.17:** EDS analysis of  $\text{KMnO}_4$  resulted in detection of oxidation of the sample. The experimental formula was determined to be  $\text{KMnO}_{5.22}$ . Electron accelerating voltage was 15 kV, SS60, and the image was taken at 750x zoom.



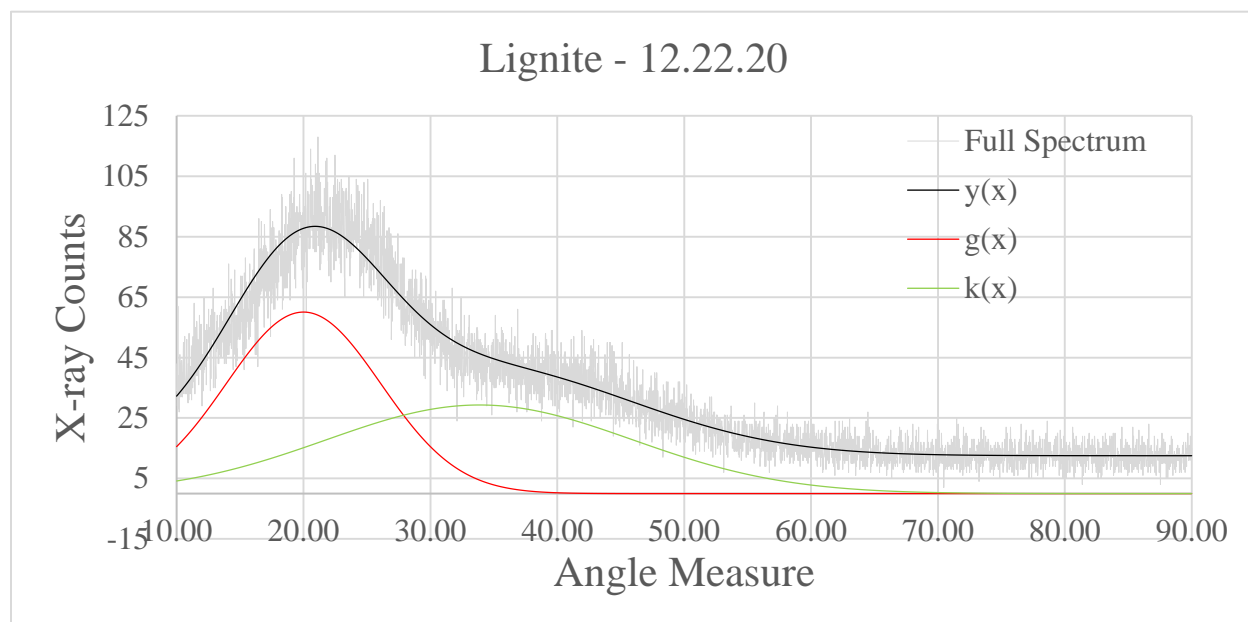
“The structure of coal has also been characterized by XRD, and the existence of crystallites in coal structure has been proven by the appearance of the peaks corresponding to the 002, 100, and 110 reflections in graphite” (Maity & Mukherjee, 2006). The lower rank the coal the less similar the structure is to graphite’s crystallographic structure. Evaluation of the two peaks using band) and  $26^\circ$  (002,  $\pi$ -band) peaks followed the formula:  $C = A * |\sigma| * \sqrt{2 * \pi}$ . Table 4.12 is a reporting of all calculations for lignite and the six IL/coal dissolution products. Appendix D.vi. show the spectrum and individual calculations for each of the samples.



**Table 4.11:** EDS results for lignite and IL-pretreated lignite. Sample nomenclature uses CXX-AXX naming scheme, with CXX referring to vial number and AXX referring to the IL used to pretreat lignite. All samples were solid and dried prior to SEM/EDS analysis. The first sample listed is the EDS spectrum for a particle, second sample represents area analysis at 750× zoom.

Coal Sample	Carbon	Oxygen	Calcium	Bromine
Lignite	63.73	35.47	0.50	0.30
	65.68	33.22	0.78	0.33
Mean	64.70	34.34	0.64	0.32
Std. Dev.	1.38	1.59	0.19	0.02
C01-A01	63.58	35.71	0.34	0.37
	63.72	35.60	0.32	0.37
Mean	63.65	35.65	0.33	0.37
Std. Dev.	0.10	0.08	0.02	0.01
C03-A12	69.68	29.80	0.31	0.21
	67.98	31.58	0.21	0.23
Mean	68.83	30.69	0.26	0.22
Std. Dev.	1.20	1.26	0.08	0.01
C05-A16	67.30	32.15	0.31	0.24
	66.51	32.98	0.30	0.21
Mean	66.90	32.57	0.31	0.23
Std. Dev.	0.56	0.59	0.01	0.02
C07-A28	66.72	32.59	0.24	0.45
C09-RG28	65.96	33.51	0.14	0.38
	66.84	32.31	0.38	0.47
Mean	66.40	32.91	0.26	0.42
Std. Dev.	0.62	0.85	0.17	0.06
C11-A30	66.64	32.63	0.17	0.56
	65.03	34.18	0.32	0.48
Mean	65.83	33.40	0.24	0.52
Std. Dev.	1.13	1.09	0.10	0.06

**Figure 4.18:** Graphical representation of the number of X-ray counts vs. angle measure detected via XRD. The gray data points represent raw data; the red and green curves were calculated via Gaussian distributions; the black curve is a linear combination of the two Gaussian distributions.



$$f(x) = A * e^{-\frac{(x-\mu)^2}{2*\sigma^2}} \quad \text{Equation 4. 1}$$

$$f_a = \frac{C_{ar}}{C_{ar}+C_{al}} \quad \text{Equation 4.2}$$

$$\text{Coal Rank} = \frac{I_{26}}{I_{20}} \quad \text{Equation 4.3}$$

$$L_a = \frac{1.84*\lambda}{B_a \cos(\varphi_a)} \quad \text{Equation 4.4}$$

$$L_c = \frac{0.89*\lambda}{B_c \cos(\varphi_c)} \quad \text{Equation 4.5}$$

$$N = \frac{L_c}{d_\gamma} + 1 \quad \text{Equation 4.6}$$

$$n = 0.32 * N^2 \quad \text{Equation 4.7}$$

The values for  $C_{al}$  and  $C_{ar}$  correspond with the calculated quantity of aliphatic and aromatic carbons in each structure, respectively. Lignite is a low rank coal, meaning it inherently has fewer aromatic carbons and more oxygen in each substructure. The peaks at 20° (100,  $\gamma$ -

band) and  $26^\circ$  (002,  $\pi$ -band) correspond with graphite's XRD profile; graphite is comprised entirely of carbon bound in a hexagonal arrangement of atoms. The measure of aromaticity is calculated as  $f_a$  and is the ratio of aromatic carbons to total measured carbons. Low rank coal should have a low  $f_a$  value as it contains less aromatic carbons than anthracene, a high rank coal.

The coal rank is calculated by taking the intensity of the peak at  $26^\circ$  and dividing it by the intensity of the peak at  $20^\circ$ ; the larger the value of the gamma peak the higher rank coal. The values listed in Table 4.12 are extraordinarily low, as is expected for working with the low rank coal lignite. Without context, though, it is difficult to say whether experimental values are consistent with theoretical values regarding coal rank.

**Table 4.12:** XRD analysis derived after the fit of two Gaussian distribution curves for the  $20^\circ$  (100,  $\gamma$ -band) and  $26^\circ$  (002,  $\pi$ -band) peaks.

	Lignite	C01-A01	C03-A12	C05-A16	C07-A28	C09-RG28	C11-A30
$C_{al}$	$1.2622 \times 10^8$	$1.2465 \times 10^8$	$1.3430 \times 10^8$	$1.4047 \times 10^8$	$1.2448 \times 10^8$	$1.2644 \times 10^8$	$1.0603 \times 10^8$
$C_{ar}$	915.68	1282.5	1633.6	1986.84	1272.1	681.23	948.12
$f_a$	$7.2547 \times 10^{-6}$	$1.0289 \times 10^{-5}$	$1.2164 \times 10^{-5}$	$1.4144 \times 10^{-5}$	$1.0220 \times 10^{-5}$	$5.3878 \times 10^{-6}$	$8.9420 \times 10^{-6}$
$I_\pi / I_\gamma$	0.20869	0.14519	0.13095	0.11111	0.11515	0.21071	1.4898
$L_a$	1.1419	1.1574	1.0853	1.1001	1.4692	1.5229	1.4898
$L_c$	$1.0906 \times 10^{-6}$	$1.0906 \times 10^{-6}$	$1.0906 \times 10^{-6}$	$1.0906 \times 10^{-6}$	$1.0906 \times 10^{-6}$	$1.0906 \times 10^{-6}$	$1.0906 \times 10^{-6}$
n	0.32000	0.32000	0.32000	0.32000	0.32000	0.32000	0.32000

## Discussion

Synthesis of ILs and the subsequent characterization resulted in copious amounts of data that will contribute to the literature, whereas dissolution of both cellulose and coal left much to be desired. This analysis section will include detailed analysis of each phase of the research project, and the lessons learned throughout will help guide future researchers to maximize the efficiency of this same process. Preliminary findings corroborate the existing evidence in ILs

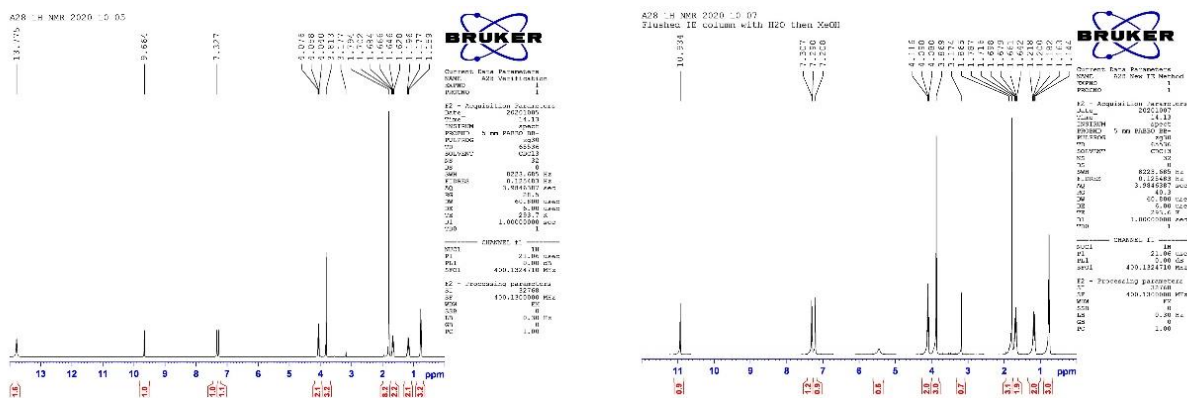
ability to dissolve and pretreat coal. Current findings indicate how future projects should be amended to avoid problems encountered in this project.

Synthesis of ILs occurred in two steps: nucleophilic substitution of nitrogen- or phosphorus-containing organic compounds with an alkyl halide, followed by the ion exchange of the halogen with acetate ion. The key to the first step is the production of a quaternary ammonium or phosphonium cation that is electrostatically bound to the halogen anion from the alkyl halide. Ethyl amine ( $\text{CH}_3\text{CH}_2\text{NH}_2$ ) does not react to form an IL in sufficient yield or purity due to the hydrogen atoms attached to nitrogen reacting after formation of the quaternary nitrogen complex. Production of brominated-ILs was achieved in  $92 \pm 6\%$  yield for all ILs. Optimal reaction conditions typically use  $\sim 150$  mL acetonitrile solvent, refluxed for 24 hours at  $50^\circ\text{C}$ . Removal of acetonitrile is achieved via rotovap at 50 mbar of pressure and  $55^\circ\text{C}$ . Washing the IL with diethyl ether will purify the IL product, followed by drying in a vacuum oven at 25 mbar of vacuum and  $80^\circ\text{C}$  will ensure all solvent is completely removed from the solution. Each IL was stored in a glass vial, sealed with parafilm, and placed in a desiccant chamber with phosphorous pentoxide ( $\text{P}_2\text{O}_5$ ) and Drierite<sup>®</sup> desiccant.

Ion exchange was performed in a 100-mL chromatography column packed with glass wool and Ambyrlest<sup>®</sup> A-26 hydroxide resin. Methanol proved most efficient as a solvent with the ion exchange due to several key properties. First, methanol does not form an azeotropic mixture with water, as ethanol does. Water complexes with hydrophilic ILs, which is near impossible to remove using available lab equipment and techniques. Second, methanol dissolves both the IL and ammonium acetate, the salt used to exchange bromide ions for acetate ions. Acetone and hexane react poorly with the resin, thus disqualifying them for use in ion exchange. The third reason methanol is used is for its ease of evaporation after the ion exchange procedure

is complete. Removal of methanol from the IL is quick and easy with the same rotovap procedure as before, and any excess solvent will evaporate in the vacuum oven.

**Figure 4.19:** NMR spectra for sample A28 before (left) and after (right) modification of the ion exchange procedure.



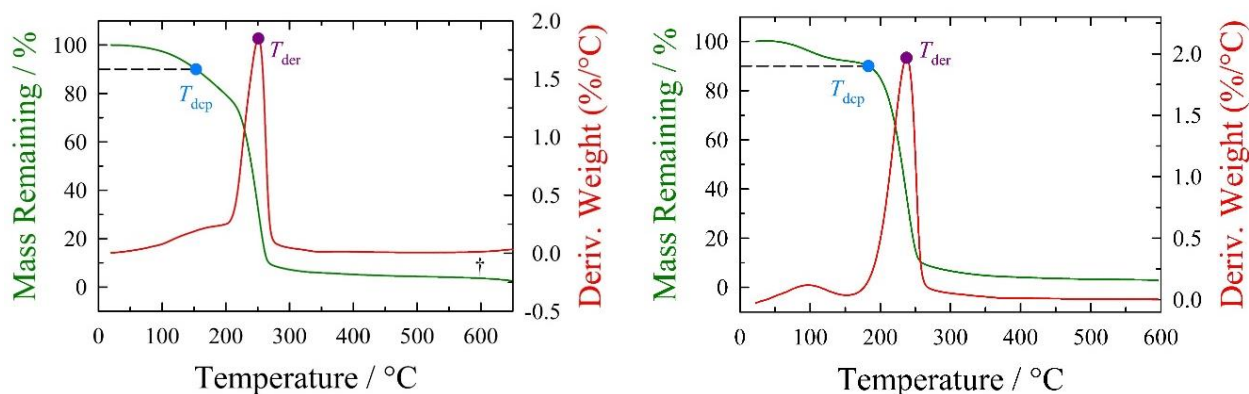
Ammonium acetate was initially added in significant molar excess compared to the IL. Loading of the column with acetate resulted in excess acetate ions available for ion exchange, and the resultant IL had too much acetic acid in the IL matrix. This was not noticed until the NMR of sample A28 was scrutinized and the integration values for the acetate hydrogens was three times higher than was expected. Modification to the ion exchange procedure, this time having the loaded column washed with water, then methanol, alleviated this complexing issue, as is evident in the NMR spectra found in Figure 4.19. The spectra on the left, taken before modification of the ion exchange procedure, has an integration value of 8.2 at  $\delta$ 1.794 ppm and a peak integrating for 1.6 at  $\delta$ 13.775 ppm. The spectra on the right was taken after the ion exchange procedure was modified, resulting in the peak at  $\delta$ 1.787 ppm integrating for the expected 3.1 and the peak at 13.775 ppm disappearing. This evidence is indicative of the initial complexing of excess acetate ion in the IL being negated by the modified procedure. Unfortunately, water is still complexed in the IL after washing the column with methanol, as evidenced by the peak at  $\delta$  5.5 ppm, a problem that must be rectified in future research.

The acetate-ILs were dried in the vacuum oven for 48 hours before water concentration and viscosity was determined. Samples tested after ion exchange using only methanol resulted in much lower water concentrations, i.e., 0.2%. Water as a solvent for the ion exchange resulted in 5% and higher water concentration, an inappropriate amount to consider our ILs neat. When methanol and water are used in conjunction the water concentration remains at 0.8%. Multiple methods were used to attempt to dry the ILs further, including  $\text{MgSO}_4$  and  $\text{K}_3\text{PO}_4$ , both of which have been shown to reduce the complexing of water in ILs to some degree (Palumbo et al., 2019). The nature of hydrophilic ILs and the propensity for ILs to complex with water results in extra steps being taken to mitigate absorption of water from the atmosphere when ILs are being stored. Operationally, the dissolution of cellulose and coal happen above the boiling point of water, therefore there is less concern with water absorption after characterization has been completed.

Thermogravimetric analysis (TGA), which will be discussed in greater detail shortly, was performed on several samples before and after modification of the ion exchange procedure. Each sample was tested for water concentration before submission for TGA, and Figure 4.20 shows the results of each TGA scan for sample A01. TGA analysis before the modified ion exchange procedure was performed on sample A01 with 0.058% water, left 3.6% residual char after TGA scan, and had  $T_{der}$  and  $T_{dcp}$  values of 251 °C and 153 °C, respectively. Analysis after the modified procedure was performed on a sample with 0.803% water, left 3.0% residual char, and had  $T_{der}$  and  $T_{dcp}$  values of 237.5 °C and 183.1 °C, respectively. The decomposition profile of the after-sample was more evident of water contamination and resulted in a higher temperature of decomposition for the first 10% of the sample. The decomposition profile did not change

drastically, and the first derivative of the profile for the sample with a higher water concentration was only slightly lower than the original sample.

**Figure 4.20:** Thermogravimetric analysis of IL A01 before (left) and after (right) modification to the ion exchange procedure.



Kamlet-Taft parameters of polarity and polarizability for ILs requires significant work to produce credible results. Reichardt's dye, a complex conjugated poly-aromatic, nitrogen-containing compound, interacts poorly with ILs. Reproduction of known KT values for organic solvents and ILs was inaccurate and unreliable. The color of the ILs affected UV-Vis analysis, and further manipulation of testing strategy is required before analysis can be considered confident. A more detailed description of each of these dilemmas follows.

First, the color of the ILs interfered with UV-Vis analysis as the intensity of absorption for each IL was out of tolerance. Decolorization, as recommended by Earle et al. (2007), consisted of a chromatography column packed with activated charcoal, silica powder, and glass wool. This technique works well to remove the chromophores present in each IL that provided the color, but it was unclear whether any other changes to the IL also occurred that would alter the interaction between ILs and dyes, or ILs and cellulose and coal. Further experimentation is required to better understand the impact of decolorization of ILs.

Reichardt's dye is a conundrum: a new container was purchased and tested, and numerical values of  $E_T^N$  and  $E_T(30)$  were significantly off for the known organic solvents.

Acetone, dichloromethane, and methanol were analyzed using 0.362 nmol of Reichardt's dye. Table 4.13 shows the theoretical and experimental values for these analyses, and the percent error shows just how inaccurate the analysis was. Inaccuracies in measurements of Reichardt's dye excluded the use of  $E_T^N$  and  $E_T(30)$  and subsequently  $\alpha$ , the hydrogen-bond-donating acidity. Further evaluation of Reichardt's dye interaction with solvents and ILs is required before further analysis can be completed.

**Table 4.13:** Analysis of UV-Vis measurements for Reichardt's dye using known organic solvents; literature values provided by Lee et al. (2008).

Organic Solvent	Literature $\lambda$	Experimental $\lambda$	% Error
Acetone	680 nm	321 nm	52.8%
Dichloromethane	702 nm	312 nm	55.6%
Methanol	516 nm	310 nm	39.9%

The first attempts at cellulose dissolution was the signal that something was wrong with the synthesized ILs. Addition of cellulose to a heated IL should result in an immediate clumping of the cellulose followed by gradual dispersion and dissolving in the IL. That was not happening; instead, the cellulose formed a colloidal suspension with the IL and did not dissolve. After reevaluating and modifying the ion exchange procedure, dissolution was attempted with the newly purified IL and success occurred. Approximately one gram of IL was heated in a vial and 20 mg aliquots of Avicell® PH-101 was added roughly every 30 minutes. Dissolution was complete when the viscosity of the solution was too high for the stir bar to move, and no further dissolving was evident. Table 4.6 includes the exact masses of IL and cellulose added to each vial and the corresponding  $\pi^*$  value for each IL.

ILs with lower viscosity and  $\pi^*$  close to or above 1.00 displayed greater percent dissolution of cellulose. This is correlation, not necessarily causation. To test the exact correlation between Kamlet-Taft values and dissolution of cellulose, better procedures for testing



ILs must be determined for the KT values and more samples need be tested with cellulose. The intent of this portion of the research was to verify that our ILs do, in fact, dissolve cellulose, a precursor to the dissolution of coal. The results were successful in all five of the ILs dissolved greater than 9% by mass of cellulose. Samples were segregated for FTIR and LC-MS testing.

Complete FTIR spectra for cellulose dissolution via ILs can be found in Appendix D.ii. Figure 4.21 displays the FTIR spectra for all six samples collected after dissolution of cellulose had completed. Present in each sample should be the IL, trace amounts of undissolved cellulose, and the fragments resulting from dissolution of cellulose. Increased IR signals in coal samples tested after dissolution, both in the carbon-carbon and carbon-hydrogen bending and stretching regions, implies an increased number of particles and functional groups to absorb the signal from the infrared source. No evidence of IL remains in the coal sample, indicating successful extraction of the IL from the coal after dissolution. Therefore, all changes to conformation are evidenced in the FTIR analysis.

Having evidence of dissolution of our model compound in ILs gave us confidence going forward with the dissolution of coal. Instead of maximizing dissolution in each IL, instead a 1:5 ratio of coal to IL was heated and stirred for 24 hours before work-up commenced. The coal particles were particularly difficult to work with, as slight air movement or static would cause the powder to disperse. Not all the coal made it to the IL solution, which leads to inaccuracies in the calculations. Washing the coal/IL mixture with water, acetone, or methanol increased the likelihood of losing coal particles during the washing procedure. Any fragments of coal not trapped in the IL matrix will be washed away. Additionally, analytical techniques for transferring solutions to different containers can be improved upon to further reduce the possibility for error during the dissolution process.

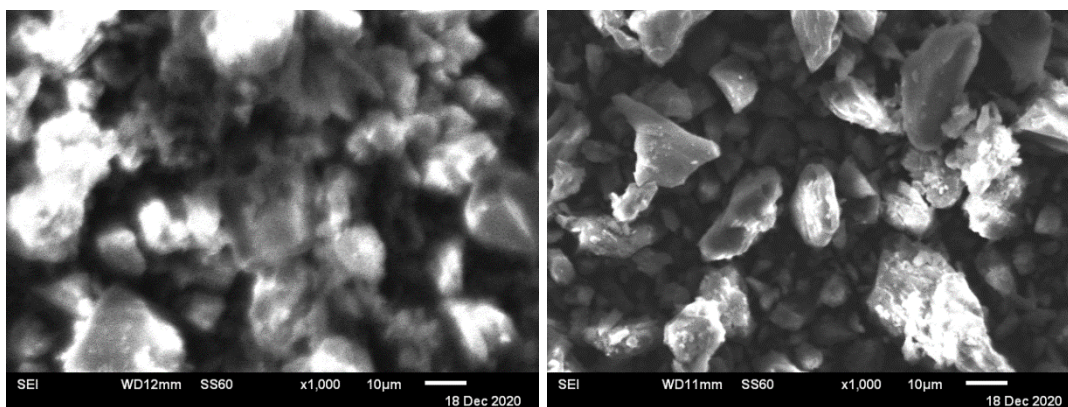
The results of coal dissolution were divided into two groups per IL: the IL/coal fragments recovered in liquid form, and the solid coal particulates remaining after the separation and washing procedures were complete. Both groups were tested via FTIR, the IL/coal solution was sent to CSU-Fort Collins for LC-MS analysis, and the solid sample was analyzed via SEM/EDS and XRD. GC-MS was initially tested in lieu of LC-MS, however two problems were insurmountable. First, not all of the coal fragments were prone to evaporation and thus would not pass through the GC, and second, the IL had a tendency to dissolve the silica-based column. Evidence of the latter phenomenon was in the form of silicon-based groups sloughing off the column and being analyzed in the mass spectrometer. Organic solvent, when tested using the same analysis profile, did not show evidence of column fragmentation. Thus, LC-MS was the analytical method of choice.

It was our intent to use the LC-MS to help evaluate the fragmentation patterns of the IL/coal mixture and extrapolate from that the extent of dissolution of coal. LC-MS provided little insight to either of these goals. Spectra provided by CSU-FC showed two basic sets of compounds separated by the liquid chromatography instrument, one belonging to the IL and the other to the coal fragmentation. Mass spectrometry results corroborated these results but gave us little insight beyond that. Mass-to-charge ratios for the IL peaks were in the approximate range of the cation for each IL, but did not match the anticipated peaks. This implies that some rearrangement or fragmentation of the IL itself is occurring during the dissolution process. Without proximate or ultimate analyses of coal, matching the much heavier fragments to possible structures was a futile effort. With mass-to-charge ratios well over 200, any combination of carbon, hydrogen, oxygen, nitrogen, and other atoms could be combined to produce suitable structures that match this profile. The LC-MS instrument's matching database contradicted the

results of our independent EDS analysis by reporting possible compounds with nitrogen, sulfur, and phosphorus, none of which were measured in the EDS analysis discussed momentarily. Further experimentation with LC-MS and coal dissolution is required to achieve more consistent and reliable results.

Solid samples were analyzed using scanning electron microscopy (SEM) and energy dispersive X-ray spectroscopy (EDS). Using SEM images, ranging from 30× to 1000× zoom, topographical comparisons of lignite and post-dissolution coal samples could be performed on all samples. Considering the images in Figure 4.21, not much information can be gleaned from the image comparisons. Charging, evident by the bright contrast of some coal fragments, was a major problem in SEM and EDS analysis, even after a 15 nm thick gold coating was applied. Fragmentation is qualitatively evidenced by the reduced particle size, however initial grinding of the coal to  $\leq 150 \mu\text{m}$  could explain the reduced particle size in each image.

**Figure 4.21:** SEM images of coal dissolution of lignite (left) versus lignite after dissolution with A30 (right). Parameters of the SEM was an accelerating voltage of 15 kV, spot size of 60, and 1000x zoom. Fiduciary in the lower right corner of each image is scaled to 10  $\mu\text{m}$ ,



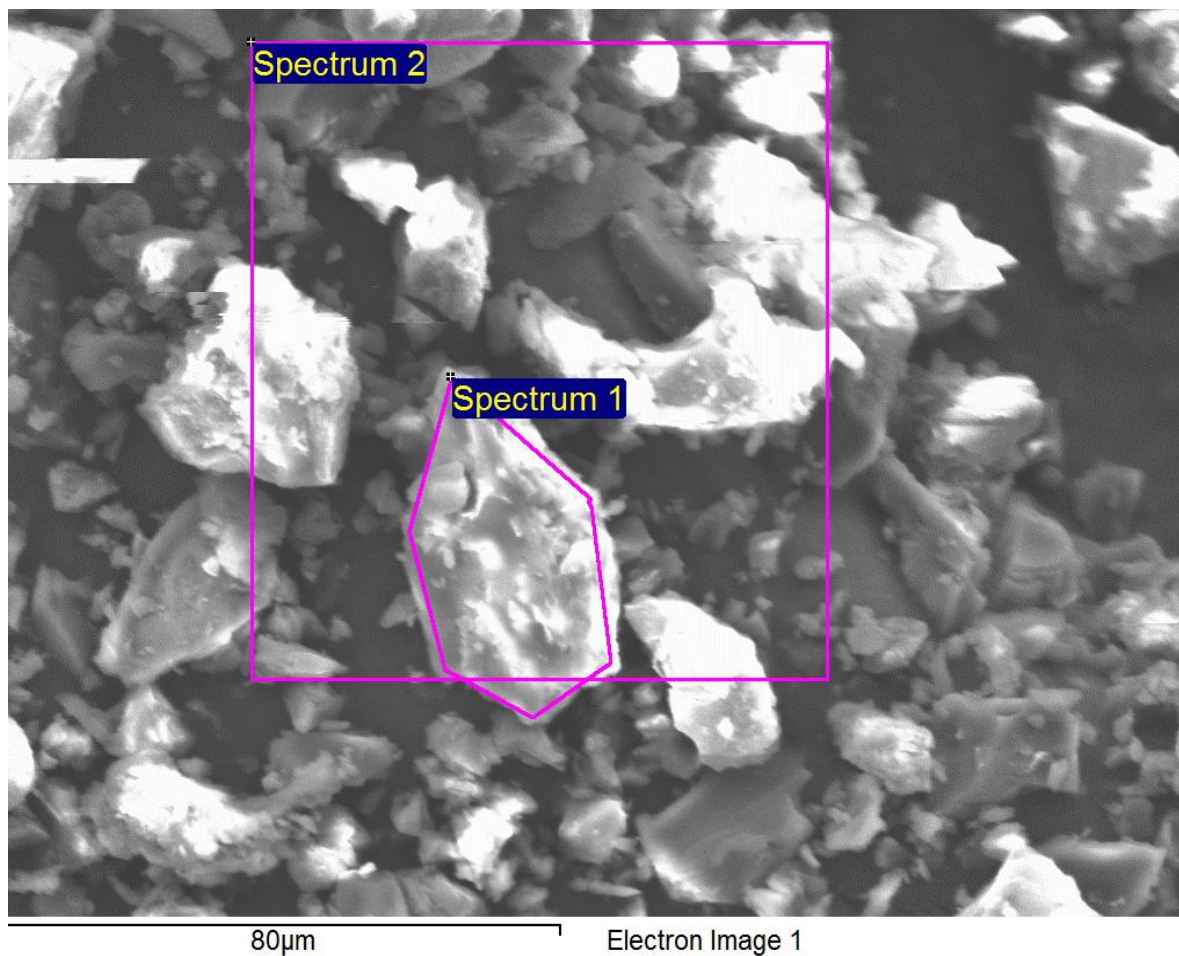
More reliable analysis was gathered via EDS analysis, detecting the X-ray particles released by the examined material during electron bombardment. Each atom has a unique X-ray energy pattern, and it was this pattern matching that allowed a crude and unconfirmed analysis of the composition of each material. According to the EDS database carbon, oxygen, calcium, and

bromine were the only atoms with a detectable energy pattern. This does not include hydrogen atoms, and the ratios are known to be skewed due to oxidation observed during analysis of  $\text{KMnO}_4$ . Suspected oxidation leads to inaccurate mass readings for both oxygen and carbon, requiring further analysis to determine the extent of oxidation before, during, and after the dissolution process. A proximate and ultimate analysis of lignite and the dissolution samples could shed light on the specific atoms found in coal and the extent of fragmentation by each IL.

X-ray diffraction was anticipated to be the most rewarding and informative analysis on the dissolution process and ended up being the biggest disappointment. Experimental results were contrary to the literature, resulting in wildly inaccurate and misleading data. Calculations used by Manoj & Kunjomana (2012) and results published by Maity & Mukherjee (2006) provided a suitable foundation for XRD data manipulation but doing so on our data proved problematic. Table 4.12 shows the results of the calculations after two Gaussian distributions were fit to the data points. Many samples displayed multiple peaks, not just those centered around  $20^\circ$  and  $26^\circ$  as described in each article.

The most reasonable explanation for these discrepancies in the data could be the rank of coal itself and the wildly different structure of lignite as compared to graphite, the model compound used by these other researchers. The lower rank coal deviates drastically from a crystalline structure, and thus crystallographic analysis falls short in analyzing lignite and IL treated coal fragments. Dissolution of higher rank coal and subsequent XRD analysis could shed light on this theory, possibly resulting in better quality and more consistent results.

**Figure 4.22:** EDS analysis of Lignite, taken with accelerating voltage of 15 kV, spot size of 60, and 750x zoom. Spectrum 1 was performed on single mass of lignite, Spectrum 2 was an area analysis outlined in the above image.

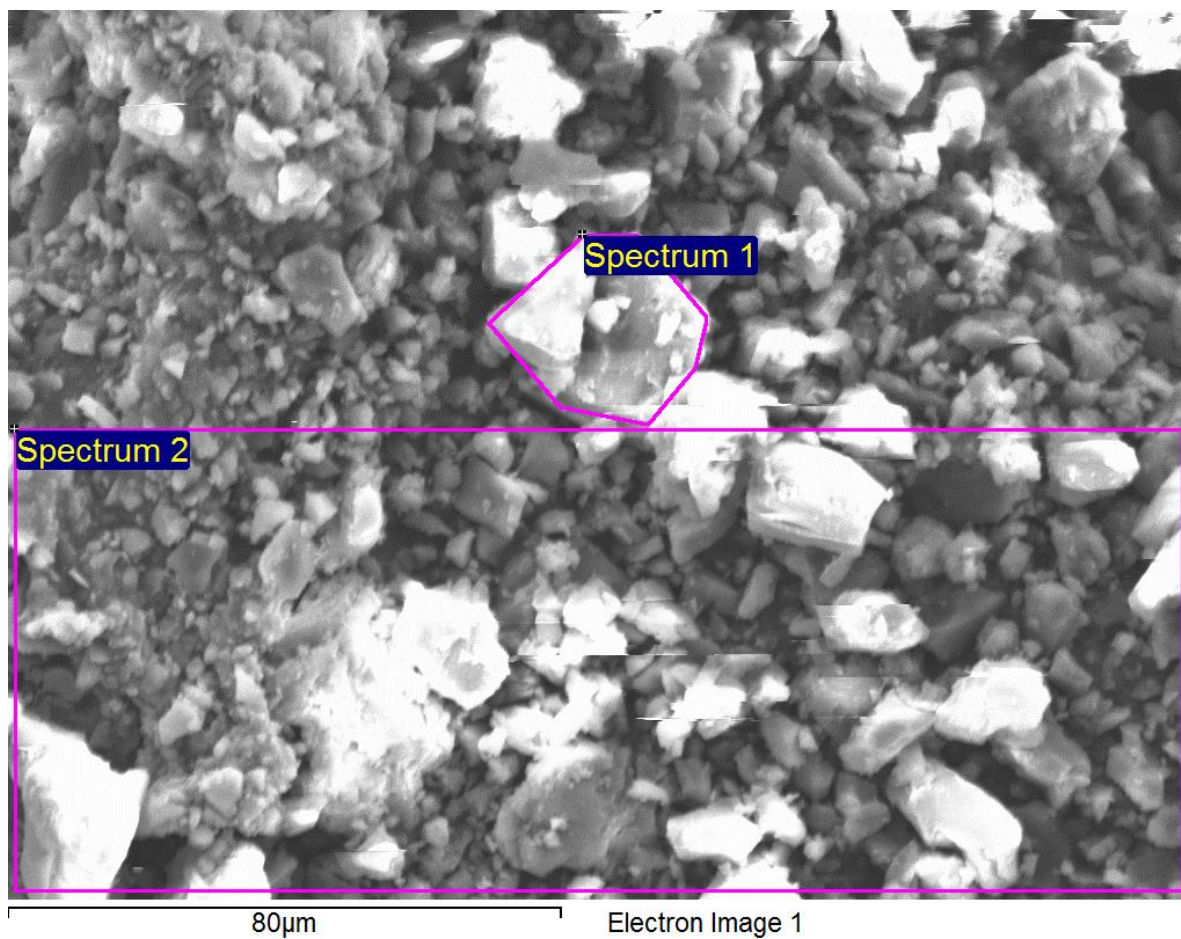


Processing option : All elements analysed (Normalised)

Spectrum	In stats.	C	O	Ca	Br	Total
Spectrum 1	Yes	63.73	35.47	0.50	0.30	100.00
Spectrum 2	Yes	65.68	33.22	0.78	0.33	100.00
Mean		64.70	34.34	0.64	0.32	100.00
Std. deviation		1.38	1.59	0.19	0.02	
Max.		65.68	35.47	0.78	0.33	
Min.		63.73	33.22	0.50	0.30	

All results in weight%

**Figure 4.23:** EDS analysis of Lignite after dissolution with IL A30, taken with accelerating voltage of 15 kV, spot size of 60, and 750x zoom. Spectrum 1 was performed on single mass of lignite, Spectrum 2 was an area analysis outlined in the above image.



Processing option : All elements analysed (Normalised)

Spectrum	In stats.	C	O	Ca	Br	Total
Spectrum 1	Yes	66.64	32.63	0.17	0.56	100.00
Spectrum 2	Yes	65.03	34.18	0.32	0.48	100.00
Mean		65.83	33.40	0.24	0.52	100.00
Std. deviation		1.13	1.09	0.10	0.06	
Max.		66.64	34.18	0.32	0.56	
Min.		65.03	32.63	0.17	0.48	

All results in weight%

## CHAPTER V

### CONCLUSIONS

The synthesis and application of acetate-based hydrophilic ILs in coal dissolution was studied thoroughly. Bromide-based ILs were synthesized by nucleophilic substitution reactions, followed by an ion exchange step to produce novel acetate-based ILs. The characterization of these ILs allowed for selection and application of ILs to the dissolution of lignite after experimenting with a model coal compound, cellulose. Results were analyzed at every step, and many lessons were learned that will contribute to the effective application of ILs in coal dissolution. The last analysis for this project includes an assessment of methodological pros and cons as well as implications of the results regarding the dissolution and pretreatment of lignite coal using ILs.

ILs were synthesized following a two-step process: first, the Appel reaction was used to synthesize brominated glycols that can be used to produce longer-chained cations in ILs, and second, the reaction of nitrogen- or phosphorus-containing nucleophiles with halogen-containing electrophiles. The Appel reaction, used for the conversion of an -OH functional group to -Br, resulted in triphenyl phosphonium oxide byproduct. The difficulty associated with removing  $\text{Ph}_3\text{P}=\text{O}$  makes this reaction implausible for IL synthesis, for the inability to fully remove this byproduct would result in contamination of the synthesized IL. Alternative reactions, for example using thionyl chloride, would prove more beneficial in the preparation of harder-to-purchase halogen-containing materials.



The ion exchange procedure was amended to include water as a washing element after the resin had been charged with the acetate ion. Using ammonium acetate in methanol to load the resin resulted in excess acetate ion being transferred to the IL during the exchange process. Flushing the column with water removed this contaminant at the expense of increased water complexed with the IL. The dissolution of cellulose and coal was possible with slightly elevated water concentrations, but the increased water is not ideal. Therefore, further experimentation to decrease acetate contamination that doesn't lead to increased water is pivotal for future ion exchange procedures.

Polarity and polarizability parameters, measured using the Kamlet-Taft parameters, was successful in our experiments. The literature  $\beta$  and  $\pi^*$  values of known solvents matched with experimental values; the parameters that required Reichardt's dye were not so successful. All measurements were consistently off by 50% of the literature value. Therefore, while 4-nitroaniline and *N,N*-diethyl-4-nitroaniline dyes make for successful analysis of the Kamlet-Taft parameters, Reichardt's dye requires significant testing before it can be used to evaluate IL properties.

In-house instrumental analysis, including XRD, SEM/EDS, FTIR, NMR, and viscometry measurements were easier to analyze due to the accessibility of the instruments and people knowledgeable of their use. LC-MS and TGA, as well as other analytical techniques that would be useful but were not accessible, were performed by third-party organizations. While it was much appreciated for each facilities assistance, having to submit a set of samples and wait for results was not efficient. Accessing additional instruments, such as DSC and XRF, would contribute greatly to the analysis of coal dissolution, going so far as to shed light on how and to what extent the dissolution occurred. Ultimate and proximate analysis would provide information



regarding atomic composition. Comparisons of these analyses between non-pretreated and pretreated coal samples would provide additional information regarding changes to lignite internal and surface changes.

Regardless of improvements that can and should be made concerning the methods used in this project, evidence of dissolution of lignite and effects of pretreatment were evidenced via instrumental analysis. FTIR showed a general trend of increased aliphatic/aromatic ratio and decreased H-bonding after pretreatment. LC-MS results evidenced the extraction of non-volatile fragments from coal during pretreatment and dissolution. SEM analysis showed visible evidence in morphology changes and EDS suggests a slight increase in carbon. XRD analysis showed a general increase in aromaticity and a slight decrease in coal rank due to pretreatment.

The results all indicate an effect of ILs on the low rank coal lignite. Association of hydrophilic ILs with coal disrupts the hydrogen bond and ether complex inherent to coal, however the degree of dissolution is still unknown. Future steps in research include more detailed analysis of the IL/fragmentation solution and the morphology changes of the solid coal samples. Furthermore, the use of ILs for the dissolution/pretreatment of higher ranked coals could result in significant advancements in the uses of coal and a broader understanding of the limitations and usefulness of ILs as green solvents.

## References

- Ahamed, M., Perera, M., Matthai, S., Ranjith, P., & Dong-yin, L. (2019). Coal composition and structural variation with rank and its influence on the coal-moisture interactions under coal seam temperature conditions – A review article. *Journal of Petroleum Science and Engineering*, *180*, 901-917. doi:10.1016/j.petrol.2019.06.007.
- Anastas, P., & Warner, J. (1998). *Green chemistry: Theory and practice*. Oxford: Oxford University Press.
- Bhoi, S., Dey, D., Banerjee, T., & Mohanty, K. (2014). Solid-liquid equilibria predictions for the dissolution of brown coal in ILs using a continuum solvation model. *Fuel Processing Technology*, *126*, 112-121. doi:10.1016/j.fuproc.2014.04.019.
- Caminiti, R., & Gontrani, L. (2014). *The structure of ionic liquids*. Springer.
- Chen, Y., Ke, F., Wang, H., Zhang, Y., & Liang, D. (2012). Phase separation in mixtures of ILs in water. *ChemPhysChem*, *13*, 160-167. doi:10.1002/cphc.201100782.
- Corchero, R., Rodriguez-Escontrela, I., Rodriguez, O., & Soto, A. (2019). Phase equilibria of 1-hexyl-3-methylimidazolium acetate with water and oil. *Fluid Phase Equilibria*, *483*, 144-152. doi:10.1016/j.fluid.2018.11.010.
- Crowhurst, L., Mawdsley, P., Perez-Arlandis, J., Salter, P., & Welton, T. (2003). Solvent-solute interactions in ionic liquids. *Physical Chemistry Chemical Physics: PCCP*, *5*(13), 2790-2794.
- Cummings, J., Tremain, P., Shah, K., Heldt, E., Moghtaderi, B., Atkin, R., Kundu, S., & Vuthaluru, H. (2017). Modification of lignites via low temperature ionic liquid treatment. *Fuel Processing Technology*, *155*, 51-58. doi: 10.1016/j.fuproc.2016.02.040
- Daintith, J. (2008). *A dictionary of chemistry* (6th ed.). New York: Oxford University Press.

- Deetlefs, M., & Seddon, K. (2006). ILs: Fact and fiction. *Chemistry Today*, 16-23.
- Dolan, A., Sherman, D., Atkin, R., & Warr, G. (2016). Kamlet-Taft solvation parameters of solvate ILs. *ChemPhysChem*, 17, 3096-3101. doi:10.1002/cphc.201600361.
- Dong, Q., Muzny, C., Kazakov, A., Diky, V., Magee, J., Widegren, J., Chirico, R. D., Marsh, K. N., & Frenkel, M. (2004). ILThermo: A free-access web database for thermodynamic properties of ILs. *Journal of Chemical Engineering Data*, 52(4), 1151-1159. doi:10.1021/jc700171f.
- DuPont de Nemours, Inc. (2019). *Amberlyst A26 OH polymeric catalyst*. Retrieved October 15, 2019, from DuPont: <https://www.dupont.com/content/dam/Dupont2.0/Products/water/literature/177-03098.pdf>.
- Earle, M., Gordon, C., Plechkova, N., Seddon, K., & Welton, T. (2007). Decolorization of ILs for spectroscopy. *Analytical Chemistry*, 79, 758-764. doi:10.1021/ac061481t
- Faghihi, E., Mokhtarani, B., Mortaheb, H. R., Heydar, K. T., Mirzaei, M., & Sharifi, A. (2020). Vapor liquid equilibria for ionic liquid/ethanol/water systems and the effect of anion hydrolysis. *Chemical Engineering & Technology*, 43(11), 2277-2285. doi:10.1002/ceat.202000114.
- Fendt, S., Padmanabhan, S., Blanch, H., & Prausnitz, J. (2011). Viscosities of acetate or chloride-based ILs and some of their mixtures with water or other common solvents. *Journal of Chemical Engineering Data*, 56, 31-34. doi:10.1021/jc1007235.
- Ghani, M., Rajoka, M., & Akhtar, K. (2015). Investigations in fungal solubilization of coal: Mechanisms and significance. *Biotechnology and Bioprocess Engineering*, 20, 634-642. doi:10.1007/s12257-015-0162-5

- Gordon, C., McLean, A., Muldoon, M., & Dunkin, I. (2003). *ILs as green solvents: Progress and prospects*. (R. Rogers, & K. Seddon, Eds.) Washington, D.C.: American Chemical Society.
- Hamad, W. Y. (2017). *Cellulose nanocrystals: Properties, production, and applications* (1<sup>st</sup> Ed.) Chichester, England: Wiley.
- Kamlet, M., & Taft, R. (1976). The solvatochromic comparison method. I. The beta-scale of solvent hydrogen-bond acceptor (HBA) basicities. *Journal of the American Chemical Society*, 98(2), 377-383. doi:10.1021/ja00418a009
- Kazakov, A., Magee, J., Chirico, R., Paulechka, E., Diky, V., Muzny, C., Kroenlein, K., Frenkel, M. (2019, June 11). *NIST ILs Database - (ILThermo)*. (National Institute of Standards and Technology) Retrieved from NIST Standard Reference Database 147: [ilthermo.boulder.nist.gov](http://ilthermo.boulder.nist.gov)
- Ladesov, A., Kosyakov, D., Bogolitsyn, K., & Gorbova, N. (2015). Solvatochromic polarity parameters for binary mixtures of 1-butyl-3-methylimidazolium acetate with water, methanol, and dimethylsulfoxide. *Physical Chemistry of Solutions*, 89(10), 1814-1820. doi:10.1134/S0036024415100167
- Lee, J. M., Ruckes, S., & Prausnitz, J. M. (2008) Solvent polarities and Kamlet-Taft parameters for ILs containing a pyridinium cation, *Journal of Physical Chemistry B*, 112, 1473-1476. doi: 10.1021/jp076895k.
- Lei, Z., Dong, L., Kang, S., Huang, Y., Li, Z., Yan, J., Shui, H., Wang, Z., Ren, S., & Pan, C. (2019). Dissociation behaviors of coal-related model compounds in ILs. *Fuel*, 241, 1019-1025. doi:10.1016/j.fuel.2018.12.117

- Lide, D. R. (Ed.). (1995). *CRC Handbook of Chemistry and Physics* (85<sup>th</sup> ed.). Boca Raton: CRC Press.
- Maity, S., & Mukherjee, P. (2006). X-ray structural parameters of some indian coals. *Current Science (Bangalore)*, 91(3), 337-340.
- Manoj, B. & Kunjomana, A. G. (2012) Study of stacking structure of amorphous carbon by X-ray diffraction technique. *International Journal of Electrochemical Science*, 7, 3127-3134.
- Marcus, Y. (2016). *Ionic liquid properties: From molten salts to RTILS*. Switzerland: Springer. doi:10.1007/978-3-319-30313-0
- Masterton, W., Slowinski, E., & Stanitski, C. (1985). *Chemical principles*. Philadelphia: Saunders College Publishing.
- Painter, P., Pulati, N. C., Sobkowiak, M., Mitchell, G., & Mathews, J. (2010). Dissolution and dispersion of coal in ILs. *Energy Fuels*, 24, 1848-1853. doi:10.1021/ef9013955.
- Palumbo, O., Trequattrini, F., Brubach, J., & Paolone, A. (2019). Crystallization of mixtures of hydrophilic ILs and water: Evidence of microscopic inhomogeneities. *Journal of Colloid and Interface Science*, 552, 43-50. doi:10.1016/j.jcis.2019.05.034.
- Pang, J., Liu, X., Yang, J., Lu, F., Wang, B., Xu, F., Ma, M., & Zhang, X. (2016). Synthesis of highly polymerized water-soluble cellulose acetate by the side reaction in carboxylate ionic liquid 1-ethyl-3-methylimidazolium acetate. *Scientific Reports*, 6(1), 1-9. doi:10.1038-srep33725.
- Plechkova, N., & Seddon, K. (2008). Applications of ILs in the chemical industry. *Chemical Society Reviews*, 37(1), 123-150. doi:10.1039/b006677j

- Postek, M. T., & Vladár, A. E. (2015). Does Your SEM Really Tell the Truth?-How Would You Know? Part 4: Charging and its Mitigation. *Proceedings of SPIE--the International Society for Optical Engineering*, 9636: 963605 (October 21, 2015).
- Rogers, R., Seddon, K., & Volkov, S. (Eds.). (2002). Green industrial applications of ILs. *NATO Science Series II: Mathematics, Physics, and Chemistry*.
- Romich, C., Merkel, N., Valbonesi, A., Schaber, K., Sauer, S., & Schubert, T. (2012). Thermodynamic properties of binary mixtures of water and room-temperature ILs: Vapor pressures, heat capacities, densities, and viscosities of water + 1-ethyl-3-methylimidazolium acetate and water + diethylmethyl-ammonium methane sulfonate. *Journal of Chemical & Engineering Data*, 57, 2258-2264. doi:10.1021/je300132e.
- Seddon, K. (1997). ILs for clean technology. *Journal of Chemical Technology and Biotechnology*, 68, 351-356. doi:10.1002/(SICI)1097-4660(199704)68:4<351::AID-JCTB613>3.0.CO;2-4
- Sekhohola, L., Igbinigie, E., & Cowan, A. (2013). Biological degradation and solubilisation of coal. *Biodegradation*, 24, 305-318. doi:10.1007/s10532-0012-9594-1.
- Shi, W., Damodaran, K., Nulwala, H. B., & Luebke, D. R. (2012). Theoretical and experimental studies of water interaction in acetate based ILs. *Physical Chemistry Chemical Physics*, 14, 15897-15908. doi: 10.1039/c2cp42975f.
- Silverstein, R. M., Webster, F. X., & Kiemle, D. J. (2005) *Spectrometric identification of organic compounds* (7<sup>th</sup> Ed). Hoboken, N.J.: J. Wiley & Sons.
- Skoog, D. A., Holler, F. J., & Nieman, T. A. (1998) *Principles of Instrumental Analysis*. Crawfordsville: Thomson Learning.

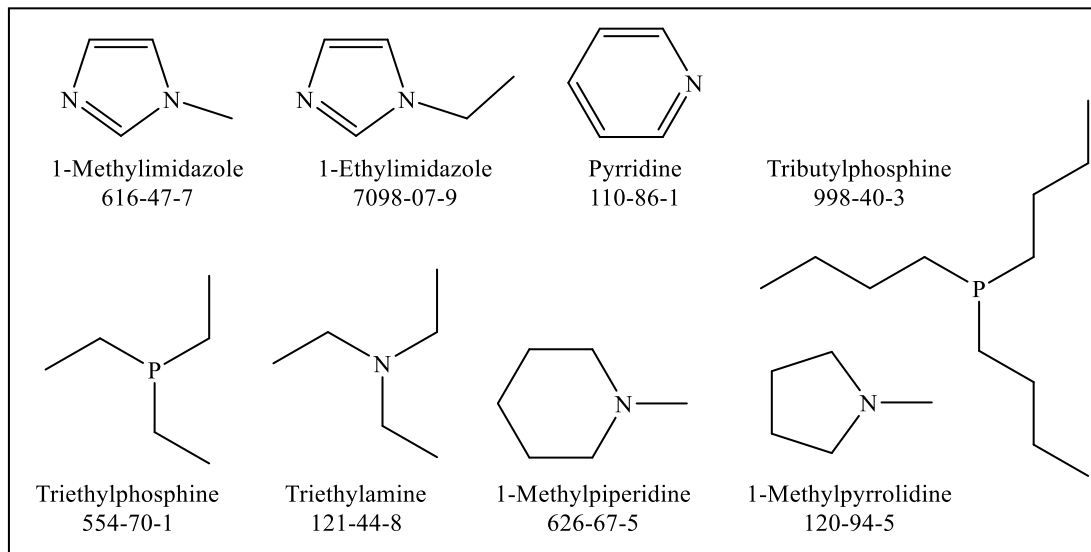
- Strzelecki, B., Kwiatos, N., & Bielecki, S. (2015). Effect of coal pretreatment on brown coal biosolubilisation by *Fusarium oxysporum* 1101. *PhD Interdisciplinary Journal*, 125-132.
- To, T., Shah, K., Tremain, P., Simmons, B., Moghtaderi, B., & Atkin, R. (2017). Treatment of lignite and thermal coal with low cost amino acid based ionic liquid-water mixtures. *Fuel*, 202, 296-306. doi:10.1016/j.fuel.2017.04.051.
- U.S. Energy Information Administration (2020). Coal explained: Use of coal. <https://www.eia.gov/energyexplained/coal/use-of-coal.php#:~:text=In%202019%2C%20about%20539%20million,of%20total%20U.S.%20energy%20consumption.>
- Viswanath, D. S., Ghosh, T. K., Prasad, D. H. L., Dutt, N. V. K., & Rani, K. Y. (2007) *Viscosity of liquids: Theory, estimation, experiment, and data*. Dordrecht: Springer. doi: 10.1007/978-1-4020-5482-2
- Watkins, D., Nuruddin, M., Hosur, M., Tcherbi-Narteh, A., & Jeelani, S. (2015). Extraction and characterization of lignin from different biomass resources. *Journal of Materials Research and Technology*, 4(1), 26-32. doi:10.1016/j.jmrt.2014.10.009
- Welton, T. (2018). ILs: a brief history. *Biophysical Reviews*, 10(3), 691-706. doi:10.1007/s12551-018-0419-2
- Wilkes, J., & Zaworotko, M. (1992). Air and water stable 1-ethyl-3-methylimidazolium based ILs. *Journal of the Chemical Society-Chemical Communications*(13), 965-967.
- Wu, B., Zhang, Y., & Wang, H. (2008). Aqueous biphasic systems of hydrophilic ILs + sucrose for separation. *Journal of Chemical Engineering Data*, 983-985. doi:10.1021/jc700729p

- Wu, H., Yao, S., Qian, G., & Song, H. (2016). Development of tropine-salt aqueous two-phase systems and removal of hydrophilic ILs from aqueous solution. *Journal of Chromatography A*, *1461*, 1-9. doi:10.1016/j.chroma.2016.06.081
- Zhang, W., Jiang, S., Qin, T., Sun, J., Dong, C., & Hu, Q. (2019). Effect of ionic liquid surfactants on coal oxidation and structure. *Journal of Analytical Methods in Chemistry*, 1-9. doi:10.1155/2019/1868265
- Zhao, H. (2006). Innovative applications of ILs as "green" engineering liquids. *Chemical Engineering Communications*, *193*, 1660-1677. doi:10.1080/00986440600586537
- Zhao, H., Afriyie, L., Larm, N., & Baker, G. (2018). Glycol-functionalized ILs for high-temperature enzymatic ring-opening polymerization. *RSC Advances*, *8*, 36025-36033. doi:10.1039/c8ra07733a
- Zhao, H., Kanpadee, N., & Jindaret, C. (2019). Ether-functionalized ILs for nonaqueous biocatalysis: effect of different cation cores. *Process Biochemistry*, *81*, 104-112. doi:10.1016/j.procbio.2019.03.018

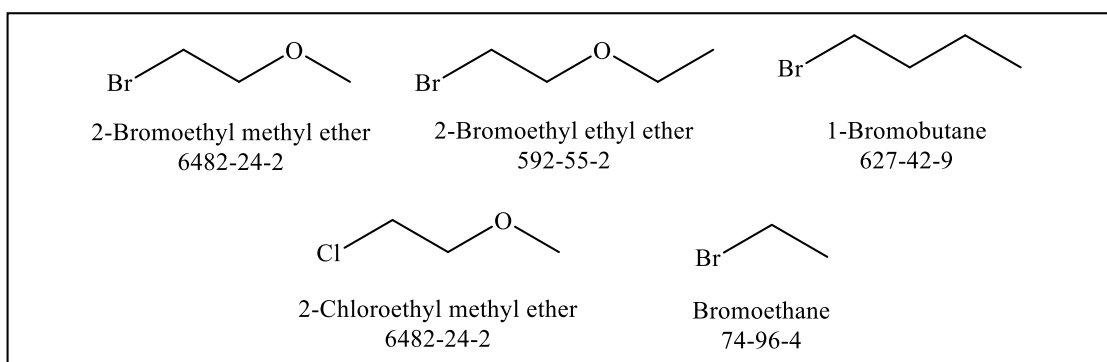


APPENDIX A  
REAGENT SPECIFICATIONS  
AND SOURCES

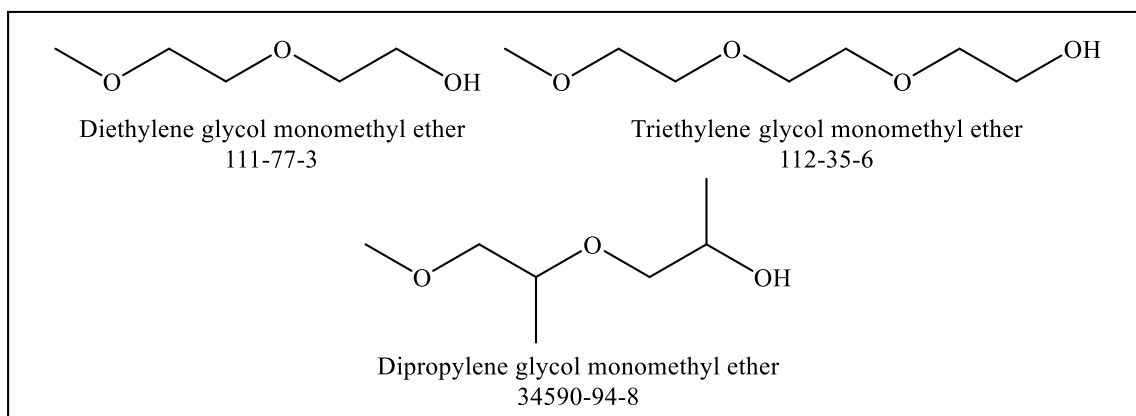
## Starting Reagents



**Figure A.1:** Nucleophilic compounds used to synthesize IL

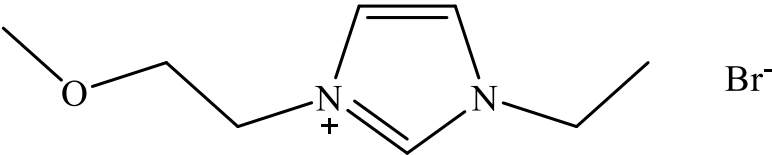
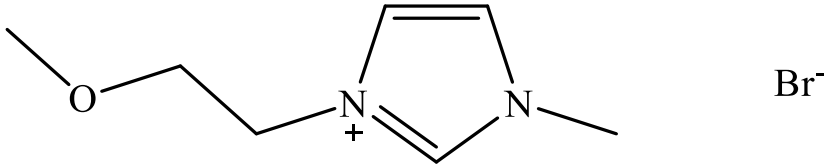
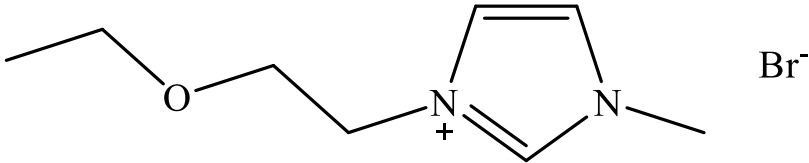
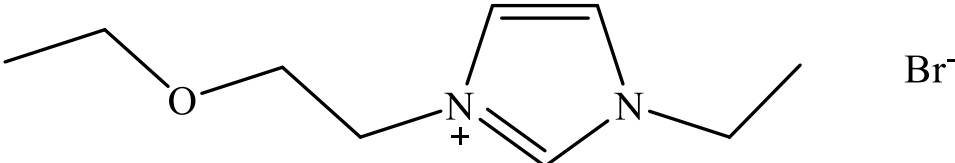


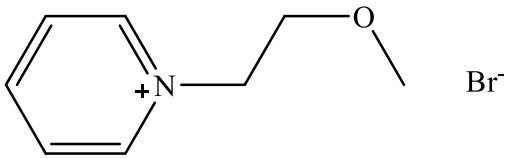
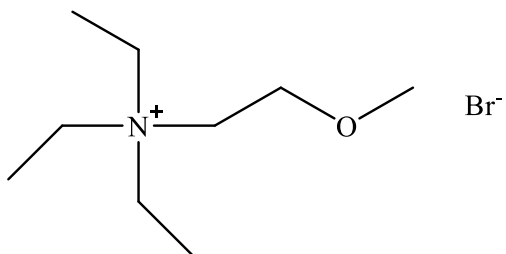
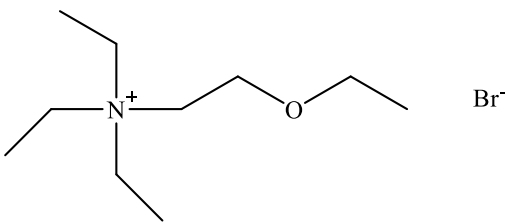
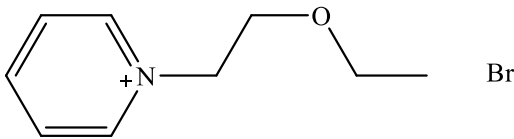
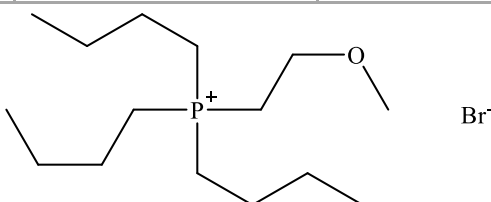
**Figure A.2:** Electrophilic halogenated compounds used to synthesize IL

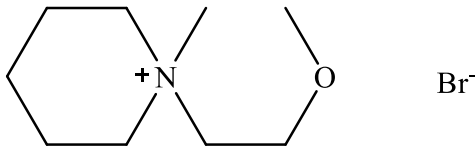
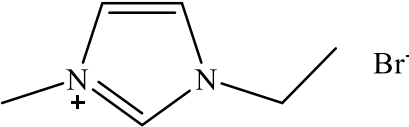
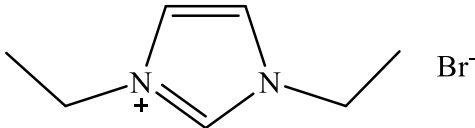
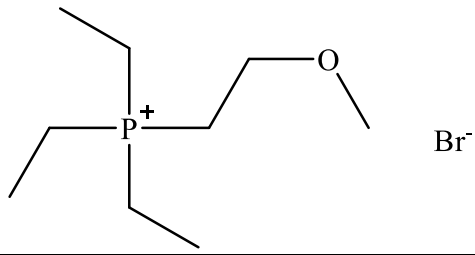
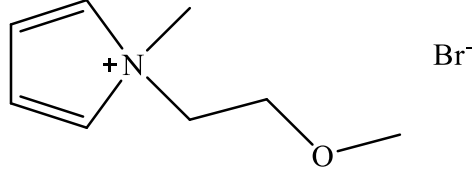


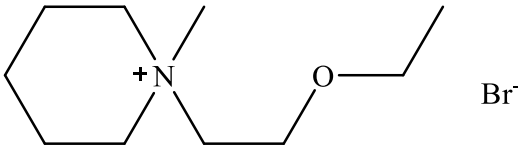
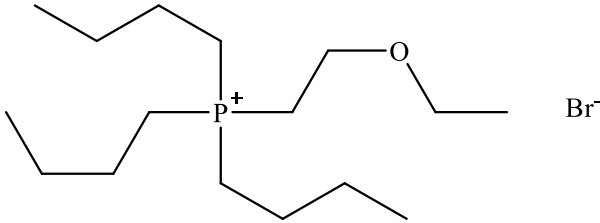
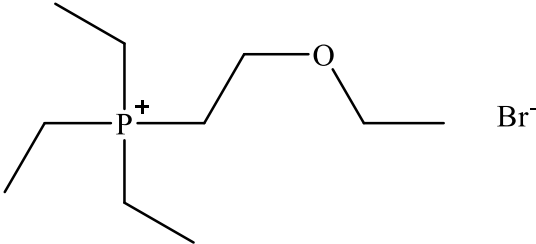
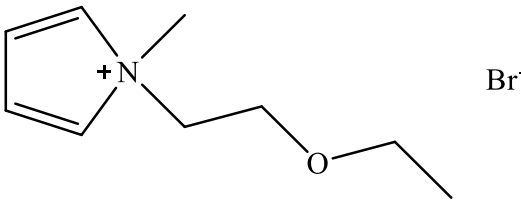
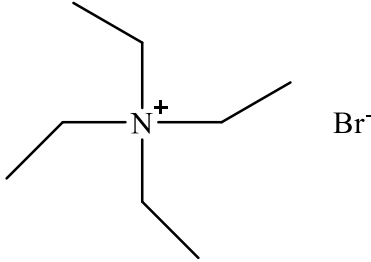
**Figure A.3:** Starting alcohols used in Appel reaction synthesis

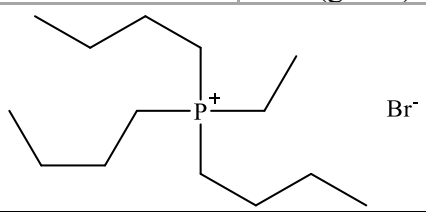
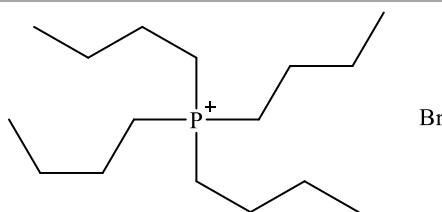
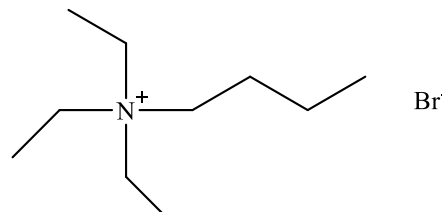
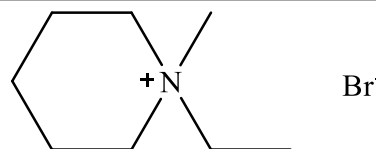
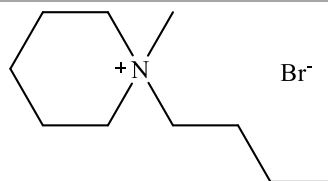
APPENDIX B  
IONIC LIQUID STRUCTURES AND  
NAMING SCHEMATIC

R01	IUPAC Nomenclature	1-ethyl-3-(2-methoxyethyl) imidazolium bromide		
	Chemical Formula	[Et-MOE-Im][Br]	Molar Mass (g/mol)	235.11
				
R02	IUPAC Nomenclature	1-methyl-3-(2-methoxyethyl) imidazolium bromide		
	Chemical Formula	[Me-MOE-Im][Br]	Molar Mass (g/mol)	221.09
				
R03	IUPAC Nomenclature	1-methyl-3-(2-ethoxyethyl) imidazolium bromide		
	Chemical Formula	[Me-EOE-Im][Br]	Molar Mass (g/mol)	235.11
				
R04	IUPAC Nomenclature	1-ethyl-3-(2-ethoxyethyl) imidazolium bromide		
	Chemical Formula	[Et-EOE-Im][Br]	Molar Mass (g/mol)	249.14
				

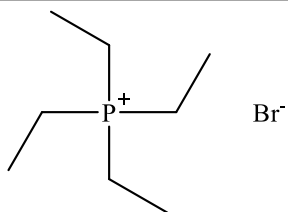
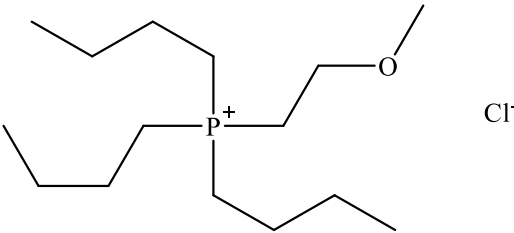
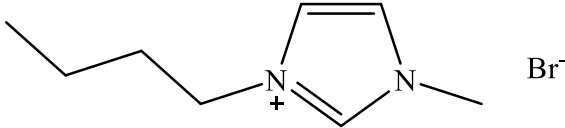
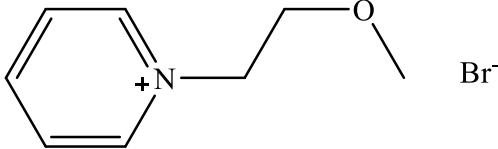
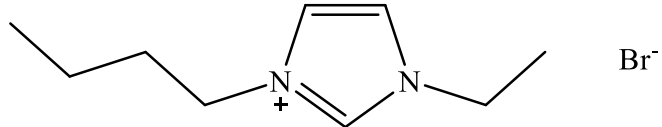
R05	IUPAC Nomenclature	N-(2-methoxyethyl) pyridinium bromide		
	Chemical Formula	[MOE-Pyr][Br]	Molar Mass (g/mol)	218.09
				
R06	IUPAC Nomenclature	N-(2-methoxyethyl) triethyl ammonium bromide		
	Chemical Formula	[MOE-Et <sub>3</sub> N][Br]	Molar Mass (g/mol)	240.18
				
R07	IUPAC Nomenclature	N-(2-ethoxyethyl) triethyl ammonium bromide		
	Chemical Formula	[EOE-Et <sub>3</sub> N][Br]	Molar Mass (g/mol)	254.20
				
R08	IUPAC Nomenclature	N-(2-ethoxyethyl) pyridinium bromide		
	Chemical Formula	[EOE-Pyr][Br]	Molar Mass (g/mol)	232.11
				
R10	IUPAC Nomenclature	P-(2-methoxyethyl) tributyl phosphonium bromide		
	Chemical Formula	[MOE-Bu <sub>3</sub> P][Br]	Molar Mass (g/mol)	341.31
				

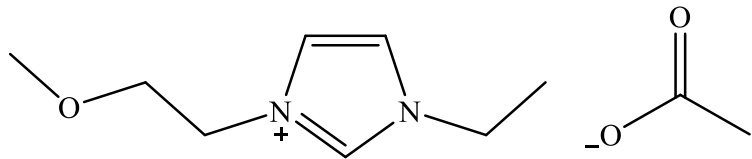
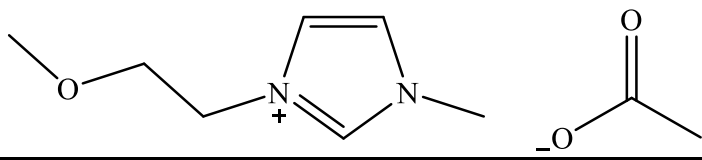
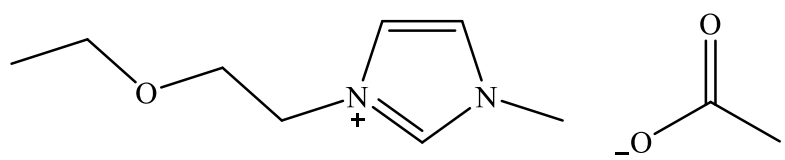
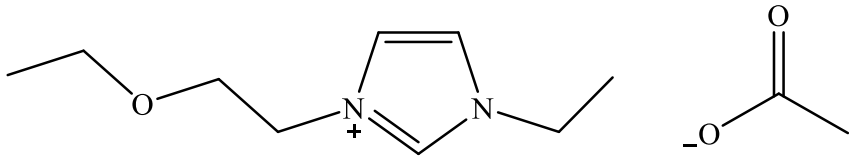
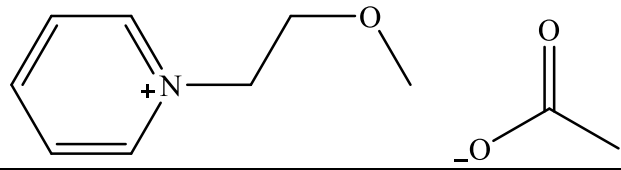
R11	IUPAC Nomenclature	N-(2-methoxyethyl)-N-methyl piperidenium bromide		
	Chemical Formula	[MOE-Me-Pip][Br]	Molar Mass (g/mol)	238.16
				
R12	IUPAC Nomenclature	1-methyl-3-ethyl imidazolium bromide		
	Chemical Formula	[EMIM][Br]	Molar Mass (g/mol)	191.06
				
R13	IUPAC Nomenclature	1,3-diethyl imidazolium bromide		
	Chemical Formula	[EEIM][Br]	Molar Mass (g/mol)	205.09
				
R14	IUPAC Nomenclature	P-(2-methoxyethyl) triethyl phosphonium bromide		
	Chemical Formula	[MOE-Et <sub>3</sub> P][Br]	Molar Mass (g/mol)	257.15
				
R15	IUPAC Nomenclature	N-(2-methoxyethyl)-N-methyl pyrrolidinium bromide		
	Chemical Formula	[MOE-Me-Pyrro][Br]	Molar Mass (g/mol)	224.13
				

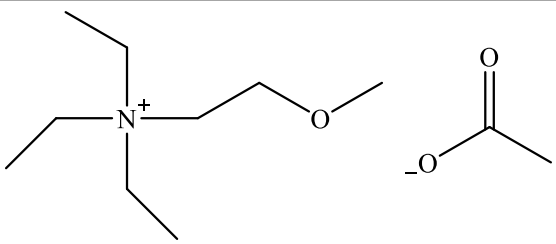
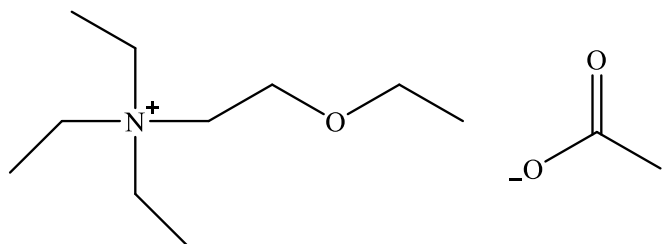
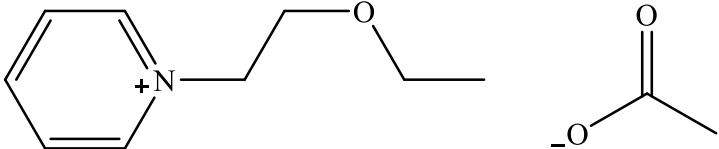
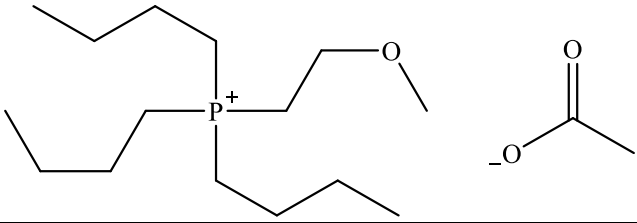
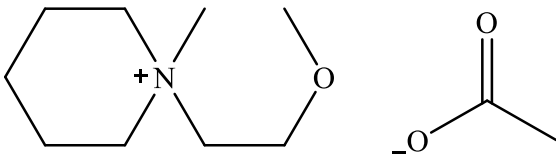
R16	IUPAC Nomenclature	N-(2-ethoxyethyl)-N-methyl piperidenium bromide		
	Chemical Formula	[EOE-Me-Pip][Br]	Molar Mass (g/mol)	252.18
				
R17	IUPAC Nomenclature	P-(2-ethoxyethyl) tributyl phosphonium bromide		
	Chemical Formula	[EOE-Bu <sub>3</sub> P][Br]	Molar Mass (g/mol)	355.33
				
R18	IUPAC Nomenclature	P-(2-ethoxyethyl) triethyl phosphonium bromide		
	Chemical Formula	[EOE-Et <sub>3</sub> P][Br]	Molar Mass (g/mol)	271.17
				
R19	IUPAC Nomenclature	N-(2-ethoxyethyl)-N-methyl pyrrolidinium bromide		
	Chemical Formula	[EOE-Me-Pyrro][Br]	Molar Mass (g/mol)	158.25
				
R20	IUPAC Nomenclature	Tetraethyl ammonium bromide		
	Chemical Formula	[Et <sub>4</sub> N][Br]	Molar Mass (g/mol)	210.15
				

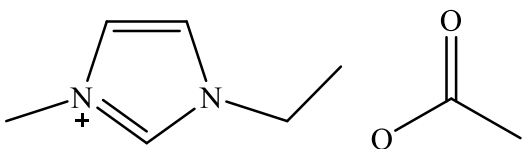
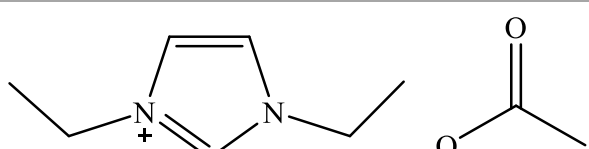
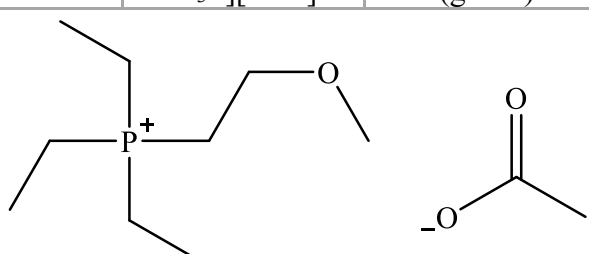
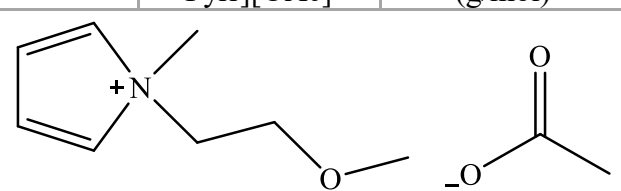
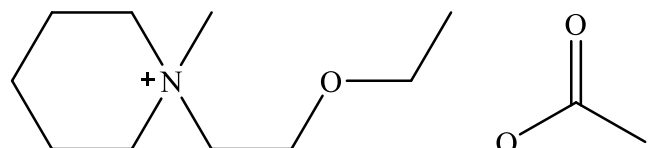
R21	IUPAC Nomenclature	Ethyl tributyl phosphonium bromide		
	Chemical Formula	[Et-Bu <sub>3</sub> P][Br]	Molar Mass (g/mol)	311.28
				
R22	IUPAC Nomenclature	Tetrabutyl phosphonium bromide		
	Chemical Formula	[Bu <sub>4</sub> P][Br]	Molar Mass (g/mol)	339.33
				
R23	IUPAC Nomenclature	Butyl triethyl ammonium bromide		
	Chemical Formula	[Bu-Et <sub>3</sub> N][Br]	Molar Mass (g/mol)	238.20
				
R24	IUPAC Nomenclature	N-ethyl-N-methyl piperidenium bromide		
	Chemical Formula	[Et-Me-Pip][Br]	Molar Mass (g/mol)	208.13
				
R25	IUPAC Nomenclature	N-butyl-N-methyl piperidenium bromide		
	Chemical Formula	[Bu-Me-Pip][Br]	Molar Mass (g/mol)	236.18
				

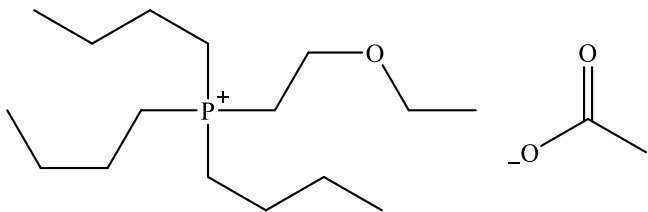
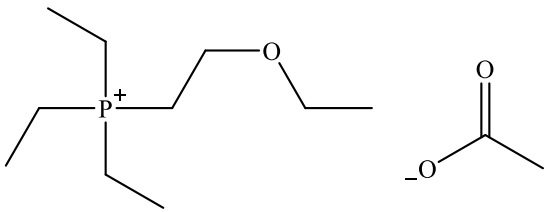
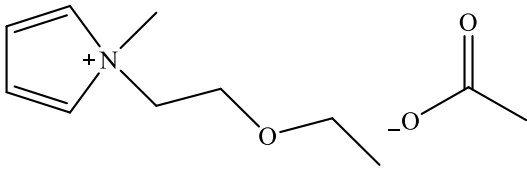
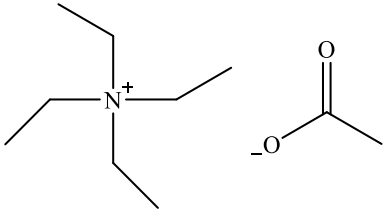
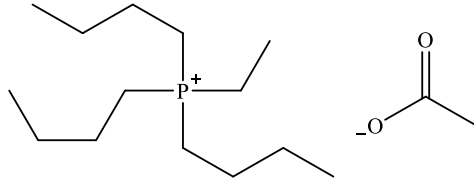


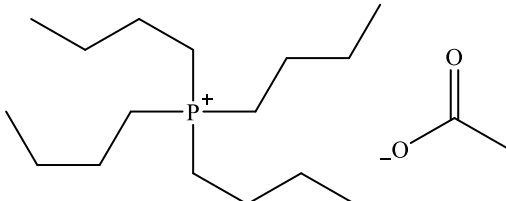
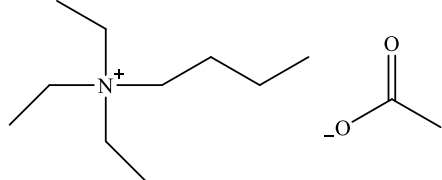
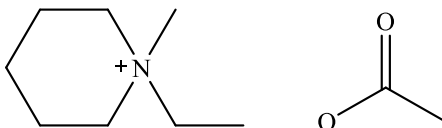
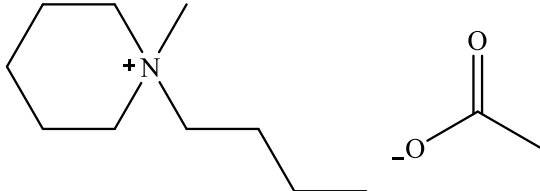
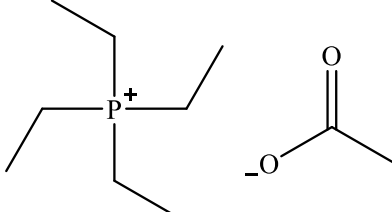
R26	IUPAC Nomenclature	Tetraethyl phosphonium bromide		
	Chemical Formula	[Et <sub>4</sub> P][Br]	Molar Mass (g/mol)	227.12
				
R27	IUPAC Nomenclature	P-(2-methoxyethyl) tributyl phosphonium chloride		
	Chemical Formula	[(MOE)B <sub>3</sub> P][Cl]	Molar Mass (g/mol)	296.86
				
R28	IUPAC Nomenclature	1-butyl-3-methyl imidazolium bromide		
	Chemical Formula	[BMIM][Br]	Molar Mass (g/mol)	219.12
				
R29	IUPAC Nomenclature	N-(2-methoxyethoxy) pyridinium bromide		
	Chemical Formula	[(MOEOE)Pyr][Br]	Molar Mass (g/mol)	238.16
				
R30	IUPAC Nomenclature	1-butyl-3-ethyl imidazolium bromide		
	Chemical Formula	[BEIM][Br]	Molar Mass (g/mol)	233.15
				

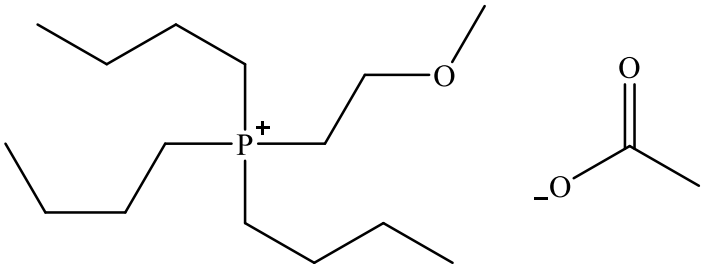
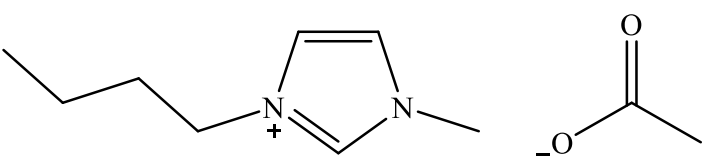
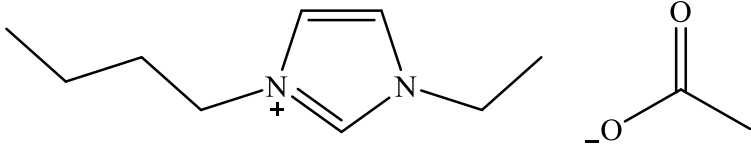
A01	IUPAC Nomenclature	1-ethyl-3-(2-methoxyethyl) imidazolium acetate		
	Chemical Formula	[Et-MOE-Im][OAc]	Molar Mass (g/mol)	214.25
				
A02	IUPAC Nomenclature	1-methyl-3-(2-methoxyethyl) imidazolium acetate		
	Chemical Formula	[Me-MOE-Im][OAc]	Molar Mass (g/mol)	200.23
				
A03	IUPAC Nomenclature	1-methyl-3-(2-ethoxyethyl) imidazolium acetate		
	Chemical Formula	[Me-EOE-Im][OAc]	Molar Mass (g/mol)	214.25
				
A04	IUPAC Nomenclature	1-ethyl-3-(2-ethoxyethyl) imidazolium acetate		
	Chemical Formula	[Et-EOE-Im][OAc]	Molar Mass (g/mol)	249.14
				
A05	IUPAC Nomenclature	N-(2-methoxyethyl) pyridinium acetate		
	Chemical Formula	[MOE-Pyr][OAc]	Molar Mass (g/mol)	197.23
				

A06	IUPAC Nomenclature	N-(2-methoxyethyl) triethyl ammonium acetate		
	Chemical Formula	[MOE-Et <sub>3</sub> N][OAc]	Molar Mass (g/mol)	219.32
				
A07	IUPAC Nomenclature	N-(2-ethoxyethyl) triethyl ammonium acetate		
	Chemical Formula	[EOE-Et <sub>3</sub> N][OAc]	Molar Mass (g/mol)	233.34
				
A08	IUPAC Nomenclature	N-(2-ethoxyethyl) pyridinium acetate		
	Chemical Formula	[EOE-Pyr][OAc]	Molar Mass (g/mol)	211.25
				
A10	IUPAC Nomenclature	P-(2-methoxyethyl) tributyl phosphonium acetate		
	Chemical Formula	[MOE-Bu <sub>3</sub> P][OAc]	Molar Mass (g/mol)	320.45
				
A11	IUPAC Nomenclature	N-(2-methoxyethyl)-N-methyl piperidenium acetate		
	Chemical Formula	[MOE-Me-Pip][OAc]	Molar Mass (g/mol)	217.30
				

A12	IUPAC Nomenclature	1-methyl-3-ethyl imidazolium acetate		
	Chemical Formula	[MEIM][OAc]	Molar Mass (g/mol)	170.20
				
A13	IUPAC Nomenclature	1-ethyl-3-ethyl imidazolium acetate		
	Chemical Formula	[EEIM][OAc]	Molar Mass (g/mol)	184.23
				
A14	IUPAC Nomenclature	P-(2-methoxyethyl) triethyl phosphonium acetate		
	Chemical Formula	[MOE-Et <sub>3</sub> P][OAc]	Molar Mass (g/mol)	236.29
				
A15	IUPAC Nomenclature	N-(2-methoxyethyl)-N-methyl pyrrolidinium acetate		
	Chemical Formula	[MOE-Me-Pyrr][OAc]	Molar Mass (g/mol)	203.27
				
A16	IUPAC Nomenclature	N-(2-ethoxyethyl)-N-methyl piperidinium acetate		
	Chemical Formula	[EOE-Me-Pip][OAc]	Molar Mass (g/mol)	231.32
				

A17	IUPAC Nomenclature	P-(2-ethoxyethyl) tributyl phosphonium acetate		
	Chemical Formula	[EOE-Bu <sub>3</sub> P][OAc]	Molar Mass (g/mol)	334.47
				
A18	IUPAC Nomenclature	P-(2-ethoxyethyl) triethyl phosphonium acetate		
	Chemical Formula	[EOE-Et <sub>3</sub> P][OAc]	Molar Mass (g/mol)	250.31
				
A19	IUPAC Nomenclature	N-(2-ethoxyethyl)-N-methyl pyrrolidinium acetate		
	Chemical Formula	[EOE-Me-Pyrr][OAc]	Molar Mass (g/mol)	147.18
				
A20	IUPAC Nomenclature	Tetraethyl ammonium acetate		
	Chemical Formula	[Et <sub>4</sub> N][OAc]	Molar Mass (g/mol)	189.29
				
A21	IUPAC Nomenclature	Ethyl tributyl phosphonium acetate		
	Chemical Formula	[Et-Bu <sub>3</sub> P][OAc]	Molar Mass (g/mol)	290.42
				

A22	IUPAC Nomenclature	Tetrabutyl phosphonium acetate		
	Chemical Formula	[Bu <sub>4</sub> P][OAc]	Molar Mass (g/mol)	318.47
				
A23	IUPAC Nomenclature	Butyl triethyl ammonium acetate		
	Chemical Formula	[Bu-Et <sub>3</sub> N][OAc]	Molar Mass (g/mol)	217.34
				
A24	IUPAC Nomenclature	N-ethyl-N-methyl piperidinium acetate		
	Chemical Formula	[Et-Me-Pip][OAc]	Molar Mass (g/mol)	187.27
				
A25	IUPAC Nomenclature	N-butyl-N-methyl piperidinium acetate		
	Chemical Formula	[Bu-Me-Pip][OAc]	Molar Mass (g/mol)	215.32
				
A26	IUPAC Nomenclature	Tetraethyl phosphonium acetate		
	Chemical Formula	[Et <sub>4</sub> P][OAc]	Molar Mass (g/mol)	206.26
				

A27	IUPAC Nomenclature	P-(2-methoxyethyl) tributyl phosphonium acetate		
	Chemical Formula	[MOE-Bu <sub>3</sub> P][OAc]	Molar Mass (g/mol)	304.45
				
A28	IUPAC Nomenclature	1-butyl-3-methyl imidazolium acetate		
	Chemical Formula	[BMIM][OAc]	Molar Mass (g/mol)	182.26
				
A30	IUPAC Nomenclature	1-butyl-3-ethyl imidazolium acetate		
	Chemical Formula	[BEIM][OAc]	Molar Mass (g/mol)	212.29
				

APPENDIX C  
COMPREHENSIVE PHYSIOCHEMICAL  
PROPERTIES OF IONIC LIQUIDS



## Water Concentration via Karl Fisher Titration

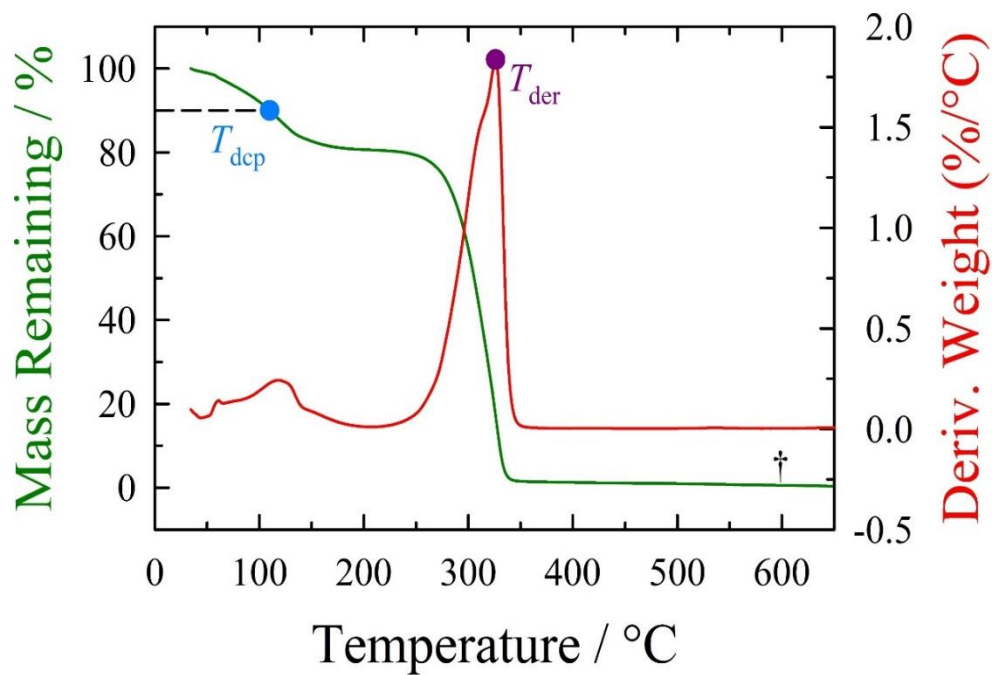
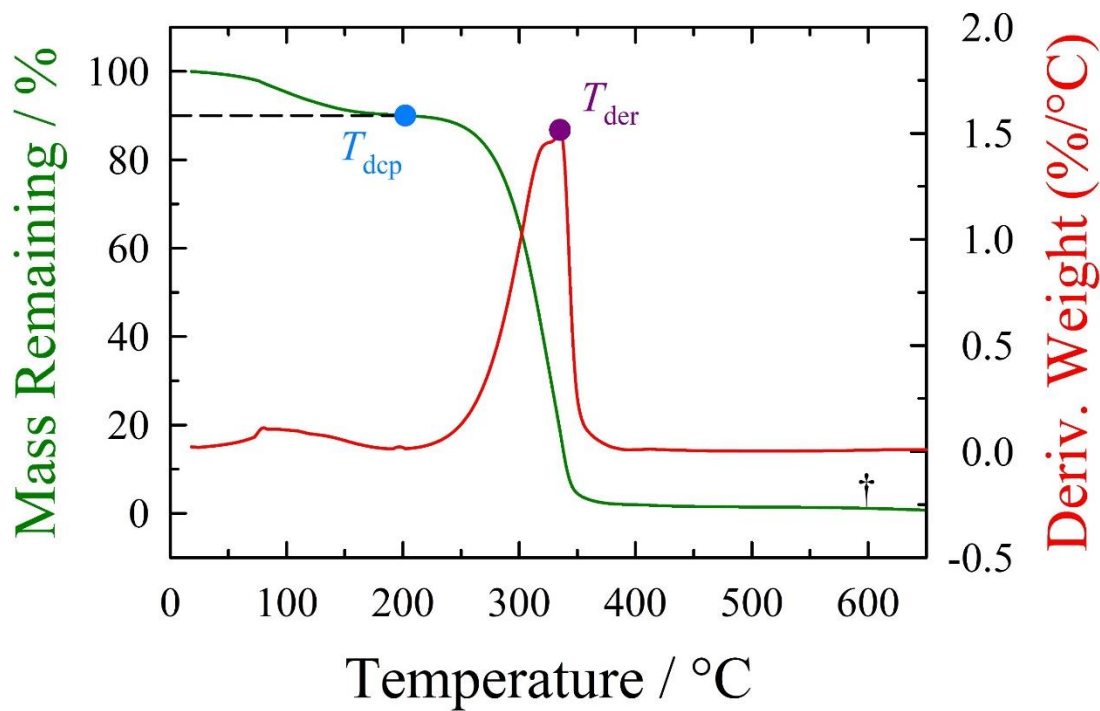
IL	Mass (mg)	Water Conc.	IL	Mass (mg)	Water Conc.
A01	514	0.058%	A16	283	0.026%
A02	466	0.049%	A17	265	0.035%
A03	360	0.096%	A18	1280	0.069%
A04	231	0.119%	A19	149	0.252%
A05	531	0.070%	A20	----- Solid @ R.T. -----	
A06	442	0.255%	A21	358	0.222%
A07	503	0.014%	A22	----- Solid @ R.T. -----	
A08	402	0.043%	A23	48	0.050%
A10	324	0.133%	A24	----- Solid @ R.T. -----	
A11	412	0.037%	A25	515	0.077%
A12	503	0.020%	A26	----- Solid @ R.T. -----	
A13	171	0.716%	A27	----- Solid @ R.T. -----	
A14	485	0.030%	A28	95	0.168%
A15	425	0.160%	A30	179	0.722%

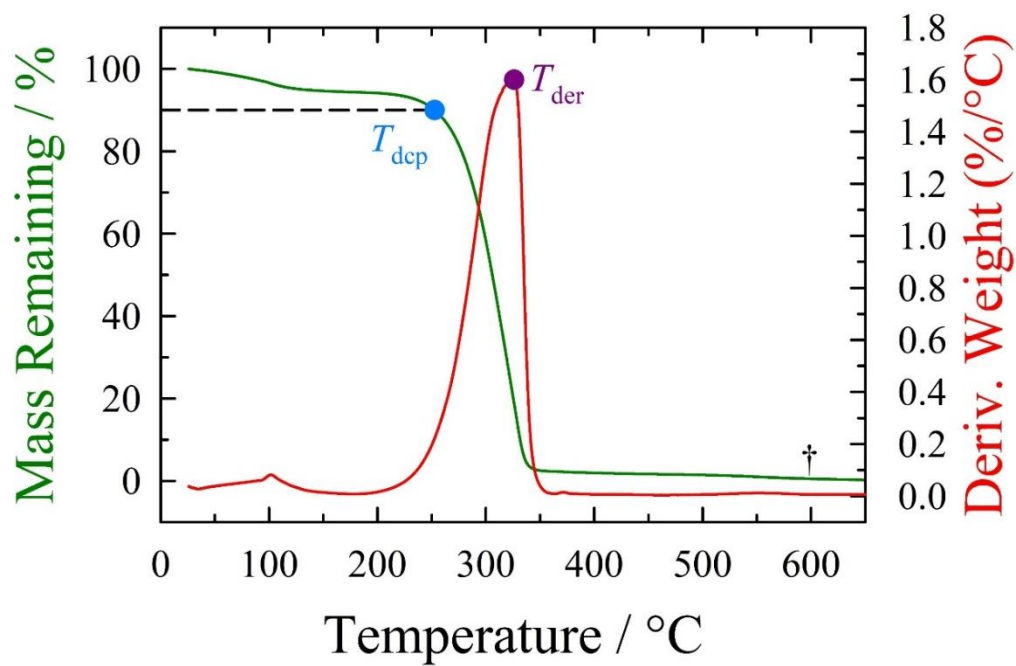
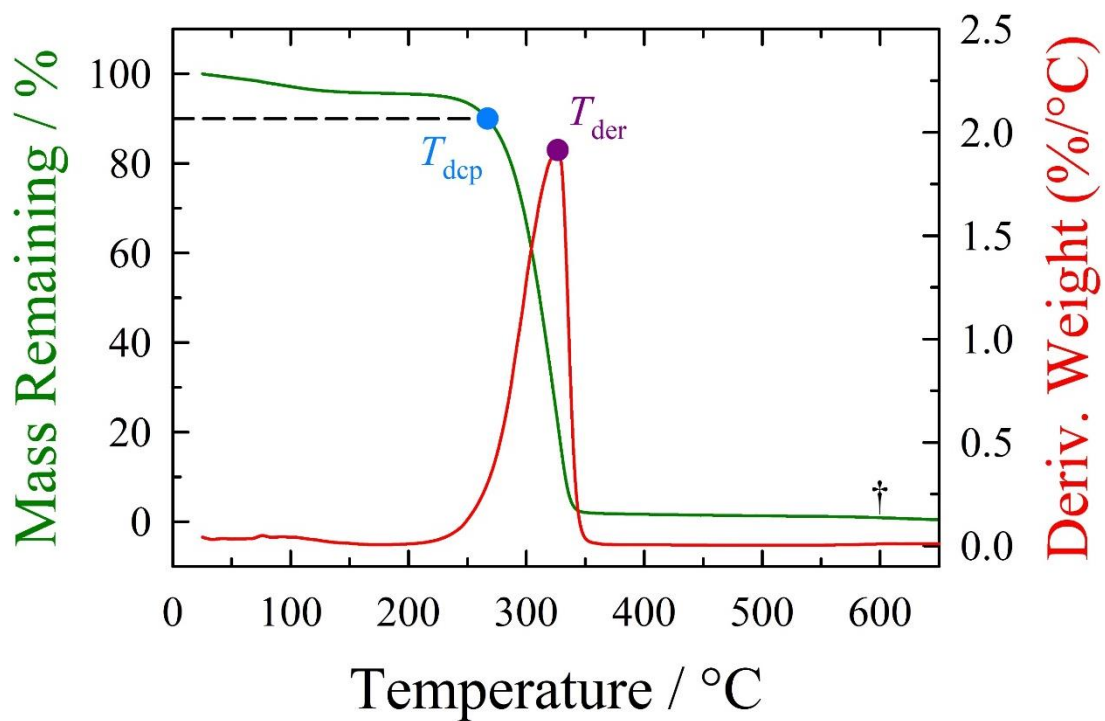
## Viscometry Measurements for Acetate-ILs

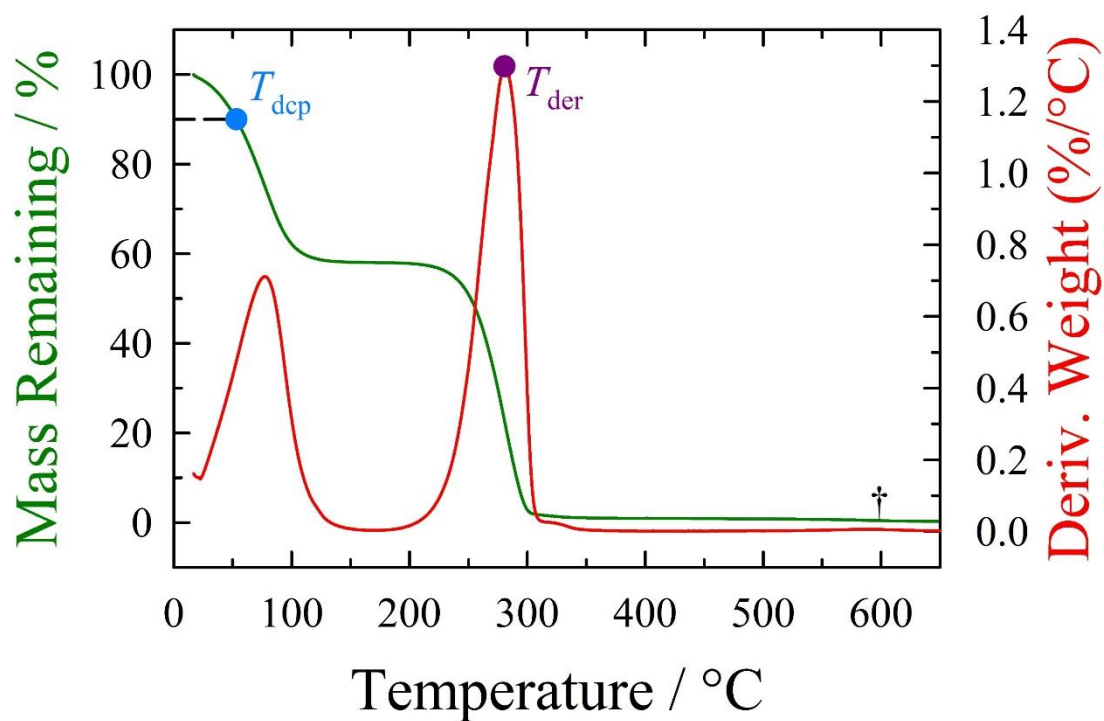
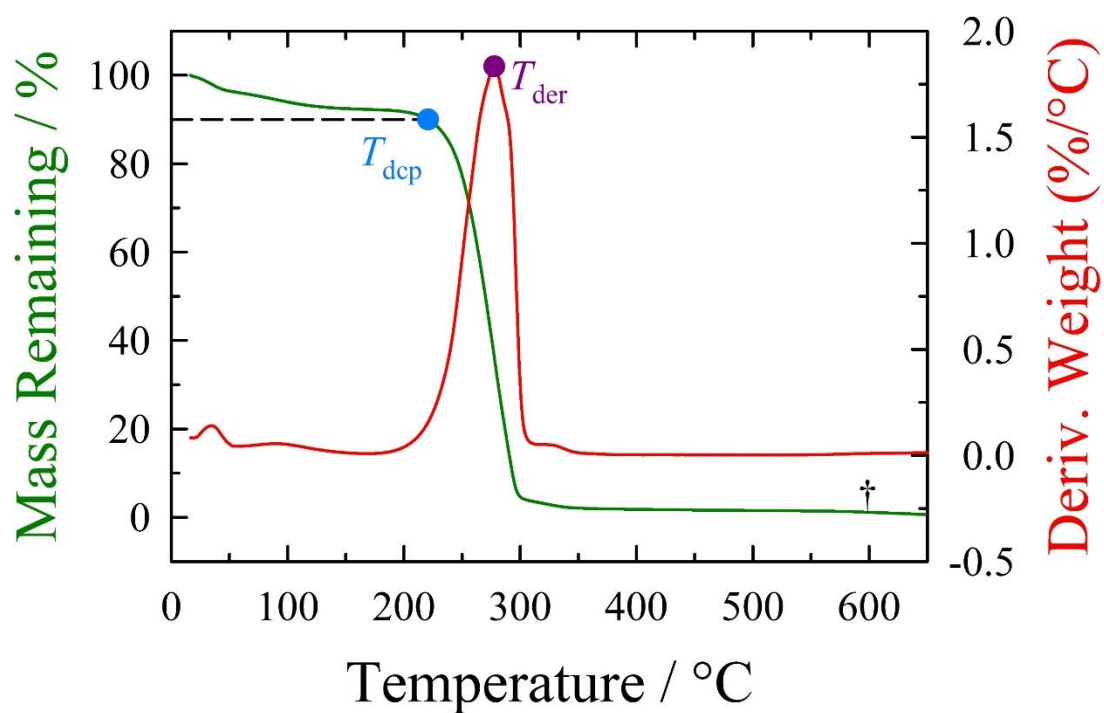
IL	Dynamic Viscosity (mPa·s)	Kinematic Viscosity (mm <sup>2</sup> /s)	Density (g/cm <sup>3</sup> )
A01	36.620	33.498	1.0932
A02	44.851	40.062	1.1195
A03	150.110	137.070	1.0952
A04	59.141	55.386	1.0678
A05	27.698	24.958	1.1098
A06	99.636	96.670	1.0307
A07	33.973	33.114	1.0260
A08	28.279	25.927	1.0907
A10	58.943	59.944	0.9833
A11	57.527	53.414	1.0770
A12	22.928	20.907	1.0967
A13	39.318	36.165	1.0872
A14	19.162	18.282	1.0482
A15	62.955	58.428	1.0775
A16	49.889	47.197	1.0570
A17	52.534	53.880	0.9750
A18	54.130	52.408	1.0328
A19	43.235	41.040	1.0535
A20	----- Solid @ Room Temperature -----		
A21	127.590	133.890	0.9529
A22	----- Solid @ Room Temperature -----		
A23	58.497	59.030	0.9910
A24	----- Solid @ Room Temperature -----		
A25	28.256	28.119	1.0049
A26	----- Solid @ Room Temperature -----		
A27	----- Solid @ Room Temperature -----		
A28	203.100	194.110	1.0463
A30	71.703	69.299	1.0547

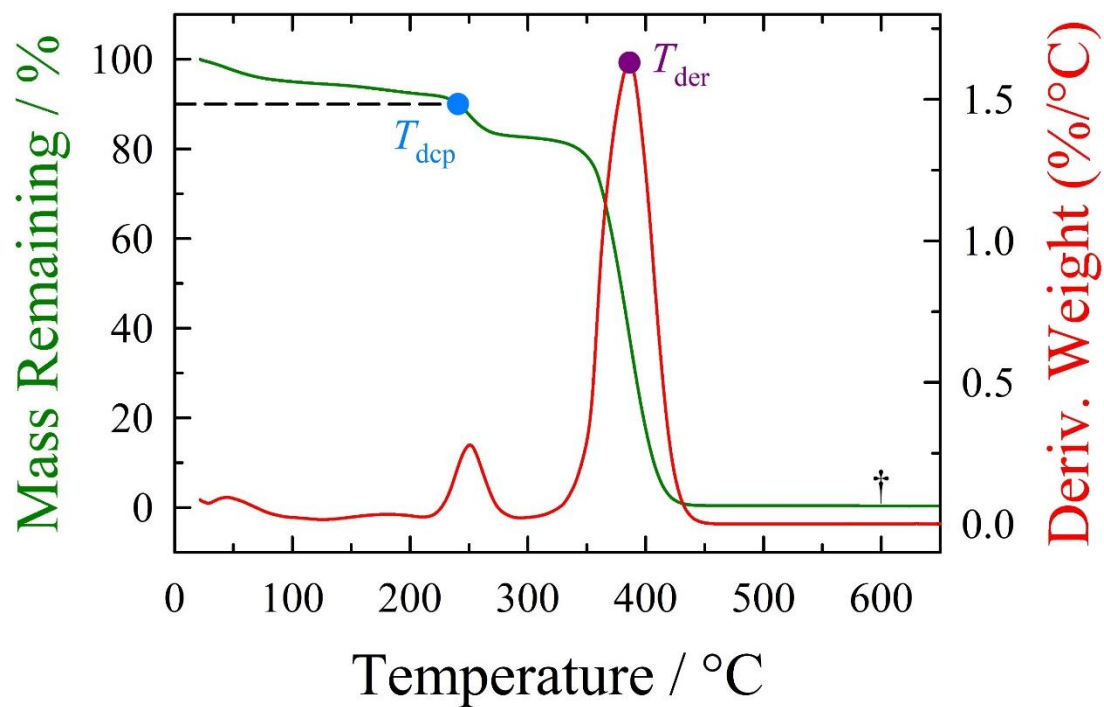
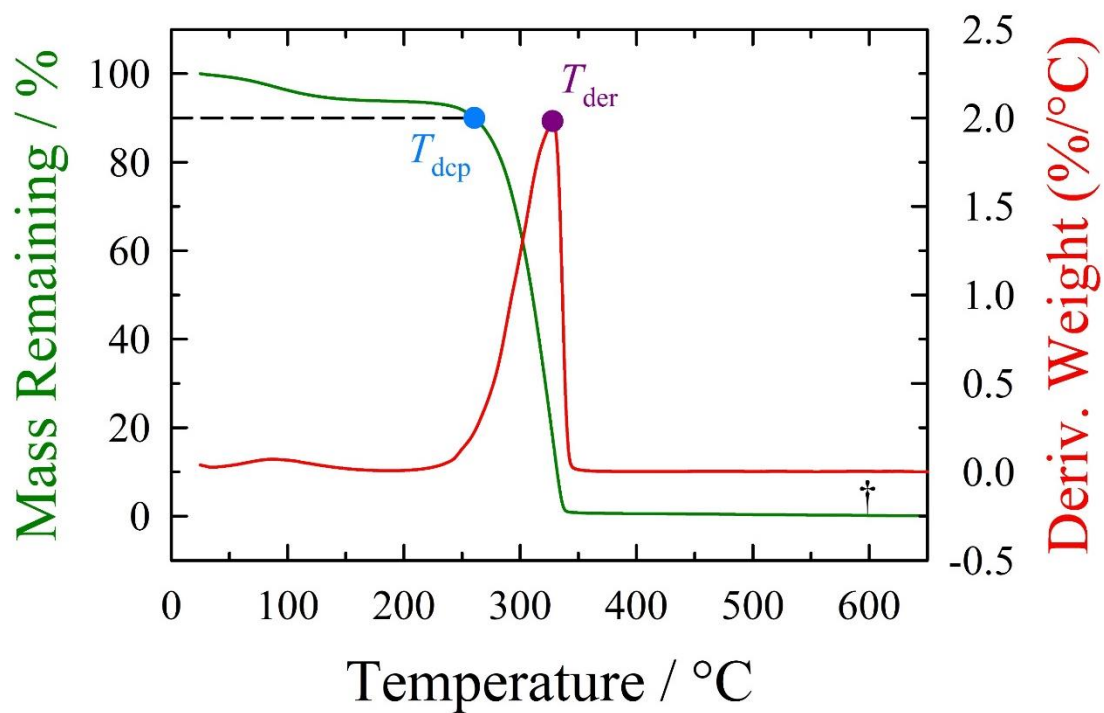
## Thermogravimetric Analysis of bromide-ILs

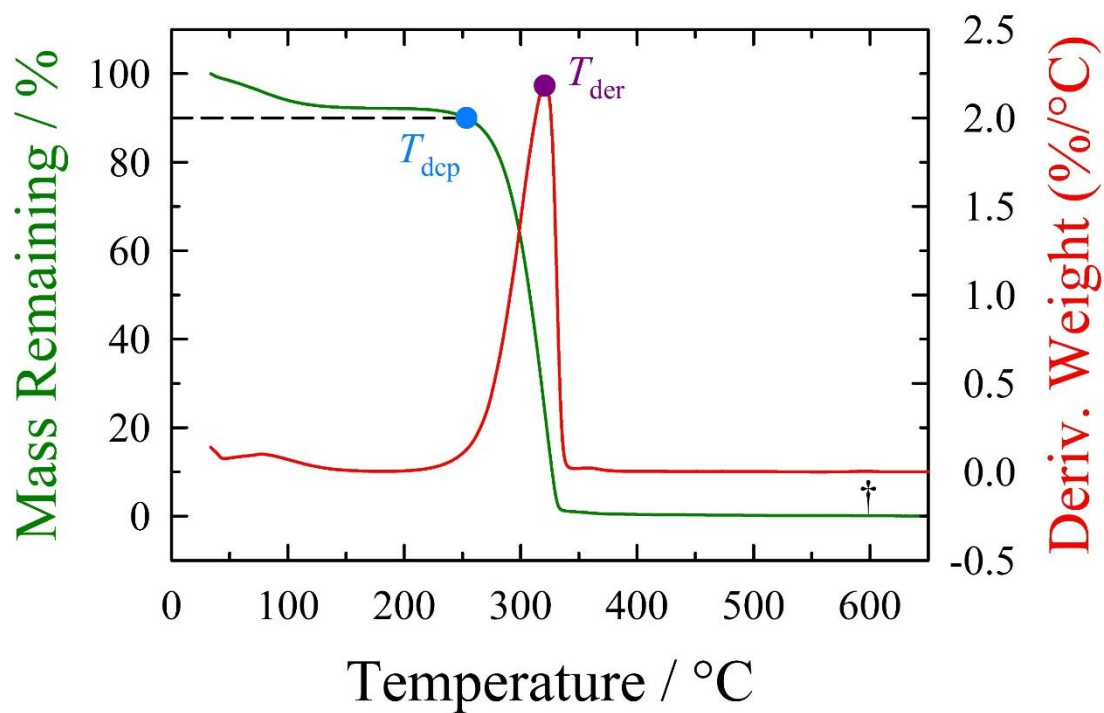
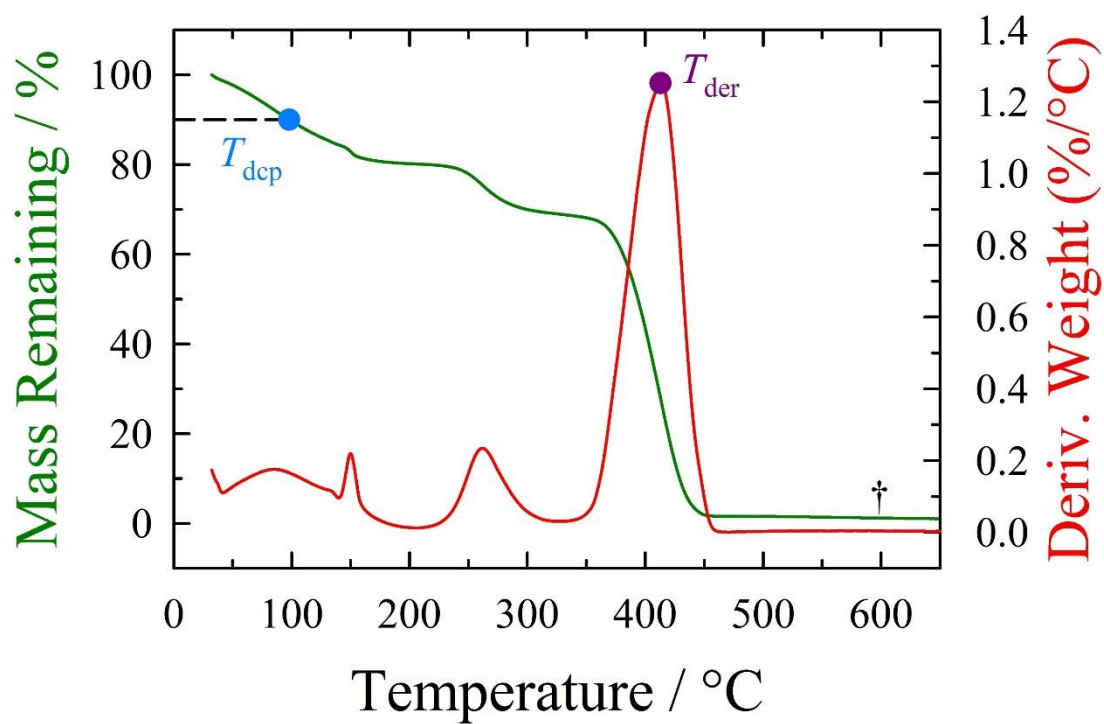
IL	T <sub>der</sub>	T <sub>dcp</sub>	Transition Shape	Residual Char
R01	325	105	M	0.00
R02	347	201	M	0.00
R03	323	250	S	0.08
R04	328	263	S	0.13
R05	286	51	M	0.00
R06	----- Solid @ Room Temperature -----			
R07	----- Solid @ Room Temperature -----			
R08	279	217	S	0.00
R10	395	247	M	0.00
R11	Solid @ R.T. – Did not submit for TGA			
R12	329	253	S	0.00
R13	310	252	S	0.00
R14	411	100	M	0.00
R15	----- Solid @ Room Temperature -----			
R16	----- Solid @ Room Temperature -----			
R17	385	48	M	0.00
R18	----- Solid @ Room Temperature -----			
R19	280	222	S	0.00
R20	----- Solid @ Room Temperature -----			
R21	----- Solid @ Room Temperature -----			
R22	----- Solid @ Room Temperature -----			
R23	----- Solid @ Room Temperature -----			
R24	----- Solid @ Room Temperature -----			
R25	----- Solid @ Room Temperature -----			
R26	----- Solid @ Room Temperature -----			
R27	392	208	M	0.00
R28	----- Solid @ Room Temperature -----			
R29	----- Solid @ Room Temperature -----			
R30	----- Solid @ Room Temperature -----			

**Figure C.1:** Thermogravimetric analysis of IL R01.**Figure C.2:** Thermogravimetric analysis of IL R02.

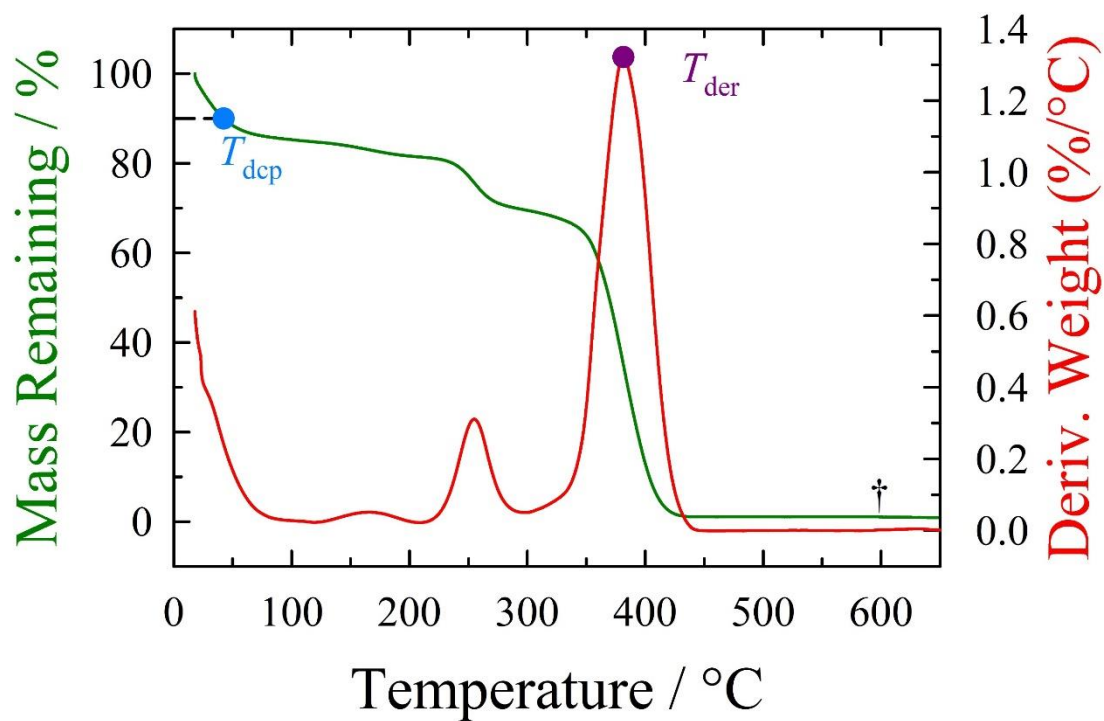
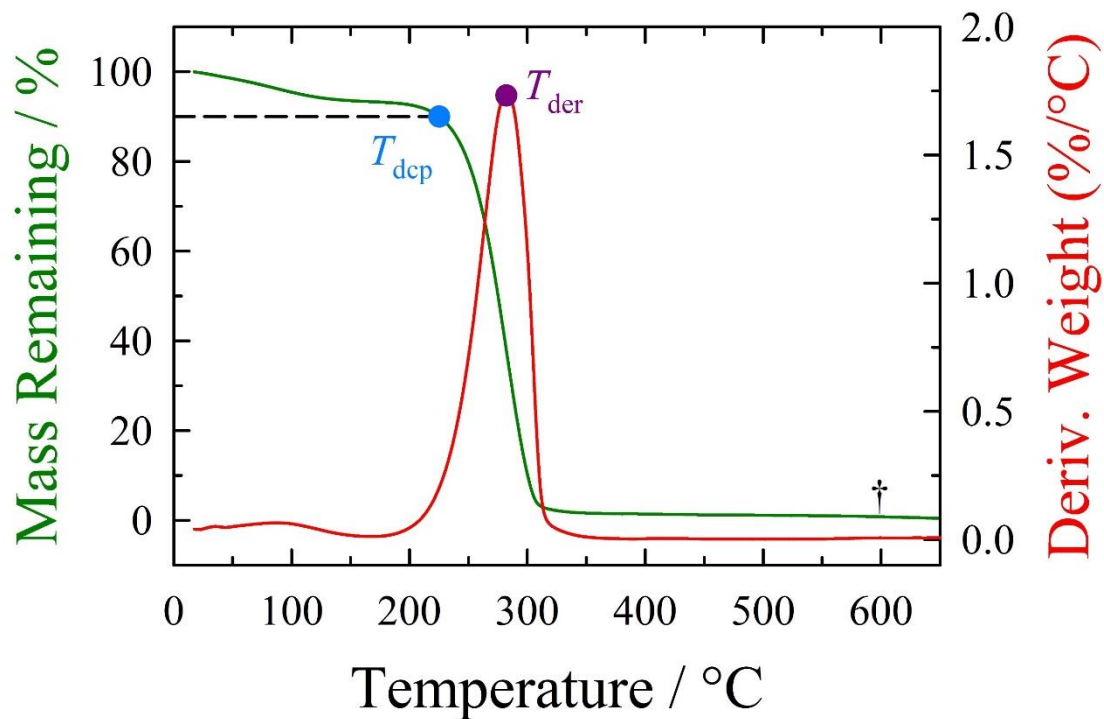
**Figure C.3:** Thermogravimetric analysis of IL R03.**Figure C.4:** Thermogravimetric analysis of IL R04.

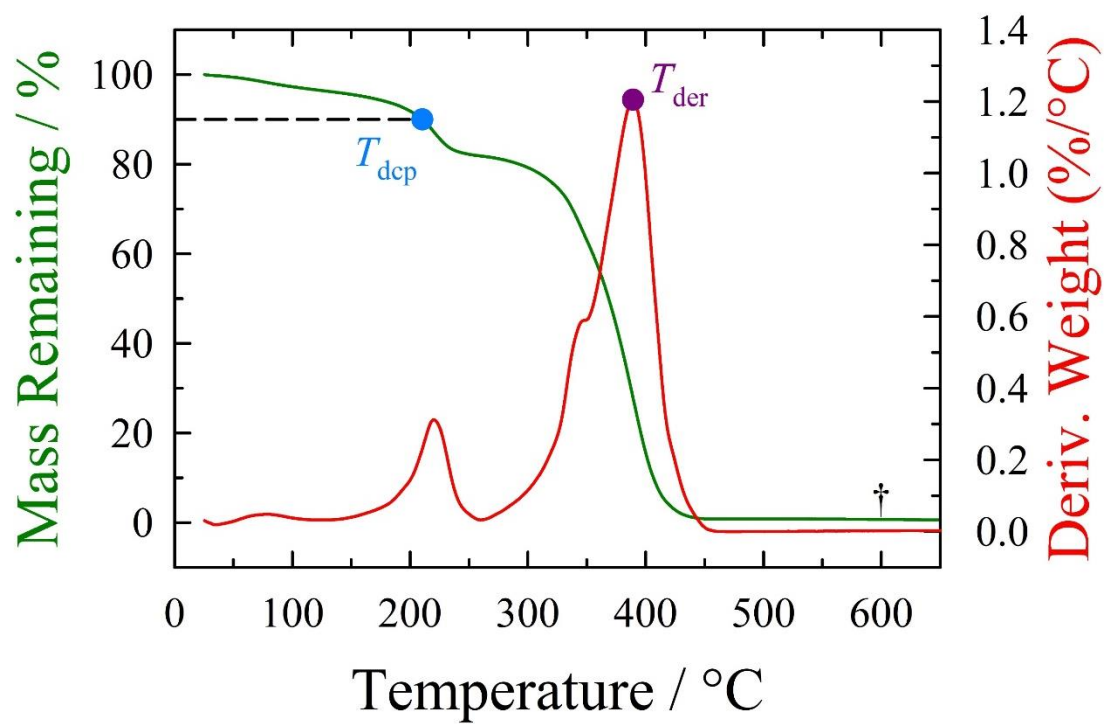
**Figure C.5:** Thermogravimetric analysis of IL R05.**Figure C.6:** Thermogravimetric analysis of IL R08.

**Figure C.7:** Thermogravimetric analysis of IL R10.**Figure C.8:** Thermogravimetric analysis of IL R12.

**Figure C.9:** Thermogravimetric analysis of IL R13.**Figure C.10:** Thermogravimetric analysis of IL R14.



**Figure C.11:** Thermogravimetric analysis of IL R17.**Figure C.12:** Thermogravimetric analysis of IL R19.

**Figure C.13:** Thermogravimetric analysis of IL R27.

## Thermogravimetric Analysis of acetate-ILs

IL	T <sub>der</sub>	T <sub>dcp</sub>	Transition Shape	Residual Char
A01	238	183	S	3.0%
A02	240	157	S	1.8%
A03	239	192	S	1.2%
A04	252	184	S	3.0%
A05	166	88	M	12.6%
A06	202	156	S	0.0%
A07	200	134	S	0.3%
A08	171	116	S	14.4%
A10	185	143	M	3.2%
A11	211	144	S	0.1%
A12	242	171	S	0.0%
A13	103	67	M	0.2%
A14	185	113	M	3.7%
A15	190	150	S	0.0%
A16	200	120	S	0.0%
A17	180	135	M	3.5%
A18	183	134	M	5.2%
A19	187	145	S	0.2%
A20	----- Solid @ Room Temperature -----			
A21	320	234	S	0.3%
A22	----- Solid @ Room Temperature -----			
A23	208	165	S	0.1%
A24	----- Solid @ Room Temperature -----			
A25	324	137	M	0.4%
A26	----- Solid @ Room Temperature -----			
A27	----- Solid @ Room Temperature -----			
A28	237	191	S	0.0%
A30	255	125	S	0.0%

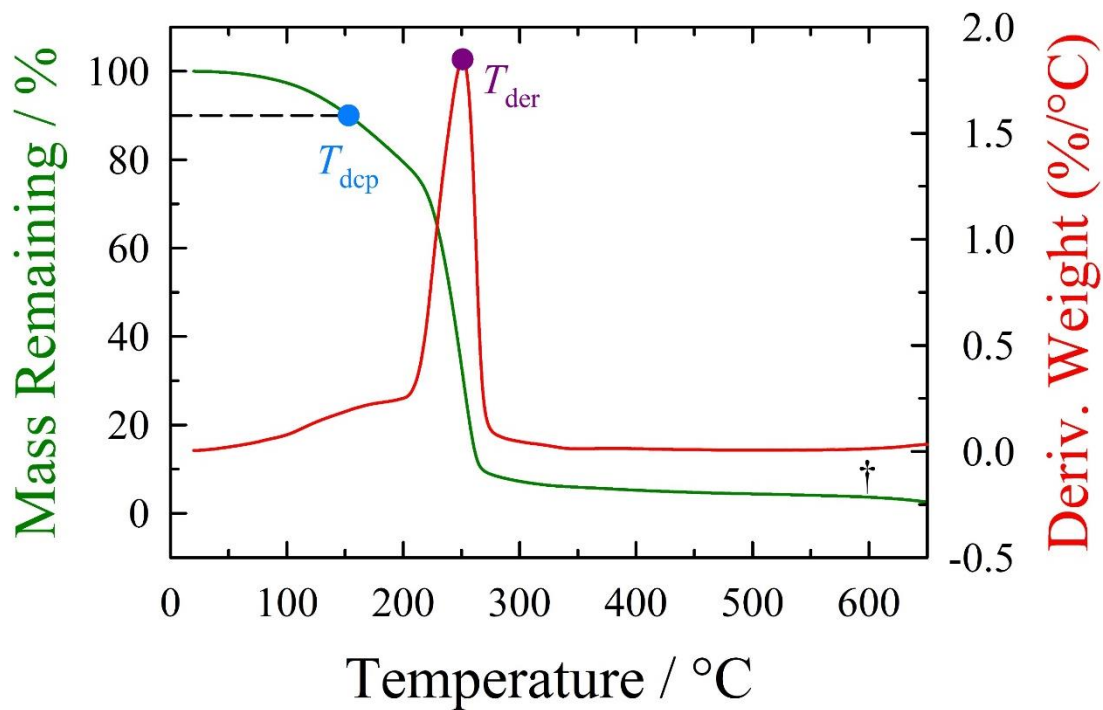
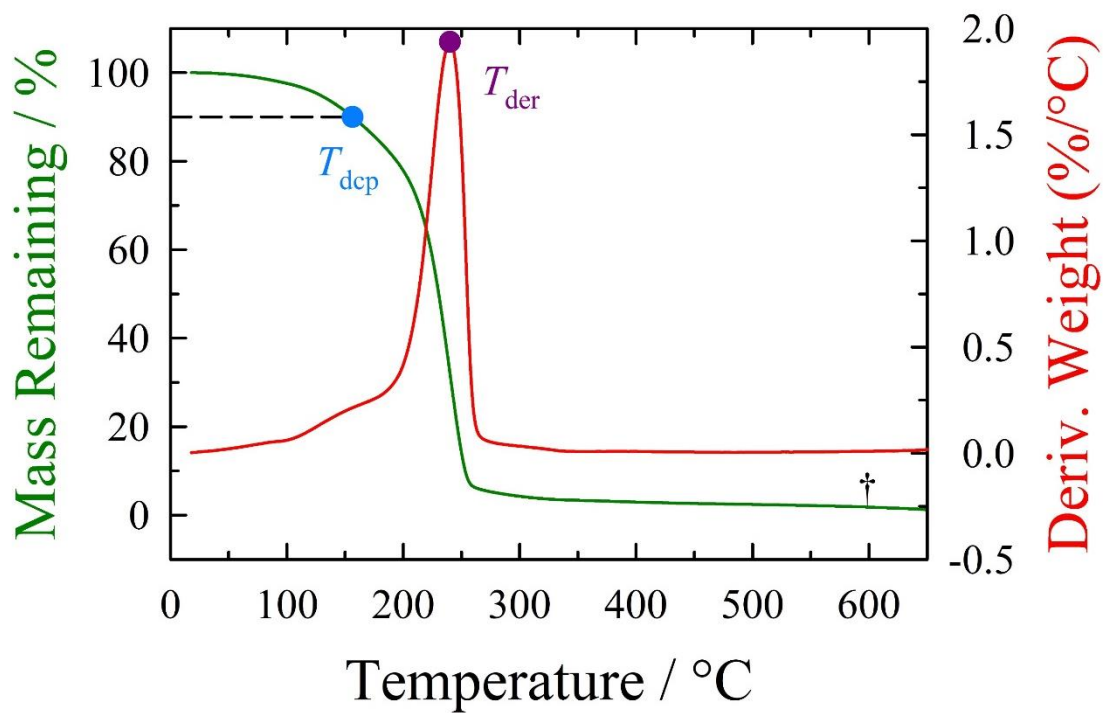
**Figure C.14:** Thermogravimetric analysis of IL A01.**Figure C.15:** Thermogravimetric analysis of IL A02.

Figure C.16: Thermogravimetric analysis of IL A03.

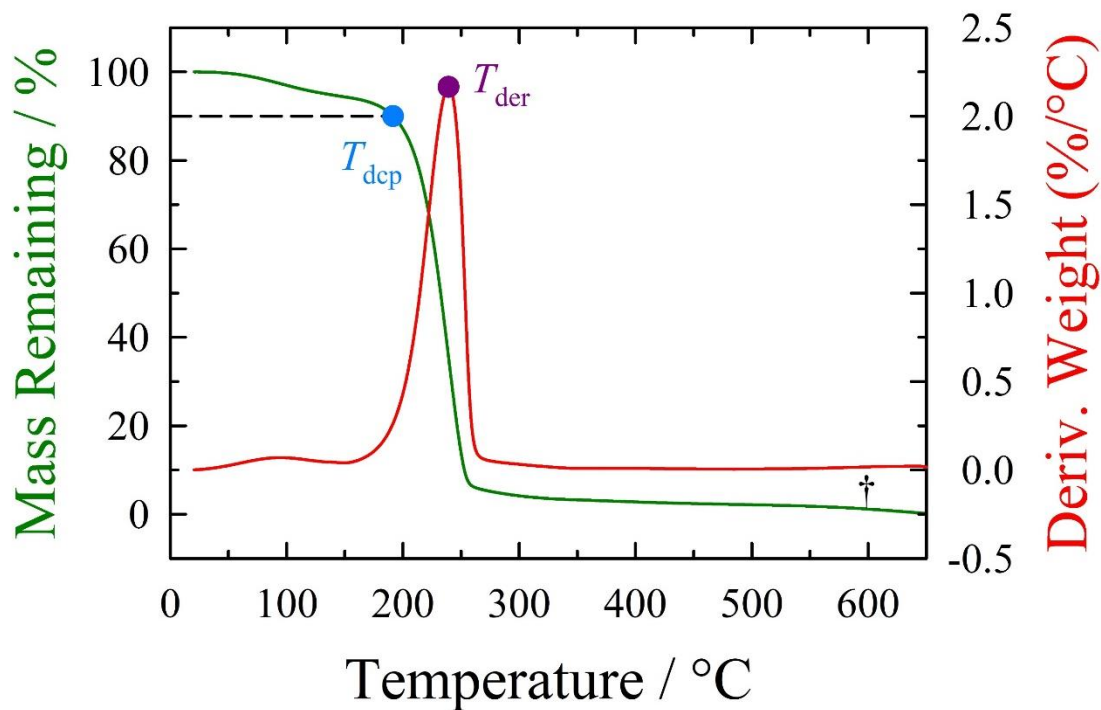
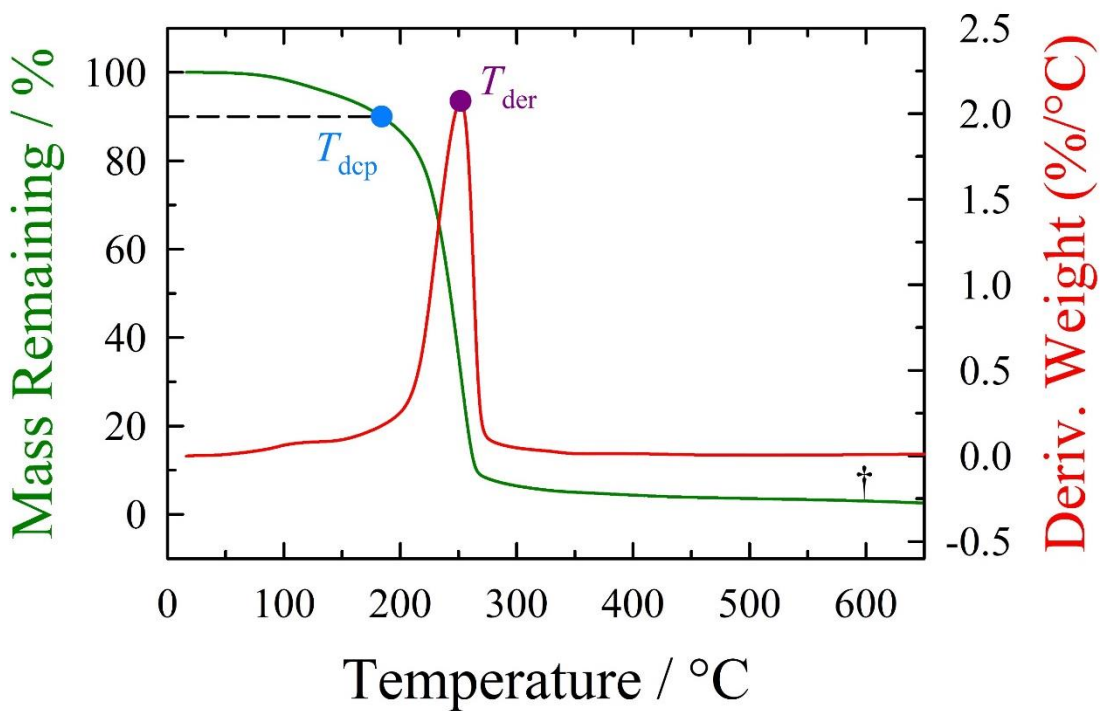
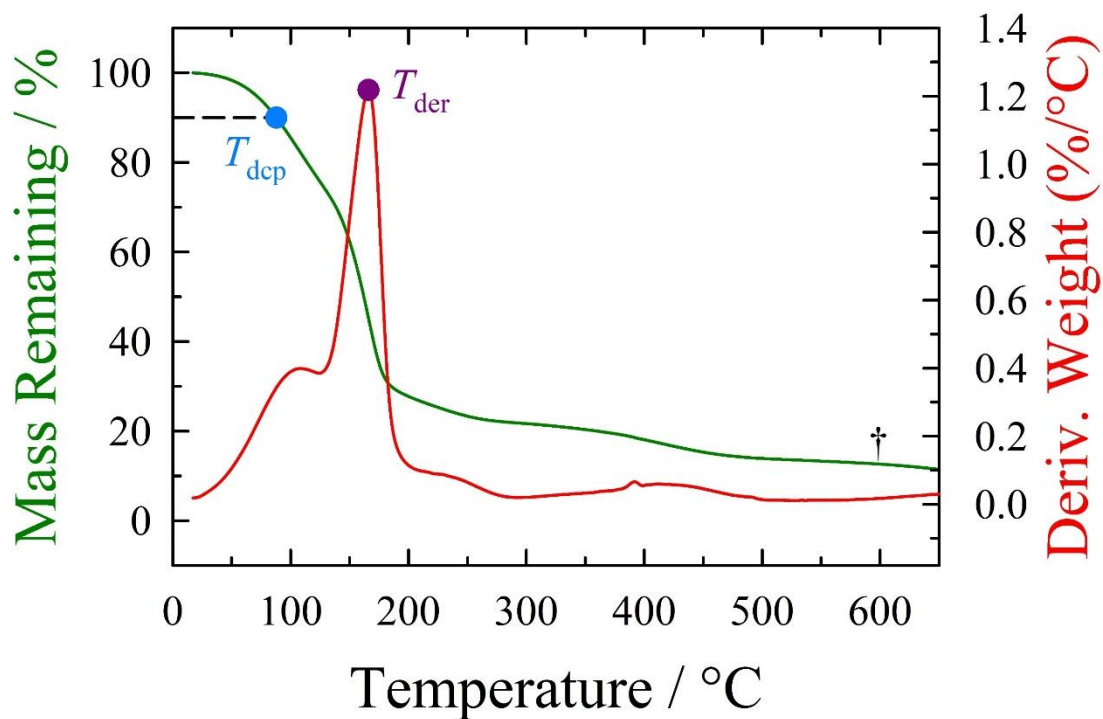
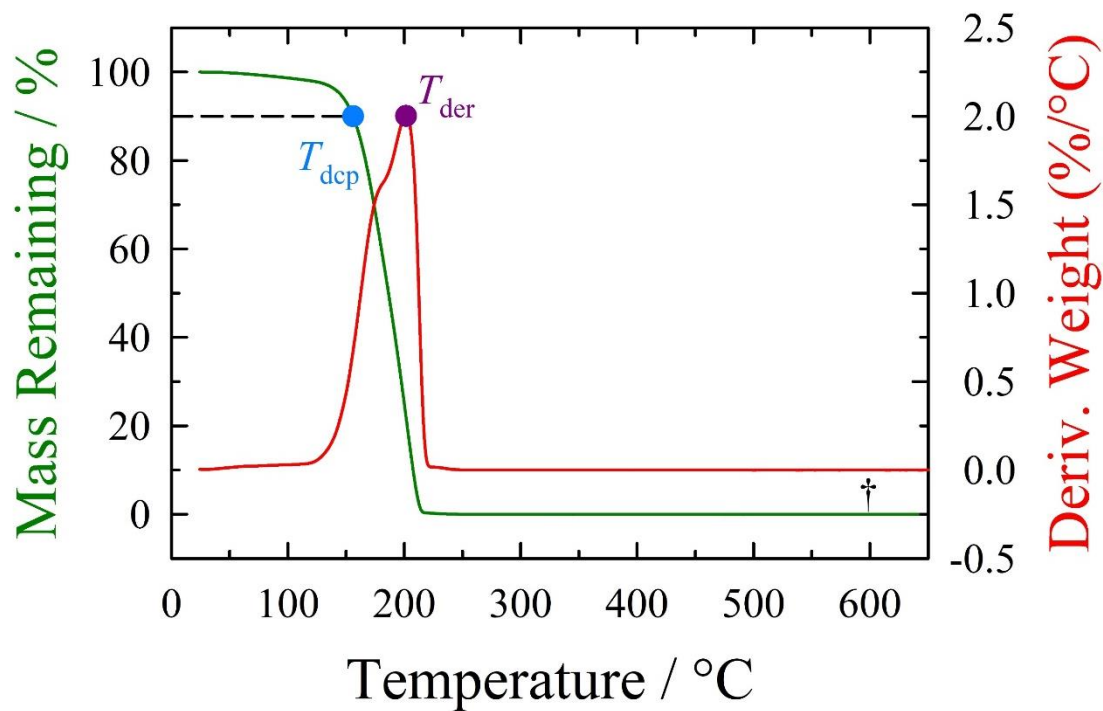
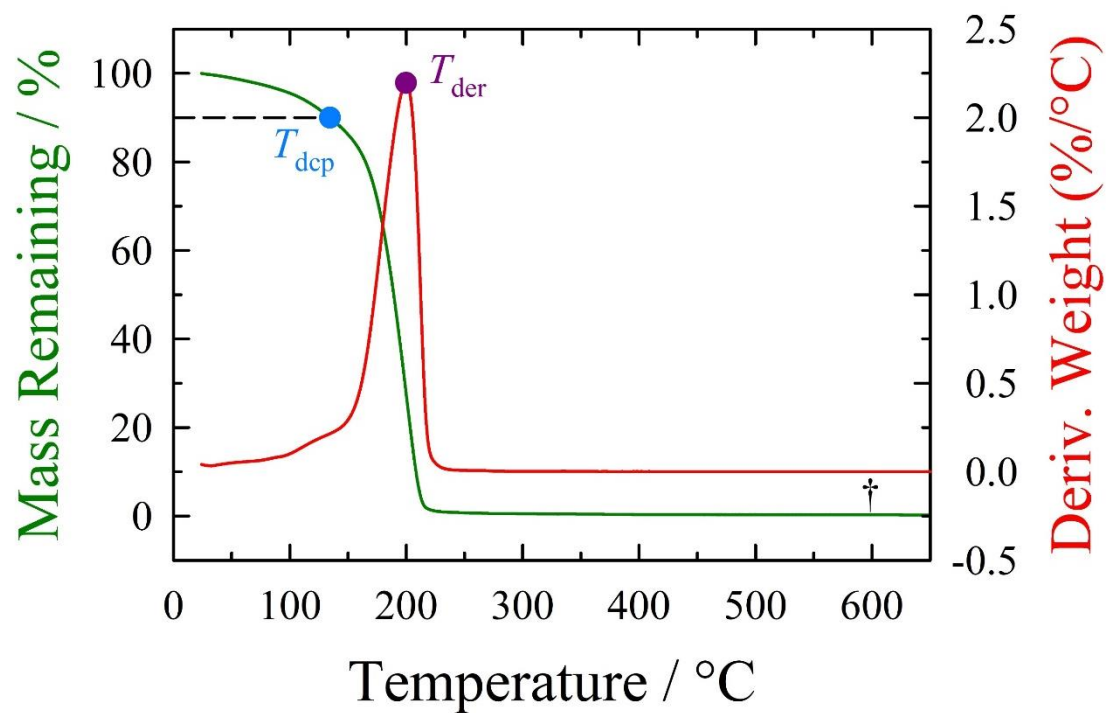
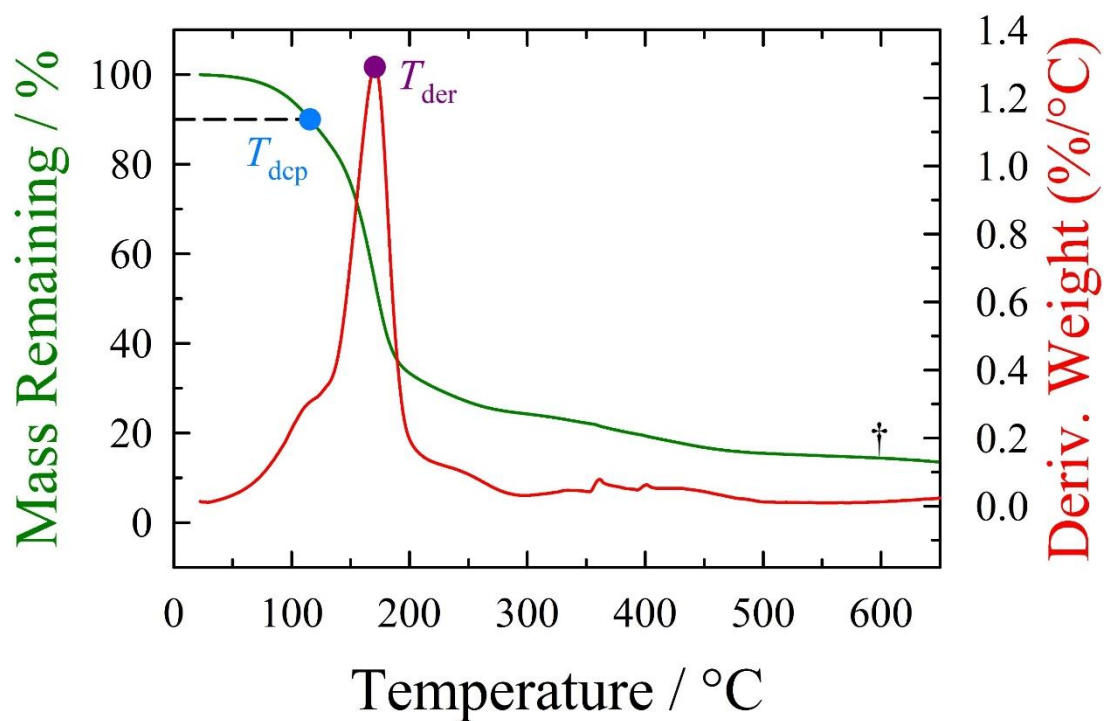


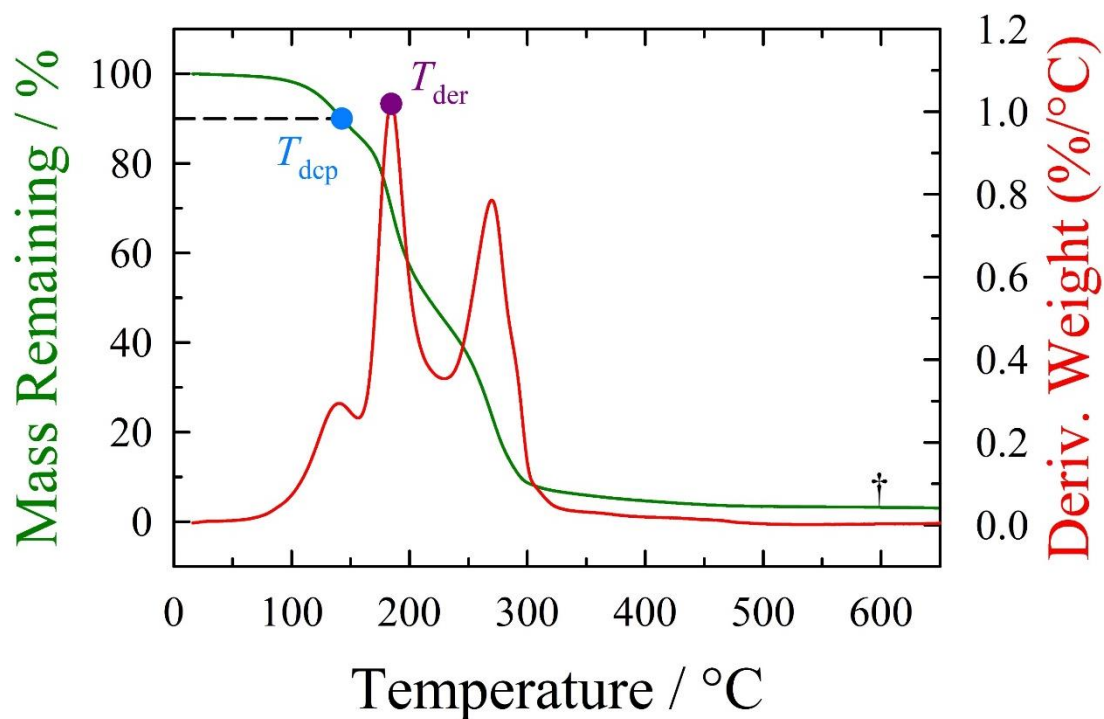
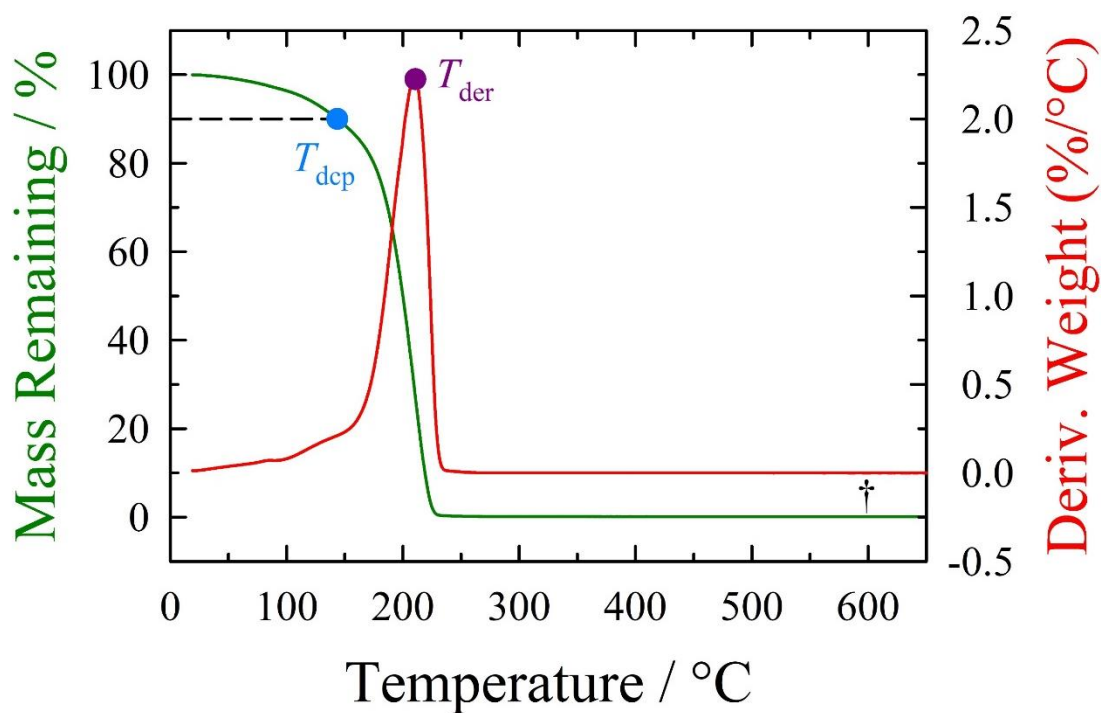
Figure C.17: Thermogravimetric analysis of IL A04.



**Figure C.18:** Thermogravimetric analysis of IL A05.**Figure C.19:** Thermogravimetric analysis of IL A06.

**Figure C.20:** Thermogravimetric analysis of IL A07.**Figure C.21:** Thermogravimetric analysis of IL A08.



**Figure C.22:** Thermogravimetric analysis of IL A10.**Figure C.23:** Thermogravimetric analysis of IL A11.



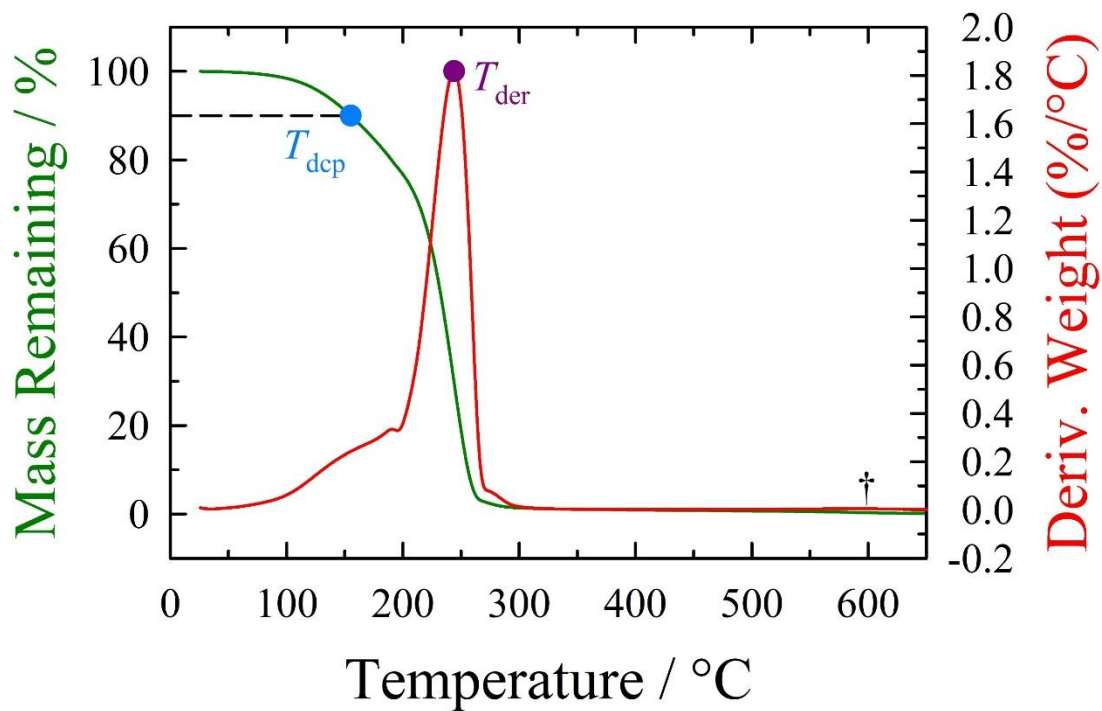
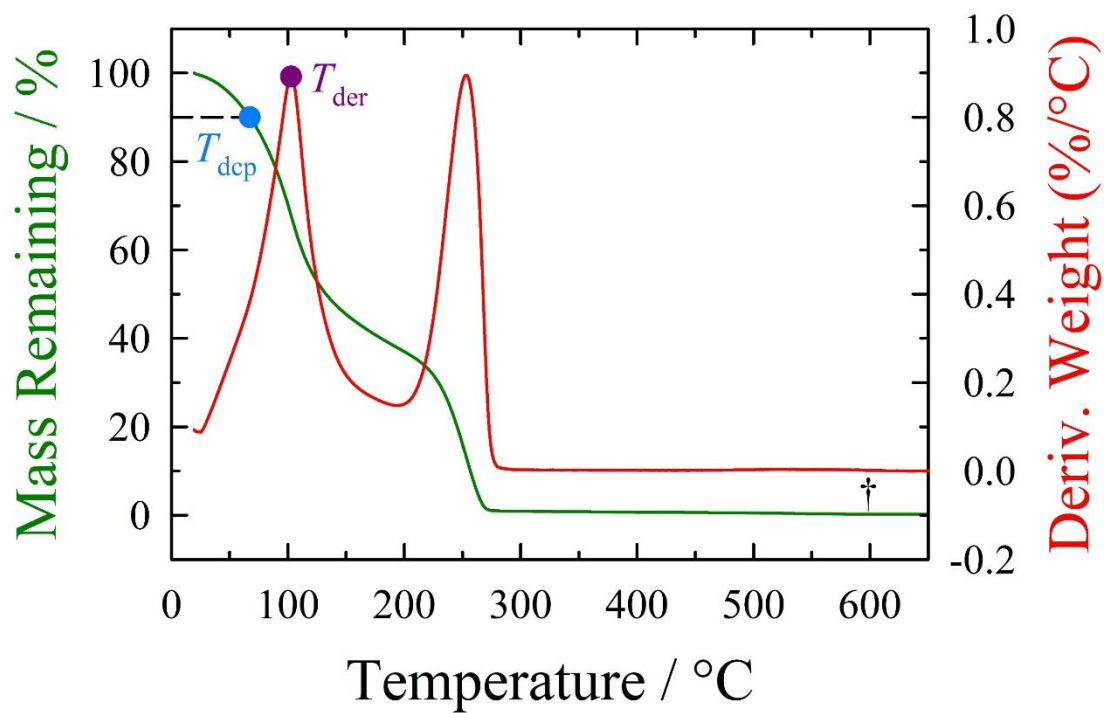
**Figure C.24:** Thermogravimetric analysis of IL A12.**Figure C.25:** Thermogravimetric analysis of IL A13.

Figure C.26: Thermogravimetric analysis of IL A14.

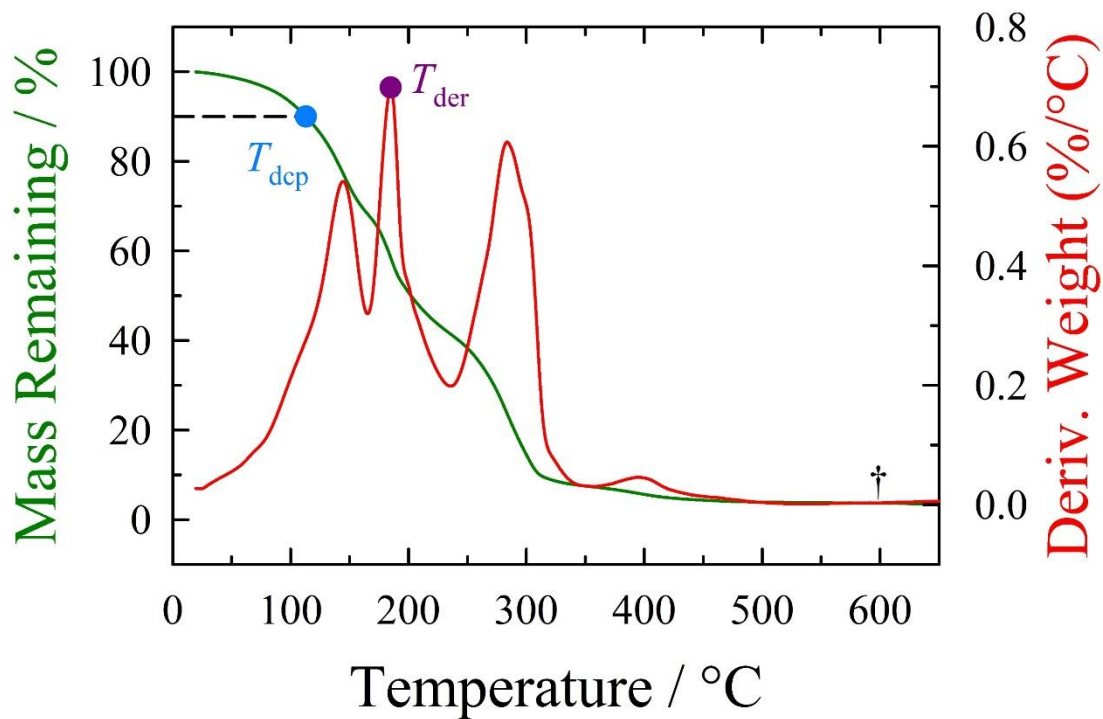
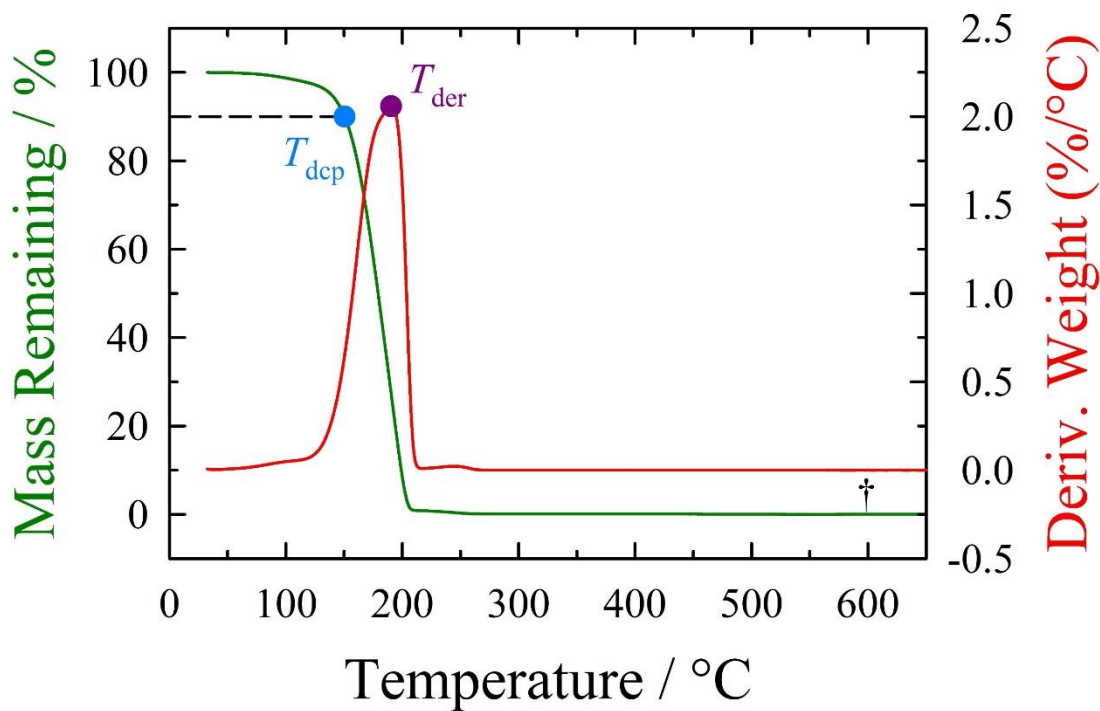
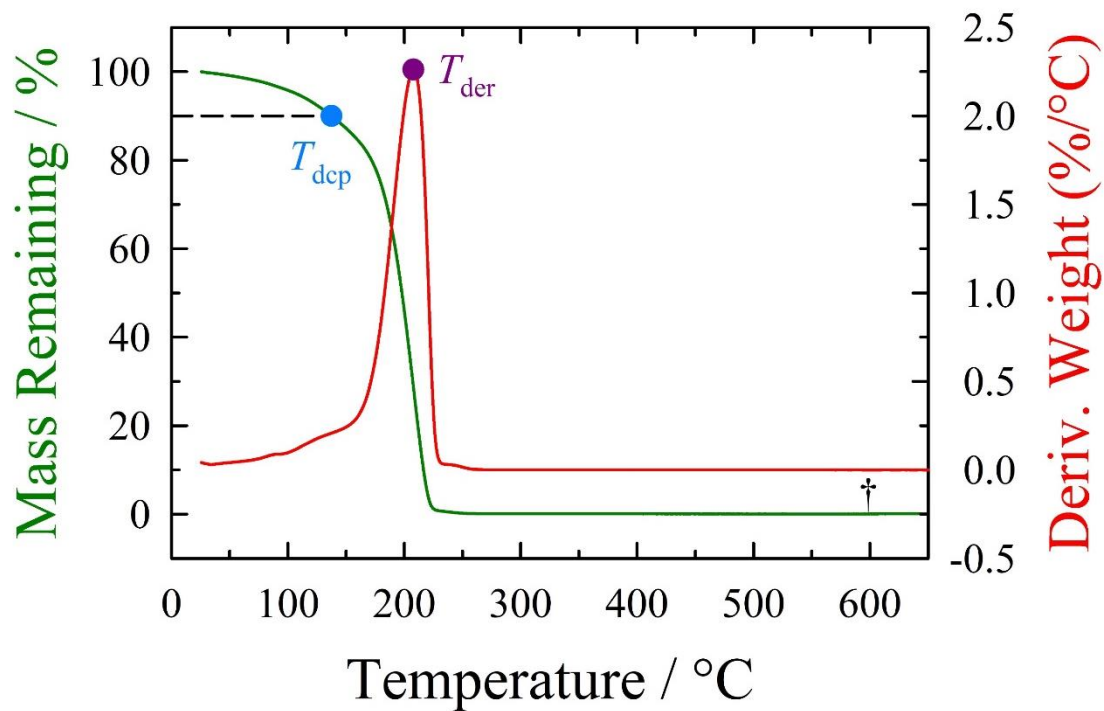
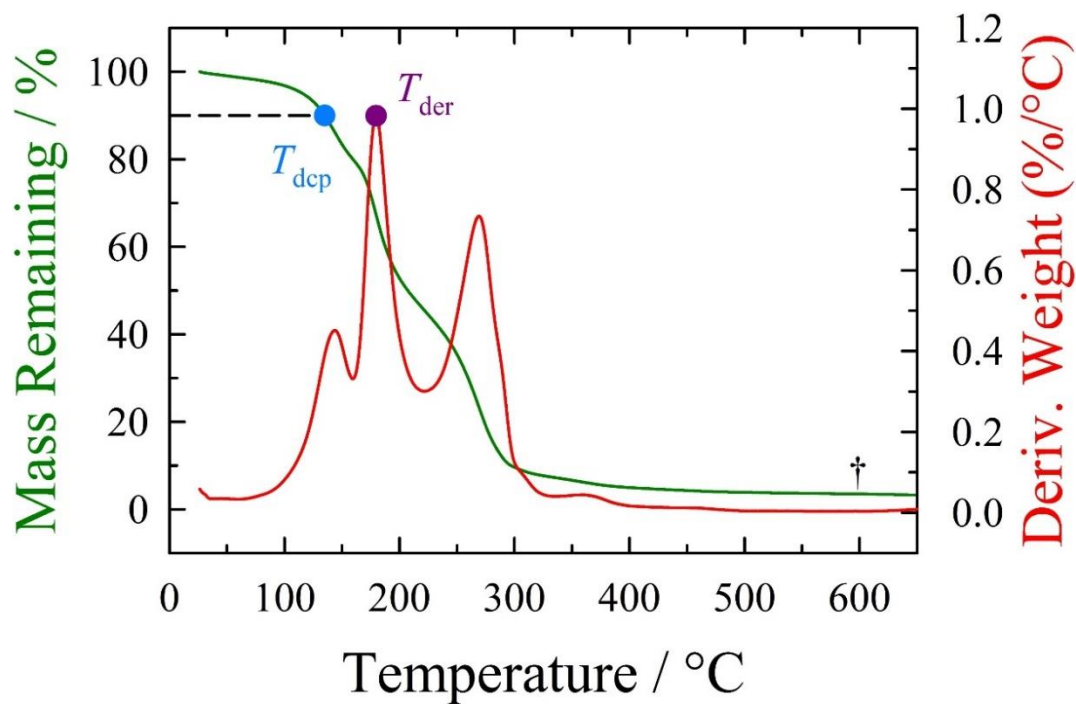
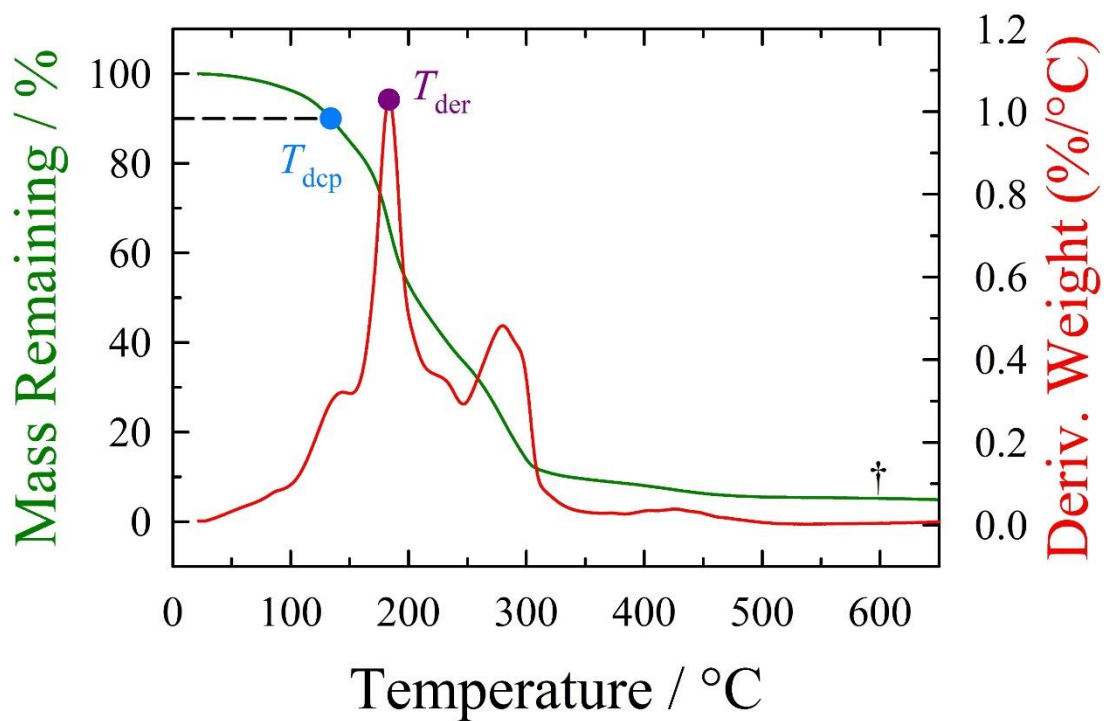
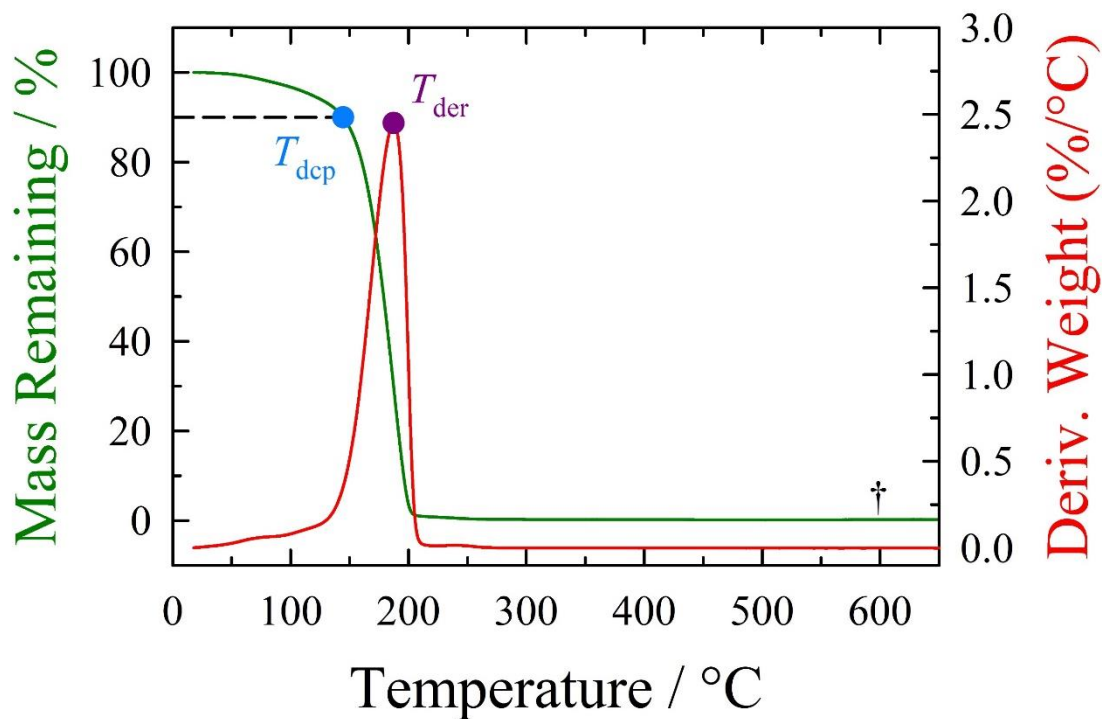


Figure C.27: Thermogravimetric analysis of IL A15.



**Figure C.28:** Thermogravimetric analysis of IL A16.**Figure C.29:** Thermogravimetric analysis of IL A17.

**Figure C.30:** Thermogravimetric analysis of IL A18.**Figure C.31:** Thermogravimetric analysis of IL A19.

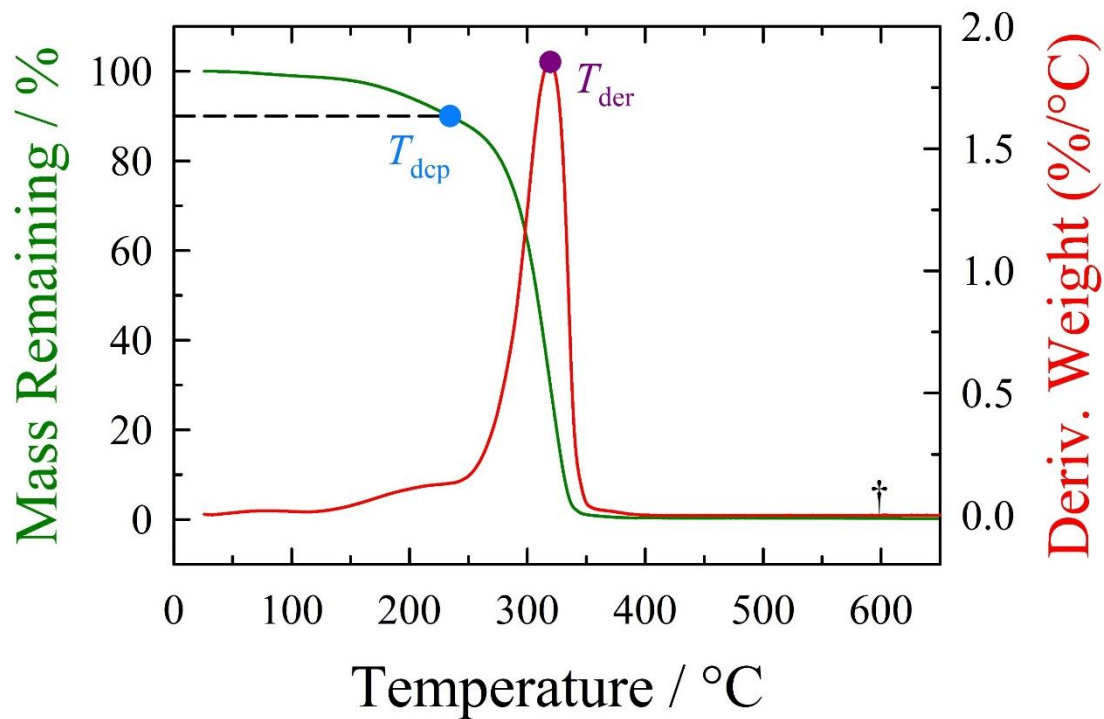
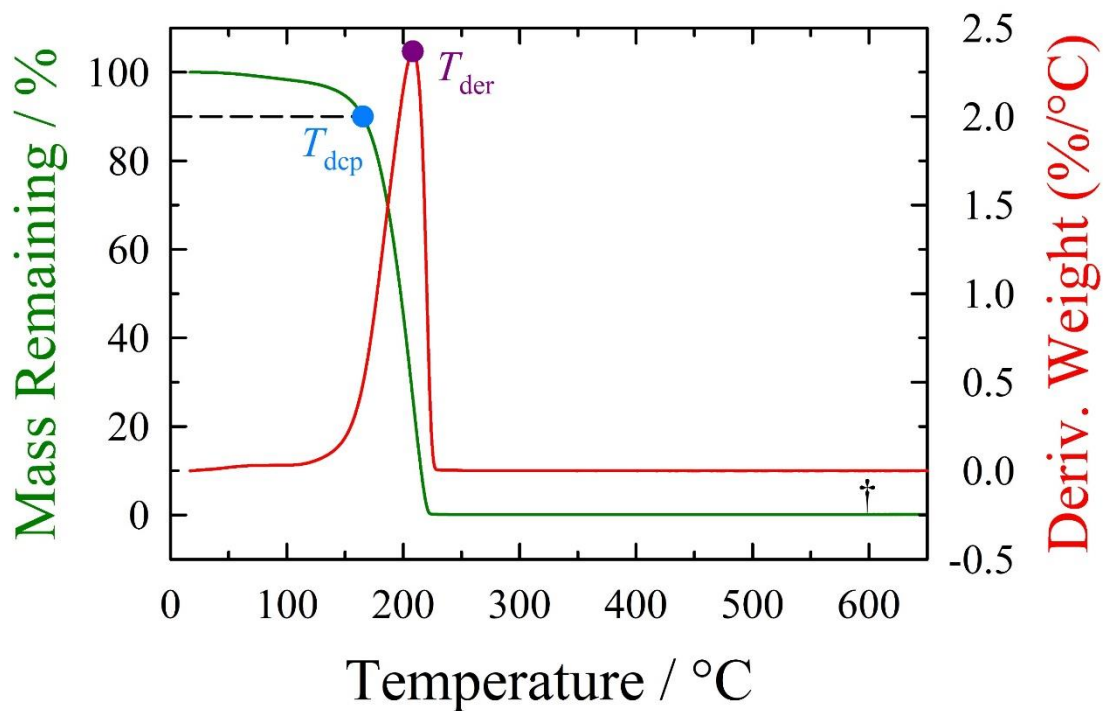
**Figure C.32:** Thermogravimetric analysis of IL A21.**Figure C.33:** Thermogravimetric analysis of IL A23.

Figure C.34: Thermogravimetric analysis of IL A25.

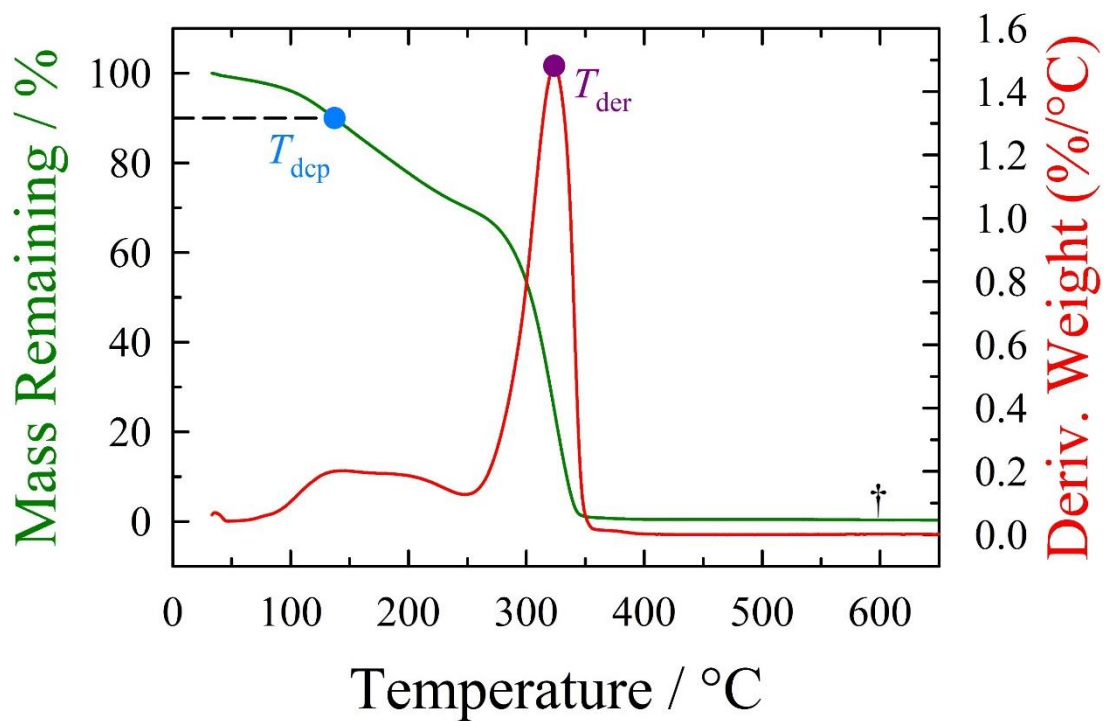
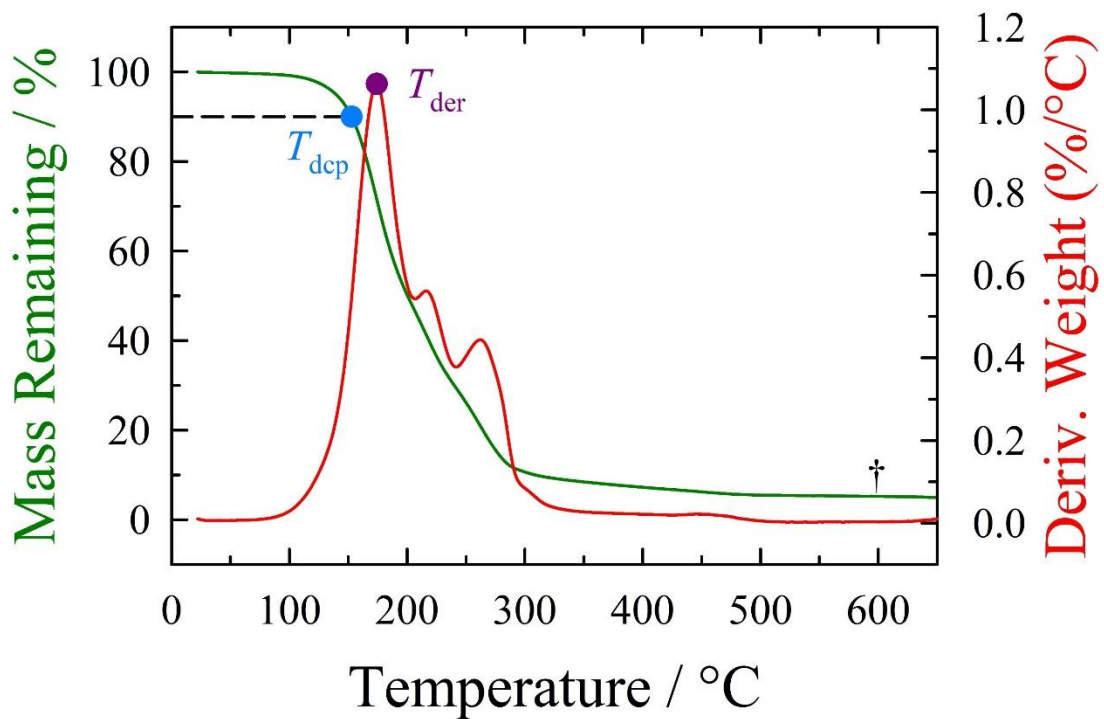
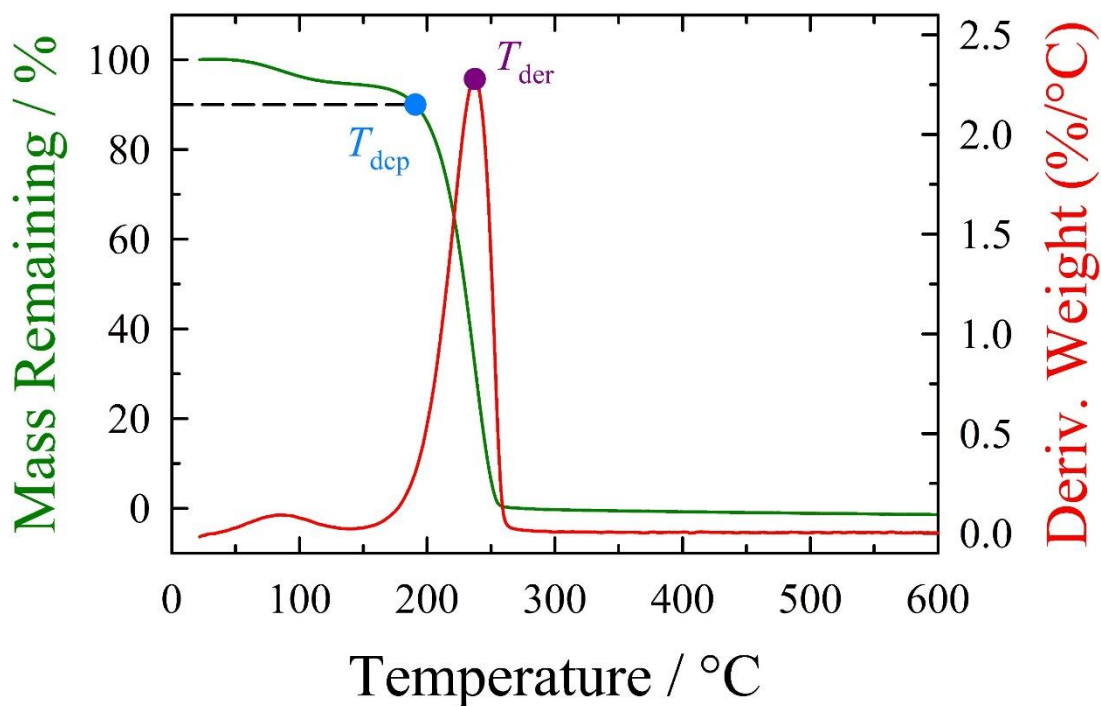
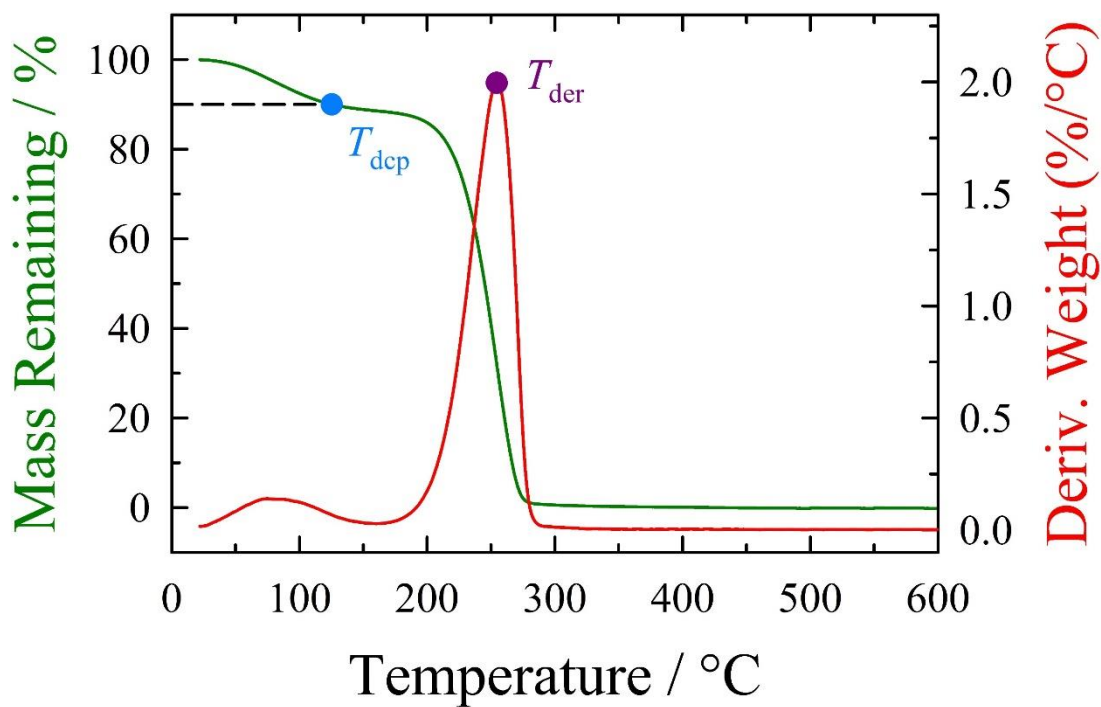


Figure C.35: Thermogravimetric analysis of IL A27.



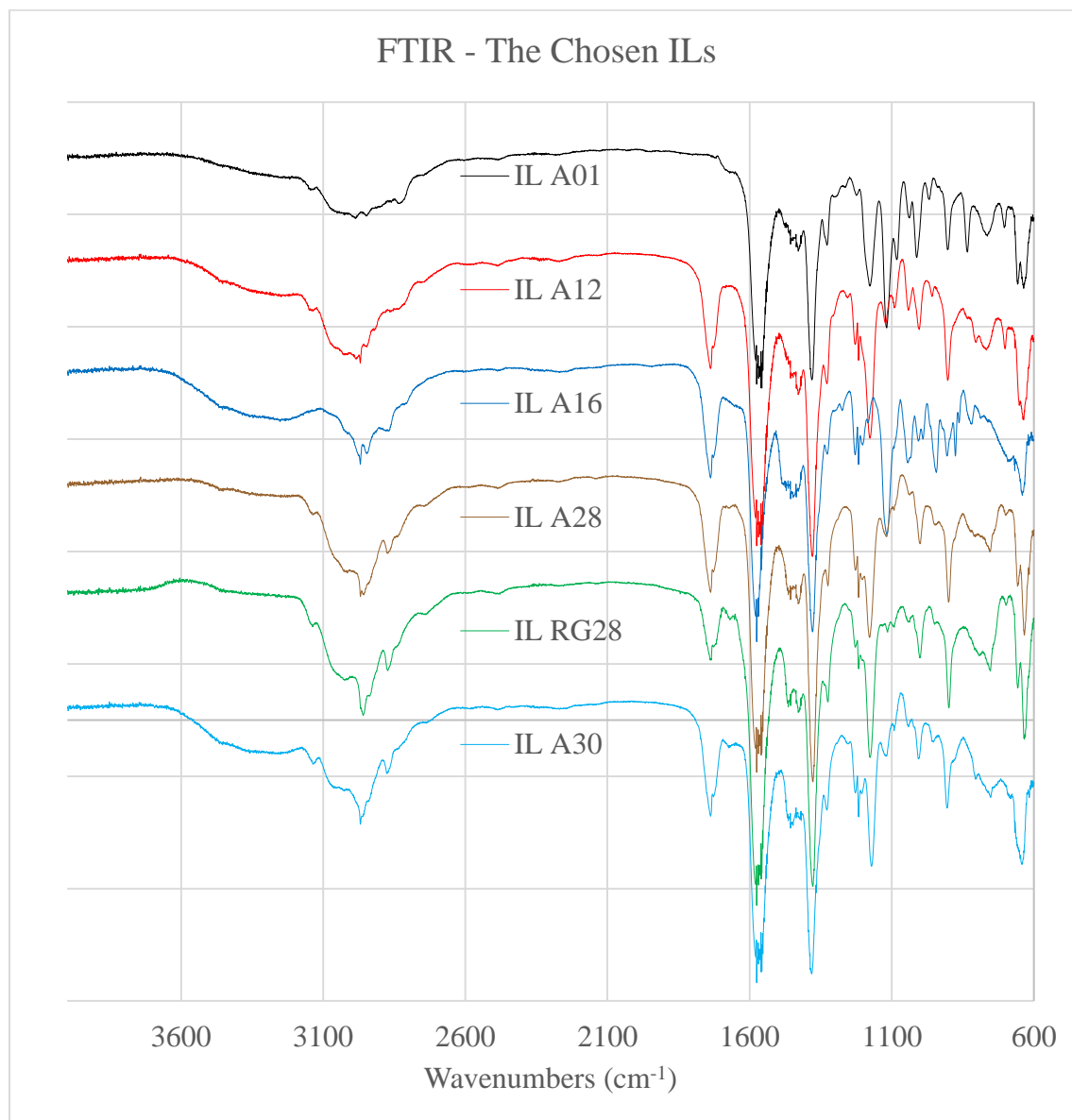


**Figure C.36:** Thermogravimetric analysis of IL A28.**Figure C.37:** Thermogravimetric analysis of IL A30.

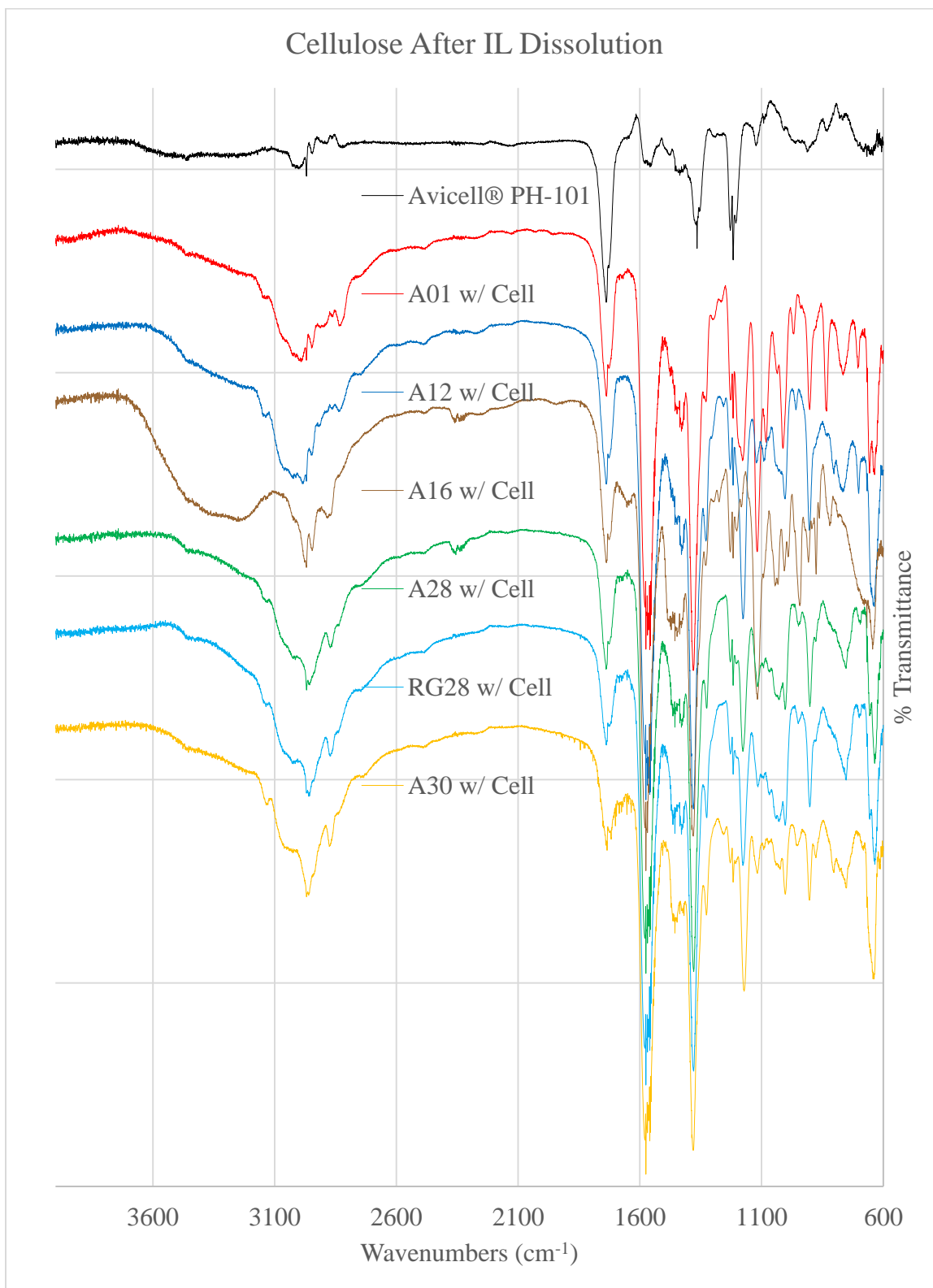
APPENDIX D  
INSTRUMENTAL ANALYSIS  
SPECTRA AND PHOTOS



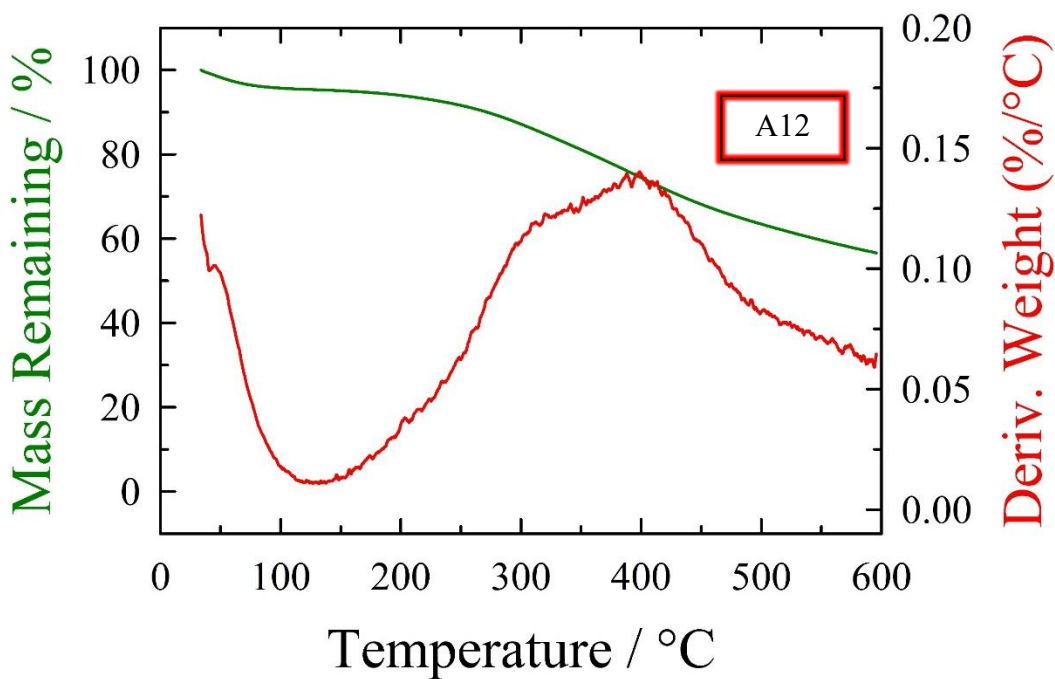
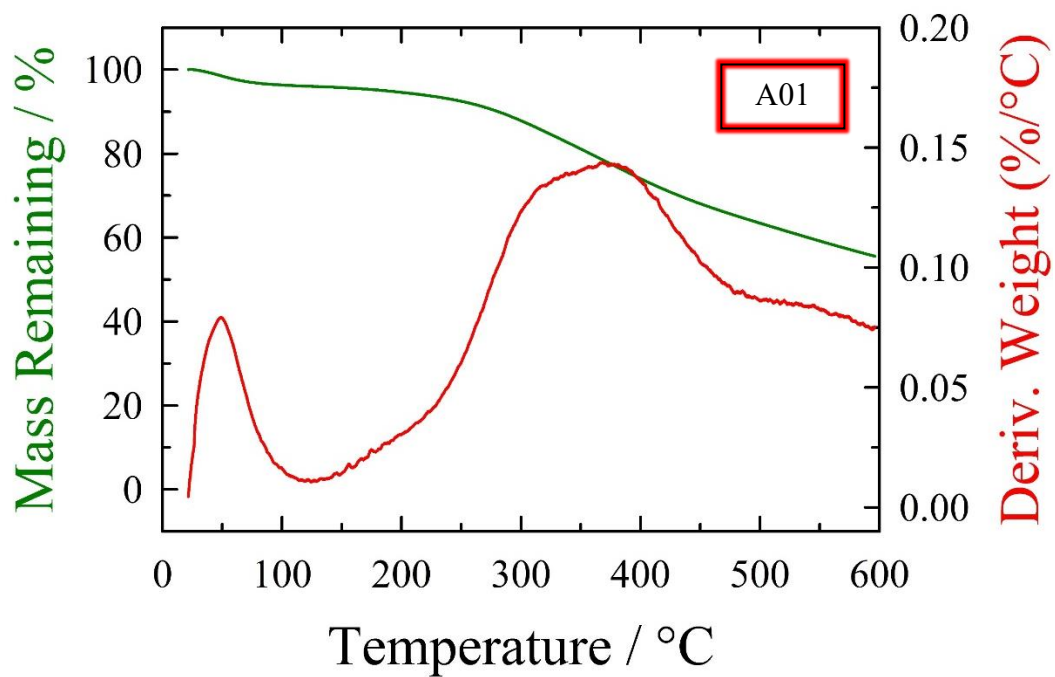
## FTIR Spectra for IL Structure Confirmation

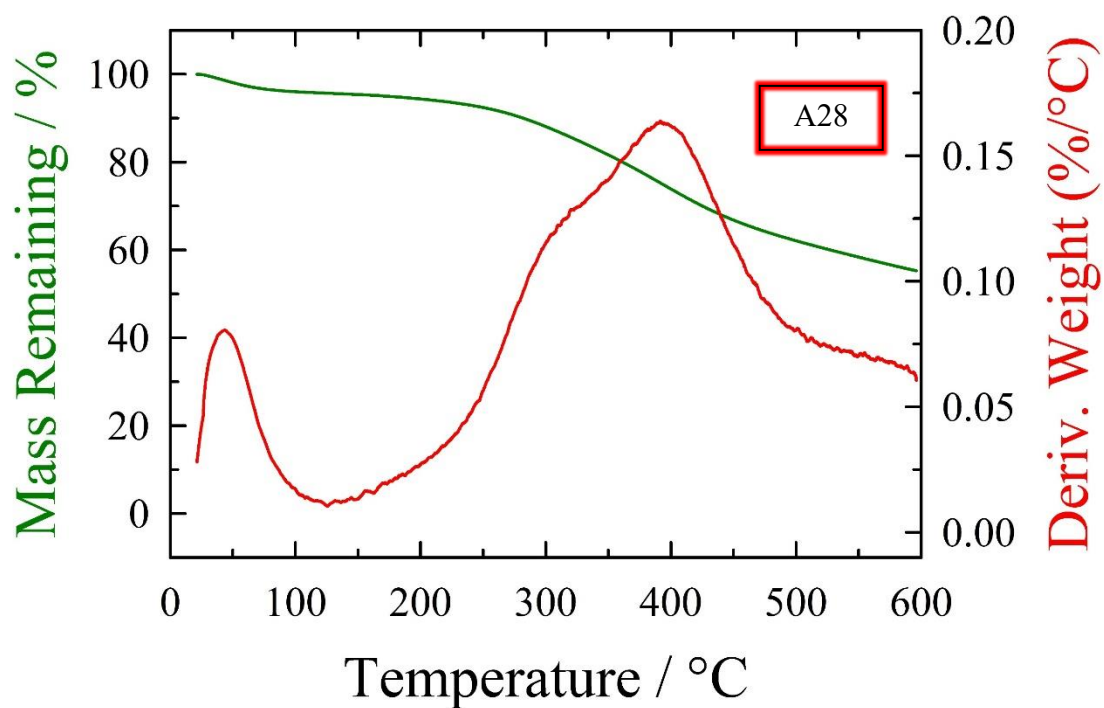
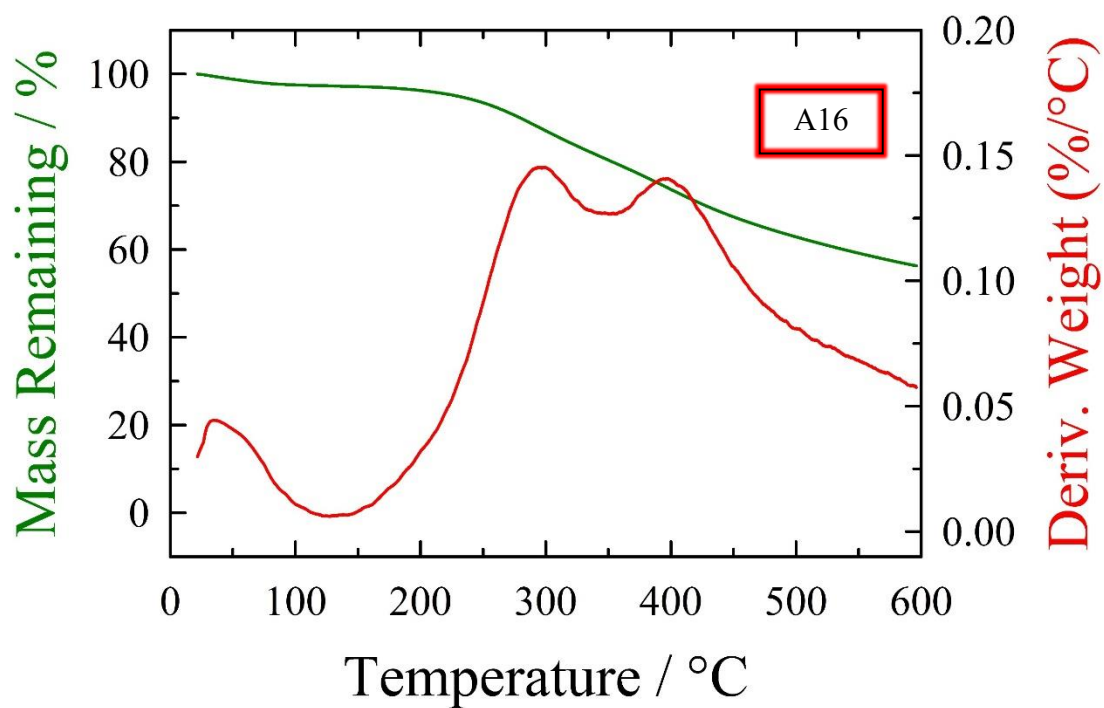


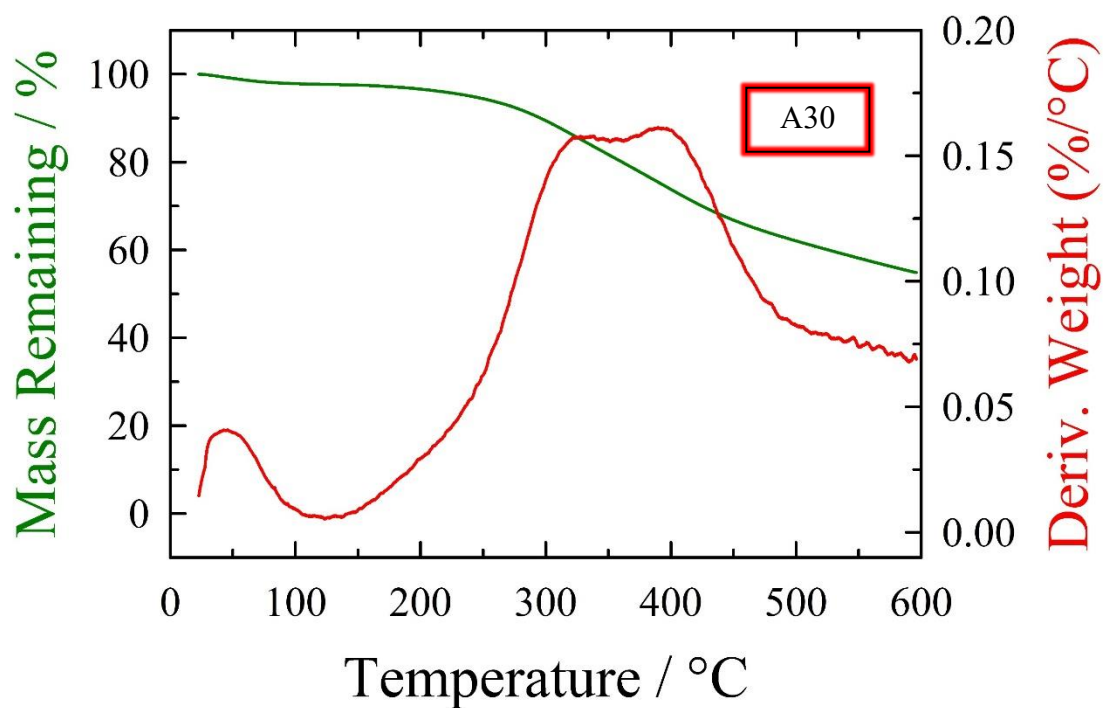
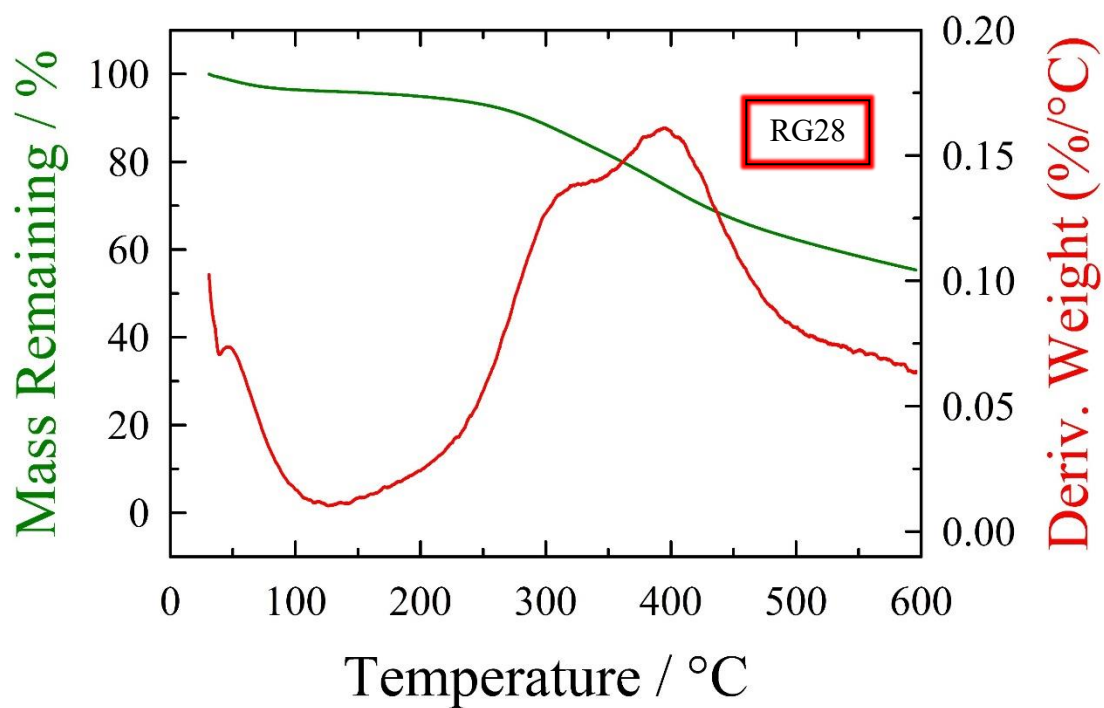
## FTIR Spectra for Cellulose Dissolution

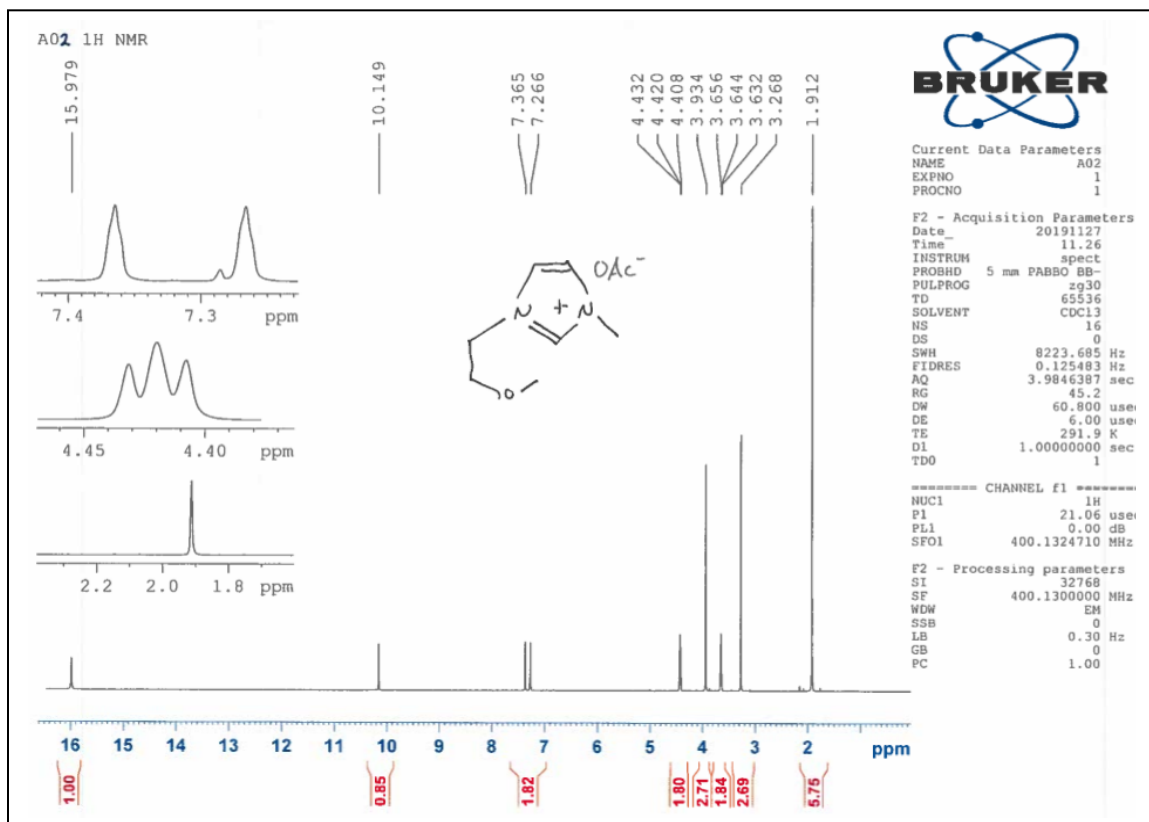
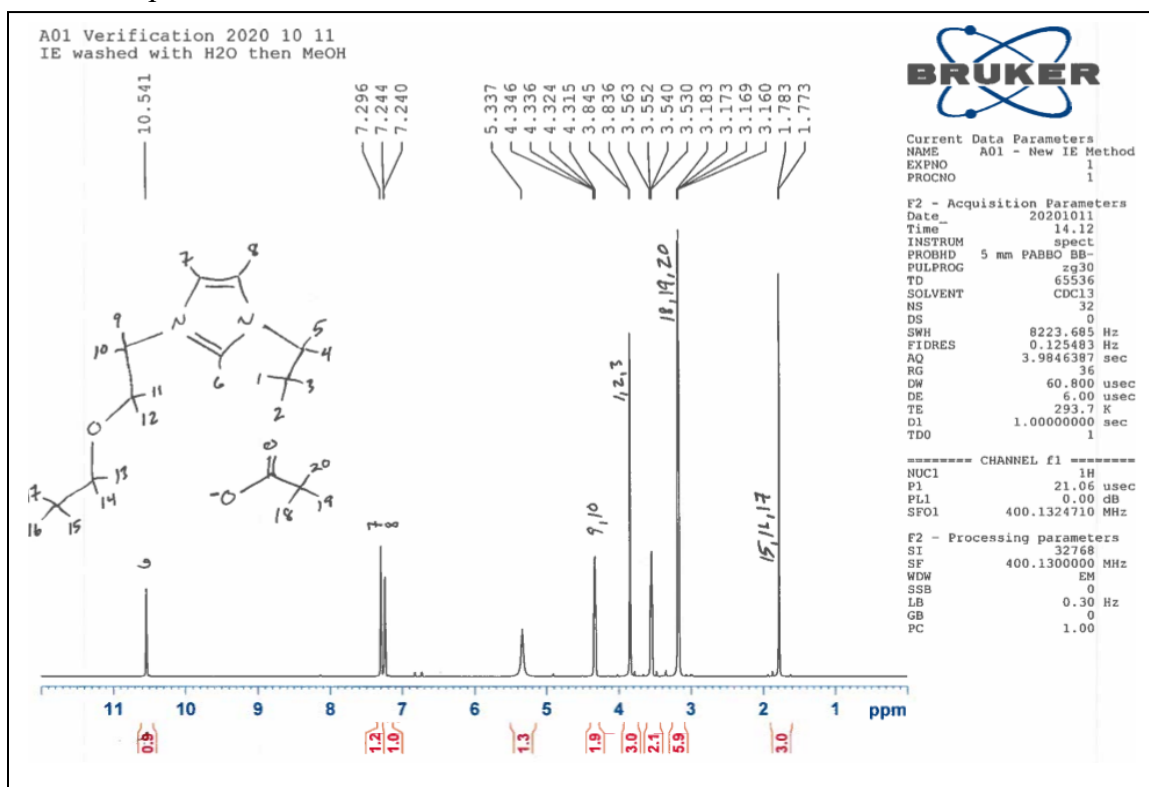


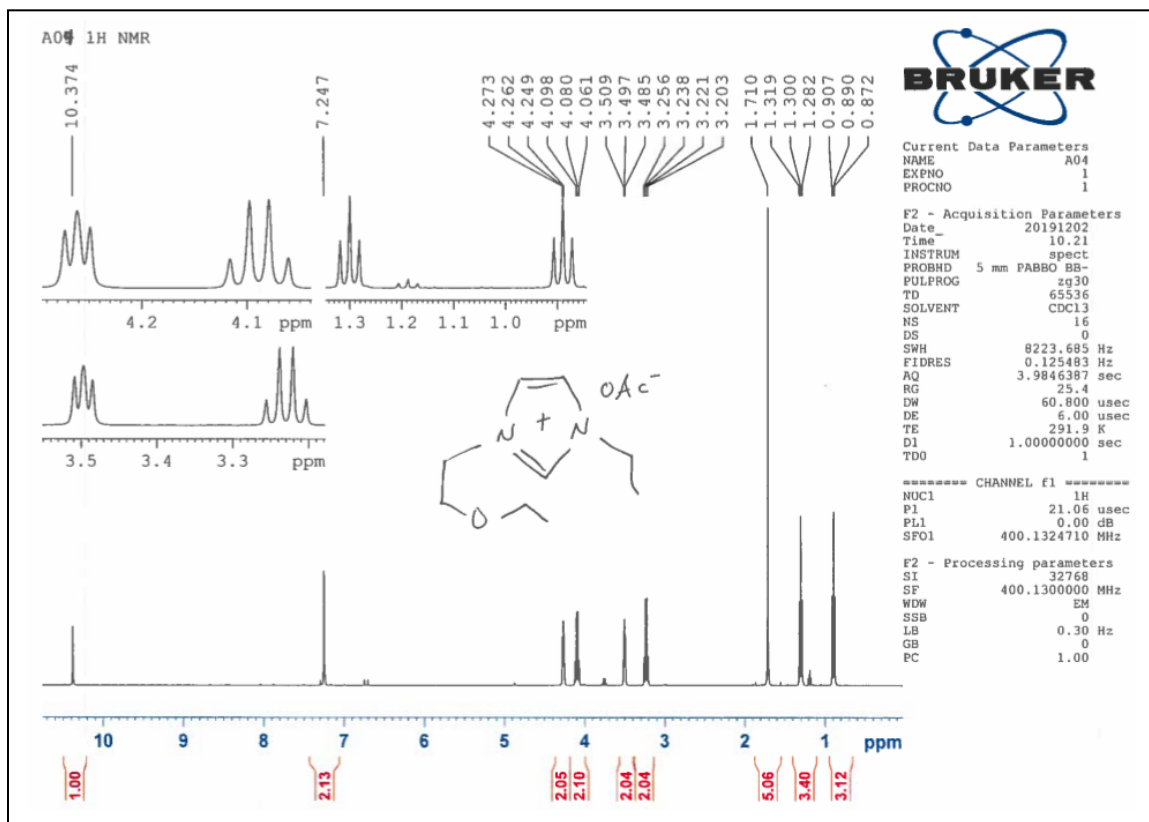
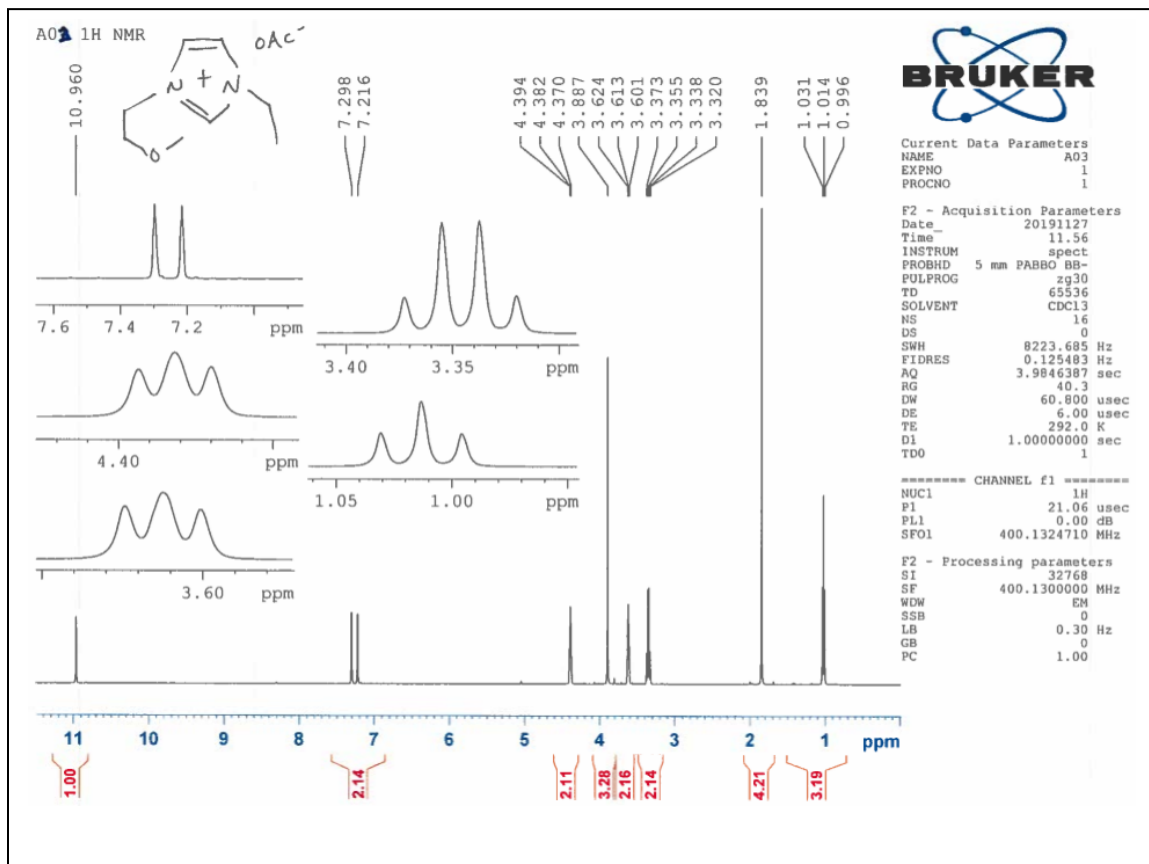
## TGA Scans for Coal Dissolution

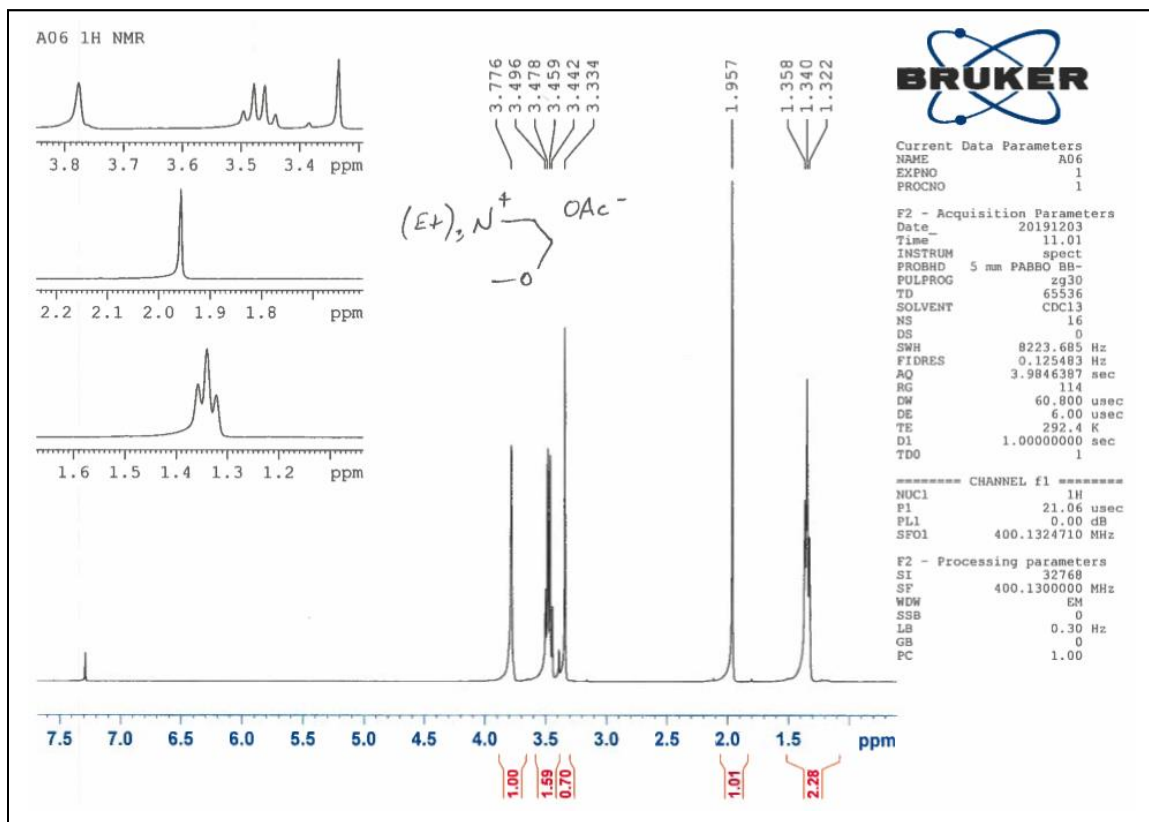
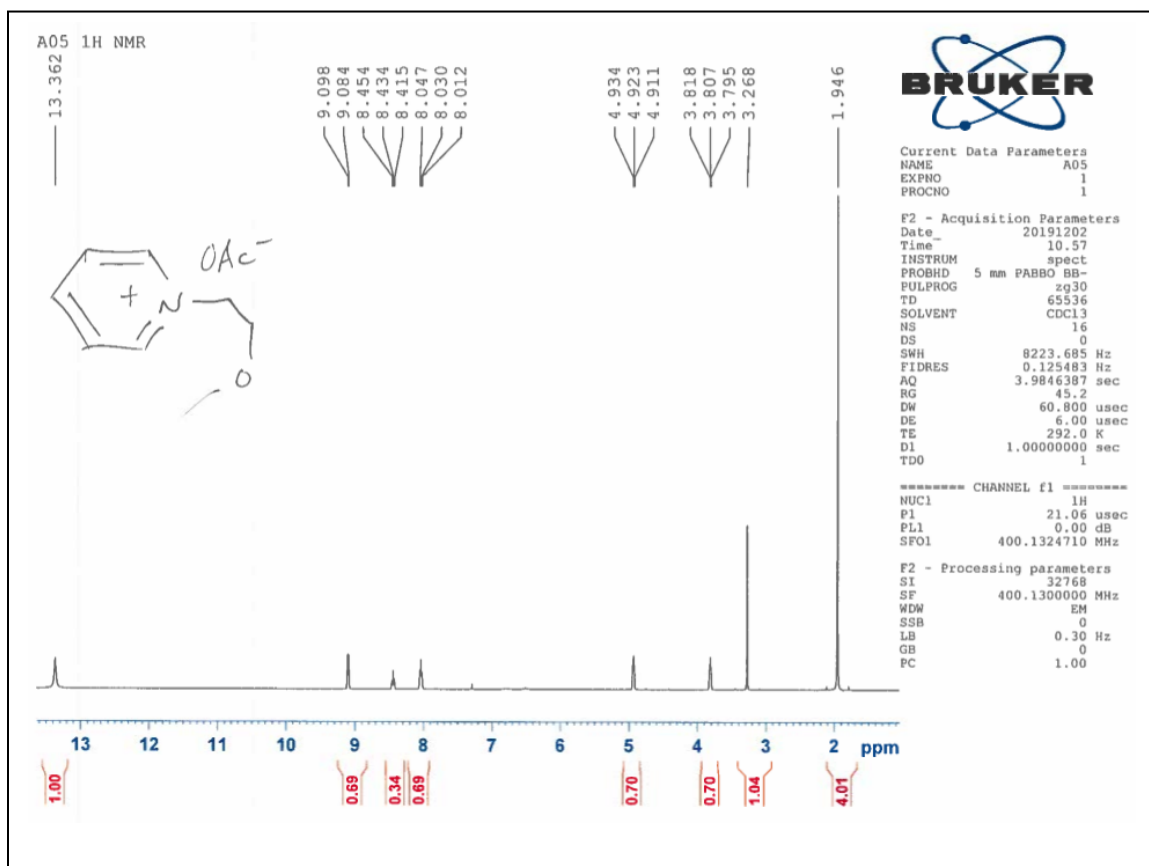




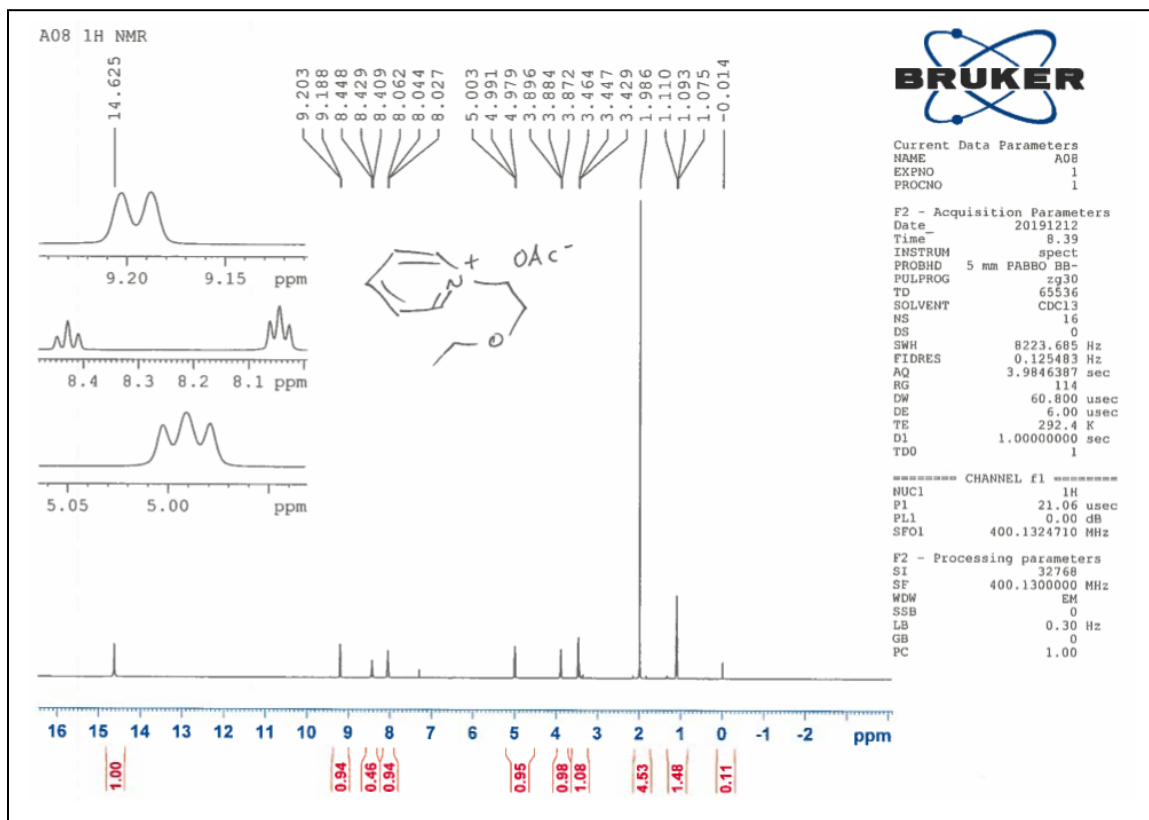
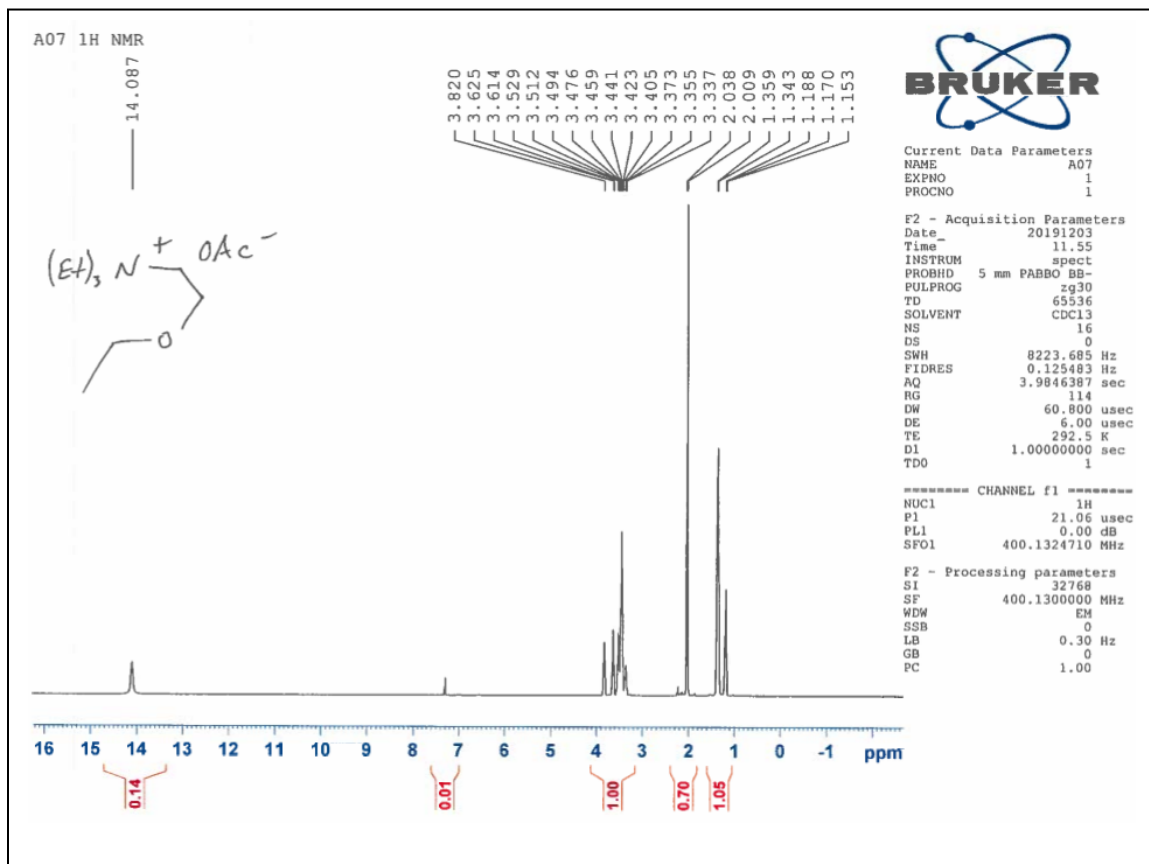


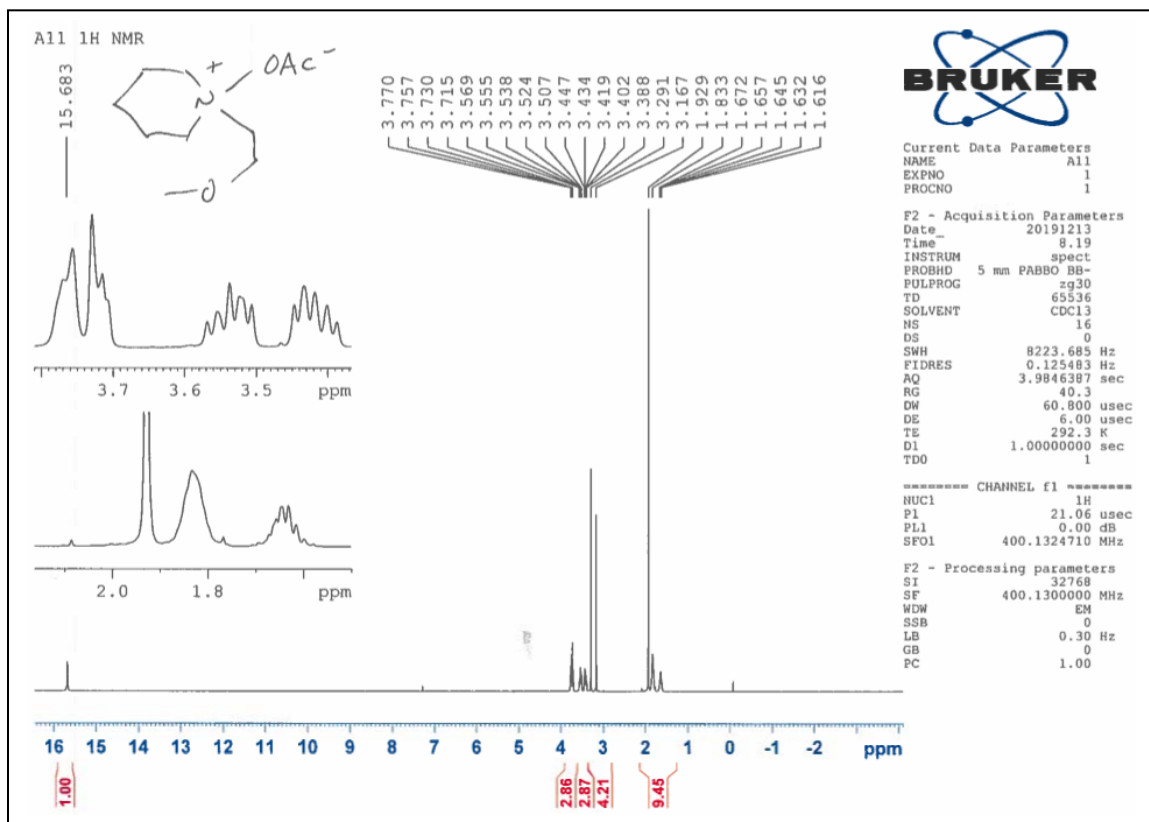
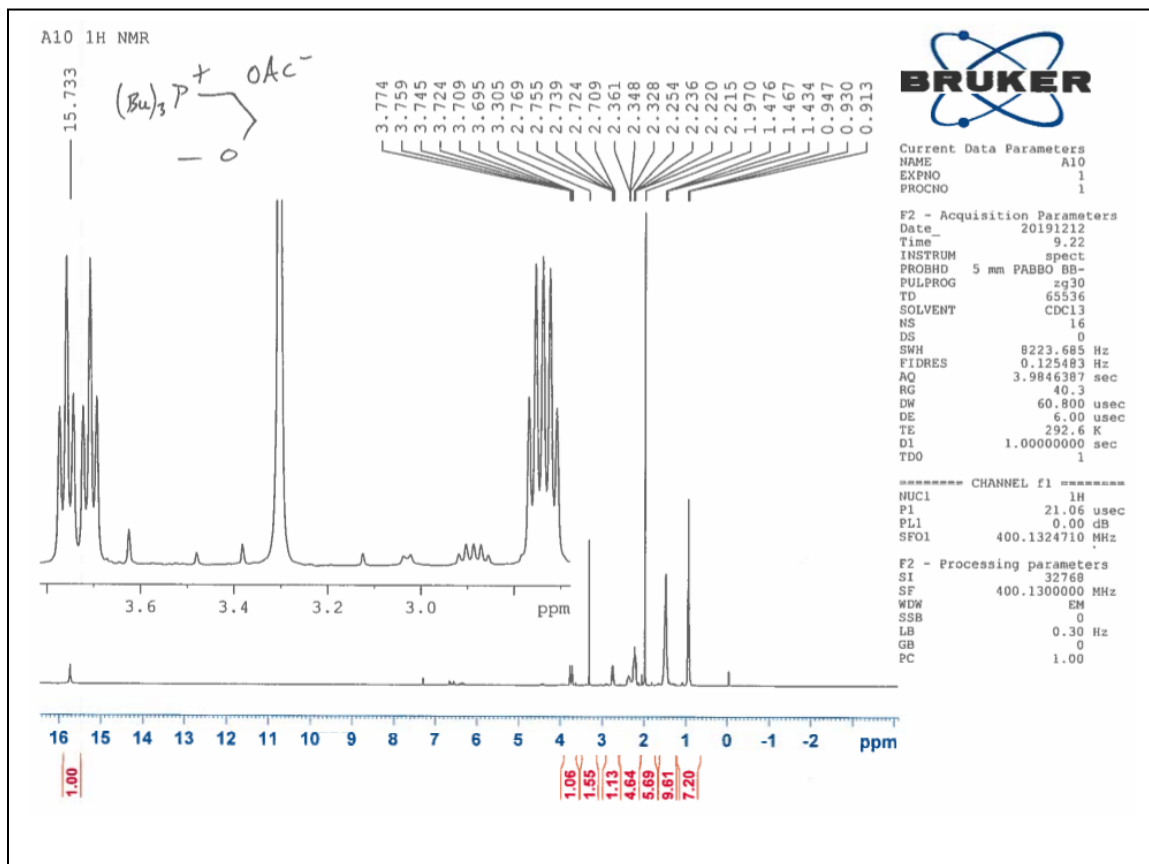
<sup>1</sup>H NMR Spectra for IL Structure Confirmation

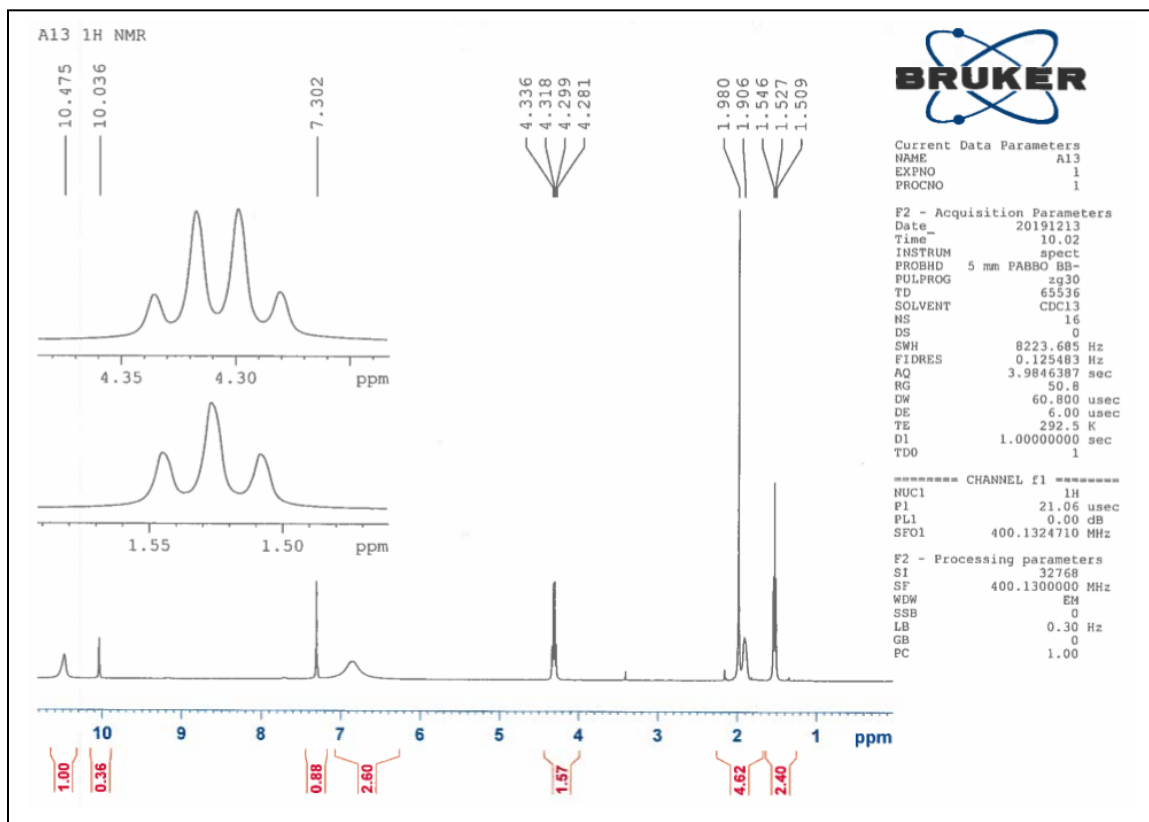
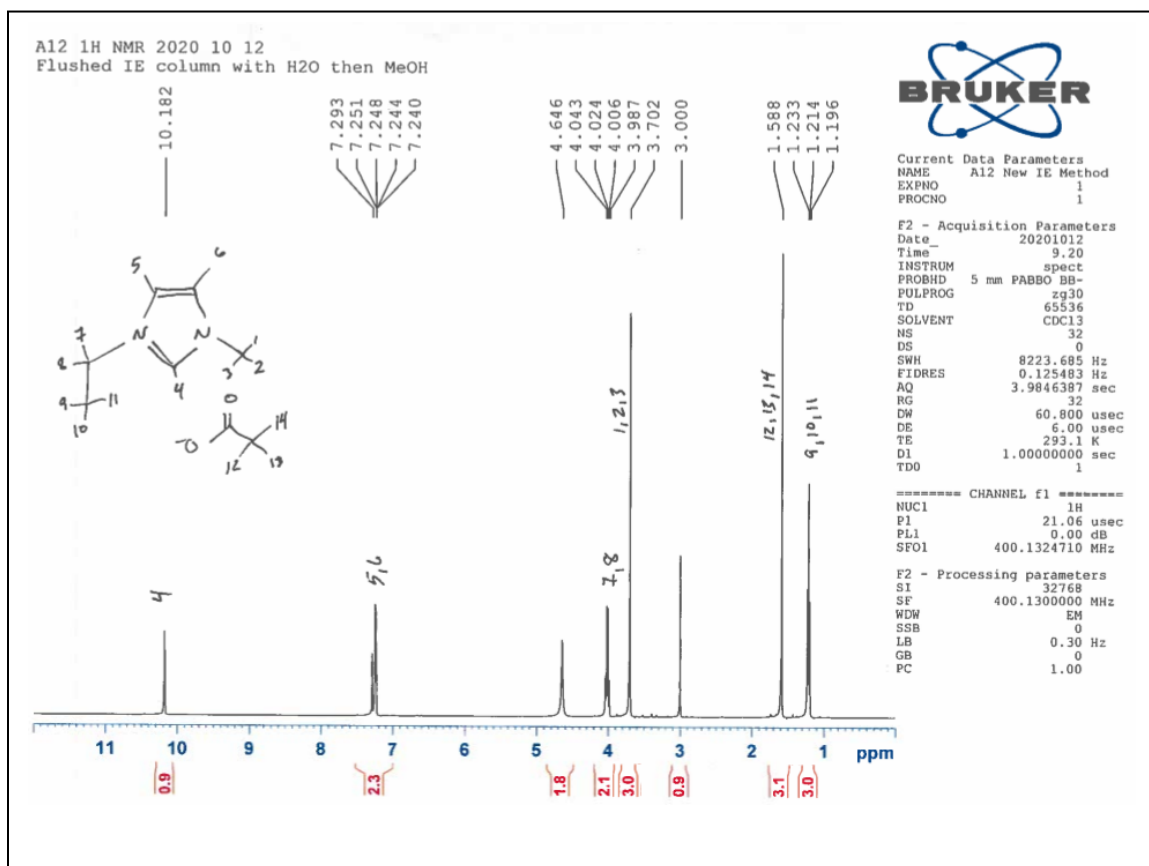


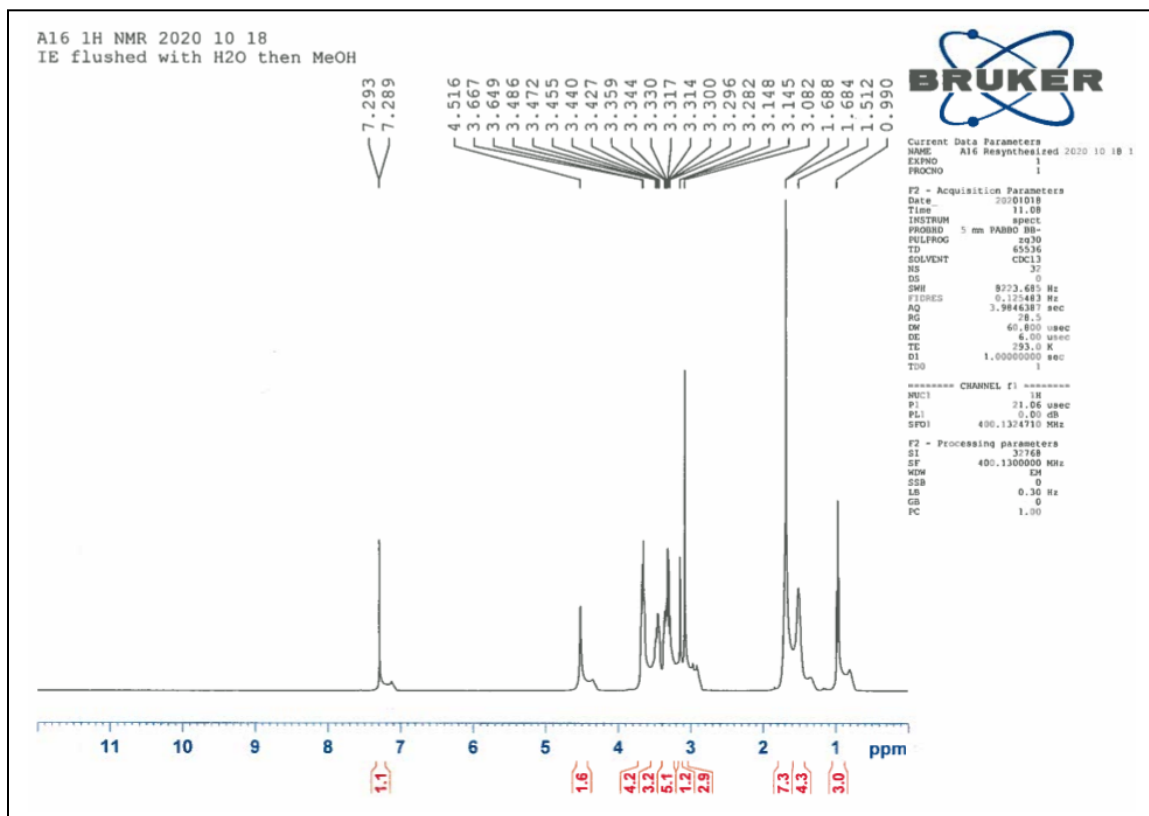
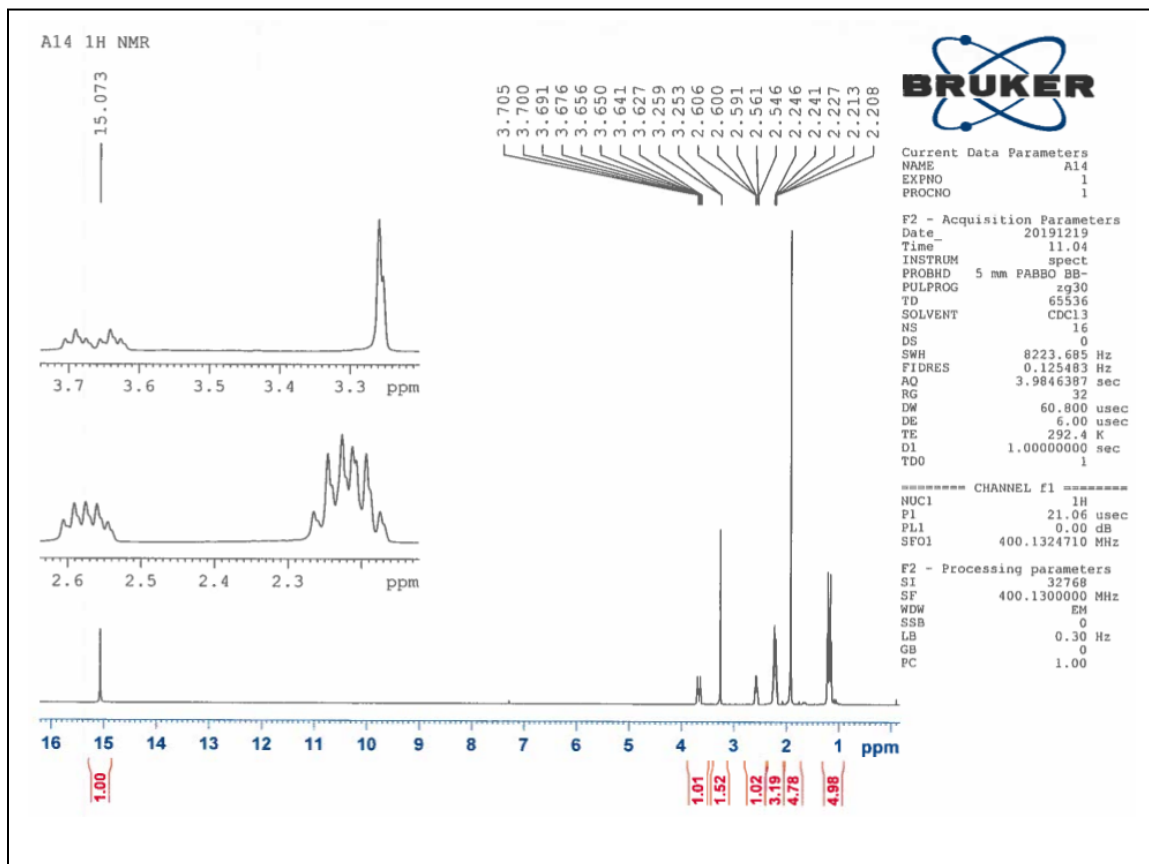


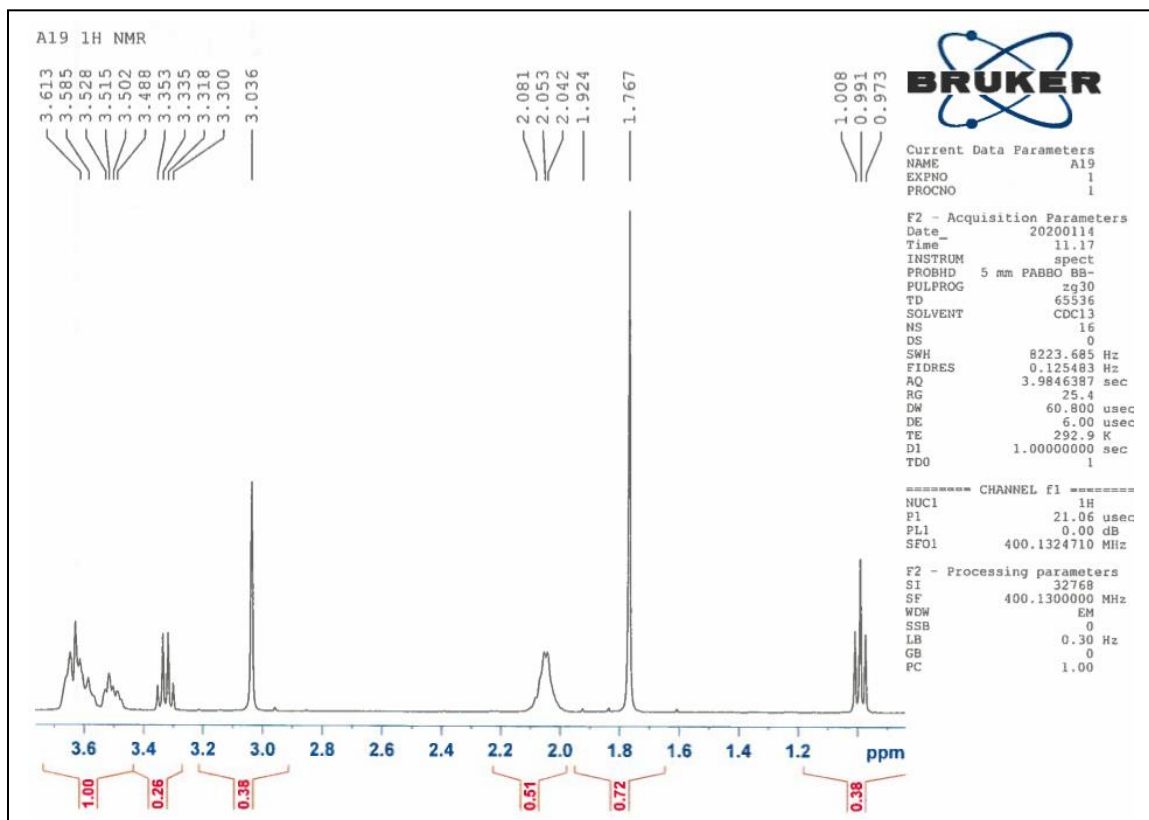
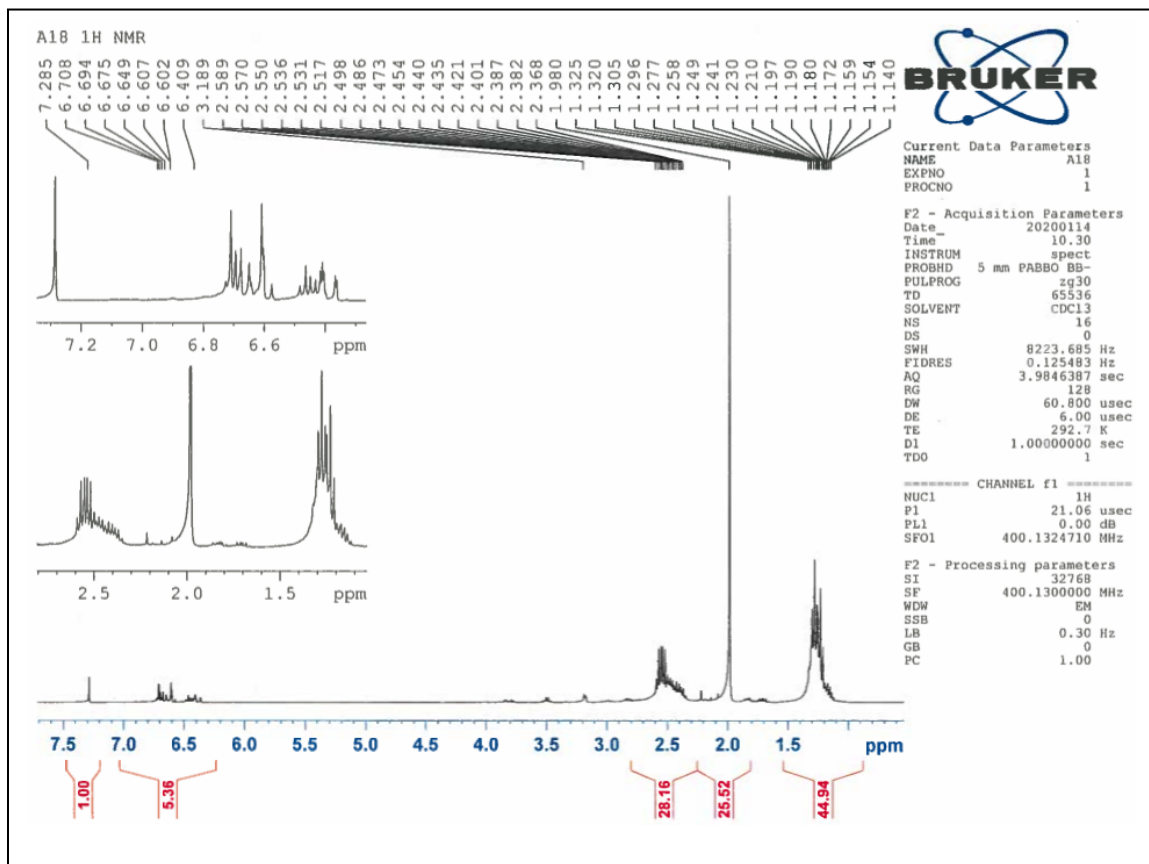


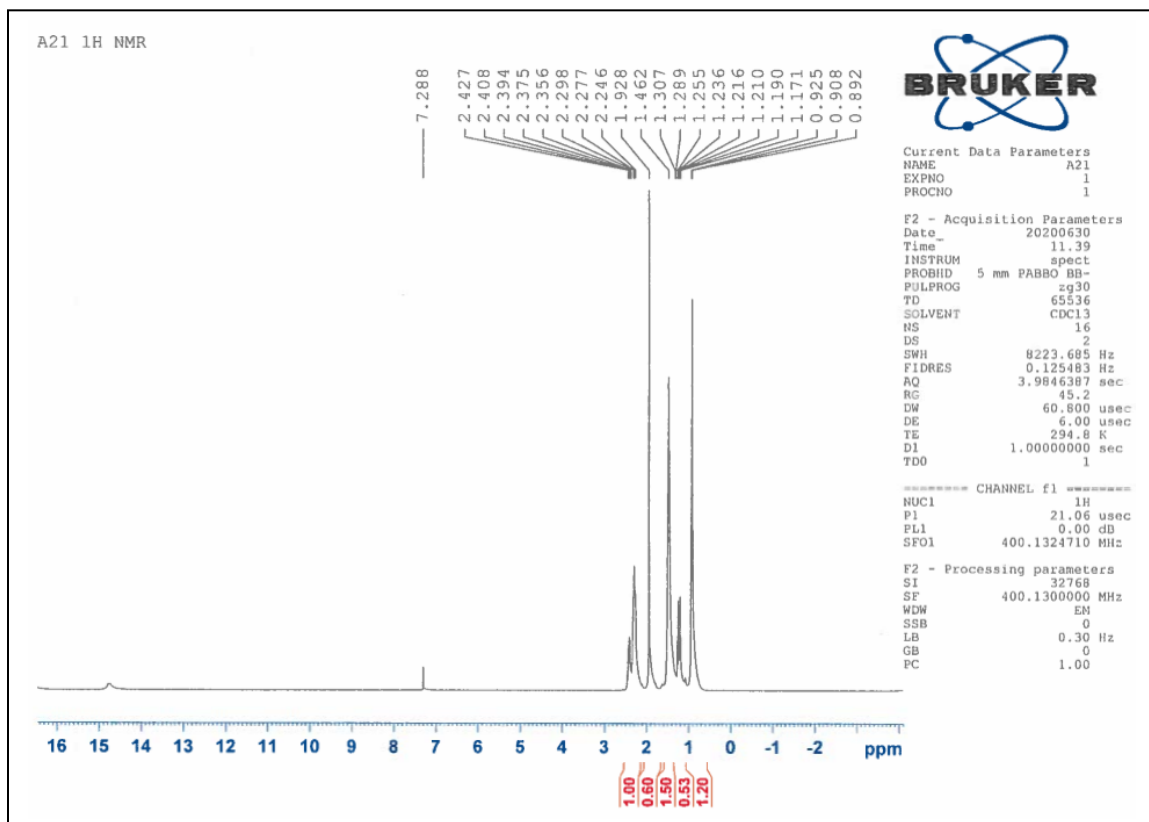
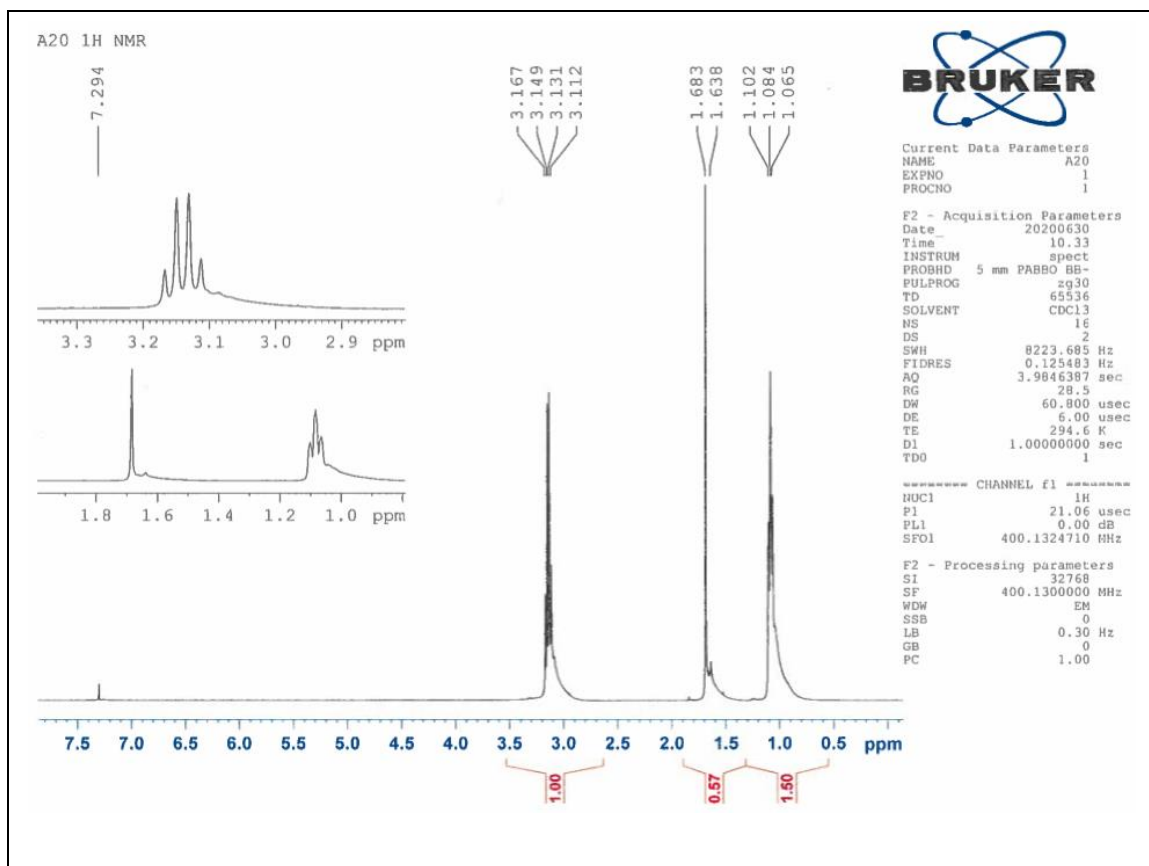


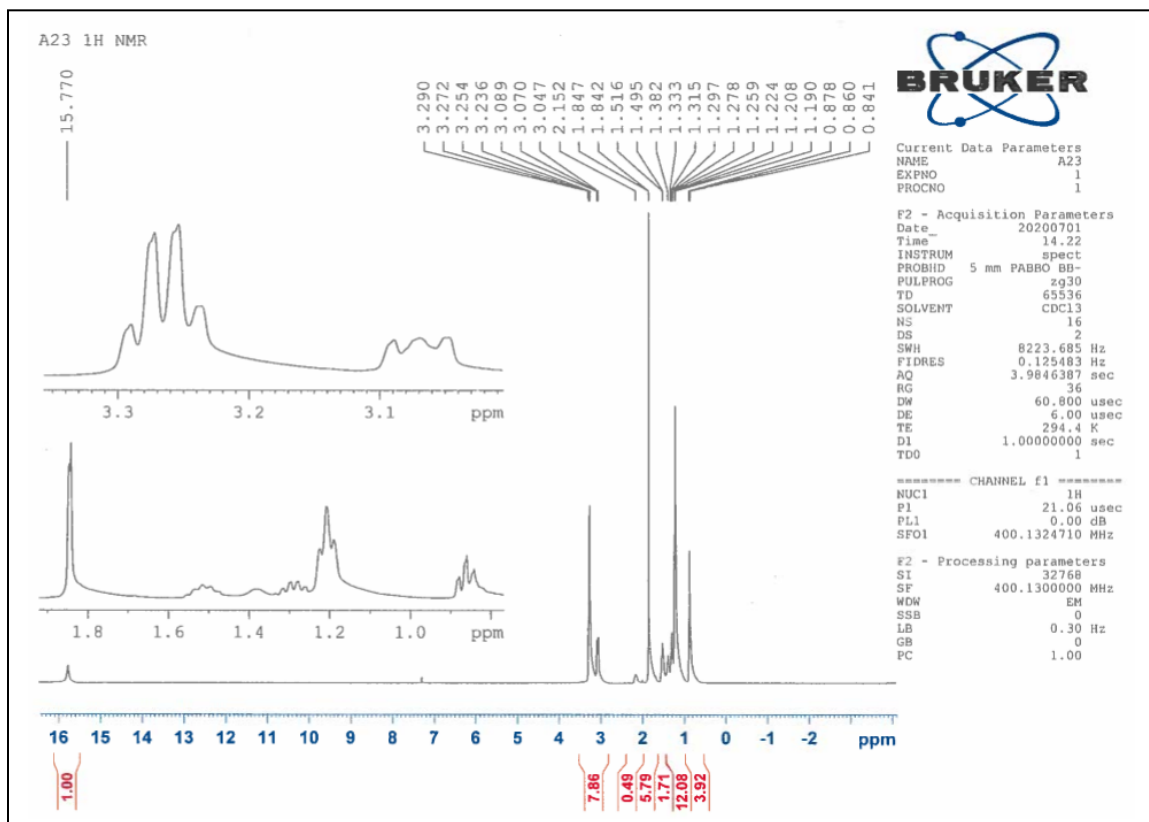
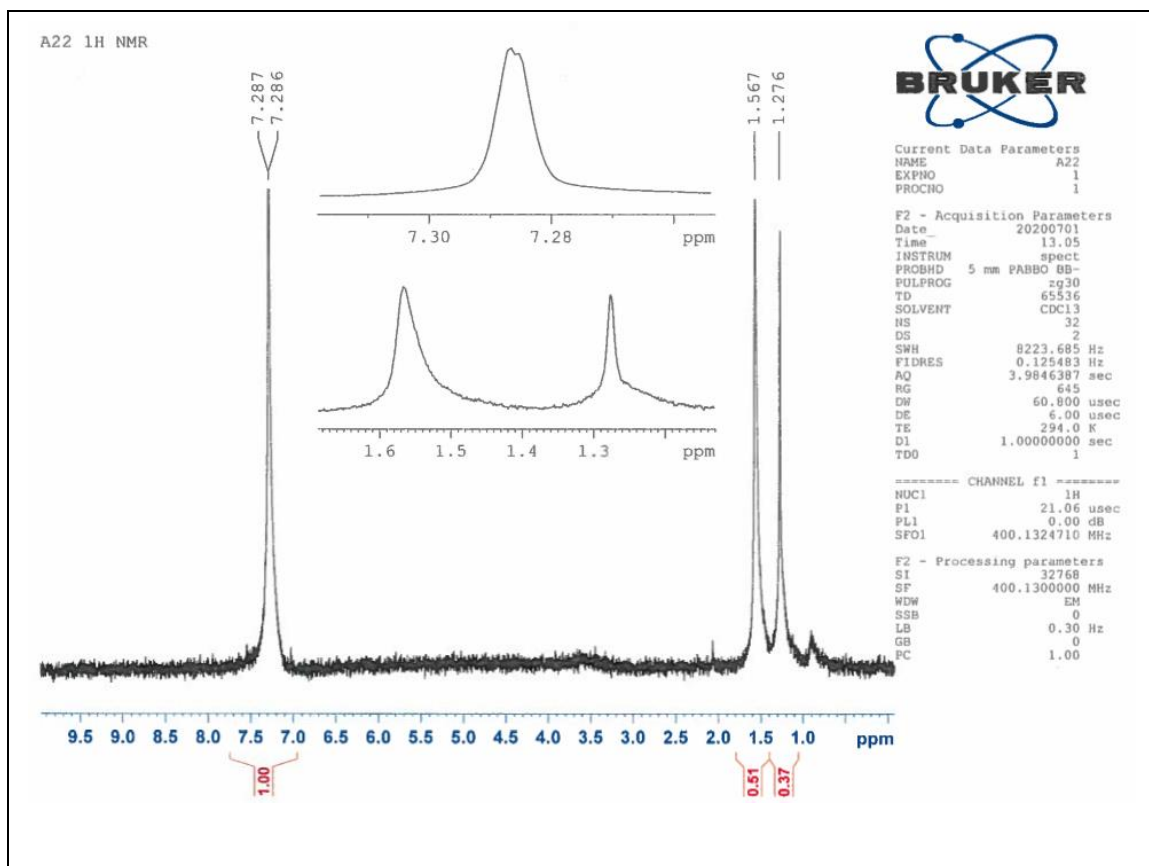




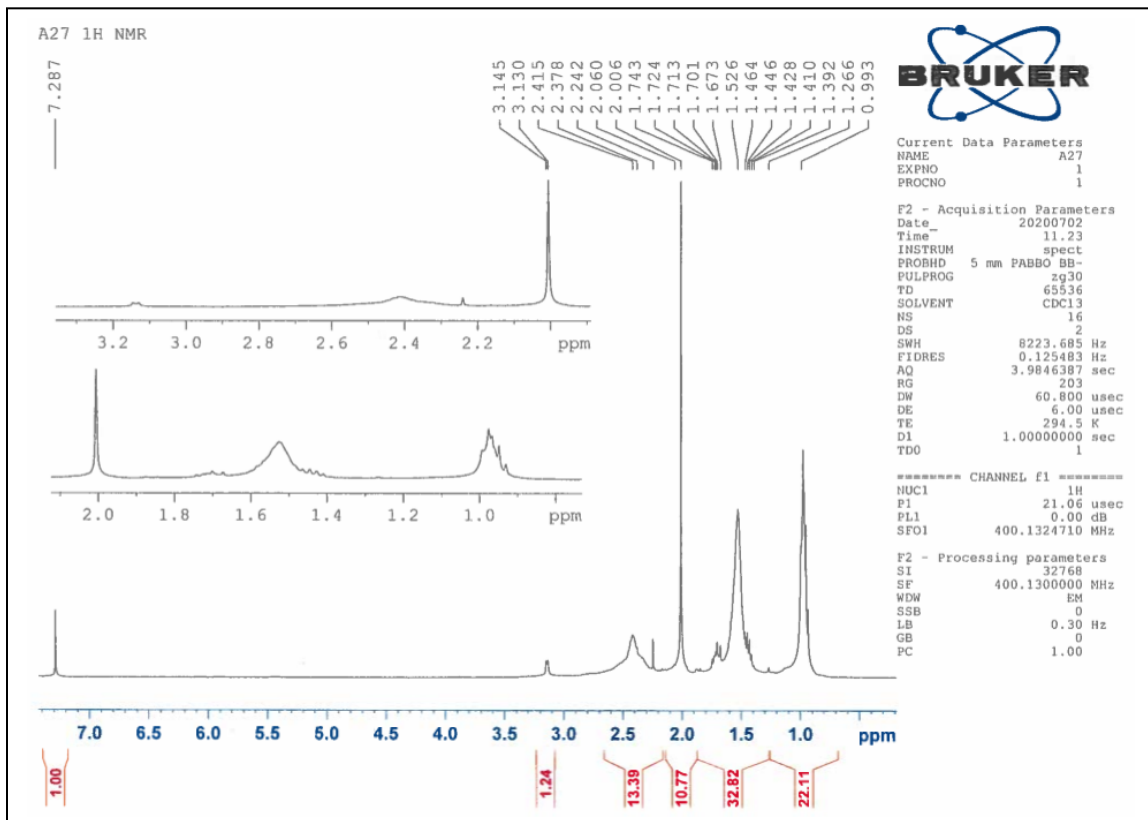
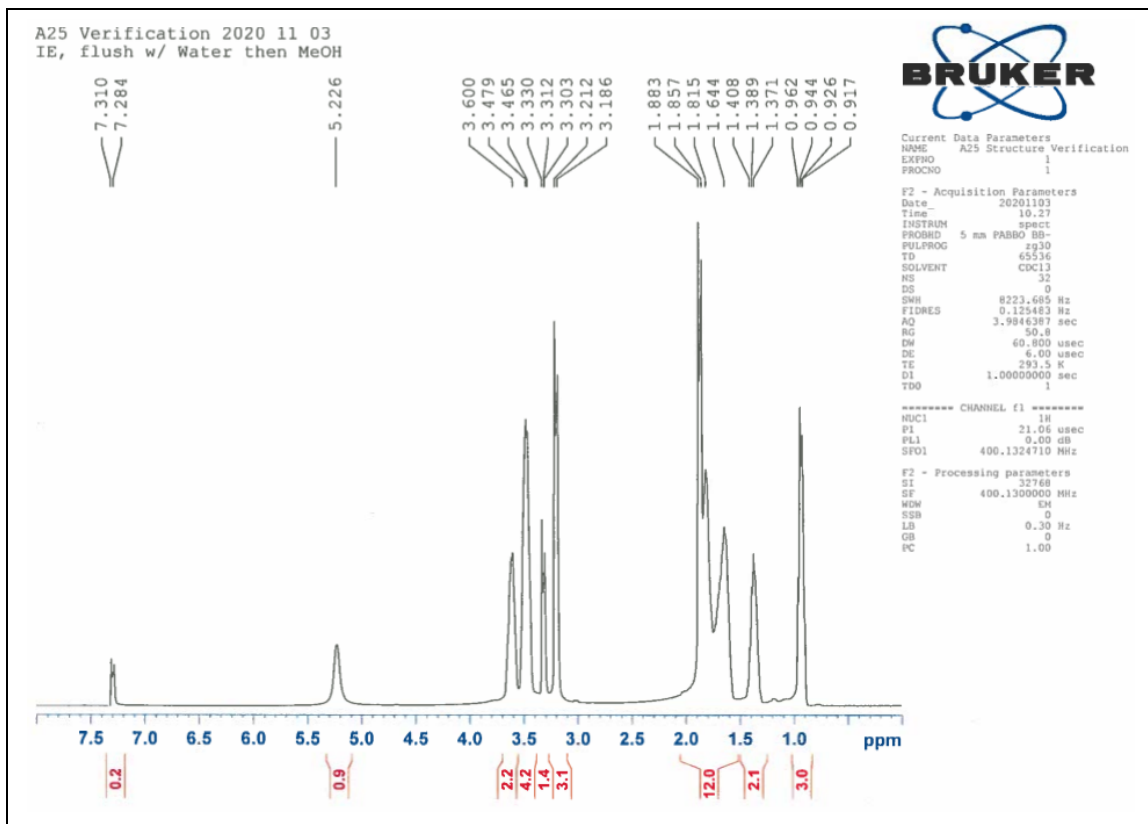




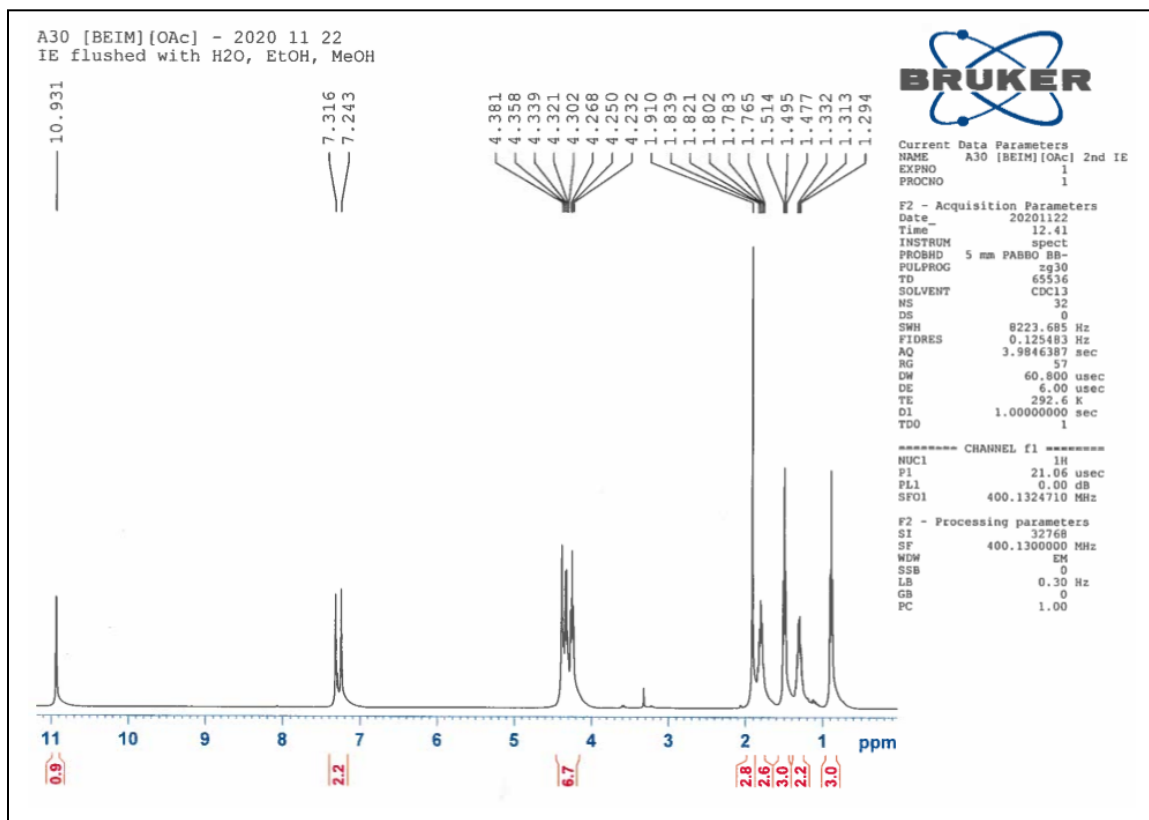
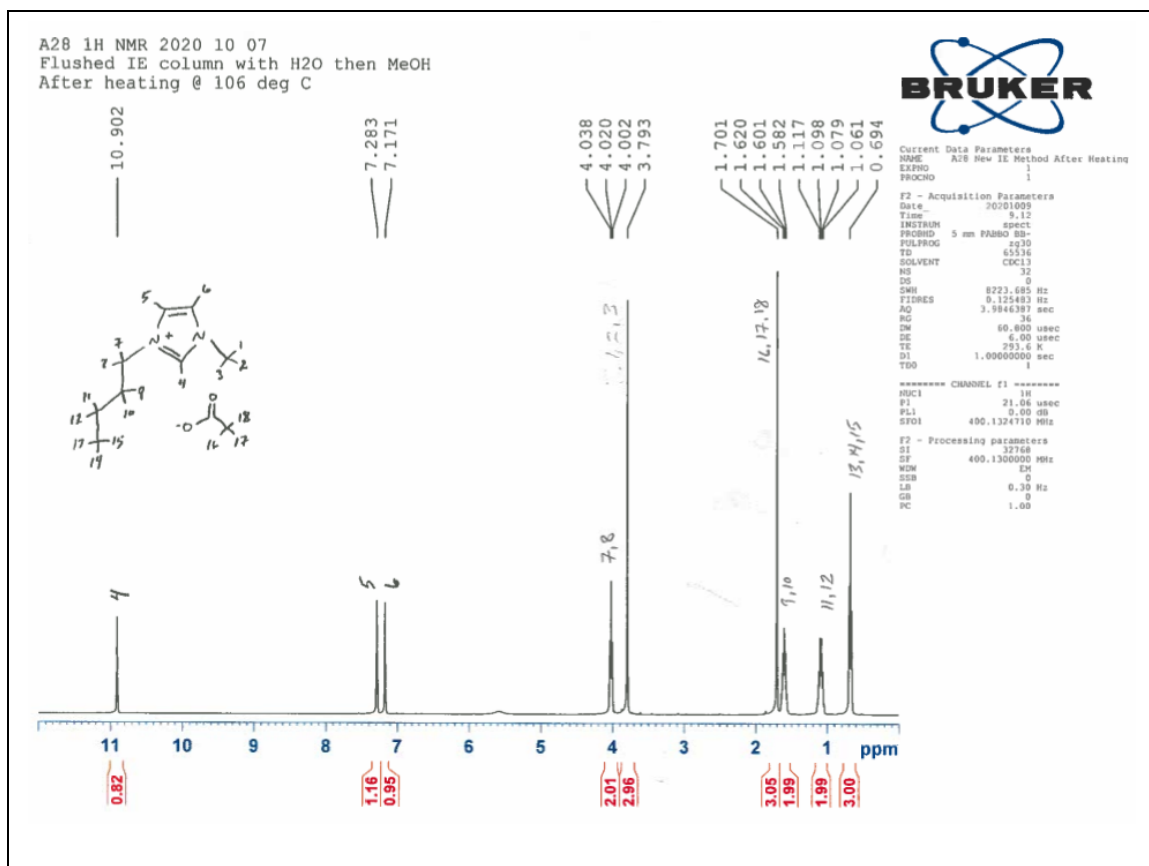




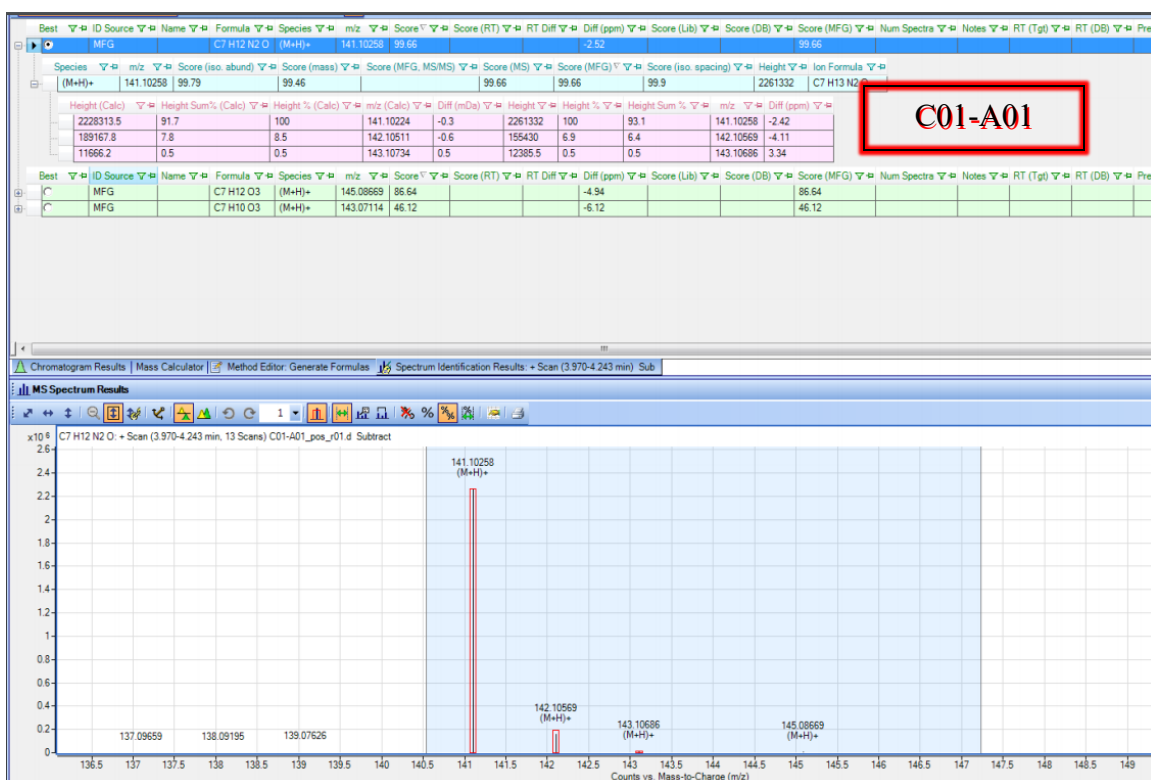
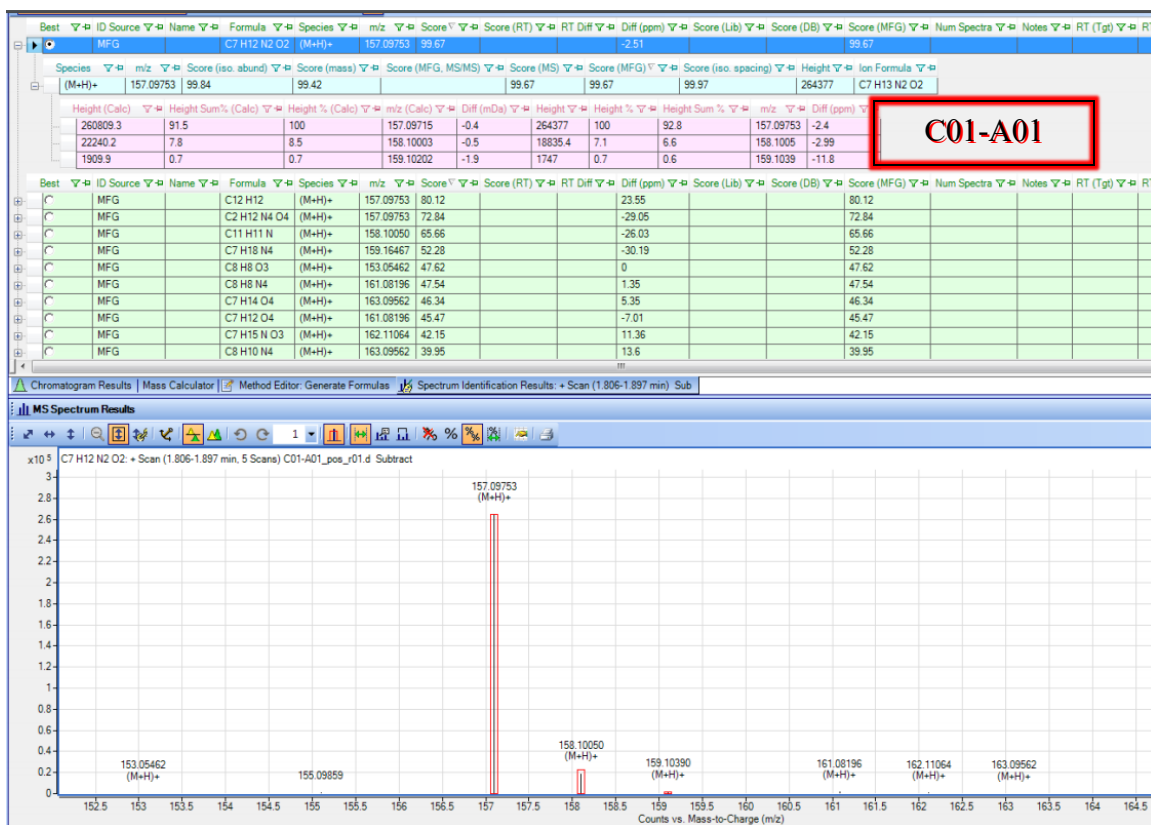


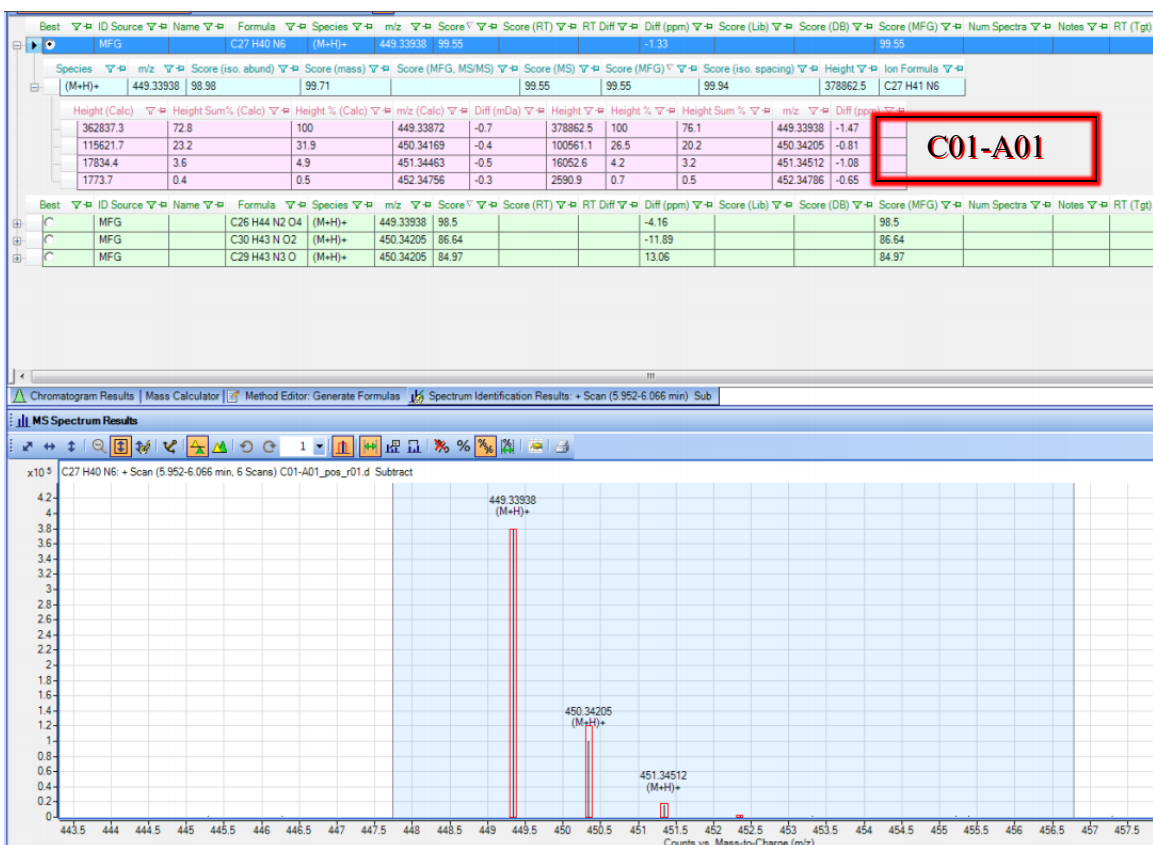




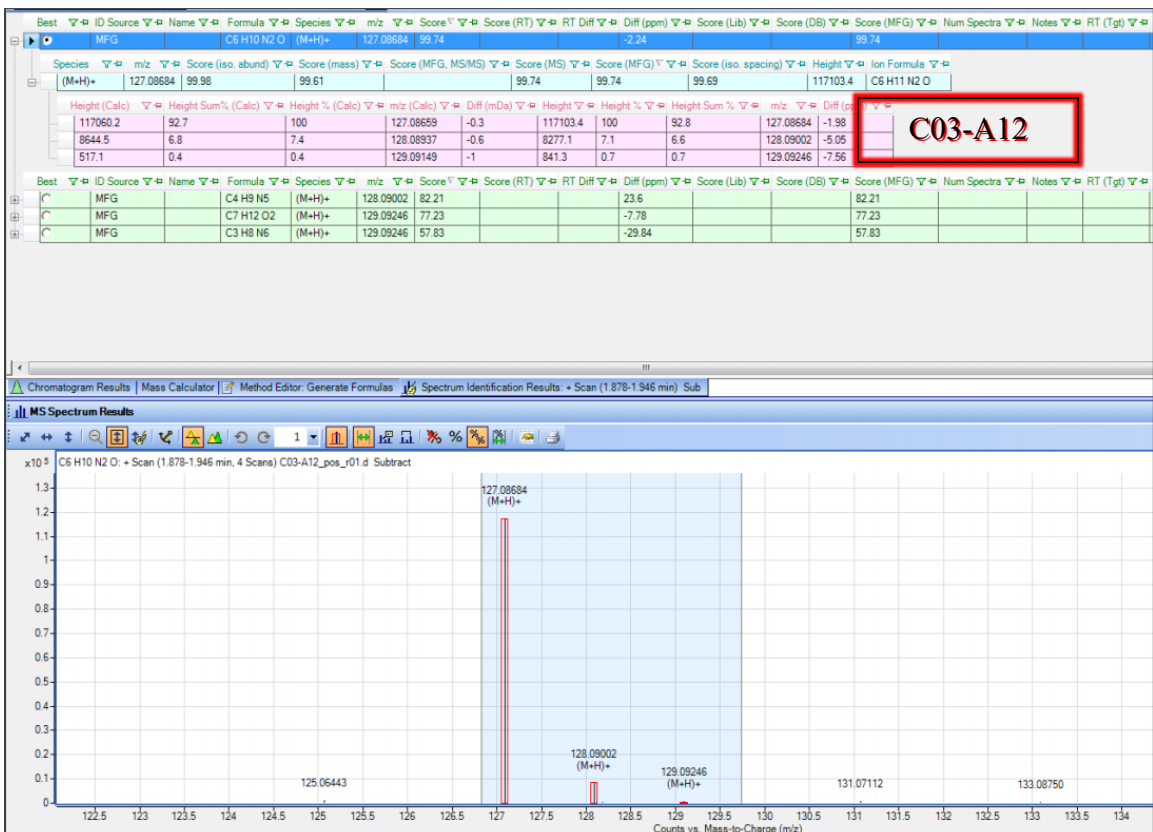


## LC-MS Spectra for Coal Dissolution Analysis





C01-A01



C03-A12

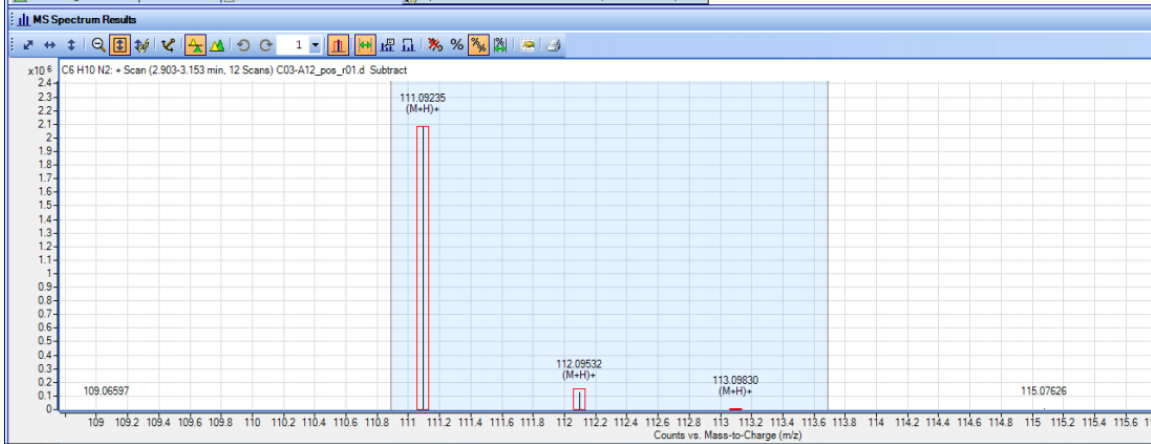
Best	ID Source	Name	Formula	Species	m/z	Score	Score (RT)	RT Diff	Diff (ppm)	Score (Lib)	Score (DB)	Score (MFG)	Num Spectra	Notes	RT (Tgt)	
MFG		C6 H10 N2	(M+H)+		111.09235	98.69			-6.25			98.63				
Species																
(M+H)+					111.09235	98.84			97.38			98.69			2082077.8	C6 H11 N2
Height (Calc)   Height Sum% (Calc)   Height % (Calc)   m/z (Calc)   Diff (mDa)   Height   Height %   Height Sum %   m/z   Diff (ppm)																
					2054829.8	93			111.09167	-0.7		2082077.8	100		111.09235	-6.09
					150960.4	6.8			7.3	112.09445	-0.9	124645.8	6	5.6	112.09532	-7.76
					4796.5	0.2			0.2	113.09712	-1.2	3863.2	0.2		113.0983	-10.45

Best	ID Source	Name	Formula	Species	m/z	Score	Score (RT)	RT Diff	Diff (ppm)	Score (Lib)	Score (DB)	Score (MFG)	Num Spectra	Notes	RT (Tgt)
MFG		C6 H8 O2	(M+H)+		113.06102	43.28			-11.75			43.28			
MFG		C6 H6 O2	(M+H)+		111.04543	42.82			-12.51			42.82			
MFG		C7 H12 O	(M+H)+		113.09830	36.4			-19.71			36.4			

C03-A12

Chromatogram Results | Mass Calculator | Method Editor: Generate Formulas | Spectrum Identification Results - Scan (2.903-3.153 min) Sub



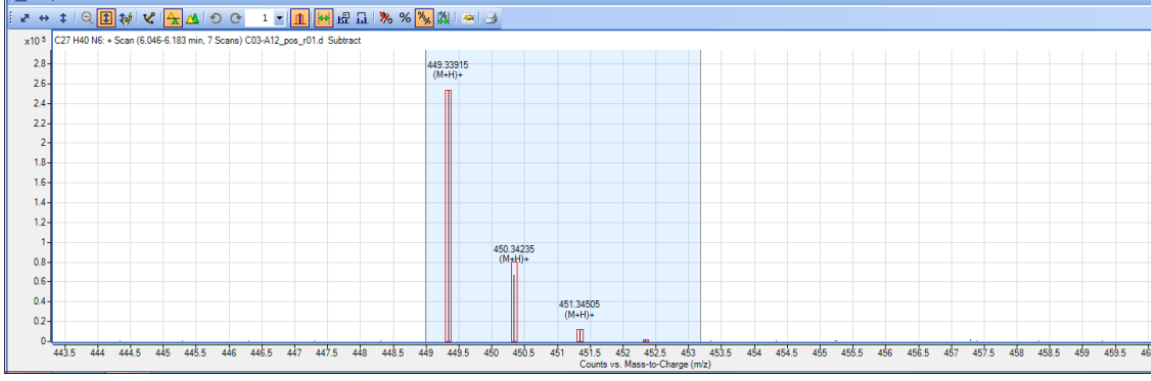
Best	ID Source	Name	Formula	Species	m/z	Score	Score (RT)	RT Diff	Diff (ppm)	Score (Lib)	Score (DB)	Score (MFG)	Num Spectra	Notes	RT (Tgt)	RT (DB)	Precursor
MFG		C27 H40 N6	(M+H)+		449.33915	99.6			-1.05			99.6					
Species																	
(M+H)+					449.33915	98.94			99.82			99.6			253076.3		C27 H41 N6
Height (Calc)   Height Sum% (Calc)   Height % (Calc)   m/z (Calc)   Diff (mDa)   Height   Height %   Height Sum %   m/z   Diff (ppm)																	
					242845	72.8			100	449.33872	-0.4	253076.3	100	75.9	449.33915	-0.95	
					77385	23.2			31.9	450.34169	-0.7	67086.1	26.5	20.1	450.34235	-1.48	
					11936.5	3.6			4.9	451.34463	-0.4	11247.2	4.4	3.4	451.34505	-0.92	
					1187.1	0.4			0.5	452.34756	0.5	1944	0.8	0.6	452.34706	1.12	

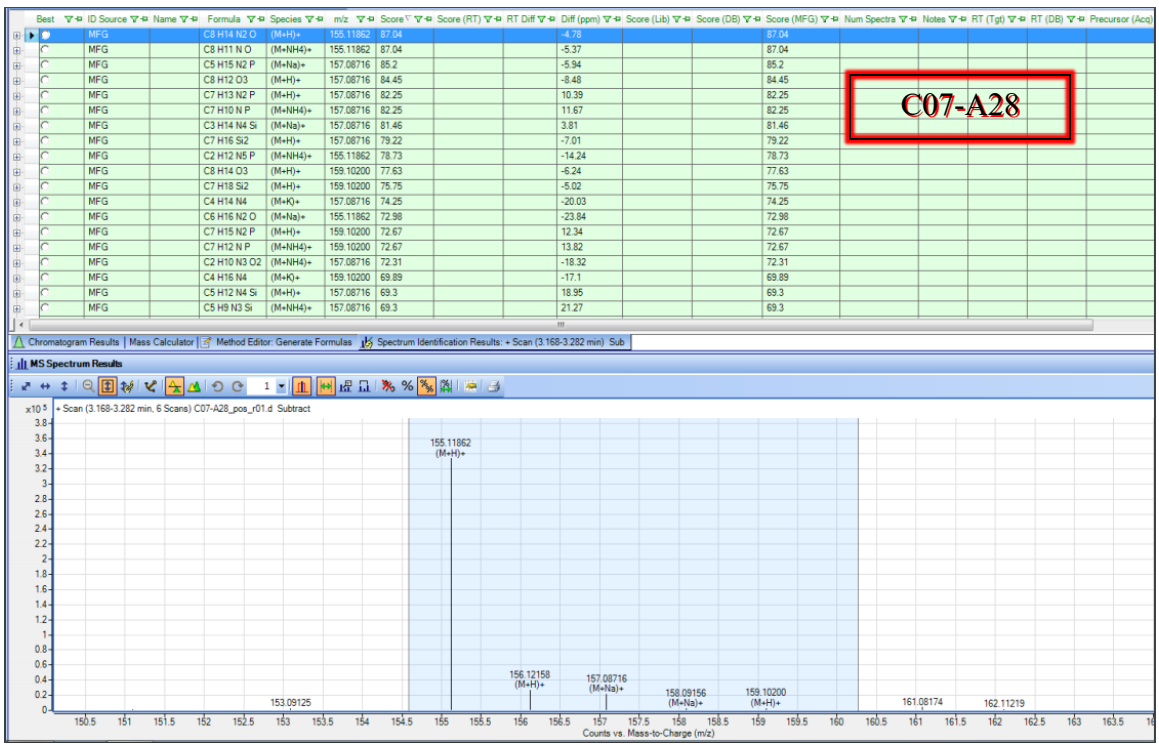
Best	ID Source	Name	Formula	Species	m/z	Score	Score (RT)	RT Diff	Diff (ppm)	Score (Lib)	Score (DB)	Score (MFG)	Num Spectra	Notes	RT (Tgt)	RT (DB)	Precursor
MFG		C26 H44 N2 O4	(M+H)+		449.33915	98.72			-3.88			98.72					
MFG		C23 H48 N2 O4 S	(M+H)+		449.33915	98.57			3.09			98.57					
MFG		C24 H50 O5 S	(M+H)+		451.34505	97.82			1.2			97.82					
MFG		C31 H44 O2	(M+H)+		449.33915	97.34			5.2			97.34					
MFG		C24 H43 N5 O3	(M+H)+		450.34235	97.34			3.52			97.34					
MFG		C24 H44 N6 S	(M+H)+		449.33915	96.61			5.9			96.61					
MFG		C25 H46 N4 O S	(M+H)+		451.34505	96.28			4.05			96.28					
MFG		C27 H47 N O2 S	(M+H)+		450.34235	95.37			-5.19			95.37					
MFG		C28 H42 N4 O	(M+H)+		451.34505	93.56			-2.69			93.56					

C03-A12

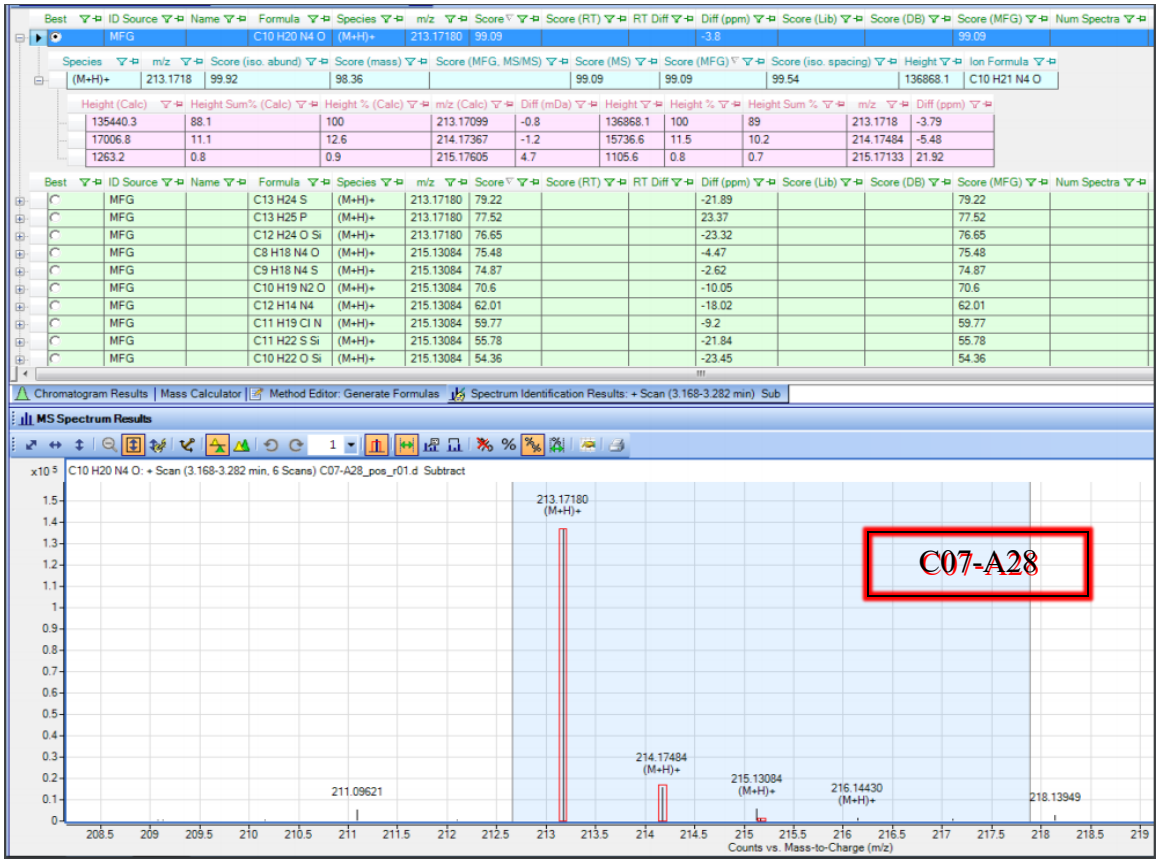
Chromatogram Results | Mass Calculator | Method Editor: Generate Formulas | Spectrum Identification Results - Scan (6.046-6.183 min) Sub





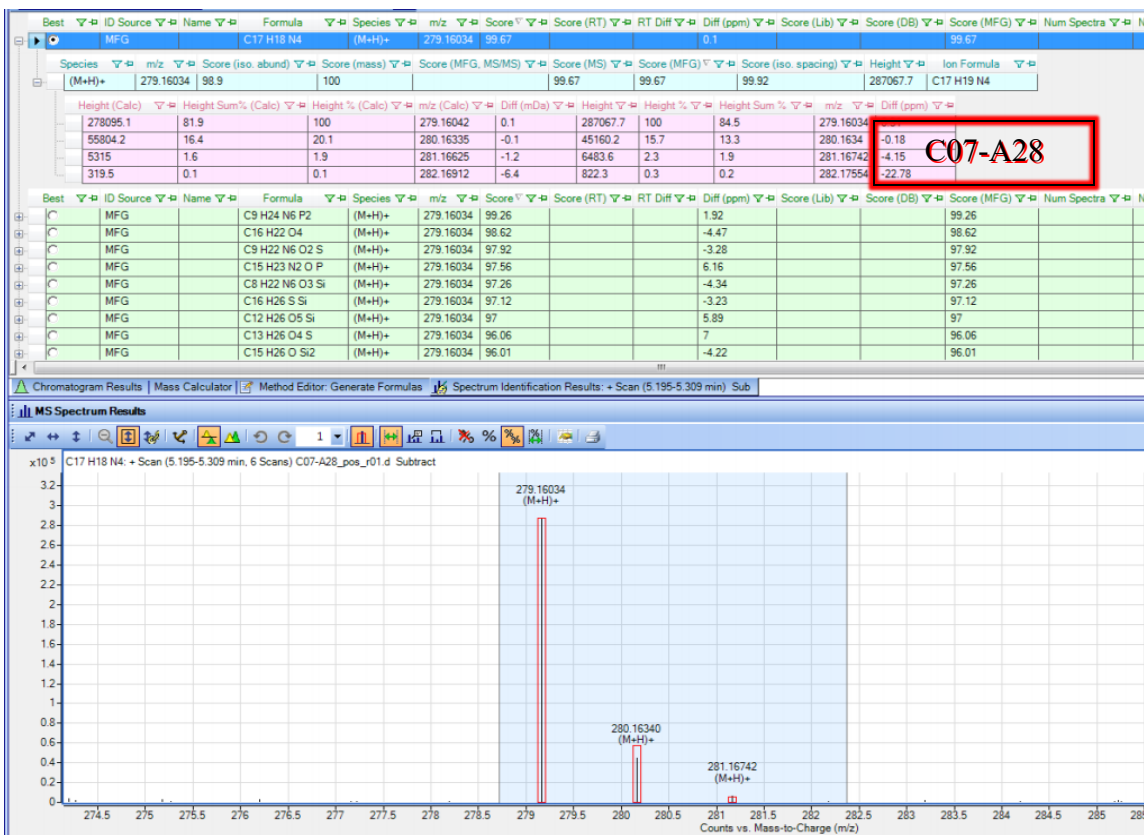


C07-A28

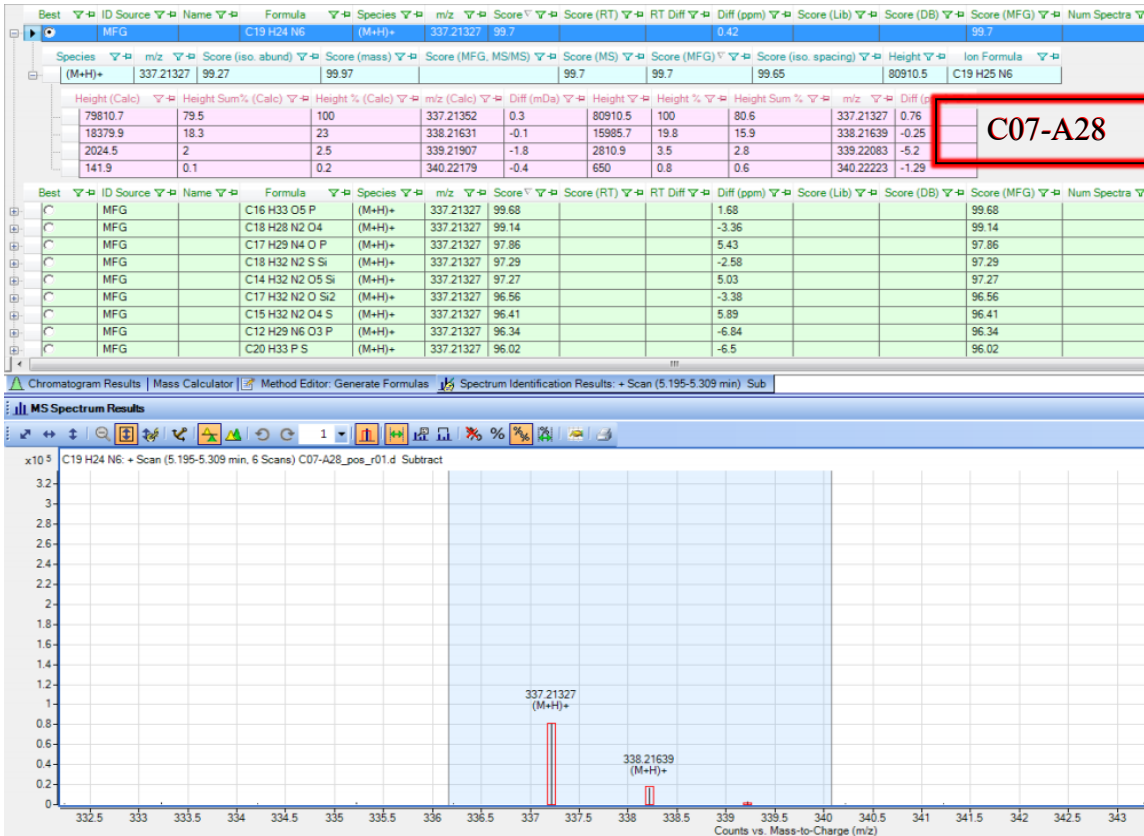


C07-A28

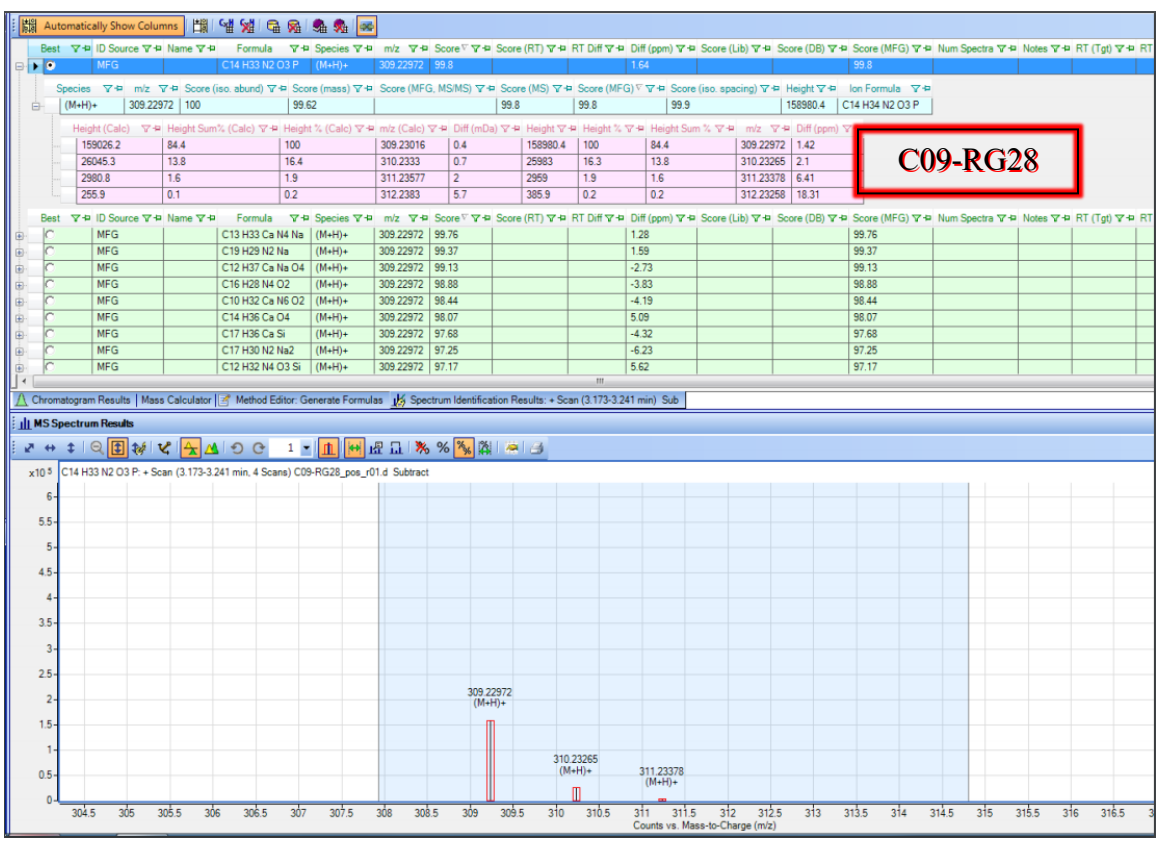
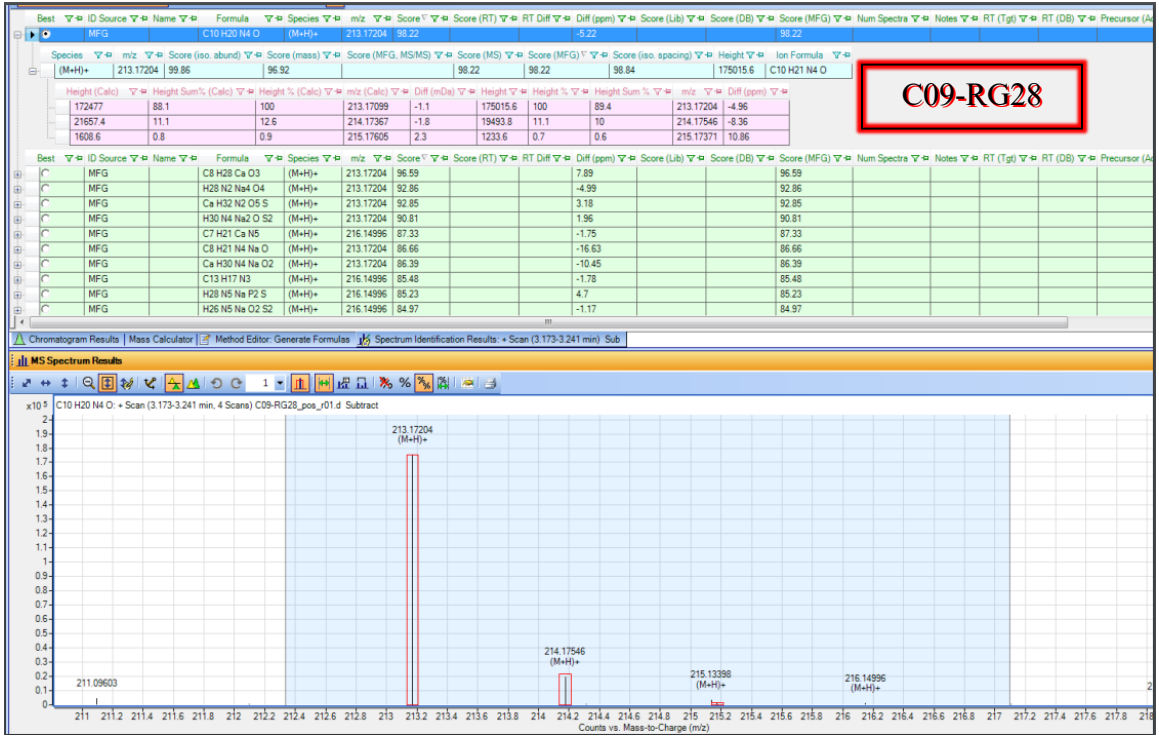




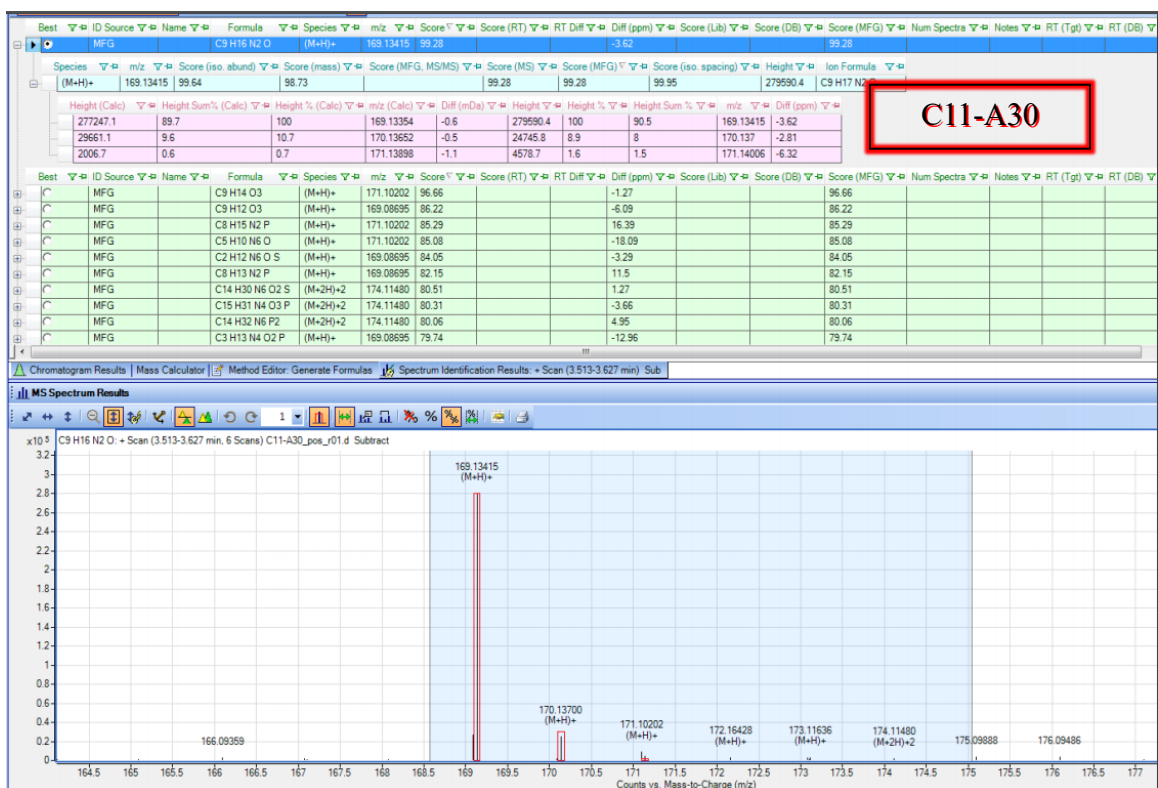
C07-A28



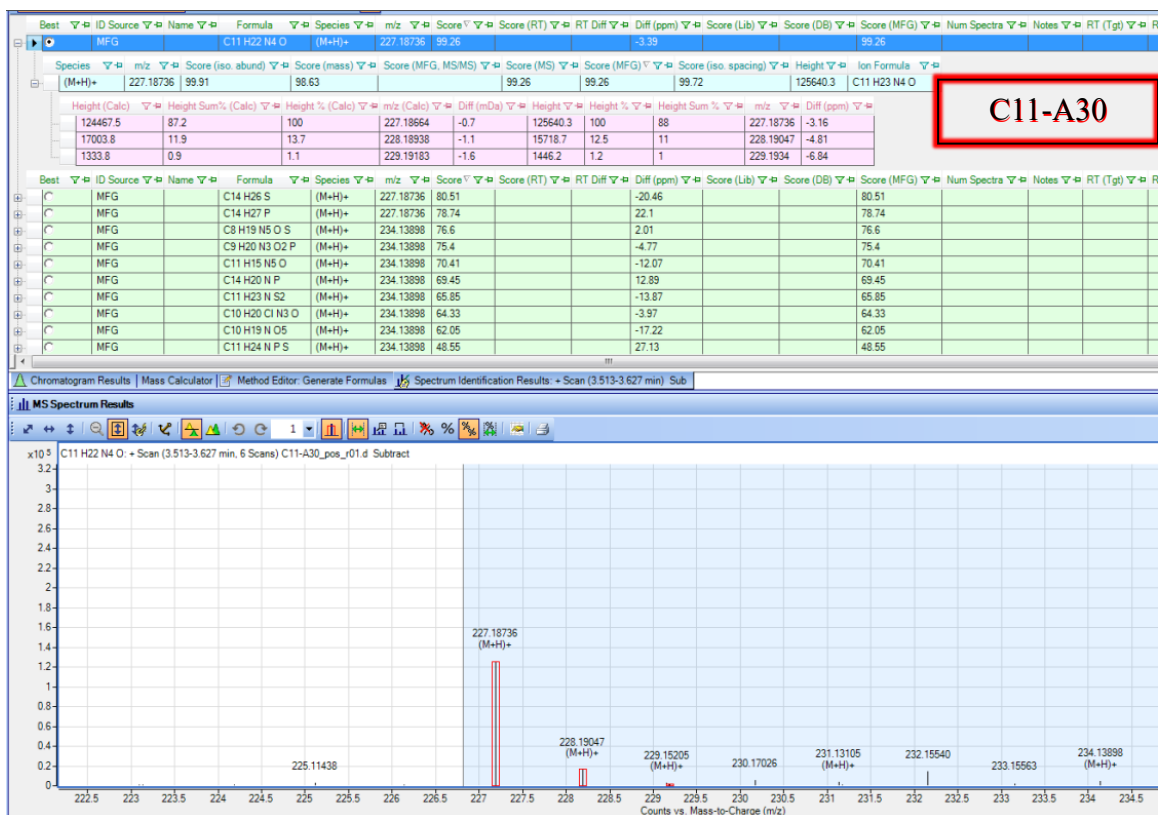
C07-A28



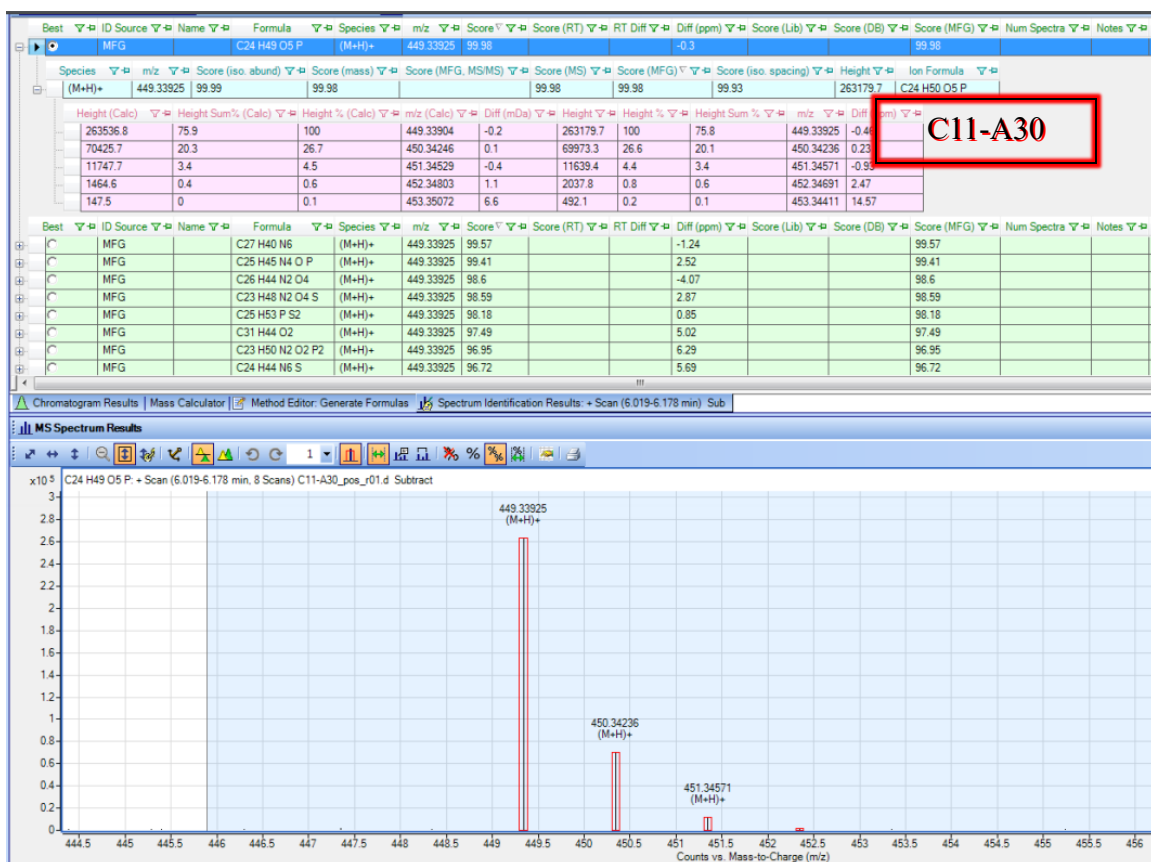




C11-A30



C11-A30



## SEM Images for Coal After Dissolution

**Figure D.iv.1:** SEM images of Lignite at 30x, 100x, 500x, and 1000x Zoom, accelerating voltage of 15 kV, and SS60.

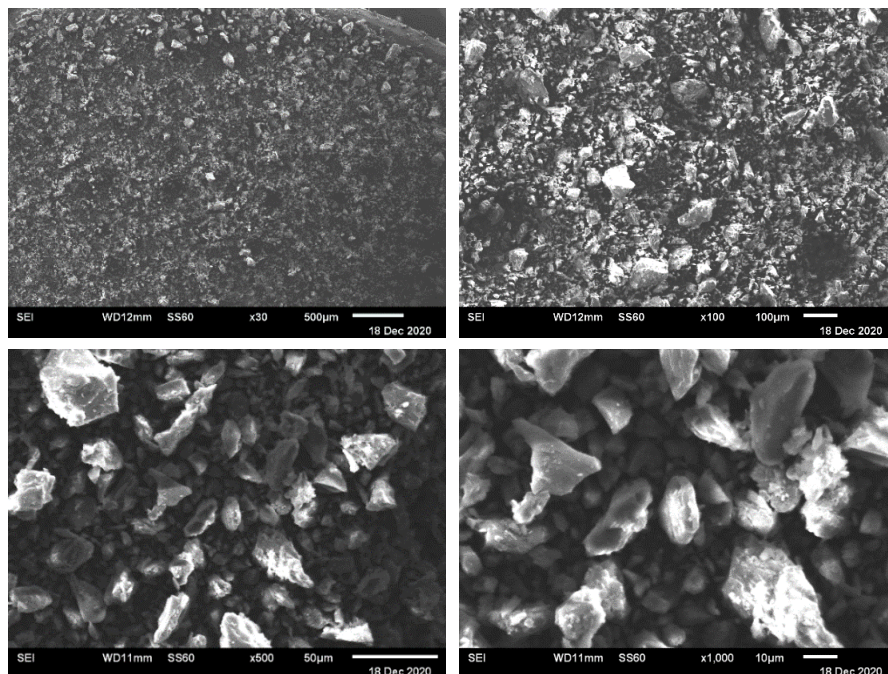


**Figure D.iv.2:** SEM images of C01-A01 at 30x, 100x, 500x, and 1000x Zoom, accelerating voltage of 15 kV, and SS60.

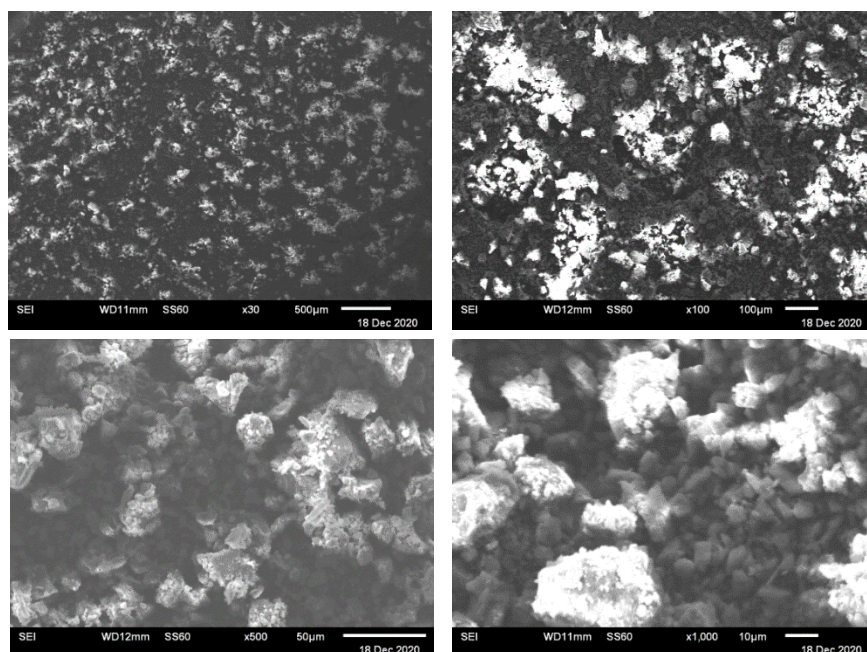




**Figure D.iv.3:** SEM images of C03-A12 at 30x, 100x, 500x, and 1000x Zoom, accelerating voltage of 15 kV, and SS60.

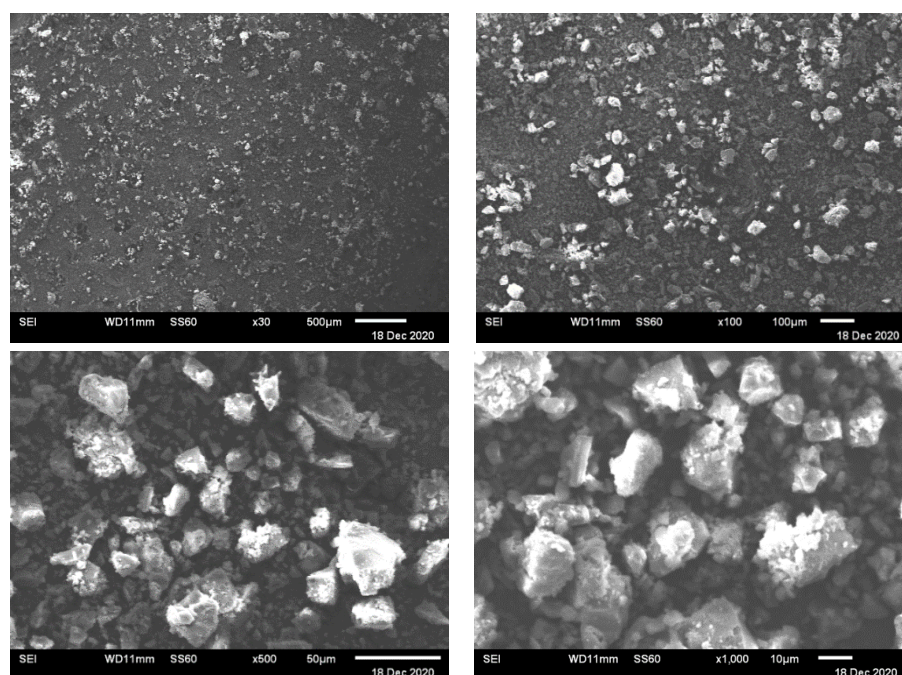


**Figure D.iv.04:** SEM images of C05-A16 at 30x, 100x, 500x, and 1000x Zoom, accelerating voltage of 15 kV, and SS60.

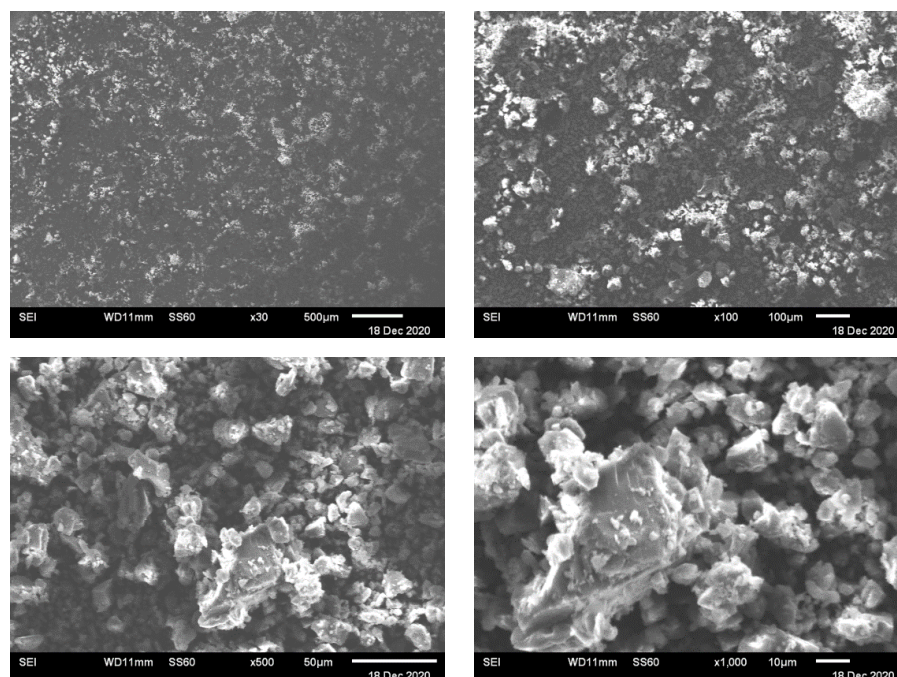


**Figure D.iv.5:** SEM images of C07-A28 at 30x, 100x, 500x, and 1000x Zoom, accelerating voltage of 15 kV, and SS60.

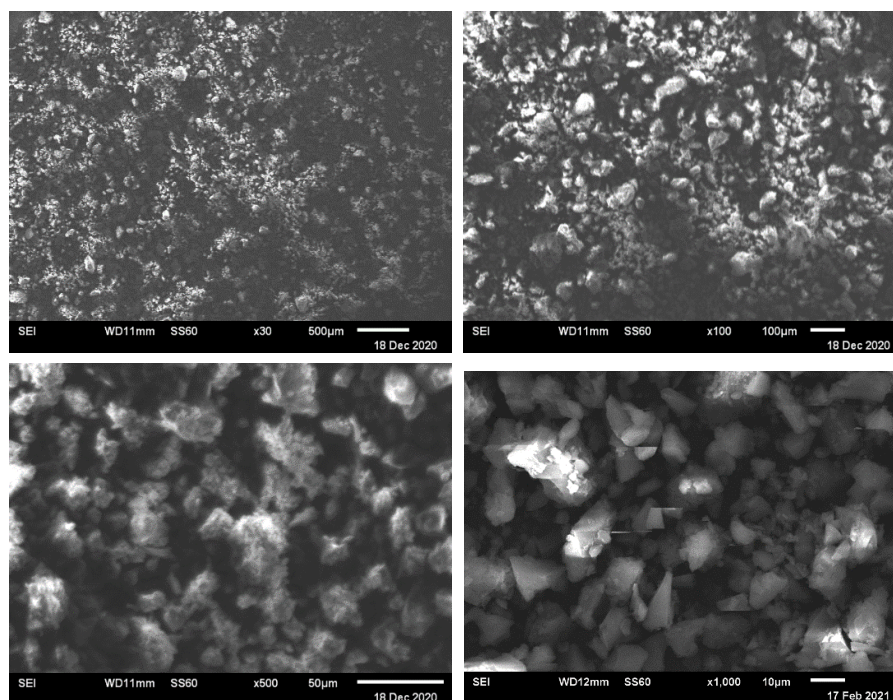


**Figure D.iv.6:** SEM images of C09-RG28 at 30x, 100x, 500x, and 1000x Zoom, accelerating voltage of 15 kV, and SS60.

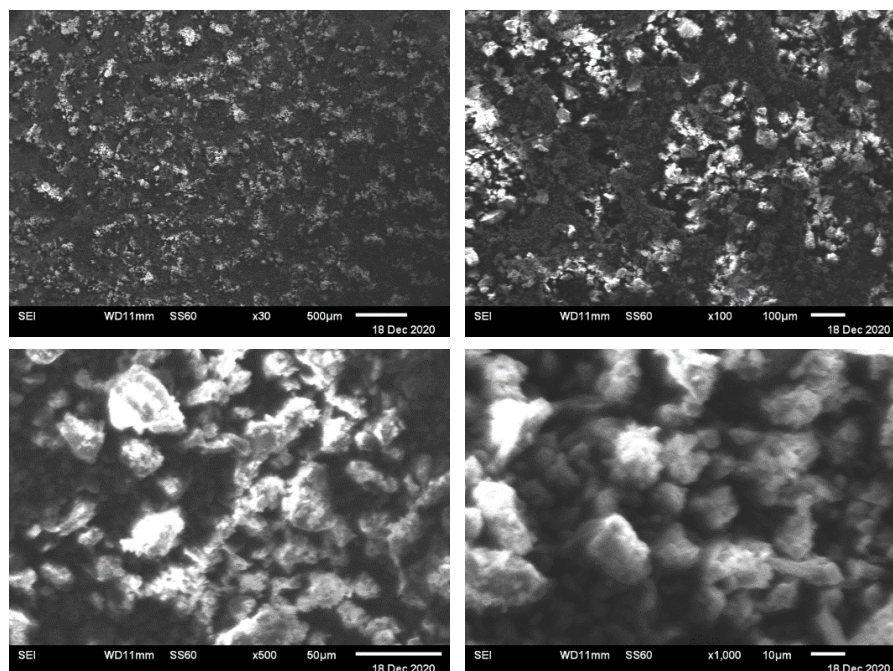
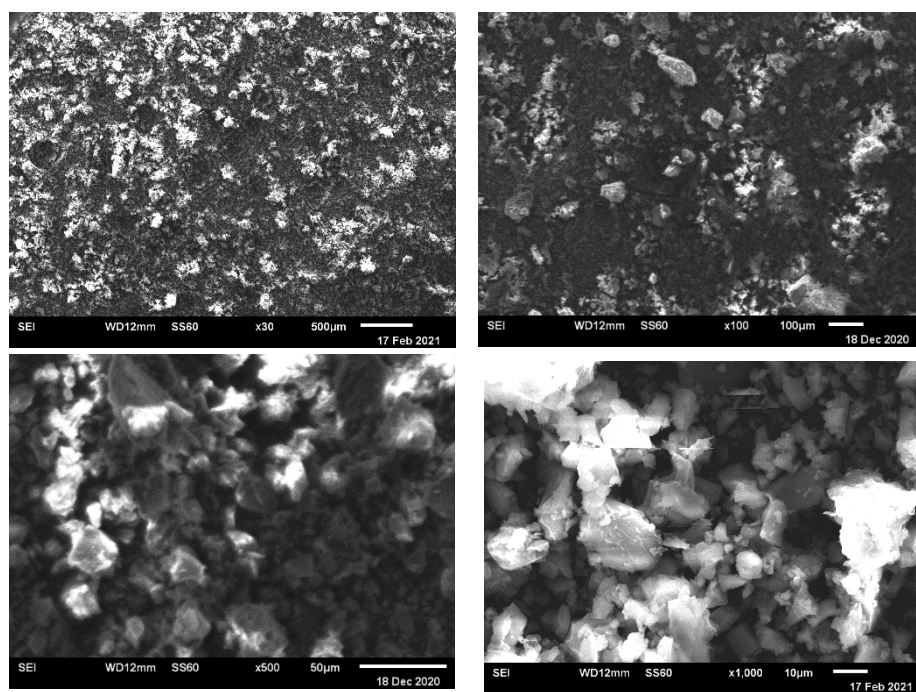


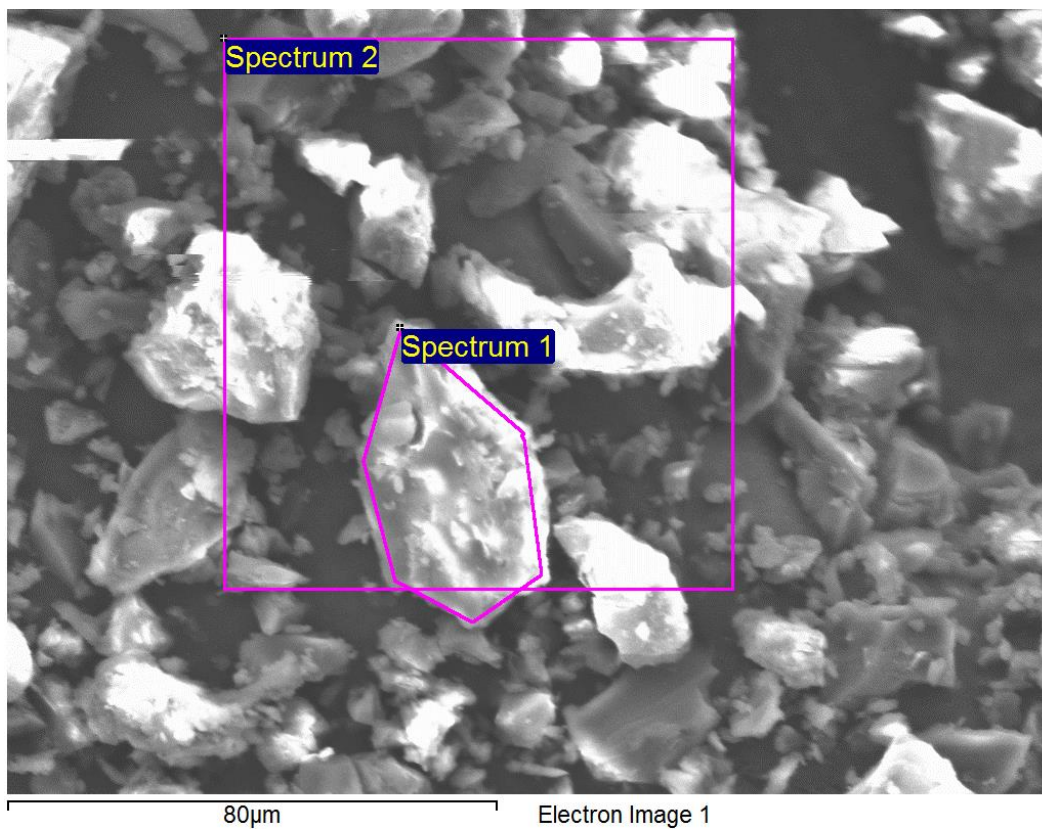


**Figure D.iv.7:** SEM images of C11-A30 at 30x, 100x, 500x, and 1000x Zoom, accelerating voltage of 15 kV, and SS60.



## EDS Analysis for Coal Samples After Dissolution

## Coal Dissolution - Au Coated Samples - Lignite 750x



Processing option : All elements analyzed (Normalized)

Spectrum	In stats.	C	O	Ca	Br	Total
Spectrum 1	Yes	63.73	35.47	0.50	0.30	100.00
Spectrum 2	Yes	65.68	33.22	0.78	0.33	100.00
Mean		64.70	34.34	0.64	0.32	100.00
Std. deviation		1.38	1.59	0.19	0.02	
Max.		65.68	35.47	0.78	0.33	
Min.		63.73	33.22	0.50	0.30	

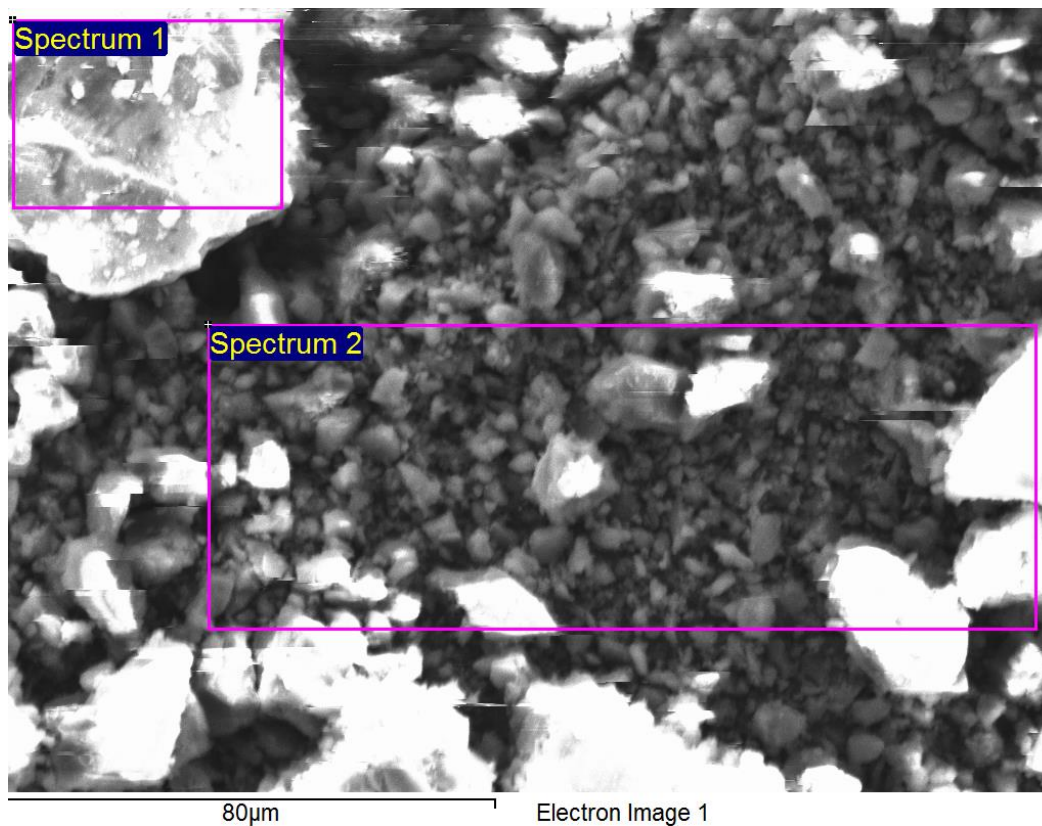
All results in weight%

Sample: Lignite 750x

Type: Default

Lignite, 15 kV, SS60, x750 Zoom

## Coal Dissolution - Au Coated Samples - C01-A01 - 750x



Processing option : All elements analyzed (Normalized)

Spectrum	In stats.	C	O	Ca	Br	Total
<b>Spectrum 1</b>	Yes	63.58	35.71	0.34	0.37	100.00
Spectrum 2	Yes	63.72	35.60	0.32	0.37	100.00
Mean		63.65	35.65	0.33	0.37	100.00
Std. deviation		0.10	0.08	0.02	0.01	
Max.		63.72	35.71	0.34	0.37	
Min.		63.58	35.60	0.32	0.37	

All results in weight%

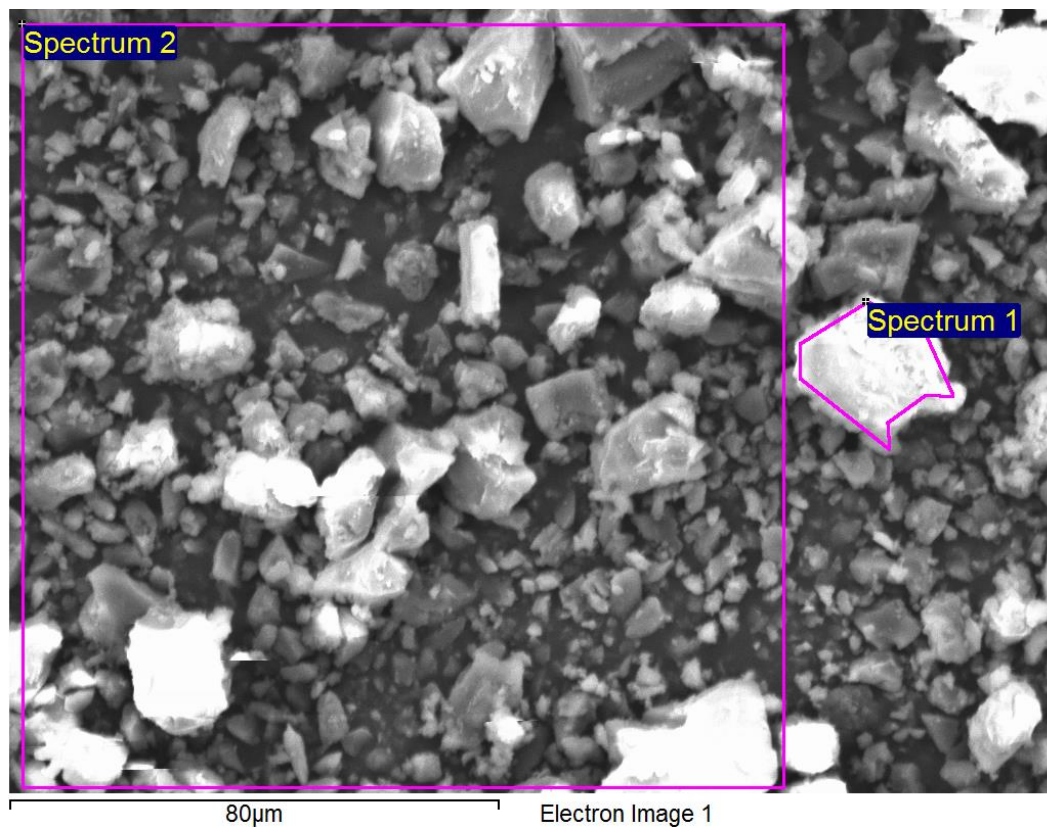
Sample: C01-A01 - 750x

Type: Default

C01-A01, 15 kV, SS60, x750 Zoom



## Coal Dissolution - Au Coated Samples - C03-A12 750x



Processing option : All elements analyzed (Normalized)

Spectrum	In stats.	C	O	Ca	Br	Total
Spectrum 1	Yes	69.68	29.80	0.31	0.21	100.00
Spectrum 2	Yes	67.98	31.58	0.21	0.23	100.00
Mean		68.83	30.69	0.26	0.22	100.00
Std. deviation		1.20	1.26	0.08	0.01	
Max.		69.68	31.58	0.31	0.23	
Min.		67.98	29.80	0.21	0.21	

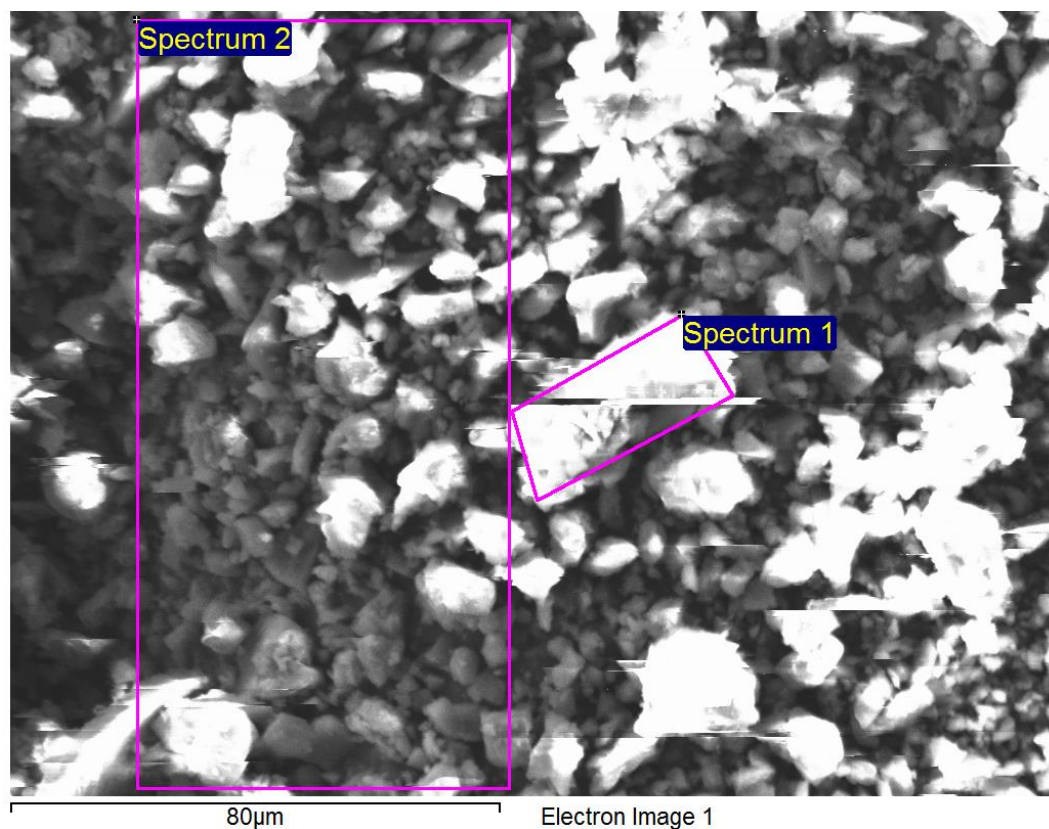
All results in weight%

Sample: C03-A12 750x

Type: Default

C03-A12, 15 kV, SS60, x750 Zoom

## Coal Dissolution - Au Coated Samples - C05-A16 750x Zoom



Processing option : All elements analyzed (Normalized)

Spectrum	In stats.	C	O	Ca	Br	Total
Spectrum 1	Yes	67.30	32.15	0.31	0.24	100.00
Spectrum 2	Yes	66.51	32.98	0.30	0.21	100.00
Mean		66.90	32.57	0.31	0.23	100.00
Std. deviation		0.56	0.59	0.01	0.02	
Max.		67.30	32.98	0.31	0.24	
Min.		66.51	32.15	0.30	0.21	

All results in weight%

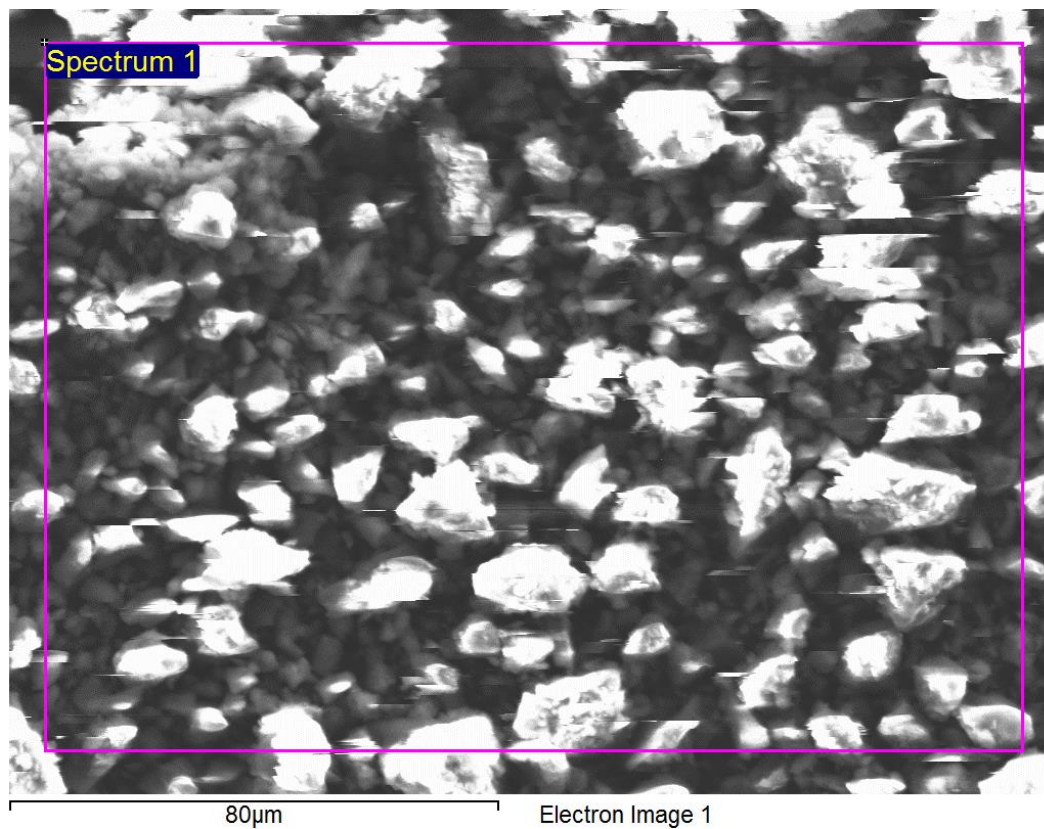
Processing option : All elements analyzed (Normalized)

Sample: C05-A16 750x Zoom

Type: Default

C05-A16, 15 kV, SS60, x750 Zoom

## Coal Dissolution - Au Coated Samples - C07-A28 750x



Processing option : All elements analyzed (Normalized)

Spectrum	In stats.	C	O	Ca	Br	Total
Spectrum 1	Yes	66.72	32.59	0.24	0.45	100.00
Mean		66.72	32.59	0.24	0.45	100.00
Std. deviation		0.00	0.00	0.00	0.00	
Max.		66.72	32.59	0.24	0.45	
Min.		66.72	32.59	0.24	0.45	

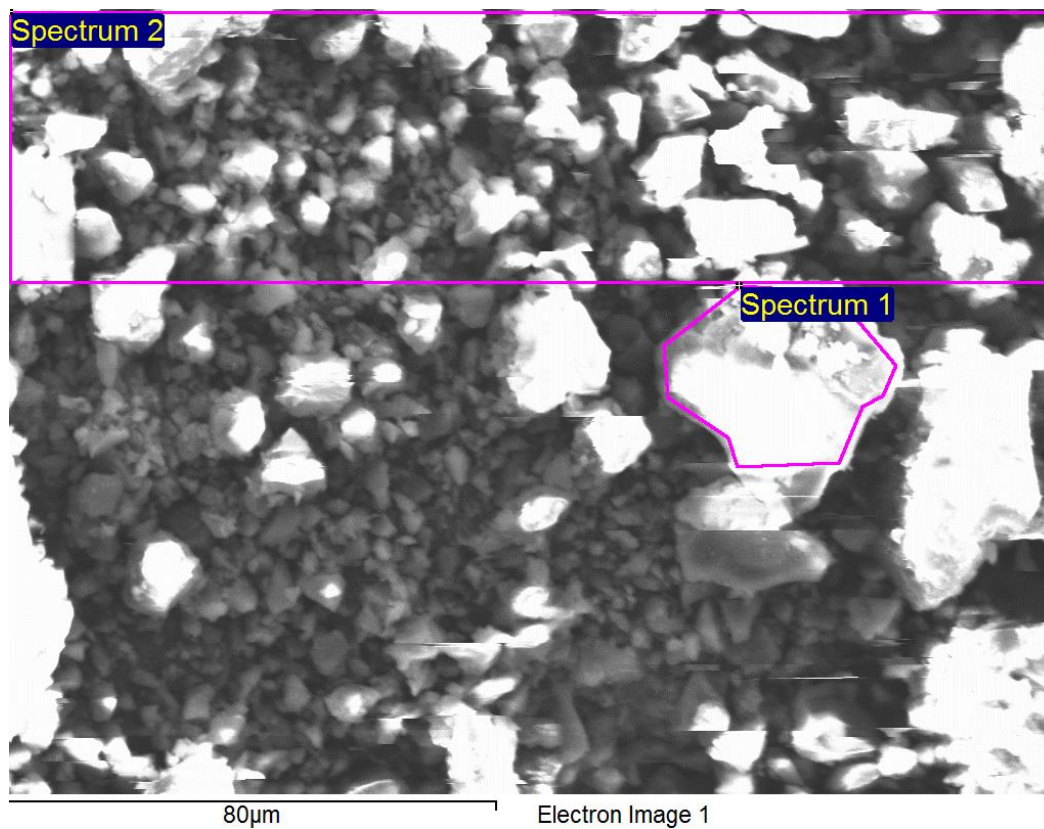
All results in weight%

Sample: C07-A28 750x

Type: Default

C07-A28, 15 kV, SS60, x750 Zoom

## Coal Dissolution - Au Coated Samples - C09-RG28 750x



Processing option : All elements analyzed (Normalized)

Spectrum	In stats.	C	O	Ca	Br	Total
Spectrum 1	Yes	65.96	33.51	0.14	0.38	100.00
Spectrum 2	Yes	66.84	32.31	0.38	0.47	100.00
Mean		66.40	32.91	0.26	0.42	100.00
Std. deviation		0.62	0.85	0.17	0.06	
Max.		66.84	33.51	0.38	0.47	
Min.		65.96	32.31	0.14	0.38	

All results in weight%

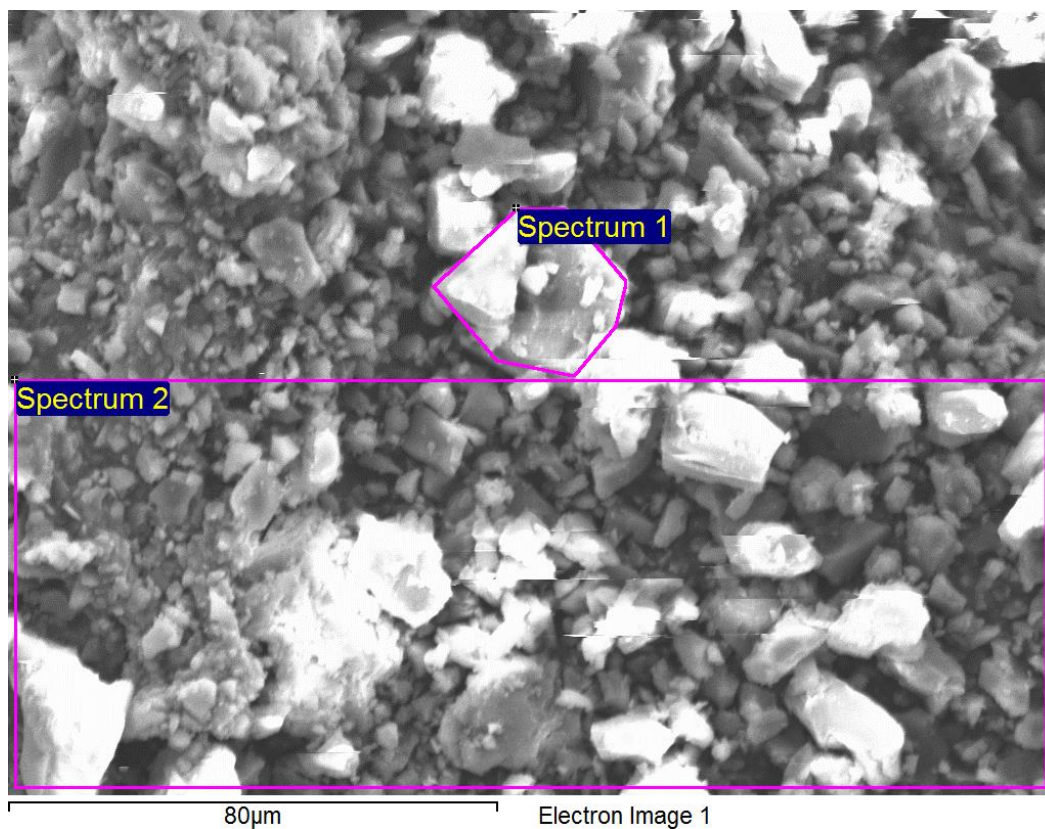
Sample: C09-RG28 750x

Type: Default

C09-RG28, 15 kV, SS60, 750x Zoom



## Coal Dissolution - Au Coated Samples - C11-A30 750x



Processing option : All elements analyzed (Normalized)

Spectrum	In stats.	C	O	Ca	Br	Total
Spectrum 1	Yes	66.64	32.63	0.17	0.56	100.00
Spectrum 2	Yes	65.03	34.18	0.32	0.48	100.00
Mean		65.83	33.40	0.24	0.52	100.00
Std. deviation		1.13	1.09	0.10	0.06	
Max.		66.64	34.18	0.32	0.56	
Min.		65.03	32.63	0.17	0.48	

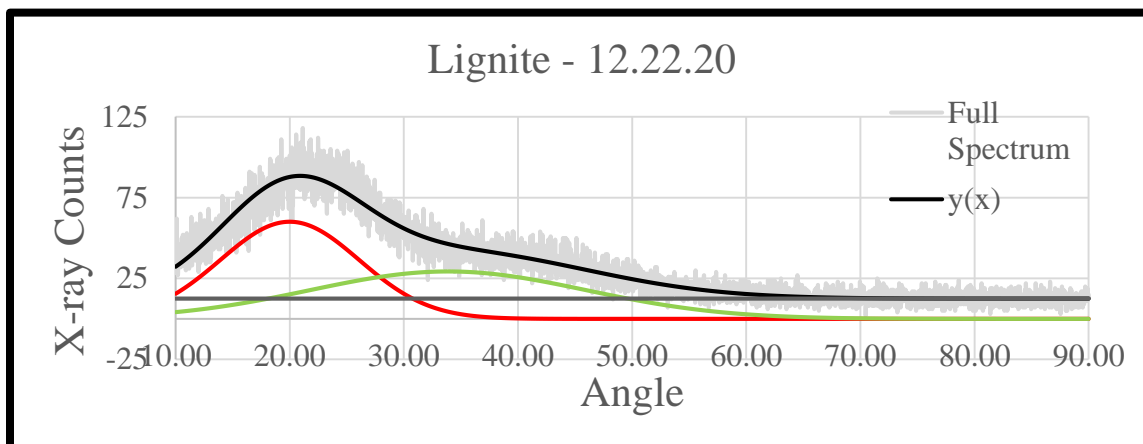
All results in weight%

Sample: C11-A30 750x

Type: Default

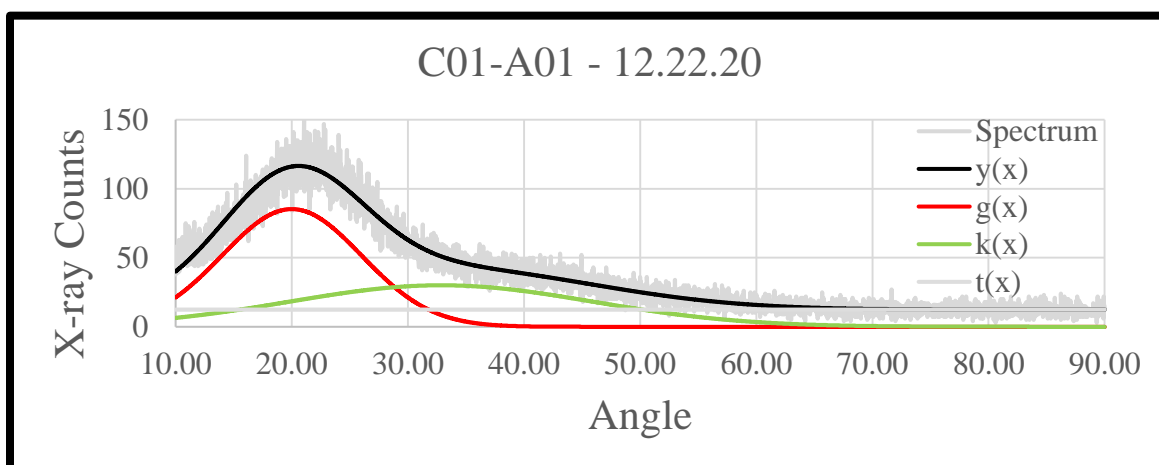
C11-A30, 15 kV, SS60, 750 x Zoom

## XRD Spectra and Calculations



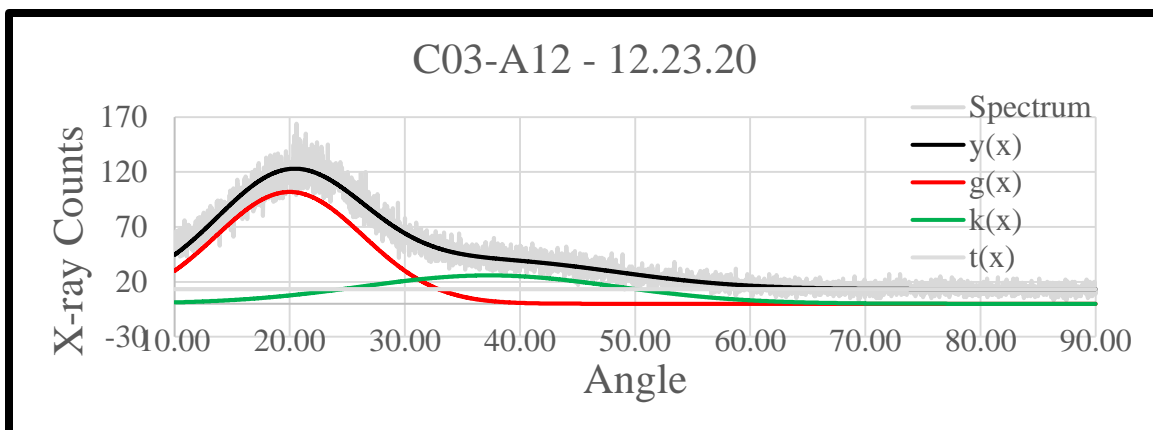
Lignite	$\gamma$ -band 100 (20°)	A	60.055	$\pi$ -band 002 (26°)	A	12.533	unk- band (~34°)	A	29.314
		$\mu$	20		$\mu$	26		$\mu$	33.870
		$\sigma$	6.0828		$\sigma$	$4.0177 \times 10^6$		$\sigma$	12.085

$C_{al}$	$C_{ar}$	$f_a$	$I_{\pi} / I_{\gamma}$	$L_a$	$L_c$	n
$1.2622 \times 10^8$	915.68	$7.2547 \times 10^{-6}$	0.20869	1.1419	$1.0906 \times 10^{-6}$	0.32000



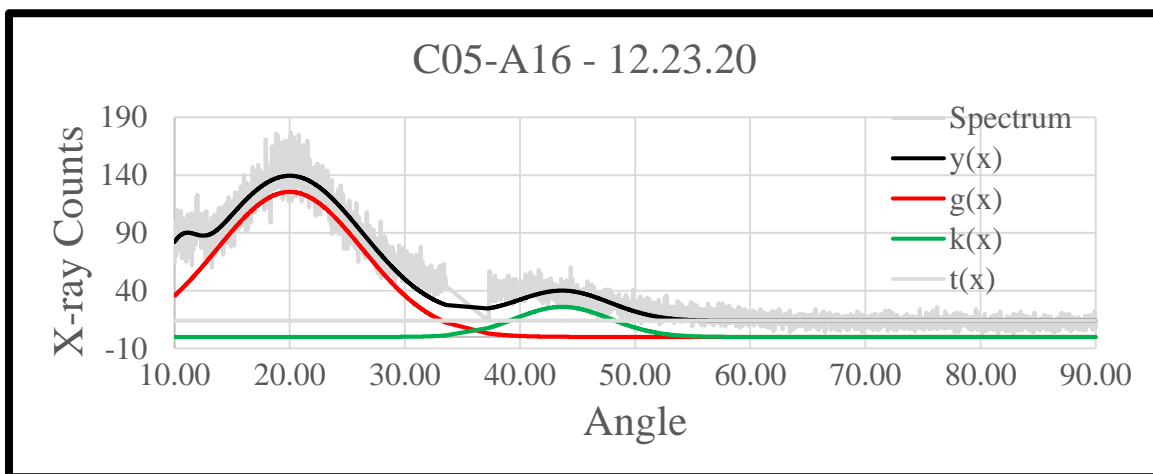
C01- A01	$\gamma$ -band 100 (20°)	A	85.248	$\pi$ -band 002 (26°)	A	12.377	unk- band (~34°)	A	30.063
		$\mu$	20		$\mu$	26		$\mu$	32.863
		$\sigma$	6.0018		$\sigma$	$4.0177 \times 10^6$		$\Sigma$	13.032

$C_{al}$	$C_{ar}$	$f_a$	$I_{\pi} / I_{\gamma}$	$L_a$	$L_c$	n
$1.2465 \times 10^8$	1282.5	$1.0289 \times 10^{-5}$	0.14519	1.1574	$1.0906 \times 10^{-6}$	0.32000



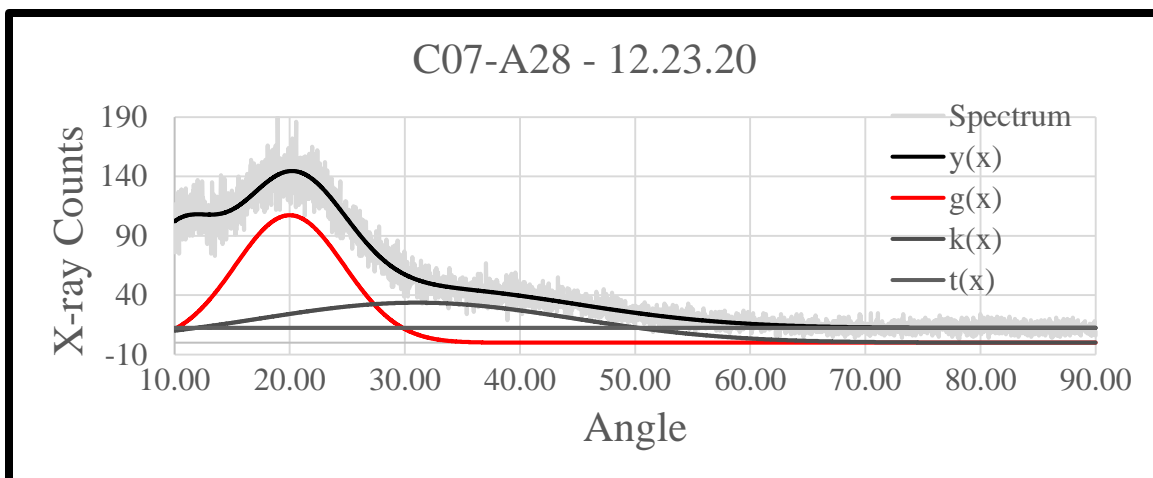
C03-A12	$\gamma$ -band 100 (20°)	A	101.83	$\pi$ -band 002 (26°)	A	13.335	unk-band (~34°)	A	25.829
		$\mu$	20		$\mu$	26		$\mu$	37.304
		$\sigma$	6.4000		$\sigma$	$4.0177 \times 10^6$		$\sigma$	11.064

$C_{al}$	$C_{ar}$	$f_a$	$I_\pi / I_\gamma$	$L_a$	$L_c$	$n$
$1.3430 \times 10^8$	1633.6	$1.2164 \times 10^{-5}$	0.13095	1.0853	$1.0906 \times 10^{-6}$	0.32000



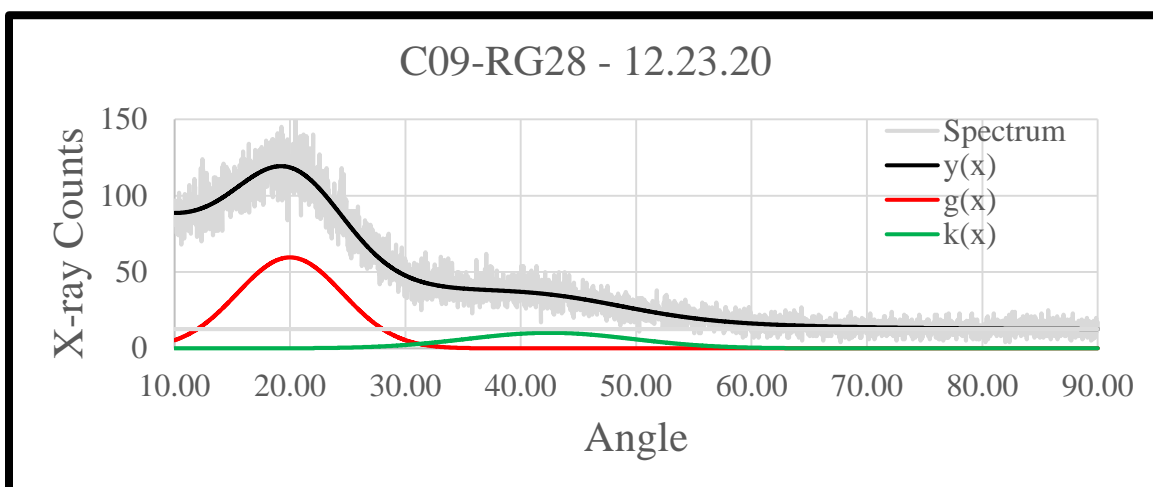
C05-A16	$\gamma$ -band 100 (20°)	A	125.53	$\pi$ -band 002 (26°)	A	13.948	unk-band (~34°)	A	26.008
		$\mu$	20		$\mu$	26		$\mu$	43.679
		$\sigma$	6.3143		$\sigma$	$4.0177 \times 10^6$		$\sigma$	4.1262

$C_{al}$	$C_{ar}$	$f_a$	$I_\pi / I_\gamma$	$L_a$	$L_c$	$n$
$1.4047 \times 10^8$	1986.84	$1.4144 \times 10^{-5}$	0.11111	1.1001	$1.0906 \times 10^{-6}$	0.32000



C07-A28	$\gamma$ -band 100 (20°)	A	107.34	$\pi$ -band 002 (26°)	A	12.360	unk-band (~34°)	A	33.690
		$\mu$	20		$\mu$	26		$\mu$	31.073
		$\sigma$	4.7280		$\sigma$	$4.0177 \times 10^6$		$\sigma$	13.612

$C_{al}$	$C_{ar}$	$f_a$	$I_\pi / I_\gamma$	$L_a$	$L_c$	$n$
$1.2448 \times 10^8$	1272.1	$1.0220 \times 10^{-5}$	0.11515	1.4692	$1.0906 \times 10^{-6}$	0.32000



C09-RG28	$\gamma$ -band 100 (20°)	A	59.585	$\pi$ -band 002 (26°)	A	12.555	unk-band (~34°)	A	10.203
		$\mu$	20		$\mu$	26		$\mu$	42.535
		$\sigma$	4.5611		$\sigma$	$4.0177 \times 10^6$		$\sigma$	7.1627

$C_{al}$	$C_{ar}$	$f_a$	$I_\pi / I_\gamma$	$L_a$	$L_c$	$n$
$1.2644 \times 10^8$	681.23	$5.3878 \times 10^{-6}$	0.21071	1.5229	$1.0906 \times 10^{-6}$	0.32000



